UNIVERSITÀ DEGLI STUDI DELL'AQUILA

DIPARTIMENTO DI SCIENZE FISICHE E CHIMICHE

DOTTORATO DI RICERCA IN SCIENZE FISICHE E CHIMICHE

XXXV CYCLE

SSD FIS/06

Stratospheric sulfate aerosols and their impact on climate:
from volcanoes to proposed human interventions

Author:
Ilaria Quaglia

Tutor:
Prof. Giovanni Pitari

Ph.D. Coordinator:
Prof. Massimiliano Aschi

A.Y. 2021/2022

2

UNIVERSITÀ DEGLI STUDI DELL'AQUILA

Abstract

Dipartimento di Scienze Fisiche e Chimiche

Doctor of Philosophy

Stratospheric sulfate aerosols and their impact on climate: from volcanoes to proposed human interventions

by Ilaria Quaglia

Aerosols are fine solid, liquid or mixed-phase particles suspended in the air. Their chemical composition, concentration, size and shape is highly variable in the troposphere, while the stratosphere contains a persistent layer of predominantly sulfate particles, due to the different sources and transport mechanisms involved in the two layers of the atmosphere.

Aerosols are a key component of the Earth's atmosphere because they affect air quality, meteorology and climate. They interact directly with solar and planetary radiation through its scattering and absorption, altering the Earth's energy balance and, in turn, affecting changes in temperature and precipitation. Indirect interaction with radiation occurs through modification of cloud reflectivity, as aerosols act as cloud condensation nuclei for cloud droplets and ice particles and thus affect the droplet size and number concentration.

The aim of this thesis is to provide an overview of atmospheric aerosols covering main sources and sinks, the chemical and microphysical processes involved, and the optical properties which affect aerosol interaction with radiation. The main focus is on sulfate aerosols, which are dominant in the stratosphere, because of their implications in climate change.

Sulfate aerosols scatter the incoming solar radiation and absorb the infrared radiation resulting in a cooling of the surface and heating of the region of the stratosphere where they resides, which in turn impact the atmospheric circulation, the stratospheric heterogeneous chemistry and the hydrological cycle.

The main contributor to stratospheric aerosols under perturbed condition are volcanic eruptions, which can inject sulfate precursor gases directly into the stratosphere along with ash, water vapor and other compounds; therefore, due to the climatic impact of sulfate aerosols, volcanic eruptions are a natural cause of climate change. Here we study the evolution of the simulated stratospheric aerosol cloud following the well-observed June 1991 Mount Pinatubo event, comparing six interactive stratospheric aerosol microphysics models with different observations, and

we show where there is agreement among the models and where there are differences in relation to differences among the dynamical, microphysical, and chemical modeling schemes.

Simulating volcanic eruptions can be considered a test case for evaluating climate models and interest in assessing the reliability of climate models in simulating stratospheric sulfur injection has recently increased because of the similarity to geoengineering experiments, aimed to counteract global warming. Here we show the advances in Stratospheric Aerosol Injection (SAI) which is one of the geoengineering strategies and involves the continuous injection of sulfate precursor gases. We propose, among the SAI strategies proposed so far, the increased surface emission of carbonyl sulfide, a sulfate precursor gas in the stratosphere, evaluate its risks and benefits compared with the more commonly studied sulfur dioxide injection strategy. Finally, we assess the hydrological impact of large explosive volcanic eruptions occurring during SAI deployment, considering a medium and large case of large volcanic eruption and define the risks and whether an SAI strategy could be modified in order to limit them.

Contents

List of Figures

List of Tables

List of Abbreviations

AMIP	**A**tmospheric **M**odel **I**ntercomparison **P**roject
AOD	**A**erosol **O**ptical **D**epth
AVHRR	**A**dvanced **V**ery **H**igh **R**esolution **R**adiometer
BDC	**B**rewer-**D**obson **C**irculation
BC	**B**lack **C**arbon
BrO_x	Bromine
BVOC$_s$	**B**iogenic **V**olatile **O**rganic **C**ompounds
CCMI	**C**hemistry-**C**limate **M**odel **I**nitiative
ClO_x	Chlorine
CORR	Correlation
CO_2	Carbon dioxide
COS	Carbonyl sulfide
CS_2	Carbon disulfide
DMS	Dimethyl sulfide
GeoMIP6	**Geo**engineering **M**odel **I**ntercomparison **P**roject Phase **6**
GHGs	Greenhouse Gases
GloSSAC	**Glo**bal **S**pace-based **S**tratospheric **A**erosol **C**limatology
GWP	**G**lobal **W**arming **P**otential
HCl	Hydrogen chloride
H_2S	Hydrogen sulfide
H_2O	Water vapor
H_2SO_4	Sulfuric acid
HErSEA	**H**istorical **Er**uptions **S**O_2 **E**mission **A**ssessment
HIRS	**H**igh **R**esolution **I**nfrared **R**adiation **S**ounder
ISA-MIP	**I**nteractive **S**tratospheric **A**erosol-**M**odel **I**ntercomparison **P**roject
ITCZ	**I**ntertropical **C**onvergence **Z**one
LW	Longwave
NH	**N**orthern **H**emisphere
NO_x	Nitrogen oxides
OC	**O**rganic **C**arbon
ODS	**O**zone-**D**epleting **S**ubstance
OH	Hydroxyl radical
OPC	**O**ptical **P**article **C**ounter
PI	Preindustrial
PSC	**P**olar **S**tratospheric **C**louds

$\mathbf{Q}_{ext}$	Extinction efficency
$\mathbf{Q}_{sca}$	Scattering efficiency
$\mathbf{Q}_{abs}$	Absorption efficiency
QBO	**Q**uasi-**B**iennal **O**scillation
RF	**R**adiative **F**orcing
RMSD	**R**oot-**M**ean-**S**quare **D**ifference
SAD	**S**urface **A**rea **D**ensity
SAGE	**S**tratospheric **A**erosol and **G**as **E**xperiment
SAI	**S**tratospheric **A**erosol **I**njection
SD	**S**tandard **D**eviation
SH	**S**outhern **H**emisphere
$\mathbf{SO}_2$	Sulfur dioxide
$\mathbf{SO}_x$	Sulfur oxides
SPARC	**S**tratosphere-troposphere **P**rocesses **A**nd their **R**ole in **C**limate
SRM	**S**olar **R**adiation **M**odification
SS	**S**ea **S**alt
SSTs	**S**ea **S**urface **T**emperatures
SW	Shortwave
$\mathbf{T}_0$	Global mean temperature
$\mathbf{T}_1$	Interhemispheric temperature gradient
$\mathbf{T}_2$	Equator-to-pole temperature gradient
TTL	**T**ropical **T**ropopause **L**ayer
UTLS	**U**pper **T**roposphere-**L**ower **S**tratosphere
UV	Ultraviolet

Introduction

Aerosols are a fundamental component of Earth's atmosphere because they affect air quality, meteorology, and climate. Aerosols are defined as fine solid, liquid or mixed-phase particles suspended in the air, and their concentration, chemical composition, size and shape are highly variable across the planet and determine their impact on climate. We can make a clear distinction between aerosols in the troposphere, the first layer of the atmosphere up to the tropopause, which lies between 8 and 16 km depending on latitude, and the stratosphere, above the tropopause up to ∼50 km, because of the different sources and processes involved in their formation and removal. This thesis focuses on the stratospheric aerosol layer and the impact on climate of its perturbation due to natural events or deliberate interventions.

The stratosphere normally contains a layer of aerosol particles that is *stable, constant in time and space, and composed mainly of sulfate particles* (Junge and Manson, 1961). Sulfate aerosols interact with radiation by scattering and absorption, and their enhancement results in global cooling of the Earth's surface and warming of the region of the stratosphere in which they reside, which in turn affects precipitation and atmospheric dynamics.

The formation of sulfate aerosols in stratosphere occurs through homogeneous or heterogeneous nucleation of sulfuric acid, present in the stratosphere from the oxidation of sulfur dioxide (SO_2). The main contributor of sulfur compounds to the stratosphere under background conditions is carbonyl sulfide (COS), which is a long-lived species that allows it to be transported up to the stratosphere where it takes part in chemical reactions that lead to the formation of SO2 (Khalil and Rasmussen, 1984; Ulshofer et al., 1996). Other sulfur compounds such as carbon disulfide, dimethyl sulfide, hydrogen sulfide and SO_2 emitted at the surface have too short a lifetime to be transported to the stratosphere however large explosive volcanic eruptions might inject these sulfur precursor gases directly in the stratosphere.

Large explosive volcanic eruptions are considered a natural source of changes in climate because of the strong perturbation they produce on the stratospheric aerosol layer. The Mount Pinatubo eruption of 1991, one of the largest volcanic eruptions in the past 100 years, along with those of Mount Agung in 1963 and Mount El Chichón in 1982 (for which fewer observations are available), and it injected between 4 and 22 Tg of SO_2 (Bluth et al., 1992a; Guo et al., 2004a) and produced a global cooling up to -0.3 K in 1992-1993 (Dutton and Christy, 1992; Hansen et al., 1992; Canty et al., 2013).

The cooling effect observed due to increases in stratospheric aerosol loading after large volcanic eruptions has prompted modeling studies of the viability of intentional stratospheric aerosol enhancement to offset the climate effects of increasing concentrations of greenhouse gases (Budyko, 1977; Crutzen, 2006). Stratospheric Aerosol Injection (SAI), which mimics volcanic eruptions by injecting aerosols or aerosol gas precursors into the stratosphere, is one of the strategies proposed under what is known as Solar Radiation Modification (SRM), a deliberate climate intervention aimed at changing the reflectivity of the atmosphere. The growing interest in SRM has highlighted the importance of assessing the reliability of chemical-climate models in reproducing the radiative forcing associated with stratospheric aerosol injection, which, by analogy, can be verified by comparing model simulations with observations of volcanic eruptions.

In Chapter 1, we provide a general overview of atmospheric aerosols covering main sources and sinks, the chemical and microphysical processes involved, and the optical properties which affect aerosol interaction with radiation. We then focus on the stratospheric aerosol layer and its formation under background conditions and the implications produced by its perturbation by explosive volcanic eruptions and SAI.

In Chapter 2 we discuss a new model inter-comparison study based on the original paper Quaglia et al. (2023) concerning the simulation of the June 1991 Mt. Pinatubo eruption, as prescribed in the Historical Eruptions SO_2 Emission Assessment experiments (HErSEA), in the framework of the Interactive Stratospheric Aerosol Model Intercomparison Project (ISA-MIP; Timmreck et al., 2018). We compare results of six global circulation models with interactive aerosol microphysics (ECHAM6-SALSA, EMAC, ECHAM5-HAM, SOCOL-AERv2, ULAQ-CCM and UM-UKCA) with a range of observations, to show the agreement and discrepancies between the models and between the models and observations, at different initial sulfur amounts and injection altitude.

In Chapter 3 we propose and simulate for the first time with the ULAQ-CCM model an enhancement of tropospheric emission of carbonyl sulfide as an alternative to the more common geoengineering strategy of injecting SO_2 into the stratosphere. The impact on radiative forcing, ozone chemistry, and acid deposition and the feasibility of the method are discussed and compared with the simulation of sulfur dioxide injection into the tropical lower stratosphere. This study is based on the original paper Quaglia et al. (2022).

In Chapter 4, we assess the impacts of a large explosive volcanic eruptions occurring during a potential SAI deployment, considering a lower- and upper- bound case of large volcanic eruption and define the risks and whether an SAI strategy could be modified in order to limit the side effects. Simulations are perfomed with CESM2(WACCM6) model for different injection settings and using a feedback algorithm to control global temperatures and their horizontal gradients which affects the pattern of precipitation change and ITCZ shift.

Finally, in Chapter 5 main findings are summarised and discussed.

Chapter 1

Literature review of background concepts

1.1 Atmospheric aerosols

Aerosols are defined as solid, liquid or mixed phase particles suspended in a gas. In the atmosphere they extend from the surface up to 40 km altitude, with composition and sizes that varies spatially (Fig. 1.1). The interest in aerosols is related to their impact on air quality and health, meteorology and climate. Impact on climate include the change in Earth's radiative balance through scattering and absorption of radiation by aerosols, and, indirectly, through changes in cloud coverage as aerosols serve as cloud condensation nuclei for cloud droplets and ice particles form. Therefore, they also affect precipitation and provide surface available for heterogeneous chemistry. Their impact depends on their composition and size which differently interact with the radiation and affects their residence in the atmosphere.

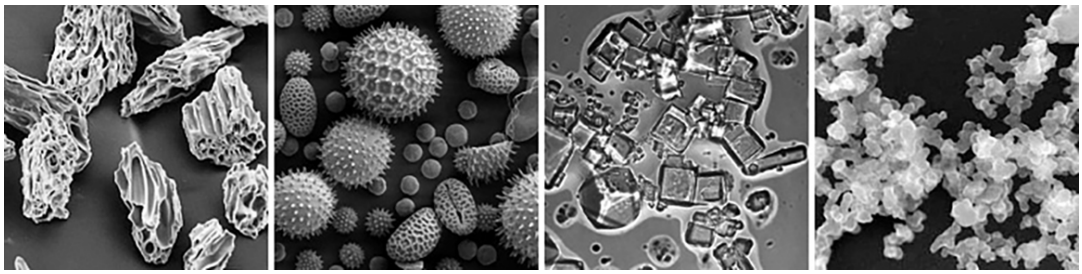

FIGURE 1.1: Examples of aerosol in the atmosphere: from left to right volcanic ash, pollen, sea salt, and soot. The image is taken from NASA, compiled from USGS, UMBC (Chere Petty), and Arizona State University (Peter Buseck).

Atmospheric aerosols composition relevant for climate contains organic matter, soot, sulfate, nitrate, ammonium, sea salt, soil dust. They are emitted in the atmosphere directly as particles (primary aerosols) or formed in the atmosphere by gas-to-particle conversion (secondary aerosols). Natural emissions include up-lift of soil dusts and sea salt by the winds over sea surface and lands, respectively, injection of silicate minerals and sulfate aerosol by volcanic eruptions, and emissions of organic matter, soot and soil dust by natural biomass burning. Cosmic dust is

another natural source of primary aerosols, called Meteoric Smoke Particles, which are mainly found in the mesosphere, upper stratosphere and winter polar regions. These are samples from comets and asteroids that, upon entering the atmosphere, ablate, giving rise to metal atoms that become oxidized and polymerize into particles (Rapp et al., 2012; Kremser et al., 2016). Anthropogenic emissions include particles as organic matter, soot, sulfate, and metals through fossil-fuel combustion, anthropogenic biomass burning and industries emissions. Secondary aerosols includes sulfate, ammonium, nitrate and organic compounds which are chemically produced by oxidation of precursor gases, as nitrogen oxides (NO_x), sulfur oxides (SO_x), and Biogenic Volatile Organic Compounds ($BVOC_s$), into gases with a lower saturation vapor pressure.

Aerosol precursor gases can form new particles through gas-to-particle conversion (or homogeneous nucleation), in which gas molecules aggregate to form a cluster that condenses to form small liquid droplets, or they participate in condensation, in which gas diffuses and changes its state to liquid or solid over the surface of the nucleated particle, increasing its size. Particle growth can also occur through coagulation, a process in which two particles collide and stick together during random motions. The prevalence of one growth process over the other, depends on the particle number concentration, precursor gases concentration and size of the particles: indeed, the rate of coagulation is increased by high numbers facilitating collisions and reduced by the presence of larger particles due to their slower random motion. As revers of condensation, evaporation occurs when aerosols are moved into a warmer environment and it is the case of stratospheric aerosols transported upward by the Brewer-Dobson Circulation (BDC) in the tropical stratosphere. Other atmospheric aerosol removal processes are wet and dry deposition and gravitational settling. Dry deposition consists of turbulent diffusion transport of gases or aerosols from the atmosphere to the surface where on contact they stick to or react with the surface. Wet deposition consists of the scavenging of atmospheric gases or aerosols by hydrometeors (incorporation into cloud droplets, fog drops, rain, snow) and consequently removed by rainout. Gravitational settling or sedimentation (or gravitational settling) is the sinking of particles at their fall speed, determined by the balance between the force of gravity and the opposing force of drag due to air viscosity. The processes of aerosol formation, growth, and removal are illustrated in Figure 1.2.

The size of these aerosols varies from a few nanometers to 100 μm in diameter and depends on their origin and formation. A first distinction in size is between fine and coarse particles, with diameters less than 2.5 μm and greater than 2.5 μm, respectively, which identify particles formed from the nucleation and condensation of vapors from those particles originating by mechanical processes, such as wind-blown dust, sea spray, and volcanoes (Fig. 1.3). Fine particles are additionally distinguished in nucleation mode with diameters up to 0.01 μm, Aitken mode with diameters from about 0.01 to 0.1 μm and accumulation mode for diameters from

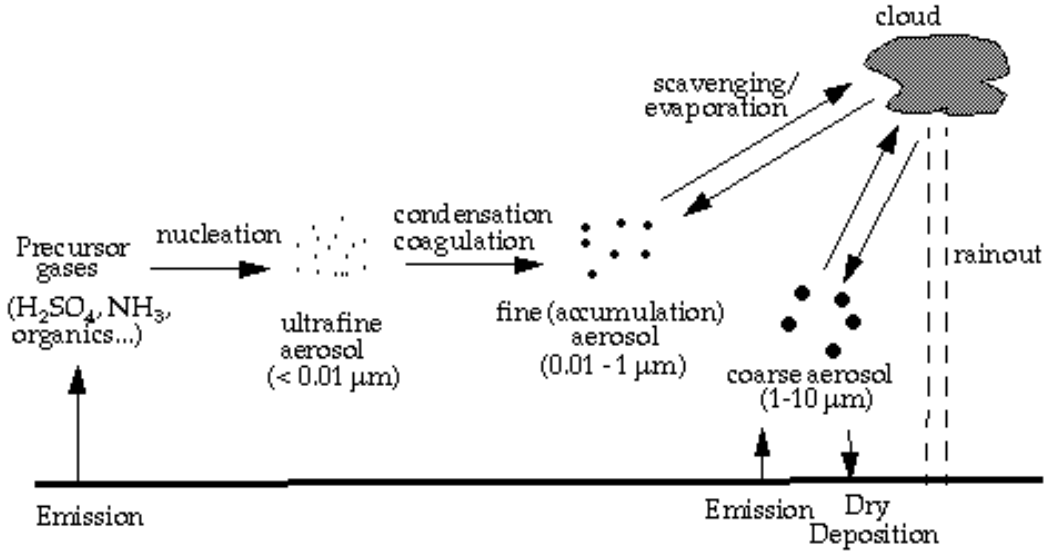

FIGURE 1.2: Schematic representation of the microphysical processes involved in aerosol formation, growth and removal. Figure taken from https://www.global-climate-change.org.uk/6-6-1.php.

about 0.1 to 2.5 μm. The nucleation mode includes fresh particles formed by the homogeneous nucleation of atmospheric gases that grow within minutes or hours in the Aitken mode. The accumulation mode includes particles grown through coagulation of Aitken mode particles and through condensation of vapors on pre-existing particles. Particles in the accumulation mode are removed mainly by wet and dry deposition, particles in coarse mode through rainout and sedimentation, which here is more efficient than for the accumulation mode because of higher sedimentation rates due to their sizes.

The size and composition of aerosols are some of the parameters that determine the radiative effects in their interaction with radiation. When an electromagnetic wave of a certain wavelength, emitted in this case by the Sun or the Earth's surface, impinges on a particle, the particle can to re-transmit it in a certain direction (scattering) and convert some of the electromagnetic energy into internal (thermal and chemical) energy of the particle (absorption). Scattering implies a change in the direction of propagation of the electromagnetic wave and, in case of inelastic scattering, change of its wavelength. The combined effect of scattering and absorption is referred to as extinction and the scattering and extinction efficiency can be retrieved resolving the Maxwell's equations of electromagnetism.

The simplification of the solutions of the equations based on assumption on size and shape of particles defines three scattering regimes: Rayleigh, Mie and Geometric scattering. Atmospheric particles are considered spherical and homogeneous to a good approximation and fall into the Mie scattering regime. Mie solutions to Maxwell's equations show that extinction and scattering efficiencies (Q_{ext} and Q_{sca}) for a single particle depend only on the size parameter (x), defined as the ratio of the

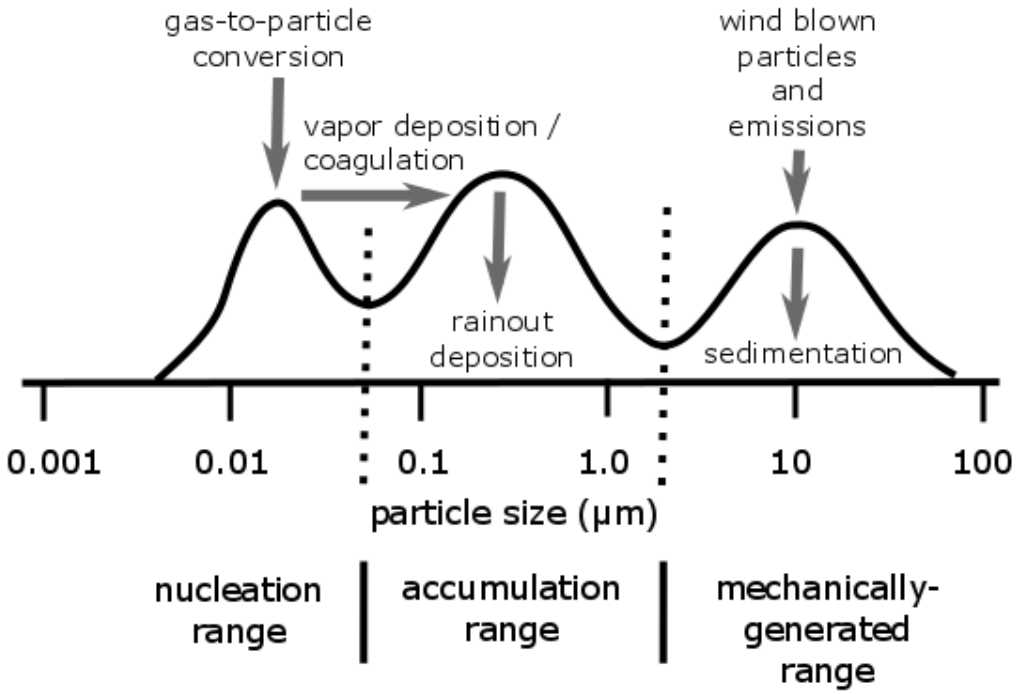

FIGURE 1.3: Schematic representation of distribution of surface area of atmospheric aerosols. Figure taken from https://www.e-education.psu.edu/meteo300/node/671.

radius of the spherical particle to the wavelength of the incident radiation, and the complex refractive index (n) of the particle, composed of a real (n_r) and imaginary (n_i) part representing respectively the non-absorbing and absorbing components. As a result, the differences between Q_{ext} and Q_{sca} is defined absorption efficiency (Q_{abs}). Figure 1.4) shows the dependence of Q_{sca} and Q_{abs} on the size parameter x and refractive index: in panel a with n_i set to zero, the maximum of Q_{sca} increases and its position shifts to smaller parameter sizes by increasing the real part of the refractive index; in panels b and c, with n_r constant at 1.53, ripples in Q_{sca} are smoothed out and the maximum value of Q_{sca} decreases by increasing n_i, while Q_{abs} increases with increasing size parameter until it reaches a maximum which, in turn, increases and its position shifts to smaller parameter sizes by increasing n_i.

For an ensemble of different sizes with identical refractive index and a number size distribution function n(r), we define the volume scattering, absorption and extinction coefficient which represent the *energy removed from a beam per unit distance by absorption, scattering and both absorption and scattering* (Grainger, 2018), given by equations 1.1 and measured in m^{-1}.

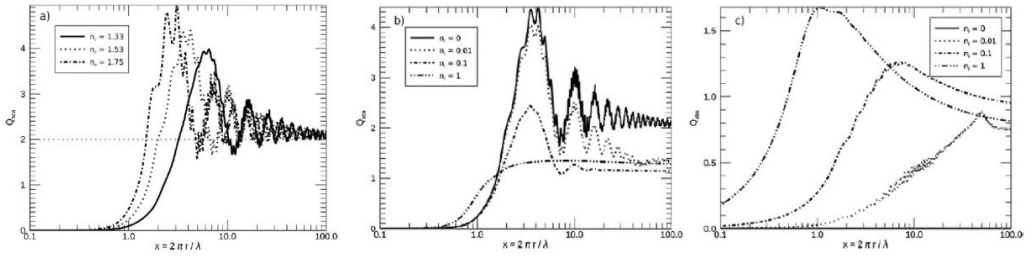

FIGURE 1.4: Dependence of Q_{sca} and Q_{abs} on the size parameter x and refractive index. Panel a shows Q_{sca} for different values of the real part of the refractive index typical of water, sulfate and soot (n_r=1.33, n_r=1.53, n_r=1.75, respectively) with n_i=0. Panels b and c show Q_{sca} and Q_{abs} or different values of the imaginary part of the refractive index (panel a) with n_r=1.53. Figure adapted from Bellouin and Yu (2022).

$$\beta_{abs} = \int_0^\infty \pi r^2 Q_{abs}(\lambda, r)\, n(r)\, dr \tag{1.1a}$$

$$\beta_{sca} = \int_0^\infty \pi r^2 Q_{sca}(\lambda, r)\, n(r)\, dr \tag{1.1b}$$

$$\beta_{ext} = \int_0^\infty \pi r^2 Q_{ext}(\lambda, r)\, n(r)\, dr \tag{1.1c}$$

$$\tag{1.1d}$$

The column-integrated extinction is called the optical depth and measures the attenuation of incident radiation passing through the atmosphere (Eq. 1.2). It depends on the size and optical properties of the particle, as well as for extinction efficiency, and the particle number density.

$$\tau(\lambda) = \int_0^\infty \beta_{ext}(z) dz \tag{1.2}$$

As a counterpart of absorption, particles re-emit radiation in the form of thermal radiation as idealized black bodies, according to Plank's law. Therefore, the perturbation of the Earth's energy budget due to the presence of aerosols depends on the balance between the scattering and absorption of solar and planetary, but also on the presence of clouds and the albedo of the underlying surface whose efficiency in reflecting radiation could be compromised. However, the overall negative change of the radiative energy result in a cooling of the atmosphere, vice versa in the case of a positive change, which in turns affect evaporation, latent heat release, and hence precipitation.

1.2 Stratospheric aerosol layer

The stratosphere contains a layer of aerosol particles with radii in the range of 0.1 to 2 μm, located between the tropopause and 30 km altitude, it is *stable, constant in time and space, and composed mainly of sulfate particles* (Junge and Manson, 1961). The composition can be distinguished in particles of tropospheric origin with radii between 0.01 and 0.1 μm, hygroscopic particles containing sulfur with radii between 0.1 - 1.0 μm, and particles of extra-terrestrial origin with radii larger than 1.0 μm (Junge, Chagnon, and Manson, 1961).

Tropospheric aerosols and aerosol gas precursors can be transported across the Tropical Tropopause Layer (TTL) into the stratosphere through deep tropical convection or, outside the tropics, convection systems such as the Asian monsoon, quasi-isentropic transport from the tropical upper troposphere into the extratropical lowermost stratosphere, and cross-isentropic transport from the TTL into the tropical stratosphere (Kremser et al., 2016) (Fig. 1.5). Once in the stratosphere, the spatial distribution of the aerosols is controlled by the strong zonal winds, the BDC and the Quasi-Biennal Oscillation (QBO).

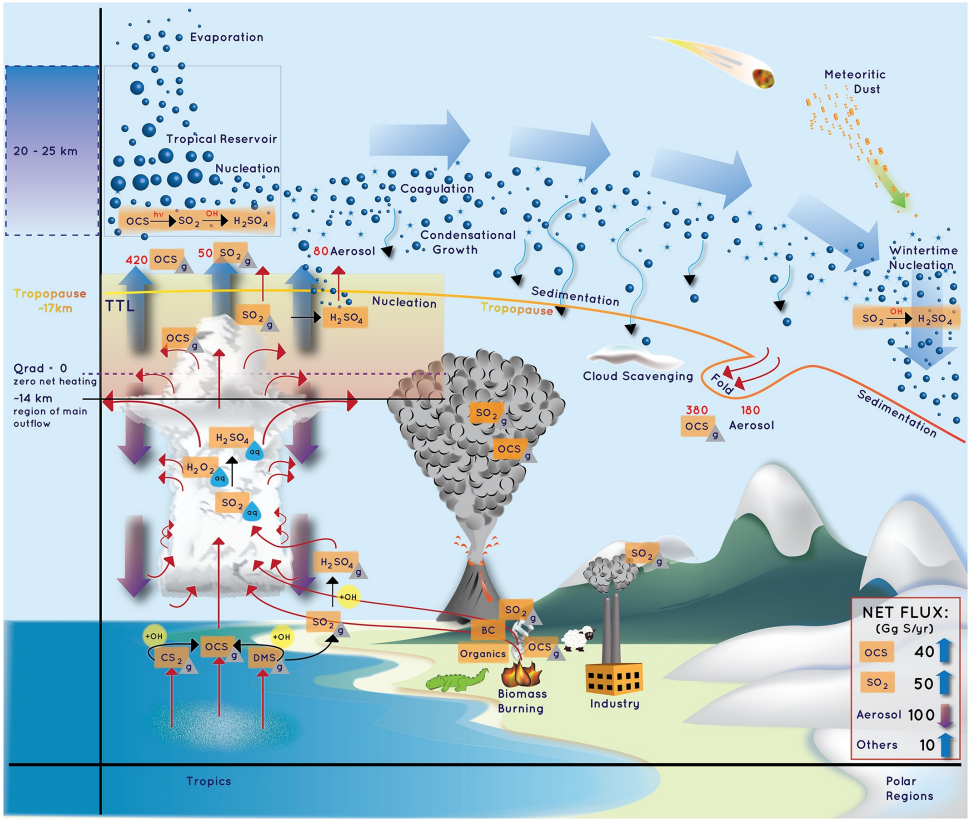

FIGURE 1.5: The figure taken from Kremser et al. (2016) summarises the most relevant sources and the chemical, dynamical and microphysical processes that governs the stratospheric aerosol layer.

The BDC consists of two circulation branches (Fig.1.6) with an upward motion in the tropics, a poleward motion in the extratropics, and a descending motion over the

polar regions. They are both driven by breaking of synoptic waves and planetary-scale Rossby waves propagating upwards from the troposphere at upper levels in the stratosphere where they deposit their momentum and cause the driving force (Holton et al., 1995; Butchart, 2014). The "deep branch" is a single cell poleward transport above 20 km that occurs in the winter hemisphere and with transport scale of few years, the “shallow branches” are two-cell structure active year-round below 20 km with transport timescales of months (Plumb, 2002). The air in the tropical stratosphere (between 30°S and 30°N) remains isolated from that in the mid-latitudes in the altitude range of 21 to 28 km (Trepte and Hitchman, 1992), and this is why it is called "tropical pipe" air (Plumb, 1996). The transport out of the tropical pipe is influenced by the QBO which is a periodic oscillation (approximately 28 months) of downward propagating easterly (easterly shear) and westerly (westerly shear) wind regimes in the equatorial stratosphere between 70 and 10 hPa (Baldwin et al., 2001). The the easterly shear of QBO amplifies the upwelling motion and increase the confinement in the tropical pipe, the westerly shear stronger produces a stronger poleward transport because of descent motions over the equator that transport the aerosol downward close to the tropopause (Trepte and Hitchman, 1992).

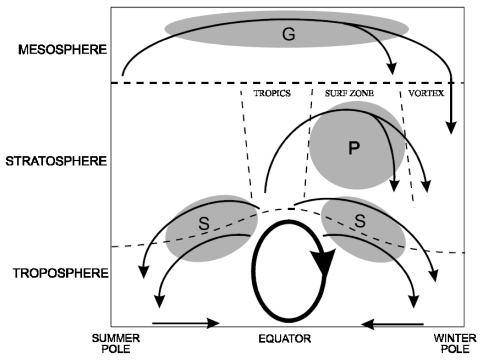

FIGURE 1.6: Schematic representation of Brewer-Dobson circulation. Shadded regions represent the regions of breaking waves such as synoptic-scale waves (S), planetary-scale waves (P), and gravity waves (G). Figure taken from Plumb (2002).

The main source of stratospheric aerosols is COS which is emitted directly from oceans or anthropogenic sources or chemically produced by sulfur species emitted from oceans or anthropogenic sources. It is water insoluble, has a low chemical reactivity in the troposphere and is efficiently lost at the surface via dry deposition on soils and vegetation. It has a long tropospheric lifetime and therefore it diffuses into stratosphere where wavelengths from 185 to 300 nm are available to break the C=S bond in COS through photodissociation, producing a sulfur atom that is further oxidised in SO_2 (Eq. 1.3).

$$COS + h\nu \longrightarrow S + CO \tag{1.3a}$$
$$S + O_2 \longrightarrow SO + O \tag{1.3b}$$
$$SO + O_2 \longrightarrow SO_2 + O \tag{1.3c}$$

Other sulfuric species emitted from various surface sources are carbon disulfide (CS_2), dimethyl sulfide (DMS), hydrogen sulfide (H_2S) and SO_2. These short-lived compounds are quickly oxidised mainly by hydroxyl radical (OH) in the troposphere, therefore do not persist enough to be transported in the stratosphere. However, CS_2 and DMS in their oxidation chain might produce COS then contributing to the enhancement of the stratospheric aerosol layer.

Large explosive volcanic eruptions are the main contributors of enhancement of the stratospheric aerosol layer over several years by injecting directly in the stratosphere ash, aerosols and gases, mainly water vapor (H_2O), carbon dioxide (CO_2), SO_2 and H_2S. The eruption of Mt. Pinatubo in June 1991, the largest eruption of the 20th century, injected between 10-20 Tg of SO_2 which resulted in a sulfate aerosol cloud peaking at 14 Tg in September (Lambert et al., 1993; Baran and Foot, 1994), up to 60 times larger compared to background condition.

For modest volcanic eruptions the volcanic plume does not reach the stratosphere and aerosols are formed in the troposphere where are are removed after a couple of weeks or a month. However, they might contribute to the stratospheric sulfate load by injection of sulfur into the upper tropical troposphere followed by transport across the TTL.

Sulfur chemistry governs the stratospheric aerosol layer, which is mainly composed of sulfate aerosols in the form of H_2SO_4-H_2O solution droplets with a weight percentage of H_2SO_4 of about 75% (Yue, 1981). The first step for sulfate formation is the oxidation of SO_2 to sulfur trioxide within a few weeks and that in turn converts almost instantaneously to gas-phase sulfuric acid (H_2SO_4) (Eq. 1.4).

$$SO_2 + OH + M \longrightarrow HSO_3 + M \tag{1.4a}$$
$$HSO_3 + O_2 \longrightarrow SO_3 + HO_2 \tag{1.4b}$$
$$SO_3 + H_2O \longrightarrow H_2SO_4 \tag{1.4c}$$

The H_2SO_4 vapor partial pressure in the stratosphere is generally supersaturated therefore it quickly condenses through homogeneous and/or heterogeneous nucleation (Kremser et al., 2016) (Fig. 1.7). Homogeneous nucleation occurs when H_2SO_4(g) and H_2O cluster in the absence of any pre-existing particles and the cluster

continues to grows and overcomes the nucleation barrier forming H_2SO_4-H_2O liquid droplets. Heterogeneous nucleation which is the condensation of H_2SO_4(g) and H_2O vapor on the surface of pre-existing particles is a competitive nucleation process that occurs at low concentrations H_2SO_4 and H_2O (Yue, 1981). Then particles grow through coagulation (collision of aerosols) or condensation (uptake of water and H_2SO_4).

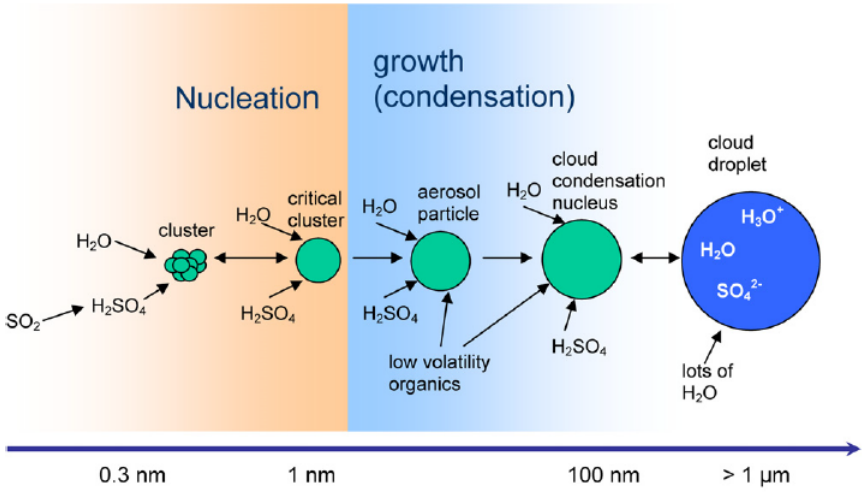

FIGURE 1.7: Schematic representation of formation and growth of sulfate aerosols in the stratosphere. Figure taken from Curtius (2006).

Non-sulfur gasses or particles such as organic and black carbon, CO_2, CO, NO_x and CH_4 can be found in the lower stratosphere by direct injection through biomass burning in the form of pyrocumulonimbus, and other refractory aerosol from cosmic dust.

Stratospheric aerosols provides surface for heterogeneous chemical reactions that affect ozone cycle. Reactions on and in sulfate aerosols relevant for atmospheric chemistry are given by 1.5 (Hendricks et al., 1999), because of the transformations of inert compounds into catalytically active species.

$$N_2O_5 + H_2O\,(l) \longrightarrow {}_2\,HNO_3 \tag{1.5a}$$

$$ClONO_2 + H_2O\,(l) \longrightarrow HOCl + HNO_3 \tag{1.5b}$$

$$ClONO_2 + HCl\,(l) \longrightarrow Cl_2 + HNO_3 \tag{1.5c}$$

$$HOCl + HCl\,(l) \longrightarrow Cl_2 + H_2O \tag{1.5d}$$

$$BrONO_2 + H_2O\,(l) \longrightarrow HOBr + HNO_3 \tag{1.5e}$$

$$HOBr + HCl\,(l) \longrightarrow BrCl + H_2O \tag{1.5f}$$

$$HOBr + HBr\,(l) \longrightarrow Br_2 + H_2O \tag{1.5g}$$

1.3 Volcanic eruption

Volcanic eruptions emits ash, sulfur-containing gases such as SO_2, CO_2, and H_2S, and other gases such as H_2O and hydrogen chloride (HCl) and other halogen compounds.

Ash are rock fragments with a high percentage of silicon, irregular shape and sizes ranging from submicrometer to millimeter in diameter (Rose and Durant, 2009). Because of their size, they are rapidly removed through sedimentation and rainout, and their residence in the atmosphere can range between 30 minutes up to couple of weeks for particles with diameters smaller than 10 μm (Rose and Durant, 2009). Ash particles absorb short-wave and long-wave radiation producing radiative heating whose climatic impact is negligible, due to their short duration, but which impacts the initial transport of the volcanic cloud (Niemeier et al., 2009; Stenchikov et al., 2021). Large ash particles have large surface areas for heterogeneous uptake of SO_2 and H_2SO_4 gas, removing sulfate precursor gases from the stratosphere (Zhu et al., 2020).

Halogen compounds which are important for their implication on the stratospheric ozone cycle are mainly removed by rainout within the troposphere (Textor et al., 2003; Kremser et al., 2016).

The contribution of volcanic CO_2 emissions as greenhouses gas to atmospheric concentrations is negligible, therefore it has no direct impact on the greenhouse effect (Robock, 2000).

Increased water vapor (or greenhouse gases in general) affects the radiative balance by warming the troposphere and cooling the stratosphere, as a result of the balance between increased absorption of ascending planetary radiation and the emission of more infrared radiation by the stratosphere (Rind and Lonergan, 1995; F. Forster and Shine, 1999; Solomon et al., 2010), Water vapor also affects the stratospheric chemistry involving ozone loss by decreasing the O_3 formation through the reaction with $O(^1D)$ that forms two OH radicals and through the increase of OH concentration in the stratosphere which react with SO_2 resulting in a much faster production of sulfate aerosols (LeGrande, Tsigaridis, and Bauer, 2016). In addition, temperature decreases in the stratosphere due to increased water can change stratospheric ozone both negatively due to cooling throughout the stratosphere, particularly in the polar lower stratosphere where increases the polar stratospheric cloud, and positively due to changes in atmospheric circulation (Rosenlof, 2018).

However, the most significant climatic impact of volcanic eruptions is due to the injection of SO_2 into the stratosphere, where aerosols persist for about 1-3 years due to slow circulation and lack of removal processes, compared to their residence in the troposphere of a couple of weeks or a month. Figure 1.8) summarises their impacts on climate, which include changes in the Earth's energy balance, changes in atmospheric dynamics, disruption of the QBO, reduced precipitation, weakening of

monsoons, shifting of the Intertropical Convergence Zone (ITCZ), ozone depletion (Timmreck et al., 2012; Marshall et al., 2022).

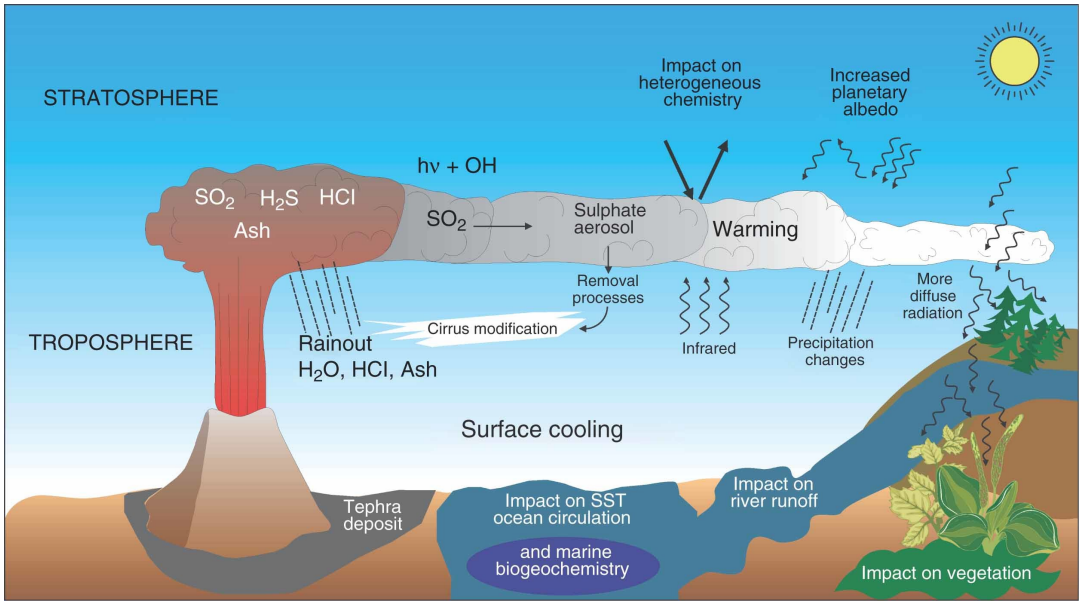

FIGURE 1.8: Schematic representation of large explosive volcanic eruptions and their impact on climate, from emissions to sulfate aerosol formation. Figure taken from Timmreck et al. (2012).

Sulfate aerosols have radii of about 0.5 μm, resulting efficient in scattering incoming solar radiation (English, Toon, and Mills, 2012) and causing a reduction in surface insolation and cooling the surface globally. They also absorb the infrared solar and planetary radiation heating of the region of stratosphere where reside. After the Pinaubo eruption in June 1991, a stratospheric warming of up to 3.5 K (Labitzke and McCormick, 1992) and a peak global surface cooling of $\simeq$ 0.5 K compared to pre-Pinatubo levels was observed from Microwave Sounding Unit measurements (Dutton and Christy, 1992), which is reduced to 0.3 K when ENSO contribution is removed (Soden et al., 2002), to 0.14 K when the contribution of the other modes of variability are removed (Canty et al., 2013).

The warming of the lower stratosphere increase the equator-to-pole temperature gradient in the lower stratosphere, which, through the thermal wind balance, leads to stronger westerly winds (Robock, 2000). Stronger westerlies resulting from the thermal wind balance and the strengthening of tropical upwelling in the ascending branch of the BDC cause a change in the QBO, which induces a permanent westerly winds in the tropical lower stratosphere and thus prolongs the easterly shear (or westerly phase) (Aquila et al., 2014; Visioni et al., 2018b; Franke, Niemeier, and Visioni, 2021).

Cooling the surface stabilizes the atmosphere and reduces evaporation both making an overall contribution to the reduction of precipitation (Bala, Duffy, and Taylor, 2008; Cao, Bala, and Caldeira, 2012). However, on a regional scale, the variation in precipitation can be either positive or negative. Indeed, the decrease of the

hemispherical thermal contrast weakens the cross-equator flow and, the decrease of land-ocean thermal contrast weakens the monsoon circulation, drying and wetting the climatological wet and dry region, respectively (Held and Soden, 2006; Iles et al., 2013; Iles and Hegerl, 2014; Zuo, Zhou, and Man, 2019).

Volcanic aerosols provide a surface for heterogeneous chemical reactions with consequences for the ozone cycle (see Section 1.2) depending on temperature and chlorine concentration in the stratosphere. In fact, the reactions that make chlorine available for ozone destruction occur in the isolated and extremely cold spring vortex of the southern hemisphere, where chlorine is transformed into the catalytically active species while nitrogen oxides are suppressed. Volcanic aerosols also provide surface at lower latitudes, where chemical ozone destruction is less effective. However, changes in atmospheric dynamics result in an upward flow of low ozone concentration from the troposphere to the stratosphere at low latitudes, while subsidence at high latitudes increases ozone concentration, masking its chemical destruction (Robock, 2000).

The capability of affecting the climate system depends on the mass of SO_2 emitted, the altitude and latitude of injection (Fig. 1.9). Low-latitude eruptions result in a longer e-folding time than high-latitude eruptions, due to the slower removal controlled by the different transport branches of the BDC and confinement within the tropical pipe. The longer e-folding time results in a larger stratospheric aerosol optical depth and larger net (more negative) radiative forcing (RF). The more negative RF for low-latitude injections is also driven by the higher insolation in the tropics. Higher SO_2 emissions result in decreased e-folding time because growth by condensation and coagulation prevails over the formation of smaller fresh particles, increasing aerosol size and sedimentation rate. The stratospheric aerosol optical depth increases and the net RF becomes more negative with increasing SO_2 emissions, but not linearly because the scattering efficiency decreases due to the formation of larger particles. Increased injection altitude results in longer e-folding, larger stratospheric aerosol optical depth, and more negative RF, up to 21 km, after which the behaviour is complicated by the microphysics and latitude on which the circulation depends (e.g. formation of larger particles if confined to the tropics) Marshall et al. (2019).

1.4 Stratospheric aerosol intervention

The effects of climate change have begun to undermine societies and ecosystems, and it is expected to get worse in the future even with strong mitigation efforts. In fact, even achieving a net zero carbon dioxide emissions target by 2100 and scaling up the removal of carbon dioxide may not prevent the risks of climate change in the short period; therefore, it is likely that society might consider the possibility of manipulating the climate to ameliorate the worst of climate change in the future. These interventions goes by the name of geoengineering and can be distinguished into two main groups: Carbon dioxide removal (CDR) and SRM as summarised in

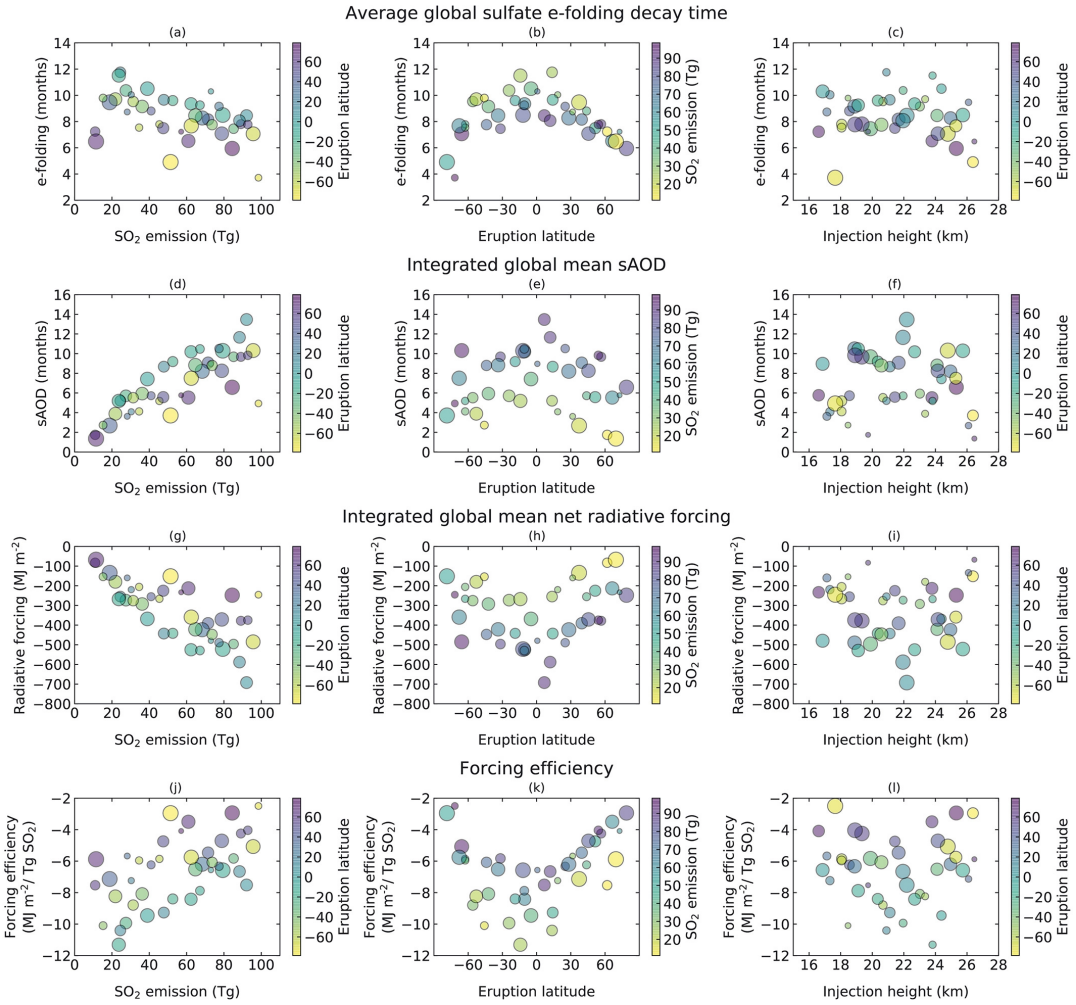

FIGURE 1.9: Dependence of e-folding time (first row), stratospheric optical depth (second row), radiative forcing (third row) and forcing efficiency (fourth row) on eruption source parameters. First column shows the dependence on SO_2 emission: the color of the points indicates the latitude of the eruption and the size the injection altitude (the larger the point, the higher the injection altitude). The second column shows the dependence on the latitude of the eruption: the color of the points indicates the amount of SO_2 emitted and the size the injection altitude. Third column shows the dependence on injection altitude: the color of the points indicates the latitude of the eruption and the size the amount of SO_2 emitted (the larger the point, higher the SO_2 emission). Figure taken from Marshall et al. (2019).

Figure 1.10. CDR aims to reduce the longwave radiation trapped in the atmosphere by reducing the levels of GHGs in the atmosphere through the enhancement of their capture and storage with different biological and engineered systems. Those are mainly focused on CO_2 removal because it is one of the long-lived species and with the highest concentration. SRM aims to reduce the incoming solar radiation increasing the planetary albedo through the enhancement of the stratospheric aerosol layer, cloud modification or introducing space mirrors (Shepherd, 2009).

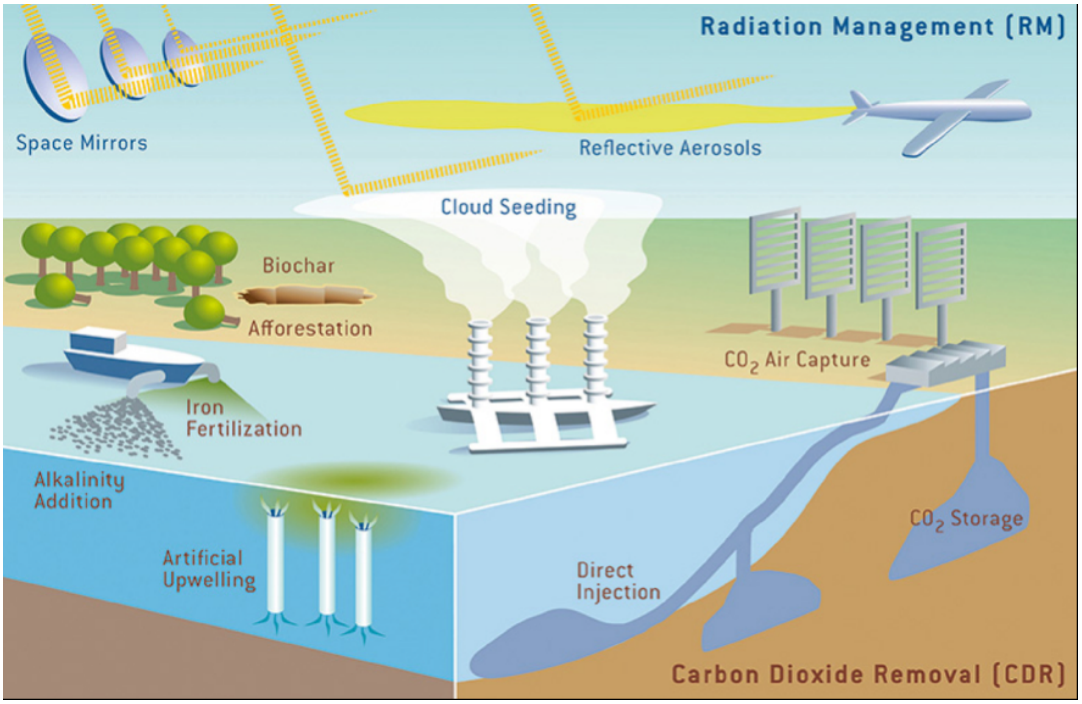

FIGURE 1.10: Summary of main geoengineering strategies, distinguished in Solar Radiation Management and Carbon Dioxide Removal. Figure by Rita Erven/Kiel-Earth-Institute.

The cooling effect observed due to increases in stratospheric aerosol loading following large volcanic eruptions has prompted modeling studies of the viability of intentional stratospheric aerosol enhancement to offset the climate effects of increasing concentrations of greenhouse gases (Budyko, 1977; Crutzen, 2006). SAI is one of the SRM strategies based on increasing the Earth's albedo, mainly with the use of SO_2 being partially justified by the analogy with volcanic injections that provide a reliability test for Earth System models for geoengineering applications (Marshall et al., 2018; Clyne et al., 2021; Quaglia et al., 2023).

The analogy with the impulsive emission of SO_2 after a volcanic eruption suggested that sustained injection of aerosols into the stratosphere could lead to similar side effects, such as reduced global precipitation, ozone depletion, and acid deposition (Robock, 2000; Timmreck et al., 2012; Marshall et al., 2022). However, the risks of SAI depend on how it would be applied, and its deployment should be weighed against the risks of non-deployment in the event that emissions reduction and carbon dioxide removal cannot prevent further risks on a short timescale. The efficiency

of SAI and the reduction of its side effects have been evaluated considering different parameters for aerosols injection such as type of reflective particle or precursor gases, altitude and latitude of injection, rate and time of the year of injection.

Pierce et al. (2010) proposed the injection of gas-phase H_2SO_4 as an intermediate product during SO_2 to aerosol conversion. H_2SO_4 vapor would form aerosol mass in the aircraft plume by nucleation or condensation within seconds after the emission compared to SO_2 injection that can condense on pre-existing particles and oxidises within a few weeks producing nucleation-mode particles that preferentially coagulate with larger particles. Therefore, the same sulfur mass of H_2SO_4 and SO_2 results in a larger burden and higher RF for H_2SO_4 injections compared to SO_2 injections, and that the overall side effects are smaller considering the less burden needed to achieve the same radiative cooling (Weisenstein et al., 2022).

To minimise the particle mass for the injection and obtain more reflective aerosols, the injection of several minerals has been proposed (Pope et al., 2012). However, this approach does not have the natural analogue and uncertainties in chemical reaction in the stratosphere are still present. Among these compounds, the use of calcite proposed to reduce the heating of the stratosphere and ozone loss (Weisenstein, Keith, and Dykema, 2015; Keith et al., 2016) has been questioned after laboratory researches because of the decrease in absorption coefficients as gases accumulate on calcite (Dai et al., 2020).

Crutzen (2006) proposed and discarded the hypothesis of increasing surface emissions of COS, as it is the main contributor of the stratospheric aerosol layer under volcanic quiescence conditions. Quaglia et al. (2022), as reported in Chapter 3, simulates and analyses for the first time this strategy with the ULAQ-CCM model. This strategy produces a more uniform global distribution of the aerosol layer and more efficient particles in scattering the solar radiation, resulting in a more latitudinally even cooling, an overall increase in stratospheric ozone, especially at the poles, and an increase in sulfur deposition.

The spatial and size distribution of aerosol for SO_2 injections can be partially managed by the combination of different latitudes and altitudes for injection to optimise the climate impact. Tilmes et al. (2017) performed with CESM1(WACCM) several simulation of the evolution of the aerosol cloud based on the different latitudes (50°S/N, 30°S/N, 15°S/N, equator), altitudes (1 and 5 km above the tropopause) and amounts of SO_2 injected (6, 8, 12 Tg of SO_2/yr), showing how these affects the stratospheric burden, the aerosol size, the optical depth and the corresponding surface temperature change which does not change linearly with the changes in the optical depth and TOA imbalance.

Figure 1.11 shows the latitudinal distribution of stratospheric sulfate aerosols for three different injection latitudes (15°S, equator, 15°N), two different injection altitudes (1 and 5 km above the tropopause) and the three different injection amount. For injections at the equator, aerosols are distributed mainly between 30°S-30°N, with a peak at the equator because of confinement within the tropical pipe, and

a second maximum around 50°S/50°N controlled by BDC and large-scale mixing. For injections at 15°S/15°N, aerosols are mainly transported to the hemisphere of injection following transport to the pole of the surface or deep branch of the BDC, depending on the altitude of injection. For injection locations more poleward, sulfate aerosols mostly remain outside the tropics and accumulate at mid- and high-latitudes; the total sulfate load is lower for injections at 50°S/50°N because of the location of the downwelling branch of the BDC. High-altitude injections result in higher sulfate burden due to increased vertical extent of aerosol particles and less removal through sedimentation than low-altitude injections. As the amount of SO_2 injected increases, the sulfate burden increases due to larger particle growth and increased gravitational sedimentation.

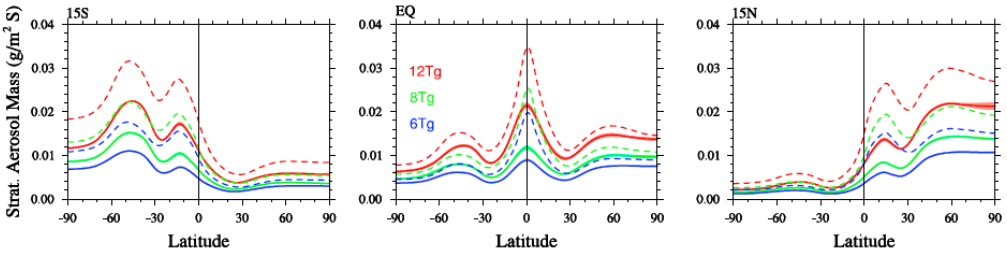

FIGURE 1.11: Annually and zonally averaged (top row) stratospheric sulfur mass for different injection locations, 15°S (left column), equator (middle column), and 15°N (right column), different injection altitudes, 1 km above the tropopause (solid lines) and 5 km above the tropopause (dashed lines), and for different injection amount, 6 Tg SO_2/yr (blue), 8 Tg SO_2/yr (green), 12 Tg SO_2/yr (red). Figure adapted from Tilmes et al. (2017).

Based on these results, MacMartin et al. (2017) demonstrated with the same model CESM1(WACCM) that injecting SO_2 simultaneously at four different latitudes allows to control three different spatial distributions of AOD: constant with the latitude, linear with sine of latitude (Ψ) increasing northward or southward, and quadratic with sine of latitude (Fig. 1.12). The temperature and RF pattern does not correspond to that of AOD, due to different latitudinal insolation, changes in cloud pattern and local feedbacks. However, each pattern of AOD results in a different pattern of temperature that allows to manage three temperature metrics (T_0, T_1, T_2), consisting of the projection of temperature onto the first three Legendre polynomial functions (L_0, L_1, L_2). This can be done with a feedback algorithm that first solves the required spatial model of AOD and then the injection rates.

$$T_0 = \frac{1}{A}\int_{\Psi} T(\Psi)\, cos(\Psi)\, d\Psi \tag{1.6a}$$

$$T_1 = \frac{1}{A}\int_{\Psi} sin(\Psi)\, T(\Psi)\, cos(\Psi)\, d\Psi \tag{1.6b}$$

$$T_2 = \frac{1}{A}\int_{\Psi} \frac{3\, sin^2(\Psi) - 1}{2} T(\Psi)\, cos(\Psi)\, d\Psi \tag{1.6c}$$

$$where \qquad A = \int_{\Psi} cos(\Psi)\, d\Psi \tag{1.6d}$$

(1.6e)

$$L_0 = 1 \tag{1.7a}$$

$$L_1 = sin(\Psi) \tag{1.7b}$$

$$L_2 = \frac{3\, sin^2(\Psi) - 1}{2} \tag{1.7c}$$

(1.7d)

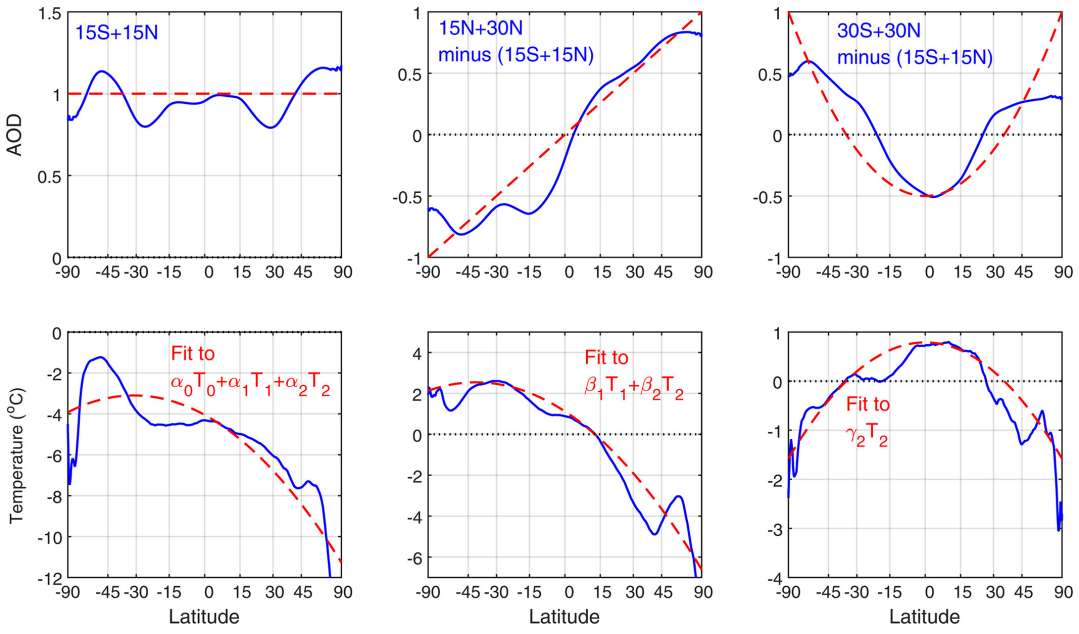

FIGURE 1.12: Relationship between different patterns of AOD and surface air temperature: a) injection at 15°S and 15°N to achieve AOD constant with the latitude; b) injection at 15°N and 30°N minus results from case a) to achieve AOD linear with sine of latitude; c) injection at 30°S and 30°N minus injection at 15°S and 15°N to achieve AOD quadratic with sine of latitude. Figure taken from MacMartin et al. (2017).

Additionally, the temperature response can be managed by changing the amount

of SO_2 injected at each latitude, with the limitations of changes in stratospheric circulation and microphysical processes that depend on the distributions of aerosol itself. The strategy can be further optimised basing the time of injection on the seasonality of the Brewer-Dobson circulation which drives the stratospheric equator-to-pole circulation, taking advantage of periods of higher intensity of solar radiation. Injecting over some season rather than all year allows to achieve the same global target and control the regional impact such as Arctic sea ice and precipitation (Laakso et al., 2017; Visioni et al., 2020b).

Chapter 2

Interactive stratospheric aerosol models' response to different amounts and altitudes of SO2 injection during the 1991 Pinatubo eruption

Large-magnitude volcanic eruptions can emit SO_2 and other gases directly into the stratosphere. An abrupt increase in stratospheric SO_2 creates a long-lived volcanic aerosol cloud that scatters incoming solar radiation, absorbs solar and infrared radiation, and affects the composition of the stratosphere. Such volcanically induced enhancements of the stratospheric aerosol layer exert strong direct effects on climate because they influence the Earth radiation budget and cool the surface via the reduced insolation (McCormick, Thomason, and Trepte, 1995; Soden et al., 2002); they also show a range of indirect effects, due to the volcanic aerosols effects on stratospheric circulation, dynamics and chemistry (e.g., Robock et al., 2009; Timmreck et al., 2012; Kremser et al., 2016).

Here we investigate the evolution of the volcanic aerosol cloud after the Mt. Pinatubo eruption in June 1991 by analyzing coordinated simulations within the HErSEA experiments, in the framework of the Interactive Stratospheric Aerosol Model Intercomparison Project (ISA-MIP; Timmreck et al., 2018). Mt. Pinatubo is located in the western part of the island of Luzon, Philippines (15.1°N, 120.4° E). After preliminary eruptions from 12 June 1991, the climatic phase started at 05:30 UTC on 15 June 1991 and lasted for approximately 9 hours. The volcanic cloud contained gases and particles of ice, ash, and sulfate and reached a maximum altitude of 40 km (Holasek, Self, and Woods, 1996). Ice and ash burden peaked at about 80 and 50 Tg respectively, and early-formed sulfate mass was estimated at 4 Tg, based on infrared satellite data from the Advanced Very High Resolution Radiometer (AVHRR), the TIROS Operational Vertical Sounder (TOVS), and High Resolution Infrared Radiation Sounder/2 sensors (Guo et al., 2004a). Initial SO_2 mass estimates from the ultraviolet Total Ozone Mapping Spectrometer (TOMS) and infrared TOVS

sensors, indicated that the eruption injected 14-22 Tg of SO_2 (Bluth et al., 1992a; Guo et al., 2004a). Other uncertainties pertain to the vertical extension of the volcanic cloud: SO_2 mass was injected between 18-30 km (Bluth et al., 1992a; Baran, Foot, and Dibben, 1993) and concentrated around 25 km, over a rich ash layer peaking around 22 km (Guo et al., 2004b). The sulfate aerosol cloud peaked at 14 Tg in September (Lambert et al., 1993; Baran and Foot, 1994), with the largest aerosol concentration between 20 and 25 km of altitude and much lower amounts between 15 and 20 km (Winker and Osborn, 1992a; Winker and Osborn, 1992b; DeFoor, Robinson, and Ryan, 1992). Recent volcanic SO_2 emission databases suggest for Pinatubo an amount and location of SO_2 emitted between 15 and 18 Tg of SO_2, at an altitude of between 19 and 28 km (Independent Volcanic Eruption Source Parameter Archive Version 1.0, ivespa.co.uk, VolcanEESM: Global volcanic sulphur dioxide emissions database from 1850 to present - Version 1.0, Multi-Decadal Sulfur Dioxide Climatology from Satellite Instruments; Aubry et al., 2021; Neely III and Schmidt, 2016; Carn, 2022).

Several modeling studies have evaluated the simulated global and tropical sulfate loadings compared to observations, with some studies (Niemeier et al., 2009; Toohey et al., 2011; Brühl et al., 2015) finding agreement when emitting in the mid-range of the best-estimate stratospheric SO_2 loading of 14-22 Tg SO_2 (Guo et al., 2004a). In contrast, a number of recent studies found agreement only when injecting an amount of SO_2 below the lower limit observed of 10 Tg-SO_2, considering different injection heights and vertical distributions (Dhomse et al., 2014; Sheng et al., 2015a; Mills et al., 2016); this difference partly motivates the design of the ISA-MIP HErSEA intercomparison (see Timmreck et al., 2018). Approaching the problem from a model intercomparison perspective, different past projects have revealed large differences in the simulation of the aerosol radiative forcing, and not just for Pinatubo.

A first multi-model intercomparison study of global stratospheric interactive aerosol models was set up in the frame of the Model Intercomparison Project on the climatic response to Volcanic forcing (VolMIP; Zanchettin et al., 2016). To create a common forcing data set for VolMIP experiments which considers a volcanic eruption with radiative forcing comparable to that of the 1815 Tambora eruption, a pre-study was set up (Marshall et al., 2018). This VolMIP-Tambora ISA experiment establishes a well-defined set of injection parameters to simulate the Tambora volcanic aerosol cloud interactively with stratospheric aerosol models. Multi-model analysis of the simulated volcanic aerosol distribution shows large inter-model differences (Marshall et al., 2018; Clyne et al., 2021).

Marshall et al. (2018) used Arctic and Antarctic ice core information about sulfate deposition to constrain the VolMIP-Tambora ISA model simulations. The four models involved in this experiment revealed large discrepancies in the simulated aerosol burden (50-58 Tg-SO_4 at the peak), resulting in deposition magnitudes in Antarctica ranging from 19 to 264 kg km^{-2}. They attributed the differences between the models,

and between models and observations, to different sulfate formation and transport through meridional circulation and stratosphere-troposphere exchange and different deposition schemes. The contribution to the overall uncertainty of the sulfate formation processes was then further investigated in a subsequent study by Clyne et al. (2021), which focused on the evolution of the global stratospheric aerosol optical depth. The reasons for the discrepancies between the models were attributed to differences in particle size, which influence the scattering efficiency and the lifetime of the stratospheric aerosols, and the treatment of OH chemistry, which in turn affects the timing of sulfate formation.

The Geoengineering Model Intercomparison Project Phase 6 (GeoMIP6; Kravitz et al., 2015) also includes experiments with injection of stratospheric sulfate aerosol precursors (G6Sulfur) in an amount necessary to reduce the net radiative forcing from the SSP5-8.5 scenario to the SSP2-4.5 one. Participating models in G6Sulfur directly injected SO_2 in the tropical stratosphere with different altitude and latitude ranges of injection or prescribed the aerosol optical depth or aerosol distribution derived from previous simulations. The amount of SO_2 required to achieve the proposed cooling varies by a factor of 2 between models, and results in a different temporal and latitudinal distribution of aerosols that affects surface temperature and local precipitation differently (Visioni et al., 2021).

In contrast to the aforementioned model intercomparison studies, the ISA-MIP HErSEA experiments offer a test of the reliability of these models by allowing a direct comparison of the simulated volcanic enhancement of the stratospheric aerosol layer with observation data sets, especially during the Mt. Pinatubo eruption, for which several satellite and in situ measurements are available. Hence, HErSEA was developed to determine which set of volcanic emission source parameters allows models to reproduce the available measurements, and understand how their different chemical and microphysical schemes, stratospheric dynamics, and radiative transfer treatment influence these choices. Specifically, HErSEA focuses on the uncertainty in the initial volcanic emission in terms of amount and injection altitude of SO_2 for the recent large-magnitude volcanic eruptions in the last 100 years (Mt. Agung in 1963, Mt. El Chichón in 1982, Mt. Pinatubo in 1991); multiple interactive stratospheric aerosol simulations of each of the volcanic aerosol clouds with common upper-, mid- and lower-estimate amounts and injection altitudes of sulfur dioxide were performed. Here we investigate the evolution of the volcanic aerosol cloud after the Mt. Pinatubo eruption by analyzing Atmospheric Model Intercomparison Project (AMIP)-type (Gates et al., 1999) simulations within the HErSEA framework. In particular, we ask whether previous results in inter-model differences are confirmed in this new MIP; the presence of multiple injection settings common between all models will also allow an exploration of the reason for these differences, based on the models abilities to reproduce observations with different sets of initial conditions of the volcanic emissions.

The experimental design, the main features of the participating models and the

observational data sets are described in Section 2.1. Section 2.2 shows model results of the optical and microphysical properties of the volcanic aerosol cloud, which are summarized and discussed in Section 2.3.

2.1 Methods and data

2.1.1 Methods

Experimental protocol

There is a degree of uncertainty over the thickness of the injected SO_2 cloud, based on available measurements. Therefore, different modeling centers may have selected different simulated injection altitudes for the Pinatubo eruption in the past. Within Dhomse et al. (2020) UM-UKCA set the SO_2 injection altitude at 21-23 km based on the altitude of the first detection of the Pinatubo cloud at Mauna Loa (Antuña, 2002). Further UM-UKCA analysis by Shallcross (2020) demonstrated improved model correspondence with the July-Aug 1991 Mauna Loa lidar measurements when running the model with "pre-nudged free-running", rather than the "approximate QBO free-running" approach used in Dhomse et al. (2020). Sheng et al. (2015b) performed atmospheric simulations of the Pinatubo eruption with AER 2-D 300 by varying the emission parameters and found agreement with several observations by injecting 14 Tg of SO_2 with a vertical distribution peaking at 18-21 km. Similar emission parameters (10-12 Tg of SO_2 at 18-20 km) were used in Mills et al. (2016) with CESM1-WACCM. Niemeier et al. (2009) showed comparable aerosol optical depth and effective radius with satellite and lidar measurements, simulating with MAECHAM5-HAM the injection of 17 Tg of SO_2 at about 24 km together with 100 Tg of fine ash at about 21 km. Stenchikov et al. (2021) simulated with WRF-Chem v3.7.1 the same amounts of SO_2 and ash but centered at 17 km showing that the radiative heating of ash can raise the sulfur cloud by 7 km during the first week of the eruption. These differences motivated the design of the ISA-MIP HErSEA intercomparison.

The HErSEA Pinatubo experiment design includes five different emission scenarios considering different amounts and altitudes of injection of SO_2, as summarized in Figure 2.1. The first three emission scenarios describe injections at medium altitude (between 21-23 km) of an amount of SO_2 that varies from the lowest value of 5 Tg-S (Low-22km) to a medium of 7 Tg-S (Med-22km) and the highest value of 10 Tg-S (High-22km). The medium injection scenario (7 Tg-S of SO_2) has three different injection altitude settings: Med-22km, as discussed; another shallow one at lower altitudes (18-20 km, Med-19km); and one over deep altitude-range (18–25 km, Med-18-25km).

The Mt. Pinatubo-like eruption is timed on June 15, 1991. SO_2 is injected in models in a single grid cell close to the Pinatubo location (15°N, 120°E) and at the prescribed altitudes, with the precision given by the specific vertical and horizontal model resolution (table A.1). UM-UKCA provided an additional set of simulations,

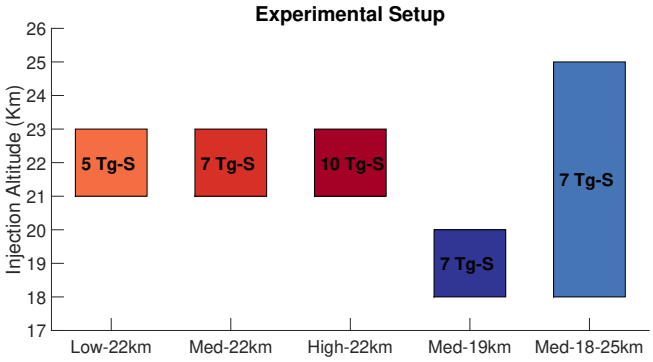

FIGURE 2.1: Graphical representation of injection setting parameters. The reddish boxes represent an injection of 5, 7, and 10 Tg-S of SO_2 centered at 22 km; the blue and light-blue boxes represent the injection of 7 Tg-S of SO_2 for injection altitudes centered at 19 km, and one deep injection between 18 and 25 km.

called meridional-spread injection simulations, and the EMAC simulation differs from the protocol: this differentiation is highlighted by the addition of a * after the model name. In UM-UKCA*, SO_2 is injected at Mt. Pinatubo longitude and in a latitude range between 0° and 15°N (12 model grid boxes), a common strategy (Dhomse et al., 2014; Mills et al., 2016) to match the initial southward spread of the aerosol cloud (Bluth et al., 1992a). In EMAC (we will use EMAC* only in the figures and tables), volcanic SO_2 injections are entered at one single point in time as 3D mixing ratio perturbations derived from satellite data using an inventory for the period 1990 to 2019 (https://doi.org/10.26050/WDCC/SSIRC_3). For the Pinatubo period also the eruptions of Cerro Hudson (August 10, 1991), Spurr (June 27, 1992) and Lascar (April 18, 1993) are included in EMAC. The amount of SO_2 injected is 8.5 and 0.65 Tg-S for Pinatubo and Cerro Hudson, respectively, and top heights of the volcanic plumes are approximately 23 km and 18 km.

All models are radiatively coupled to the volcanically enhanced stratospheric aerosol in order to resolve the composition–radiation–dynamics interactions. Previous model studies (e.g., Young, Houben, and Toon, 1994; Timmreck, Graf, and Kirchner, 1999; Aquila et al., 2012; Sukhodolov et al., 2018) showed that inclusion of the interaction between volcanic sulfate aerosol and radiation is essential for a reliable simulation of the transport of the volcanic cloud. Radiative heating of ash and SO_2 is also important for the initial uplift of the volcanic cloud (Lary, Balluch, and Bekki, 1994; Young, Houben, and Toon, 1994; Gerstell, Crisp, and Crisp, 1995), but the contribution of SO_2 is smaller than that of ash, in the first week, or sulfate aerosols, in the subsequent weeks (Stenchikov et al., 2021). About 80 Tg of ash was injected during the Pinatubo eruption (Guo et al., 2004b). However, both ash and SO_2 radiative effects are not included in all model simulations as it is outside the scope of the project which focuses on the long-term evolution of the Pinatubo volcanic cloud.

Modeling groups performed transient AMIP-type runs of the Mt. Pinatubo eruption in which sea surface temperatures and sea ice extent are prescribed as monthly

climatologies from the Met Office Hadley Center Observational data set (Rayner et al., 2003). Boundary conditions are also prescribed for greenhouse gases and ozone-depleting substances as recommended for the SPARC CCMI (Stratosphere-troposphere Processes And their Role in Climate Chemistry-Climate Model Initiative) hindcast scenario REFC1SD (Eyring et al., 2013), in order to match those for the time period. The evolution of the QBO must be consistent through the post-eruption period, as it affects the dispersion of the volcanic plume to mid-latitudes (Trepte and Hitchman, 1992; Baldwin et al., 2001; Punge et al., 2009) and consequently the size distribution and lifetime of stratospheric aerosols (Hommel et al., 2015; Pitari et al., 2016b; Visioni, Pitari, and Aquila, 2017). Accordingly, models with internally generated QBO re-initialized it in order to be consistent with the actual meteorological conditions, or used specified dynamics approaches (e.g. Telford et al., 2008). All groups submitted a three-member ensemble for each different injection setting, except for ULAQ-CCM and EMAC, which submitted only one realization. The generation of the ensemble for each model is explained in the respective sections describing the model. Unless otherwise specified, all results shown refer to the ensemble mean.

Cerro Hudson simulations To evaluate the role of the Cerro Hudson eruption, we performed two additional simulations with the ULAQ-CCM model that, while outside the scope of ISA-MIP, helped clarify some issues raised by the initial results. The two simulations add the Cerro Hudson eruption to the Med-22km experiment with lower and upper estimates of SO_2 injection based on the Neely III and Schmidt (2016) and MSVOLSO2L4 inventory (Carn, 2022), respectively. The additional eruption consists in the injection of SO_2 with a uniform vertical distribution on August 10, 1991 in the grid cell corresponding to the Cerro Hudson location (45.9°S, 72.9°W). The lower-end emission, termed Med-22km + Low-Hud, includes 1.5 Tg of SO_2 between 11 and 16km, and the upper-end emission Med-22km + High-Hud includes 4 Tg of SO_2 at 12-18km.

Participating models

The ISA-MIP multi-model ensemble includes simulations from five global aerosol models: ECHAM6-SALSA, ECHAM5-HAM, SOCOL-AERv2, ULAQ-CCM,
UM-UKCA. In addition closely related simulations from a sixth model, EMAC, are considered. The main characteristics of the participating models are reported in Table 2.1. ECHAM5-HAM, SOCOL-AERv2 and EMAC are based on the same general circulation model (GCM), ECHAM5 (Giorgetta et al., 2006), but with different horizontal and/or vertical resolutions, while ECHAM6-SALSA uses the updated version ECHAM6.3 (Stevens et al., 2013); all have different chemical and aerosol modules.

ECHAM6-SALSA ECHAM6-SALSA (ECHAM6.3-HAM2.3-MOZ1.0) is an interactive aerosol-chemistry-climate model based on ECHAM6.3 general circulation model (Stevens et al., 2013). A T63L95 resolution was used in ECHAM6-SALSA simulations, which corresponds to an approximately 1.9°x1.9° horizontal grid and 95 vertical layers reaching up to 80 km. The QBO is internally resolved by the model (Laakso et al., 2022). The GCM is interactively coupled with the HAMMOZ aerosol-chemistry model (Schultz et al., 2018), which is a combination of the Hamburg Aerosol Model (HAM) and the Model for OZone And Related chemical Tracers (MOZART) chemistry model. However MOZART was not used in the simulations for this study, and OH and ozone concentrations were prescribed by a monthly mean climatology; a simplified sulfate chemistry scheme of HAM was used. The aerosol model HAM calculates the emissions, removal, and radiative properties of aerosol. It simulates five major global aerosol compounds: sulfate, organic carbon, black carbon, sea salt and mineral dust. The aerosol emissions from anthropogenic sources were based on the Community Emission Data System (CEDS) for the CMIP6 anthropogenic emission inventory. Sea salt and dust emissions were calculated online. Aerosol microphysics were calculated by the sectional aerosol module SALSA. A detailed description of the model is given in Kokkola et al. (2018). SALSA describes aerosols using 10 size bins in size space, and the 7 largest bins are separated into externally mixed soluble and insoluble populations. Ensemble members were produced by using insignificantly different values for one of the tuning parameters (the rate of snow formation by aggregation) for January 1991 of each ensemble member.

ECHAM5-HAM ECHAM5-HAM has the ECHAM5 GCM (Giorgetta et al., 2006), used as a high-top model in the middle atmosphere (MA) version, and is interactively coupled to the aerosol microphysical model HAM (Stier et al., 2005). The horizontal resolution is about 2.8° in longitude and latitude, in a spectral truncation at wave number 42 (T42), with 90 vertical layers up to 0.01 hPa (about 80 km) and an interactive simulation of the QBO. The aerosol microphysical model HAM (Stier et al., 2005) calculates the oxidation of sulfur and sulfate aerosol formation, including nucleation, accumulation, condensation, and coagulation processes. The width of the HAM modes has been adapted to the conditions under a high sulfur load. The aerosols are prescribed in three modes with a fixed width (Niemeier et al., 2009). HAM was further adopted to stratospheric conditions by applying a simple stratospheric sulfur chemistry above the tropopause (Timmreck, 2001; Hommel, Timmreck, and Graf, 2011). ECHAM prescribes oxidant fields of OH, NO_2, and O_3 on a monthly basis, as well as photolysis rates of OCS, H_2SO_4 SO_2, SO_3, and O_3. The sulfate was radiatively active for both SW and LW radiation and coupled to the radiation scheme of ECHAM. Further details are described in Niemeier, Riede, and Timmreck (2021). The ensemble members were produced by increasing the stratospheric horizontal diffusion from one level to the next above on January 1 of the year

of the eruption. The parameter generating different dynamical state is perturbed between 1.0, 1.0001 and 1.001.

SOCOL-AERv2 SOCOL-AERv2 is an interactive aerosol-chemistry-climate model that is also based on the ECHAM5 GCM but coupled to the MEZON chemistry (Egorova et al., 2003) and AER sulfate aerosol microphysics (Weisenstein et al., 1997) modules. The model version used here has a horizontal resolution of about 2.8° in longitude and latitude (T42) and 39 vertical layers up to 0.01 hPa. Because of the coarse vertical resolution (∼1.5 km in the lower stratosphere), the QBO is nudged to the observed equatorial wind profiles. The chemistry module calculates the interactions of 89 chemical species of the oxygen, hydrogen, nitrogen, carbon, chlorine, bromine, and sulfur groups in gas-phase, photolysis, and heterogeneous reactions, including reactions in/on aqueous sulfuric acid aerosols. The sulfate aerosol module resolves the aerosol particles in 40 size bins (the highest aerosol size resolution compared to other participating models), ranging in dry radius from 0.39 nm to 3.2 μm, and calculates nucleation, condensational growth, evaporation, coagulation, and sedimentation of sulfate aerosol bins. H_2SO_4 weight percent is calculated online based on actual temperature and relative humidity. Dry and wet deposition of species are interactively calculated based on actual meteorological conditions in the model (Feinberg et al., 2019). Modeled aerosols and chemical species are coupled with the shortwave- and longwave-radiation schemes. Aerosol radiative properties are treated following a lookup-table approach with precalculated values using Mie theory for actual H_2SO_4 weight percent and temperature. All boundary conditions follow the recommendations of ISA-MIP (Timmreck et al., 2018). Three ensemble members were produced by scaling the global CO_2 concentration by ±0.05%, which started in January 1991 and was maintained for the whole simulation. Besides the 39-level version, SOCOL-AERv2 can also be run on 90 levels, as the other two ECHAM5-based participating models ECHAM5-HAM and EMAC. However, increased resolution more than doubles the computational expenses of the already heavy calculations of interactive chemistry and highly resolved sectional aerosol microphysics. Therefore, the model is mostly used in the 39-level configuration. To test the effects of increased resolution, SOCOL-AERv2 has been additionally used here for the Low-22km experiment with the 90 levels instead of the 39 reference levels. With this configuration, the model has been spun up to the conditions of 1991. Besides changed resolution, all other settings have been kept the same.

ULAQ-CCM ULAQ-CCM (University of L'Aquila Chemistry Climate Model) is a global-scale climate-chemistry coupled model with a horizontal resolution of 5°x6° (T21) and 126 log pressure levels (approximate pressure altitude increment of 568 m), from the surface to the mesosphere (0.04 hPa). However, the QBO is not internally resolved and is nudged to observed values (Morgenstern et al., 2017) and its future values are repeated from the historical time series. The chemistry module includes

medium- and short-lived species (O_x, NO_y, NO_x, CHO_x, Cl_y, Br_y, SO_x) and the major component of stratospheric and tropospheric aerosols (sulfate, nitrate, organic and black carbon, soil dust, sea salt, polar stratospheric clouds). The microphysical code for aerosol formation and growth includes a gas-particle conversion scheme, homogeneous and heterogeneous nucleation, coagulation, condensation and evaporation (Pitari et al., 2002; Pitari et al., 2016a). It also includes heterogeneous chemical reactions on sulfuric acid aerosols and polar stratospheric cloud particles; both heterogeneous and homogeneous upper tropospheric formation processes are also included (Visioni et al., 2018a). The aerosol module calculates the aerosol extinction, asymmetry factor, and single scattering albedo, given the calculated size distribution of the particles for different wavelengths and they are passed daily to the radiative transfer modul, which is is a two-stream delta-Eddington approximation model (Toon et al., 1989).

UM-UKCA UM-UKCA model simulations are performed using the Global Atmosphere 4.0 configuration (Walters et al., 2014, GA4) of the UK Met Office Unified Model (UM v8.4) general circulation model with the UK Chemistry and Aerosol chemistry–aerosol sub-model (UKCA). The GA4 atmosphere model has a horizontal resolution of 1.875°×1.25° and 85 vertical levels (N96L85) ranging from the surface to about 85 km, with an interactive simulation of the QBO. The UM-UKCA configuration adapts GA4 with aerosol radiative effects from the interactive GLOMAP aerosol microphysics scheme and ozone radiative effects from the whole-atmosphere chemistry, which is a combination of the detailed stratospheric chemistry and simplified tropospheric chemistry schemes (Archibald et al., 2020). The GLOMAP stratospheric aerosol microphysics scheme is described in Dhomse et al. (2014), and model setup is described in Dhomse et al. (2020). Briefly, the model uses the GLOMAP aerosol microphysics module coupled with the troposphere-stratosphere chemistry scheme, and modeled aerosols are coupled with the radiation scheme. The model also uses greenhouse gas (GHG) and ozone-depleting substance (ODS) concentrations from Ref-C1 scenario used in the CCMI-1 (Morgenstern et al., 2017) activity. Simulations are performed in atmosphere-only mode, and CMIP6-recommended sea surface temperatures and sea ice concentration that are obtained from `https://esgf-node.llnl.gov/projects/cmip6/` (last access: 25 March 2021) are used. Three ensemble members were initialized using the fields of 3 model years of 20-year time-slice simulations prior 1990 that gave a QBO transition approximately matching that of ERA-Interim reanalysis (for more details Dee et al., 2011; Dhomse et al., 2020).

EMAC EMAC is the ECHAM5 general circulation model coupled with the Modular Earth Submodel System Atmospheric Chemistry (Brühl et al., 2015; Brühl et al., 2018). The resolution is T63/L90, i.e. about 1.9° latitude and longitude and 90 layers up to about 80 km with a vertical resolution of about 500 m near the tropopause. The QBO is internally generated but slightly nudged to observations compiled by the

Free University of Berlin. Below 100 hPa and above the boundary layer dynamics and temperature are nudged to ERA-Interim. It contains comprehensive gas-phase and heterogeneous chemistry. The applied aerosol module GMXE (Pringle et al., 2010) accounts for seven modes using lognormal size distributions (nucleation, soluble and insoluble Aitken, accumulation, and coarse modes). The boundary between accumulation mode and coarse mode, a model parameter, is set at a dry particle radius of 1.6 μm to avoid too-fast sedimentation of a too-large coarse-mode fraction in case of major volcanic eruptions. Optical properties for the types sulfate, dust, organic carbon and black carbon (OC and BC), sea salt (SS), and aerosol water are calculated using Mie-theory-based lookup tables for each mode consistent with the selected size distribution widths of the modes. This also means that no overall effective radius is used. The resulting total optical depths, single-scattering albedos and asymmetry factors are used in radiative transfer calculations which feed back to atmospheric dynamics. The results from EMAC were taken from an existing 30-year transient simulation for comparison (Schallock et al., 2021).

TABLE 2.1: Main chemical, microphysical and dynamic characteristics of the participating models.

Model	Injection region	Interactive OH	Stratospheric aerosol components	Aerosol dynamics scheme	Simulated aerosol in heterogeneous chemistry	Nucleation scheme	QBO
ECHAM6-SALSA	Point	No	Sulfate, Dust, OC, BC and SS	2-moment sectional, 10 bins	No	Vehkamäki et al. (2002)	Internally generated
ECHAM5-HAM	Point	No	Sulfate	2-moment modal, 7 modes	No	Vehkamäki et al. (2002)	Internally generated
EMAC	3D-plume	Yes	Sulfate, Dust, OC, BC, aerosol water	Modal, 7 modes	Yes	Vehkamäki et al. (2002)	Internally generated but slightly nudged
SOCOL-AERv2	Point	Yes	Sulfate	Sectional, 40 size bins	Yes	Vehkamäki et al. (2002)	Nudged
ULAQ-CCM	Point	Yes	Sulfate (also other components in troposphere)	Sectional, 22 bins	Yes	Pitari et al. (1993)	Nudged
UM-UKCA*	0-15°N, 120°E	Yes	Sulfate and Meteoric Smoke particles	2-moment modal, 7 modes	No	Mann et al. (2010)	Internally generated

2.1.2 Observation data sets

AVHRR

The Advanced Very High Resolution Radiometer (AVHRR/2) is a space-borne sensor that measures the reflectance of the Earth in five spectral bands covering visible and infrared wavelengths (0.63, 0.86, 3.7, 11, 12 μm). AVHRR/2 instrument was on board of the polar-orbiting satellites (POES) NOAA-11 that provided global coverage data with a resolution of 1.1 km and a frequency of Earth scans of twice per day (https://www.avl.class.noaa.gov/release/data_available/avhrr/index.htm, last access: 12 January 2023). The data used here are on a 1°x1° grid as monthly averages (as archived at NOAA's National ClimateData Center). As in Long and Stowe (1994) and Aquila et al. (2012), the stratospheric optical depth at 0.5 μm is calculated by removing monthly mean background values (June 1989 to May 1991) from AVHRR observations. The optical depth at 0.5 μm is retrieved through a radiative transfer surface/atmosphere model (RAO, STOWE, and McCLAIN, 1989) therefore, combined with the previous assumption, AVHRR cannot detect the changes in stratospheric AOD smaller than 0.01 but can detect values up to 2.0 (Russell et al., 1996).

SAGE II

The Stratospheric Aerosol and Gas Experiment II (SAGE II) is a satellite-based sun photometer that was launched in October 1984 aboard the Earth Radiation Budget Satellite (ERBS) and retired in August 2005. The instrument measures the extinction of the solar radiation through the limb of the Earth's atmosphere in seven channels ranging from 385 to 1020 nm, with a global coverage from 80°S to 80°N latitude and a vertical resolution of 1 km for the retrieved data (Mauldin et al., 1985). We used the effective radius and the surface area density of aerosol particles from SAGE II version 7.0 (Damadeo et al., 2013; NASA/LARC/SD/ASDC, 2012). The SAD (and thus the effective radius) is derived by a method that is a linear mix between the Thomason, Poole, and Deshler (1997) method, which is valid for the 525-1020 nm extinction ratio below 1.5, and the Thomason and Burton (2008) method for ratios above 2.0 (Damadeo et al., 2013). Both methods assume that aerosols are spherical droplets of H_2SO_4-H_2O solution with a constant composition of 75% H_2SO_4 and 25% H_2O by weight. The Thomason, Poole, and Deshler (1997) method uses the principal component analysis to derive the SAD from a linear combination of four aerosol extinction measurements (386, 452, 525, 1020 nm). In the Thomason and Burton (2008) method, SAD is derived from the 525 and 1020 nm channels using an empirical parameterization based on the 525-1020 nm extinction ratio.

The stratospheric sulfate burden is taken from the SAGE-3λ data set (ftp://iacftp.ethz.ch/pub_read/luo/CMIP6/, last access: 12 January 2023) that was compiled for Phase 6 of the Coupled Model Intercomparison Project (CMIP6). H_2SO_4 particle number density (and other secondary products not used here) is derived via

the SAGE-3λ algorithms that assume a single mode lognormal size distribution of stratospheric aerosol where number density, mode radius and width are obtained by fitting the SAGE II extinction coefficients at three wavelengths (452, 525 and 1024 nm) (Revell et al., 2017).

HIRS

The High Resolution Infrared Radiation Sounder (HIRS) is an infrared-scanning radiometer that has been onboard several NOAA platforms starting with the first satellite of the Television Infrared Observation Satellite series (TIROS-N), followed by NOAA-6 up to NOAA-19 (Borbas and Menzel, 2021). It measures the reflectance of the Earth in 19 infrared channels (3.7 to 15 μm) and 1 solar channel (0.69 μm) with a spatial resolution at nadir of 20.4 km on HIRS/2. Baran and Foot (1994) used HIRS/2 cloud-cleared radiances at 8.3 μm (NOAA-10/12) and 12.5 μm (NOAA-11) to retrieve the column number density of sulfuric acid aerosols from May 1991 to November 1993. Among the assumption and the approximations, the stratospheric aerosols are assumed to be 75% H_2SO_4 and 25% H_2O, with a spectral transmittance based on dustsonde measurements by Deshler et al. (1992) and a *single-scattering albedo calculated from Mie theory by integrating the extinction and scattering coefficients over a lognormal size distribution using a mode radius 0.35 µm and a normalized standard deviation of 1.6* (Baran and Foot, 1994). The data cover the latitudes from 80°N to 80°S and all longitudes with 5° of resolution and are affected by a systematic error of 10% due to the sensitivity of the retrieved method and uncertainties in the background.

OPC

The University of Wyoming balloon-borne Optical Particle Counter (OPC) is a spectrometer that measures the light-extinction cross section of the particles using a broadband incandescent light source, developed by Rosen (1964), providing the particle size and the number concentration. The stratospheric aerosol measurements from 1991 to 2012 are made over Laramie (Wyoming) with the so-called OPC40, which can detect particles throughout the size range 0.1-10.0 μm, distinguished in 8 or 12 channels, depending on the instruments (Deshler, 2003). Here we used the revised data set (UWv2.0; `http://www.atmos.uwyo.edu/~deshler/Data/Aer_Meas_Wy_read_me.htm`, last access: 12 January 2023) of the OPC measurements (Deshler et al., 2019). Surface area density and volume density are calculated from the size distribution derived from particle size and concentration by fitting the data to a unimodal or bimodal lognormal distribution (depending on the number of measurements and on which of the two minimizes the difference between the calculated and the measured number concentration) (Kovilakam and Deshler, 2015).

GloSSAC

The Global Space-based Stratospheric Aerosol Climatology (GloSSAC) is a global and gap-free data set of zonally averaged optical properties of stratospheric aerosols (focused on aerosol extinction coefficient at 525 and 1020 nm) from 1976-2018. It is mainly based on the Stratospheric Aerosol and Gas Experiment (SAGE) and on the Optical Spectrograph and InfraRed Imager System (OSIRIS) and the Cloud-Aerosol Lidar and Infrared Pathfinder Satellite Observation (CALIPSO). Ground, airborne, and balloon-based instruments were used to fill major gaps in the data set (Thomason et al., 2018). Here, we used the updated version v2 (NASA/LARC/SD/ASDC, 2012) from Kovilakam et al. (2020).

2.2 Results

The various sets of initial conditions of SO_2 injections result in an aerosol cloud with different optical properties depending on the dispersion of the cloud over time and the size of the aerosols produced.

In the following section, we start by analyzing the AOD and how the models reproduce the measured AOD with different volcanic emission source parameters. Since the amount of attenuation depends on the particle number concentrations and size, we then investigated both the magnitude and distribution of the sulfate burden and the size of the sulfate aerosols.

2.2.1 Aerosol optical depth

The stratospheric AOD simulated by the different interactive aerosol microphysical models is evaluated by comparing it with satellite observations from AVHRR and GloSSAC (Fig. 2.2). The AOD is calculated at a wavelength of 550 nm in EMAC, ECHAM5-HAM, ULAQ-CCM and UM-UKCA, 533 nm in ECHAM6-SALSA, 525 nm in SOCOL-AERv2 and GloSSAC, and 600 nm in AVHRR. Differences between those wavelengths are however negligible. GloSSAC provides zonal values with a latitudinal resolution of 5° and uniform spatio-temporal coverage up to the year 1994. As it is mostly based on SAGE II measurements, the instrument saturates for optical depth of about 0.15, therefore it is less accurate in the center of tropical clouds in the first months after the eruption (Russell et al., 1996). Conversely, AVHRR can only measure stratospheric AOD larger than 0.01. Because of the paucity of data points, "global values" when comparing against AVHRR are calculated between 60°S-60°N.

Figure 2.2 shows the time evolution of the zonal-mean stratospheric AOD for each model and ensemble mean. It is clear that medium and high injection of SO_2 (Med-22km and High-22km, respectively) overestimate the stratospheric AOD in the tropics or/and in the Northern Hemisphere (NH) extratropics compared to both observations. The ability to reproduce the observed values in the Southern Hemisphere (SH) extratropics depends on both the model and the injection parameters.

TABLE 2.2: Correlation (COR) and root-mean-square-difference (RMSD) of the stratospheric AOD calculated between observations and model results, for the experiments that best reproduce the observations.

	AVHRR (June 91 - May 92)			GloSSAC (June 91 - May 92)			GloSSAC (June 92 - May 93)		
Model	Experiment	COR	RMDS	Experiment	COR	RMDS	Experiment	COR	RMDS
ECHAM6-SALSA	Med-18-25km	0.74	0.08	Med-19km	0.60	0.07	Med-19km	0.79	0.02
ECHAM5-HAM	High-22km	0.74	0.09	Low-22km	0.71	0.07	Med-22km	0.82	0.02
EMAC		0.79	0.07		0.54	0.10		0.63	0.03
SOCOL-AERv2	Med-19km	0.73	0.08	Med-19km/Low-22km	0.61	0.09	Med-19km	0.86	0.02
ULAQ-CCM	Med-19km	0.84	0.07	Med-19km	0.74	0.07	Med-19km	0.69	0.03
UM-UKCA	Low-22km	0.56	0.12	Low-22km	0.63	0.11	Med-19km	0.47	0.05
UM-UKCA*	Low-22km	0.87	0.07	Low-22km	0.82	0.09	Med-19km	0.86	0.02

* highlights models with spatially distributed SO_2 injections.

UM-UKCA* and EMAC, contrary to other models, show more southward transport, probably due to the different injection settings (see section 2.1.1). In UM-UKCA* the meridional-spread emission (0-15°N) accounts for the initial west-southwestward drift of the volcanic cloud (Bluth et al., 1992a), contributing to a more hemispherically symmetric aerosol distribution (Dhomse et al., 2014; Mills et al., 2016; Jones et al., 2017). EMAC used a 3D-plume injection and also included smaller eruptions such as that of Cerro Hudson in the Southern Hemisphere in August 1991 (45.9°S, 72.9°W). The additional injection is a 3D-plume injection of 0.65 Tg-S of SO_2, whose maximum in terms of mixing ratio is at 18 km, and differs from the two additional cases performed with ULAQ-CCM (2.1.1.1). In ULAQ-CCM, the Med-22km+Low-Hud includes a similar amount of SO_2 but at lower altitudes compared to the Cerro Hudson eruption in EMAC, and its effect on the stratospheric burden and AOD is negligible. In contrast, Med-22km+High-Hud enhances them in the Southern Hemisphere, approaching observation, but only for a few months after the eruption (Fig. A.6).

A quantitative comparison with the observations is shown with the use of Taylor diagrams (see Appendix A) in Figure 2.3. Model results are compared for the first year after the eruption with both AVHRR and GloSSAC (first row and second row, respectively) and for the second year only with GloSSAC (third row). Three-member ensembles, when provided, are represented with smaller circles of the same color with respect to the ensemble mean of a specific simulation. In ECHAM6-SALSA, the differences between members of the same scenario are greater than those between scenarios because of differences in local winds at the time of the eruption in each ensemble member. The impact of local winds is weaker when SO_2 is injected over the deep altitude range between 19 and 25 km (blues circles in Figure 2.3 panels a and h). There are various sets of initial conditions for SO_2 injections which, depending on the model, are close to the observations. The experiments that best reproduce the observations are those with similar variability to that of the observations, defined by their standard deviations (SDs), higher correlation (COR) and lower root-mean-square difference (RMSD). The values of COR and RMSD for these experiments are summarized in Table 2.2.

During the first year after the eruption, all models show better agreement with

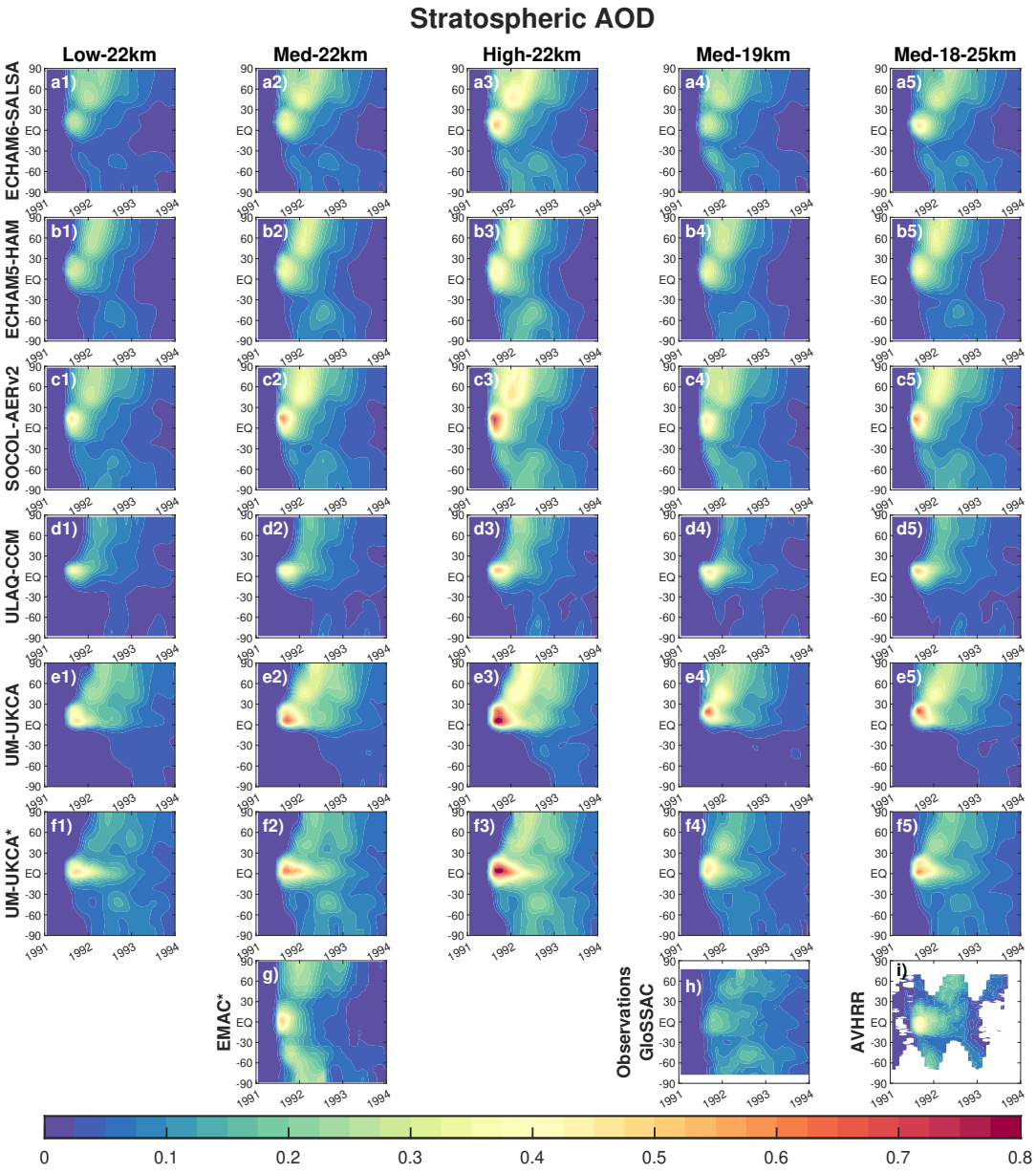

FIGURE 2.2: Time evolution of zonal stratospheric AOD for all models, in Low-22km (first column), Med-22km (second column), High-22km (third column), Med-19km (fourth column), Med-18-25km (fifth column). The last row includes the different scenario simulated by EMAC* and the two observations used for comparison: GloSSAC and AVHRR. AOD is calculated at a wavelength of 550 nm in ECHAM5-HAM, EMAC, ULAQ-CCM and UM-UKCA, 533 nm in ECHAM6-SALSA, 525 nm in SOCOL-AERv2, 525 nm in GloSSAC, 600 nm in AVHRR. * Models with spatially spread SO_2 injections.

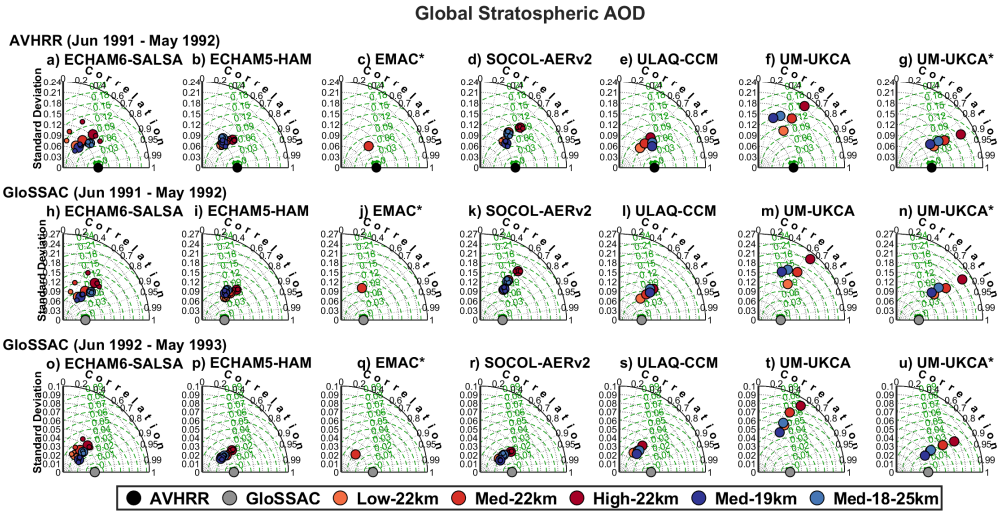

FIGURE 2.3: Taylor diagrams for the global stratospheric AOD. Zonal monthly mean values for different time periods have been used to calculate the standard deviation, correlation, centered root mean square difference between model experiments and measurements. In the 1st row, model results are compared with respect to AVHRR over the period June 1991 to May 1992; in the second row with respect to GloSSAC over the period June 1991 to May 1992; and in the third row with respect to GloSSAC over the period June 1992 to May 1993 (See appendix A for more details). * Models with spatially spread SO_2 injections.

AVHRR than GloSSAC: correlations range between 0.73 and 0.78 with AVHRR versus 0.54 and 0.82 with GloSSAC, for which RMSDs are also higher. In ECHAM6-SALSA, SOCOL-AERv2 and ULAQ-CCM, the injection of 7 Tg-S of SO_2 closer to the tropopause is a good compromise between the too-high and too-low stratospheric AOD produced in the tropics by an injection of 5 and 10 Tg-S of SO_2, respectively, and this scenario also produces a better southward and northward transport (Fig. 2.2). The best set of initial parameters also depends on the observation considered for comparison: in ECHAM6-SALSA Med-18-25km and Med-19km reproduce better AVHRR and GloSSAC measurements, respectively, and in the comparison with GloSSAC the correlation increases, and the RMSD decreases over time (Fig. 2.2a5). For SOCOL-AERv2 and ULAQ-CCM, Med-19km is in good agreement with both AVHRR and GloSSAC in the two different periods considered (Fig. 2.2 panels c4 and d4). During the first year after the eruption, the correlation between Med-19km and the observations is higher for ULAQ-CCM (0.84 and 0.74 compared with AVHRR and GloSSAC, respectively) as it better reproduces the tropical confinement, while in the following year (June 1992 - July 1993), in SOCOL-AERv2 comparable values of stratospheric AOD persist for longer in the extratropics compared with GloSSAC (correlation of 0.86). In ECHAM5-HAM the injection at 21-23 km results in a comparable stratospheric AOD in the tropics and SH extratropics compared to both observations, but overestimates NH extratropics values by up to a factor of 2 (Fig. 2.2b1, b2 and b3). The amount of SO_2 to obtain the highest correlation between modeling

experiments and observations depends on the observation and on the period considered: High-22km and Low-22km when compared with AVHRR and GloSSAC during the first year after the eruption, respectively, Med-22km when compared with GloSSAC the following year. In UM-UKCA, the point injection and meridional-spread emission agree that Low-22km better reproduces the stratospheric AOD of both observations during the first year after the eruption, as it shows a good tropical confinement and comparable values in the NH, and for the meridional-spread emission also in the SH (Fig. 2.2e1 and f1). Therefore, the correlation is higher and the RMSD is lower for the meridional-spread emission experiment. The poleward transport, especially in the NH, is enhanced in Med-19km (Fig. 2.2e4 and f4) and found to have a higher correlation with GloSSAC one year after the eruption (COR of 0.86 and 0.47 for UM-UKCA* and UM-UKCA, respectively). During the first year after the eruption, EMAC has comparable values in the tropics and northern mid-latitudes with respect to AVHRR, while in the southern mid-latitudes the stratospheric AOD is up to twice as large and results in a correlation of 0.79. The correlation decreases to 0.63 when comparing with GloSSAC during the following year because of the more rapid decline in the stratospheric volcanic cloud.

The persistence of the volcanic aerosol in the stratosphere is shown in Figure 2.4, which represents the global normalized stratospheric optical depth, calculated as explained at the beginning of section 3.1. The Med-19km experiment is shown for all models, as it is the experiment which best reproduces the GloSSAC observations after June 1992 for all models, with the exception of Med-22km for ECHAM5-HAM and EMAC with the only experiment provided. The e-folding time, calculated as the time between the maximum and the 1/e value, is 13 months in AVHRR and 15 months in GloSSAC. This range includes ULAQ-CCM and UM-UKCA with an e-folding time of 14 months and UM-UKCA*, with an e-folding time of 15 months. Lower values were found for SOCOL-AERv2 with 12 months, ECHAM6-SALSA and ECHAM5-HAM with 11 months, and EMAC with 10 months.

2.2.2 Sulfate burden

Figure 2.5 shows the time evolution of the global and tropical stratospheric sulfate burden of different injection setups for each model. The results of each model are compared with satellite measurements from HIRS and the SAGE-3λ data set. Large differences are evident in the temporal evolution of the sulfate burden between the aerosol model simulation on one hand and the satellite data set on the other, which show similar values and a similar temporal evolution for the sulfate burden.

In the 6 months following the eruption (July-December, termed the build-up phase), ECHAM6-SALSA, ECHAM5-HAM, SOCOL-AERv2, and ULAQ-CCM best match the global stratospheric sulfate burden of HIRS and SAGE-3λ with the injection 5 Tg-S of SO_2 (Low-22km), a lower amount compared to the one required for a comparable stratospheric aerosol optical depth (Fig. 2.5 panels a,b,d and e). For SOCOL-AERv2, Med-19km also shows values within the uncertainties in the

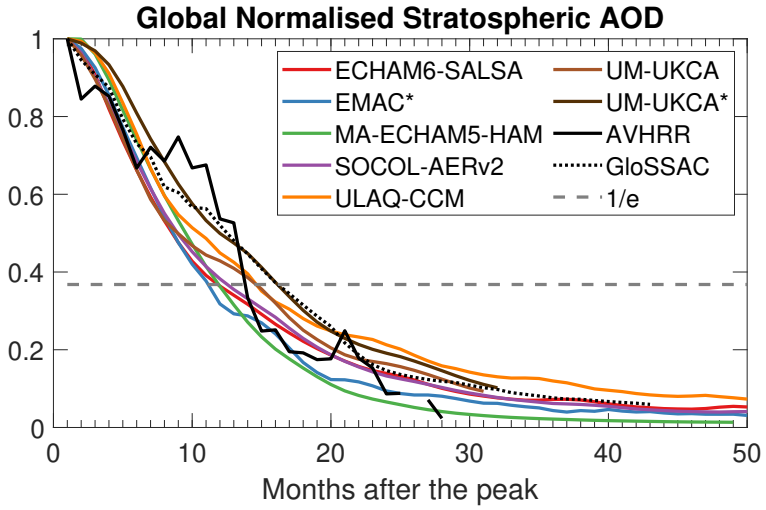

FIGURE 2.4: Time evolution of monthly values of the normalized global stratospheric AOD for models (colored lines) and AVHRR and GloSSAC observations (black lines). The dashed gray line represents the $1/e$ value. The experiments shown are Med-19km for ECHAM6-SALSA, SOCOL-AERv2, ULAQ-CCM, UM-UKCA and UM-UKCA* and Med-22km for ECHAM5-HAM. For EMAC*, it refers to the only experiment provided. * Models with spatially spread SO_2 injections.

HIRS measurements. However, Low-22km, and also Med-19km for SOCOL-AERv2, anticipates the peak and underestimates the tropical burden in ECHAM6-SALSA, ECHAM5-HAM and SOCOL-AERv2, while the peak is reached later and larger values are produced in ULAQ-CCM (Fig. 2.5 panels h,i,k and l). In UM-UKCA, point and meridional-spread injection show similar results for the global stratospheric sulfate burden and agree with observations with Med-19km and Med-18-25km experiments (Fig. 2.5 panels f and g). The differences between the two strategies emerge in the tropics where values are lower for point injection experiments due to the lack of aerosols transported to the southern tropics and that are therefore confined to the Northern Hemisphere. For the point injection, Low-22km and Med-18-25km approaches SAGE-3λ for the first months and HIRS for the last 3 months of the build-up phase. All the experiments with larger amounts of injected SO_2, including the EMAC experiment with 8.5 Tg-S of SO_2, overestimate the measured global sulfate burden; all experiments in ULAQ-CCM and the single scenario in EMAC overestimate the tropical burden, while in ECHAM6-SALSA, ECHAM5-HAM and SOCOL-AERv2 overestimate the burden in the NH extratropics (Fig. A.5).

In the build-up phase, SAGE-3λ assumes the lowest values and slowly reaches a peak of 5.0 Tg-S in December, compared to 5.4 Tg-S of HIRS in September. Lower values in SAGE-3λ are related to the saturation effects of the limb-occultation instrument, therefore HIRS measurements are to be considered more reliable for this initial period (Sukhodolov et al., 2018). For EMAC, the injection of 8.5 Tg-S of SO_2 produces a sulfate aerosol cloud that peaks in September at 7.0 Tg-S, a value comparable to the results of the Med-22km experiment (performed by the other models), in

which 7 Tg-S of SO_2 is injected. For SOCOL-AERv2 and UM-UKCA with both injection strategies, Med-19km shows the best agreement with HIRS in terms of peak and timing of the peak (September for SOCOL-AER, October for UM-UKCA), whereas in Low-22km and the other experiments it is reached 1 month later. This is followed by ECHAM6-SALSA in October (November only in High-22km) and ULAQ-CCM in November. ECHAM5-HAM is more sensitive to the altitude of injection: it peaks between October in Med-19km, November in Med-18-25km and December in the experiments with the same altitude of injection (Low-21km, Med-21km and High-21km); the values of the peak are 14.3% lower in Med-19 km and 7.1% lower in Med-18-25km compared to Med-22km.

The sensitivity to injection altitude depends on the model: during the build-up phase, the Med-18-25km and Med-22km curves coincide in ECHAM6-SALSA and SOCOL-AERv2, and, compared to these experiments, the values in Med-19km are up to 9% and 20% smaller for each model, respectively. In ULAQ-CCM, ECHAM5-HAM, and UM-UKCA, the more SO_2 is injected at lower altitudes the smaller the value of the peak is, but for ULAQ-CCM the peak is only 1% and 6% lower in Med-18-25km and Med-19km compared to Med-22km. The value and time of the peak for all models and experiments are summarized in table A.2. In general, when the amount of SO_2 injected is exclusively in the lowest levels or in some vertical levels that include the lowest levels (Med-19km and Med-18-25km respectively), the sulfate burden is lower, and therefore this effect is less pronounced at Med-18-25km, as the aerosol distribution is more dependent on the balance between gravitational sedimentation in the lower stratosphere and the strength of vertical transport by the Brewer-Dobson Circulation, as well as the height of the tropopause.

Differences among models and experiments in terms of amount and timing during the build-up phase are influenced by the oxidation of SO_2 by OH that determines the timescale for aerosol formation (Clyne et al., 2021). For this reason, we distinguish between models with prescribed OH (ECHAM6-SALSA and ECHAM5-HAM) and those with interactive OH (SOCOL-AERv2, ULAQ-CCM, UM-UKCA) when looking at the SO_2 evolution. The global normalized SO_2 burden curves (Fig. A.4a) coincide for all models with prescribed OH. An exception is Med-19 km in ECHAM6-SALSA, which has lower values and might depend on an early removal through tropopause flux, facilitated by injection near the tropopause. In ULAQ-CCM and UM-UKCA, when comparing High-22km with Low-22km we find that a higher injected SO_2 mass produces a longer initial e-folding time for SO_2. The same applies when comparing injections concentrated in a few kilometers (Med-22km and Med-19km), i.e. where SO_2 oxidation depletes OH more quickly (Mills et al., 2017), with those where the same amount of SO_2 is injected over a wider altitude band. Consequently, initial values of the stratospheric sulfate burden in Med-18-25km are slightly higher compared to Med-22km and Med-19km.

In order to better understand the models sensitivity to the different emission scenarios and eventual non-linearities, in Figure 2.6 we normalize the resulting global

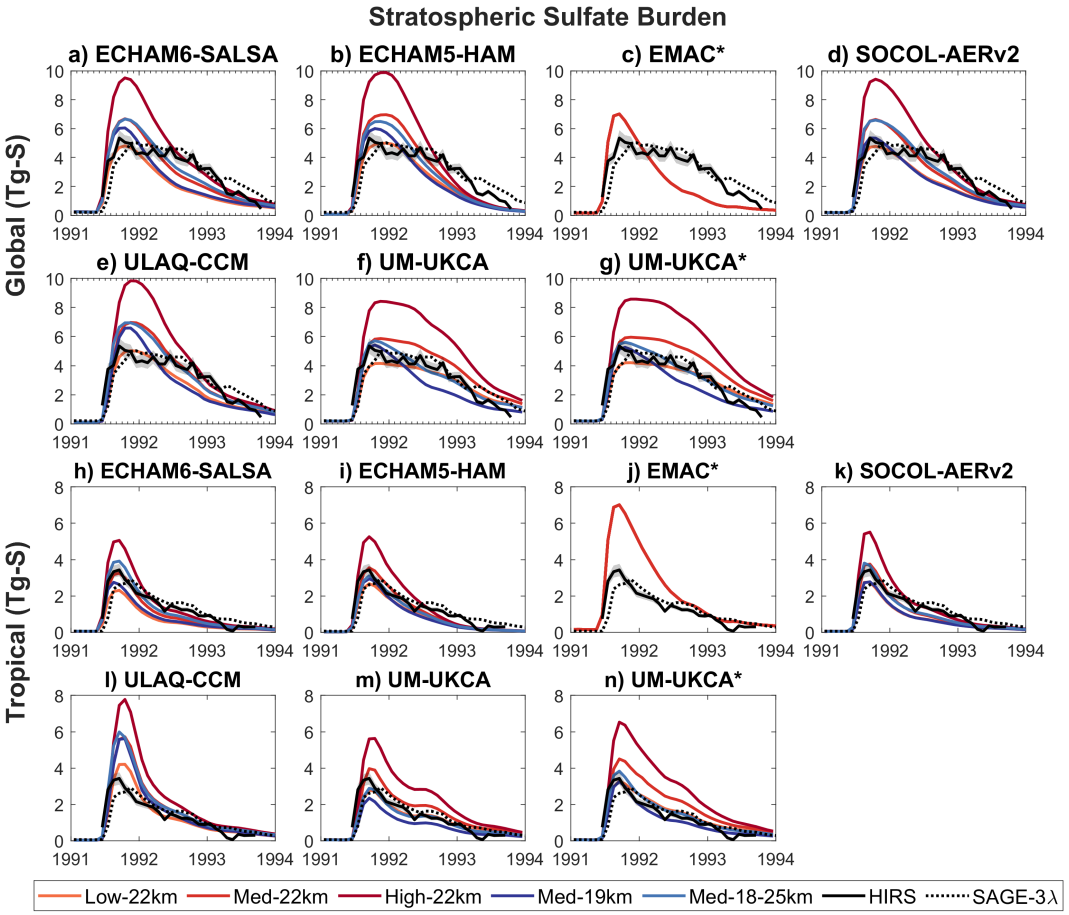

FIGURE 2.5: Time evolution of monthly values of global and tropical stratospheric sulfate burden in Tg-S (first and second column, respectively). Each panel refers to the respective model in which the different results of the experiments (colored lines; different line styles for different experiments, see legend on the left) are compared with the HIRS and SAGE-3λ data sets (black lines, see legend on the right). * Models with spatially spread SO_2 injections.

sulfate burden by the amount of SO_2 injected. Thus, in the build-up phase we would expect all the curves for all experiments to reach a value of 1, since no SO_2 and sulfate aerosols have yet been removed from the atmosphere. This will highlight the differences in the aerosol removal (wet removal, deposition, sedimentation) depending on the injection altitude and differences in microphysical growth, especially in the descending phase. Not all models and experiments, however, reach the value of 1: ECHAM5-HAM in Med-19 km and Med-18-25 km and ULAQ-CCM in Med-19 km do not, nor do any experiments in ECHAM6-SALSA, SOCOL-AERv2, and UM-UKCA. This is due to the use of monthly averages for our analyses and the faster removal, near the tropopause, of sulfate aerosol and SO_2 not yet converted to aerosols, especially in Med-19km and Med-18-25km experiments. To confirm this, we observe that this is particularly evident in Med-19km with the lowest injection height. The curves of the experiments with injection between 21-23 km coincide in the build-up phase and the differences emerge later, after 1992: the aerosol lifetime decreases with increasing mass of SO_2 injected (table A.2), which corresponds to the increase in the aerosol size in all models. In UM-UKCA, the lifetime is increased by 1 to 2 months for the meridional-spread emission compared with the point injection. In ECHAM6-SALSA the lifetime increases when increasing the injected SO_2 mass. However, Figures 2.3 and A.1 show that the differences in results between ensemble members of the same scenarios are larger in ECHAM6-SALSA than in other models. This indicates that differences in aerosol lifetimes between Low-22km, Med-22km and High-2km scenarios are probably not statistically significant in ECHAM6-SALSA. Figure A.11 panel a shows the sulfate burden from SOCOL-AERv2 for the Low-22km experiment calculated with two vertical model resolutions. This figure further confirms the faster removal of volcanic sulfur during the first months after the eruption in SOCOL-AERv2 even in the 22 km injection experiments. The lower-vertical-resolution version shows much lower burden peak already in the late 1991, while the higher-resolution version peaks at exactly the emitted amount of 5 Tg-S plus the background value of $\sim$0.17 Tg-S and maintains this peak till early 1992. This is an effect of increased vertical diffusion in the lower-resolution version, which quickly redistributes the volcanic cloud vertically in both directions. This brings some of the volcanic sulfur mass closer to the tropopause and the shallow branch of the Brewer-Dobson circulation, reducing its confinement in the tropical reservoir and enhancing removal from the stratosphere (Brodowsky et al., 2021). This agrees with the results of 22km experiments of high-resolution ECHAM5-HAM, which also maintain the emitted amount for some months after the eruption (Fig. 2.6).

Among all models and experiments, the shortest e-folding time of the global stratospheric sulfate burden is 8 months for EMAC, ranges between 10 and 14 months for ECHAM6-SALSA, ECHAM5-HAM, SOCOL-AERv2 and ULAQ-CCM, and reaches the highest values for UM-UKCA with values between 17 and 23 months, which more closely matches those of HIRS and SAGE-3λ of 21 and 20 months, respectively. The e-folding time of the tropical stratospheric sulfate burden is 12 and 13 months in

HIRS and SAGE-3λ and half for the models with the exception of ECHAM5-HAM for Low-22km, Med-22km and Med-18-25km with a longer duration of 9 months, and UM-UKCA for which it varies between 8 and 14 months, based on the experiments and injection strategy. No model except UKCA can reproduce the observed slow-descent phase during 1992 of the stratospheric sulfate burden, and only the High-22km scenario approaches the measured values at the end of 1992 for these models, while strongly overshooting them in the preceding months.

Overall, we find that Low-22km and High-22km are the experiments that, in all models, better reproduce the observations in the build-up and descent phase, respectively (Fig. 2.5 and A.6). The spatio-temporal development of the sulfate burden (Fig. A.6) reflects in general that of the AOD (Figs. 2.2, 2.3). In the SH, the stratospheric burden shown in SAGE-3λ is not reproduced by the models in Low-22km, therefore more SO_2 (High-22km) must be injected for the aerosol cloud to persist for as long as in SAGE-3λ and reach the same values. This way, however, the burden in the NH is overestimated (Fig. A.5). There are clear differences in the position of the stratospheric AOD peak, which lies between 5-20°N in the models, but around 5°S-10°N in the observations pointing to differences in the meridional transport in the early phase after the eruption (Fig. 2.2). In addition, Figure A.11b-c illustrate that the volcanic aerosol mass redistribution between the hemispheres could also be affected by the vertical resolution of the models, because it affects the timings of tropical confinement and across-tropopause removal.

In order to discuss the meridional transport, Figure 2.7 shows the aerosol mass fraction of the simulated sulfate burden in the tropics (20°N-20°S), in the northern mid-latitudes (35°-60°N) and in the southern mid-latitudes (35°-60°S) with respect to the global value, for SAGE-3λ (black line), and for all models and scenarios (first row for the different injection amounts, second row for the different injection altitudes). Tropical confinement (panels 2.7a and d) as shown in the observations, is not captured by ECHAM6-SALSA, ECHAM5-HAM, SOCOL-AERv2, and EMAC, which underestimate the tropical aerosol mass fraction, resulting in a stronger transport to the NH for the first three models and to the SH for EMAC. ULAQ-CCM overestimates the fraction during the first 6 months after the eruption and becomes comparable thereafter. UM-UKCA shows tropical confinement comparable to that of SAGE-3λ for the 21-23km injection experiments for point injection and shallow and deep injection for meridional-spread emission, otherwise underestimated or overestimated in the other experiments, respectively. However, the similarity between observations and the 21-23km injection experiments for the UM-UKCA point injection masks the lack of aerosols in the southern tropics (0-20°S) and a higher load in the northern extratropics (0-20°N). Indeed, the fraction of burden for the NH mid-latitudes (panels 2.7b and e) is overestimated with differences of up to 20% compared to SAGE-3λ (2.7h) while for the SH (2.7c and f) it is underestimated but to a smaller extent with differences of 10% compared to SAGE-3λ (2.7i). The same happens for ECHAM6-SALSA, ECHAM5-HAM, and SOCOL-AERv2. Overall, NH

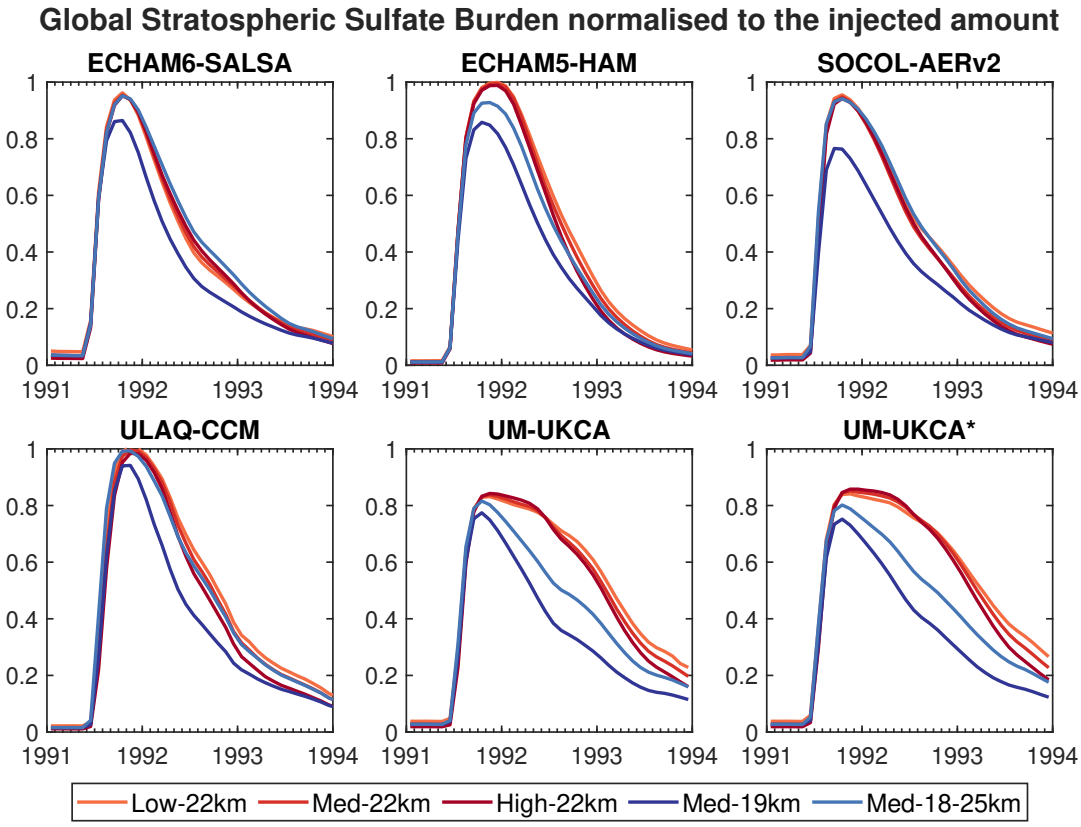

FIGURE 2.6: Time evolution of global stratospheric sulfate burden normalized to the amount of injected SO_2. Each panel refers to the respective model in which the different experiments are compared.

transport is favored in all models at the expense of tropical confinement.

In most models, varying the injected SO_2 mass does not affect the fraction of aerosols transported out of the tropics towards both hemispheres (2.7a, b, and c). The only exception is ECHAM6-SALSA, where an increased injected SO_2 mass increases the tropical confinement, especially in the first 6 months after the eruption. All models, except ULAQ-CCM, show that the tropical confinement is reduced in favour of transport towards both hemispheres when SO_2 is injected below 20 km (Med-19km). Compared to high-altitude injection settings (>20 km), Med-19km has the greatest transport in SH. The increase in altitude of injection (Med-22km and Med-18-25km) produces a higher confinement in the tropics with a consequent reduced transport toward both hemispheres in ECHAM6-SALSA, SOCOL-AERv2 and UM-UKCA. In ECHAM5-HAM, the strongest confinement is achieved in Med-22km, while Med-18-25km shows a similar behavior to Med-19km as most of the sulfate aerosols are found below 20 km. In ULAQ-CCM differences among the injection settings emerge six months after the eruption and the injection at lower altitudes (Med-19km) shows a more efficient polewards transport, especially towards the NH.

2.2.3 Effective radius and surface area density

Figure 2.8 shows the time evolution of the observed and simulated stratospheric effective radius in the tropics (20°S-20°N) and over Laramie (41°N-105° W) (calculation of the effective radius and error bar in Appendix A2). In the tropics (Figs. 2.8 a-g) the stratospheric effective radius is calculated as the SAD-weighted average between 21-27 km because of a paucity of tropical measurements below 21 km in SAGE II. Over Laramie (Figs. 2.8 h-n), the stratospheric effective radius is defined as the SAD-weighted average between 14-30 km in order to compare it with in situ OPC measurements (Deshler et al., 2019). Model results are calculated as the value of the nearest grid cell to Laramie; therefore, the ability to reproduce the OPC measurements is more influenced by atmospheric circulation patterns as zonal-mean comparisons discussed earlier and depends also on the horizontal resolution (see Table A.1).

Before the eruption, the simulated evolution of the tropical-mean effective radius in most models is almost steady compared to SAGE II. Only ULAQ-CCM reproduces the observed seasonal variation and matches the pre-eruption measurements, resulting in particles with a radius of 0.27 μm, similar to SAGE II (calculated over the 5 months before the eruption). The other models have smaller background particles with a constant value of 0.14 in ECHAM6-SALSA, 0.17 in ECHAM5-HAM, 0.17 in EMAC, 0.15 in SOCOL-AERv2 and 0.10 in UM-UKCA. Over Laramie, ECHAM6-SALSA, ECHAM5-HAM, EMAC and SOCOL-AERv2 have comparable radii to the OPC ones, while ULAQ-CCM and UM-UKCA lie outside the uncertainty range with larger and smaller radii, respectively. The causes of these differences are unclear; however, an in-depth exploration of the background behavior is out of the scope of this paper and needs to be addressed by studies specifically designed to study

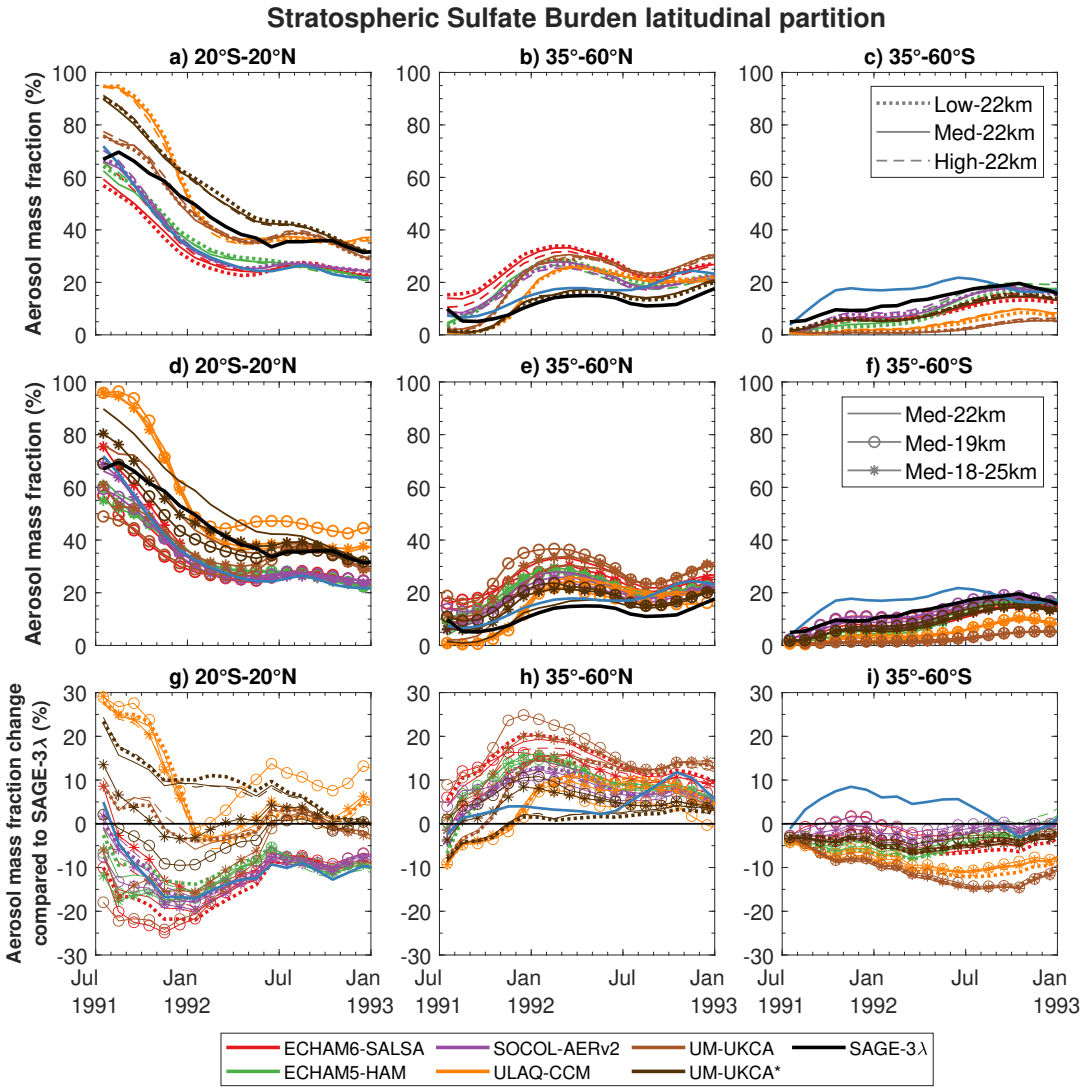

FIGURE 2.7: Time evolution of the latitudinal partition of the stratospheric sulfate burden. The aerosol mass fraction is calculated with respect to the total burden, for the tropical burden (20°N-20°S) (a, d, g), for the burden integrated over the northern mid-latitudes (35°-60°N) (b, e, h), and for the burden integrated over the southern mid-latitudes (35°-60°S) (c, f, i). The first row includes the experiments with different amounts of SO_2 injected, the second row experiments with different injection altitudes. The third shows the percentage change in the latitudinal partition for all model experiments compared to SAGE-3λ. Experiments are identified here with different line styles; the different colors refer to the models. * Models with spatially spread SO_2 injections.

aerosol microphysics and transport under volcanically quiescent conditions such as the ISA-MIP Background experiment (Timmreck et al., 2018).

After the eruption, all models are able to capture the same decay rate as the SAGE II measurements, remaining flat around the peak reached approximately after October 1991. Most produce a comparable tropical effective radius for about a couple of years, based on different injection settings. The models agree that particle size increases with increasing injected SO_2 mass, with differences from the medium-injection scenario within 15% in ECHAM6-SALSA and 10% in ECHAM5-HAM, SOCOL-AERv2, ULAQ-CCM and UM-UKCA. The differences are larger when comparing different injection altitude scenarios, and corresponding increase in the particle size is model-dependent. In ECHAM6-SALSA and SOCOL-AERv2, High-22km shows a tropical stratospheric effective radius within 10% of SAGE II until the end of 1993, peaking, respectively at 0.47 and 0.49 μm compared to 0.51 in SAGE II. In ECHAM5-HAM, all experiments except High-22km, which best fits the observed AOD, produce similar effective radii, ranging between 0.46 and 0.51 μm, and are comparable with SAGE II until the end of 1992. High-22km differs by larger radii reaching a maximum of 0.56 μm. One year after the eruption, the differences among the different ECHAM5-HAM experiments disappear, and the effective radius decreases more rapidly than in SAGE II. EMAC peaks at 0.33 μm in October and radii stay around 0.30 μm for less than 1 year. The low bias hides the faster decrease in the effective radius at about 22 km altitude than in most other models, while in the stratosphere below it is similar to observations. In ULAQ-CCM, the effective radius of Med-19km reproduces the SAGE II measurements with a similar time decrease, as differences stay within 10% until the end of 1995, while other experiments produce larger particles, with peaks ranging between 0.53 and 0.71 μm. In UM-UKCA, the growth of the effective radius is slower compared to other models, particularly for point injection, but both injection strategies show the slowest decay, which is closest to that of SAGE II. After peaking at different times, the radii between the two injection strategies are similar and range between the smallest value of 0.10 for Med-19km and the largest value of 0.49 in High-22km, which is comparable with the observations.

Over Laramie, all experiments of ECHAM6-SALSA, SOCOL-AERv2 and UM-UKCA produce radii within the estimated uncertainties in the OPC measurements for all 5 years in the first two models and after the end of 1991 in UM-UKCA. ECHAM5-HAM and EMAC show comparable values during the pre-eruption phase but in ECHAM5-HAM radii rise faster compared to the observation during the build-up phase while in EMAC, after reaching a peak that is about 30% smaller than that of OPC, the radii assume the smallest values, below the uncertainty. In ULAQ-CCM, all experiments overestimate OPC measurements until early 1992, in particular Med-19km peaks at 0.78 μm in November 1991, and the effective radius remains at the upper extreme of measurement uncertainty from there on. Increased vertical resolution calculations with SOCOL-AERv2 reveal no difference to the aerosol size

before and 1.5 years after the eruption compared to the reference configuration (Figs. A.11 f-g). During the period of the tropical residence, however, the effective radius noticeably increases due to more aerosol staying in the tropics and the stratosphere and thus available for coagulational growth.

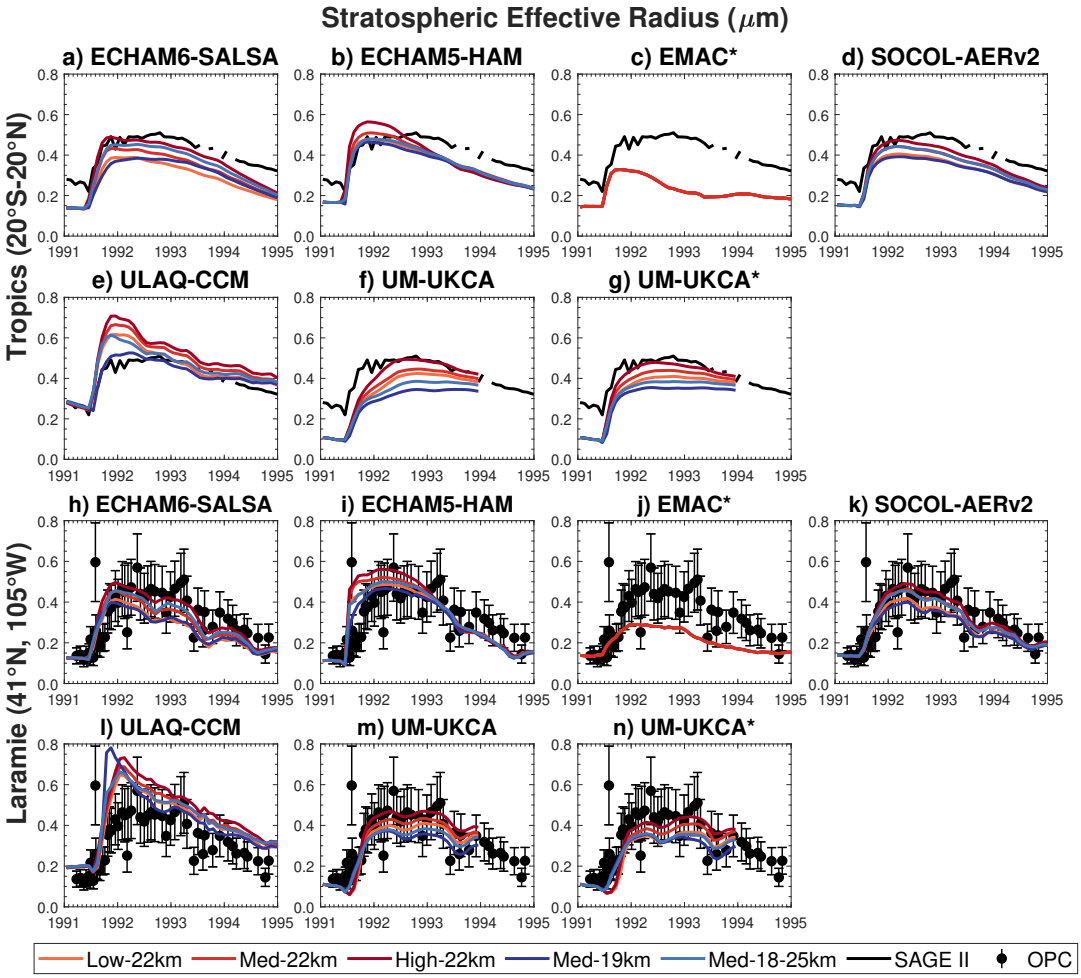

FIGURE 2.8: Time evolution of stratospheric effective radius (μm) in the tropics (panels a-g) and over Laramie (41°N, 105° W, panels h-n). In the panels of the first row, the stratospheric effective radius of the models is calculated between 21-27 km (50-20 hPa) to be compared with the available SAGE II observations. In the panels of the second row, it is calculated between 14-30 km (130-10 hPa) to be compared with the OPC observations. * Models with spatially spread SO_2 injections.

Figure 2.9 summarizes the information regarding the vertical distribution of the effective radius, SAD and extinction at 0.5 μm for the Med-22km experiment, in the tropical area (20°S-20°N), and over Laramie, 6 months after the eruption. A corresponding figure including all available experiments is shown in Figure A.10. By looking at the vertical profiles of various quantities, biases that are hidden in integrated variables emerge. Figure 2.9c reveals that the vertical profiles differ not only between models and observations but also strongly between the observations themselves.

In the tropics, the effective radius peaks between 100-50 hPa in ECHAM6-SALSA, EMAC, and ULAQ-CCM and between 50-20 hPa in ECHAM5-HAM and UM-UKCA as in SAGE II, with values within 30% of that measured, except for ULAQ-CCM, where the radii are up to 4 times larger. In UM-UKCA, the peak of SAD for point injection is centered at higher altitude, around 30 hPa compared to 20 hPa for meridional-spread emission, and with smaller values. SOCOL-AERv2 shows good agreement with SAGE II between 100-20 hPa with values that remain constant around 0.44 μm above 70 hPa. The tropical SAD simulated by the models follows the same vertical distribution as that of SAGE II, and all models have a peak between 50-20 hPa, with the exception of EMAC whose peak is around 50 hPa. In that range of altitudes, the values of the SAD are comparable with the observations for SOCOL-AERv2 and ULAQ-CCM for most of the attitudes, and are up to 2 times larger in the other models.

The tropical extinction follows the same distribution of the SAD. In this case, the extinction is compared with SAGE II and GloSSAC, and large differences exist between them: below 20 hPa the extinction in GloSSAC is larger than in SAGE II, and the differences increase with decreasing height up to 100% compared to SAGE II because of its gap-filling with ground-based measurements (Thomason et al., 2018; Kovilakam et al., 2020). Above 70 hPa, around the lower bound of the injection altitude, models extinction is even larger than GloSSAC: ECHAM6-SALSA, SOCOL-AERv2, and ULAQ-CCM approach the measurements at the limit of maximum uncertainty around at 70-25 hPa, and EMAC does so between 40-20 hPa, while ECHAM5-HAM and UM-UKCA overestimate measurements up to twice their value. Below 70 hPa, all models underestimate the GloSSAC data, but the models extinction is still larger than that of SAGE II, with the exception of EMAC, which shows the greatest extinction below 50 hPa, where it peaks. Considering that the SAD depends on the size and the number of particles, we can assume, for the models that show a comparable radius and a larger SAD compared to SAGE II in the tropics, that they overestimate the number of optically active particles and therefore show a larger extinction (ECHAM5-HAM and UM-UKCA).

Over Laramie, the vertical distribution of the effective radius is within the error bar of the OPC measurements up to 20 hPa in ECHAM6-SALSA, ECHAM5-HAM, and SOCOL-AERv2, while ULAQ-CCM produces larger particles especially below 50 hPa. In EMAC the effective radius is at the lower limit of the uncertainty but is the only model able to reproduce the vertical profile of the SAD from OPC measurements for most of the altitudes. The models that showed faster transport in the northern mid-latitudes overestimate the observed SAD for most of the altitudes.

The ability to reproduce the observations also depends on the period considered (Figs. A.8 and A.9): in the first months after the eruption models and observations show large differences, especially for SAD and extinction, which are overestimated at both latitudes considered. This may be related both to the sensitivity to the actual meteorological conditions that climate models are unable to accurately replicate, and

to the absence in HErSEA simulations of volcanic ash injection that could remove some of the initial SO_2 gas or affect the local winds and the SO_2 dispersion (Ayris et al., 2013; Zhu et al., 2020; Dhomse et al., 2020; Kloss et al., 2021; Niemeier, Riede, and Timmreck, 2021). This sensitivity to the initial conditions of SO_2 injections decreases the more time passes after the eruption. One year after the eruption, the models still show a vertical profile of the effective radius comparable to observations, while the simulated SAD starts to decrease everywhere after six months from the eruption, underestimating tropical values but still overestimating OPC measurements.

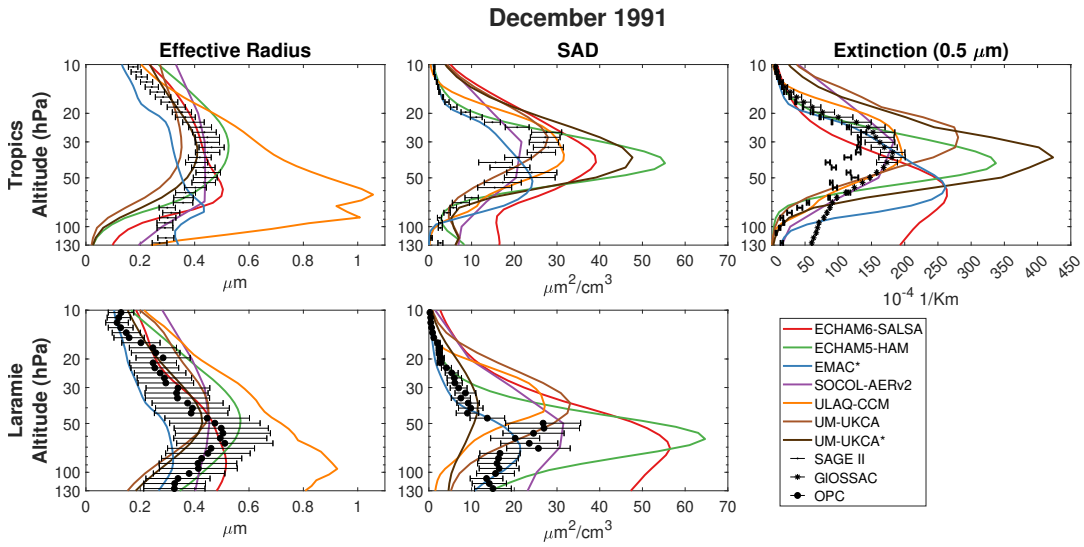

FIGURE 2.9: Vertical profile of the effective radius in μm (left panels), surface area density (SAD) in $\mu m^2/cm^3$ (middle panels), and extinction at 0.5 μm in km^{-1} (right panel) in the tropics (first row) and over Laramie (second row) for Med-22km in December 1991. Model results are compared with SAGE II and GloSSAC in the tropics and with OPC over Laramie. * Models with spatially spread SO_2 injections.

2.3 Discussion

With the use of Taylor diagrams, we highlighted the experiments that better match the observations in terms of stratospheric AOD, in two different time periods, based on the reliability of the measurements. Each model requires different injection scenarios to reproduce the observations, due to differences in the transport and microphysical processes and their mutual interaction. Even considering the best set of initial parameters based on AOD (Fig. 2.2), differences with observations more or less persist in the models, and we cannnot unequivocally define a "best" model as that varies depending on the variable considered and the timing of the observation.

Comparing the results of the models between the experiments with the same injection setup, we observe a large difference between models in reproducing the stratospheric optical depth compared to the similar evolution of the global stratospheric sulfate burden. It is hard to disentangle the transport and the microphysics

contribution to the differences in the considered variables, i.e., what fraction of it depends on microphysical schemes or different dispersion of the aerosol cloud. We first considered the contribution of SO_2 oxidation by OH to differences in the timing of the peak for the stratospheric sulfate burden (Fig. 2.5) and, consequently, AOD (Fig. A.2). For models with prescribed OH, differences in the stratospheric rate of SO_2 conversion may depend on the injection altitude, due to an earlier removal through the tropopause flux when the injection is closer to the tropopause. For models with interactive OH we observe a longer e-folding time for higher mass of SO_2 injected and when injected in a narrow altitude range (Med-22km vs Med-18-25km). Due to the availability of only monthly values, some observations of the SO_2 behavior at a more finely resolved temporal scale are not possible here. Furthermore, since the lifetime of sulfate depends on OH concentration and transport and mixing into adjacent grid boxes, when comparing different models, the timing of the peak cannot be simply related to the treatment of OH.

However, we find a common problem in transport, either too fast from the tropics to high northern latitudes (ECHAM6-SALSA, ECHAM5-HAM, SOCOL-AERv2), confined in the NH (UM-UKCA for point injection), or too confined to the tropics (ULAQ-CCM). The different tropical confinement can be affected by a different vertical advection scheme between ULAQ-CCM and the other models, based on the same dynamical core ECHAM5 or ECHAM6. Here, the tropical confinement depends on the different horizontal resolution (Niemeier, Richter, and Tilmes, 2020) while the particular definition of the tropical pipe (see Waugh et al., 2018) may also strongly affect this conclusion. The vertical resolution of a model can also affect the transport from the tropics to high northern latitudes: Brodowsky et al. (2021) showed for the SOCOL-AER model that a longer tropical confinement was found with increased vertical resolution. Hence, the transport to NH and SH can depend on model version and injection setting: the previous MAECHAM5-HAM simulation of the Mt. Pinatubo eruption by Niemeier et al. (2009) showed a similar pattern for the stratospheric AOD compared to AVHRR and SAGE II, by injecting a mid-range amount of (8.5 Tg S) into one grid box at the location of Pinatubo and a model layer around 24 km, but assuming fewer vertical levels without internally generated QBO. The Typhoon Yunya, which cannot be reproduced with coarse resolution in models, might have played a role in the equatorward transport of the volcanic cloud as well, causing a stronger transport into the SH than in most model results. Better transport to the SH showed EMAC, which has been nudged to the real meteorological conditions and the UM-UKCA version with emissions between 15°N and the Equator.

The meridional transport in the models depends on the vertical wind structure and on the vertical distribution of the simulated volcanic cloud in the first months after the eruption. Labitzke and McCormick (1992), based on SAGE II measurements, showed for the early post-Pinatubo period an upper transport regime (above 20 km) in which aerosols remain confined to the tropical reservoir spreading between 30°N and 10°S and a lower transport regime (below 20 km) in which aerosols

mainly spread to northern high latitudes. Between August and September, aerosols above 20 km spread across most of the SH, reaching latitudes of 50°S, followed in November and December by an enhancement in the NH due to the transition from boreal summer to winter circulation in the middle and upper stratosphere. Most of the models show that a faster transport in the NH is favored when aerosols are mainly distributed in the lower transport regime (Timmreck, Graf, and Kirchner, 1999). The lower-stratospheric part of the injection profiles is also strongly affected by the inconsistencies between the modeled and real tropopause heights at the time of eruption (Brodowsky et al., 2021). This effect can be additionally enhanced in the models with low vertical resolution (Fig. A.11). We note that the strength of the meridional transport is also seasonally dependent, and therefore eruptions happening in other seasons would result in different distributions of the aerosol cloud (Visioni et al., 2019; Toohey et al., 2011). We find that the injection rate does not affect the fraction of aerosols transported out of the tropics towards both hemispheres with the exception of ECHAM6-SALSA where an increased injected SO_2 mass increases the tropical confinement, especially in the first 6 months after the eruption. This is probably due to a stronger radiative interaction from the absorption of more longwave radiation by larger particles. The behavior of the other models is consistent with the findings of Young, Houben, and Toon (1994) and Aquila et al. (2012) where the aerosol heating by absorption of the infrared radiation induces a lofting and a divergent motion that affects only the initial transport (within 1 month) of the aerosols towards and within both northern and southern tropics.

Even when models and measurements look comparable for the integrated variables (Figures 2.8 and A.2), these similarities hide the models inability to reproduce the observed vertical structure depending on the latitude and time period after the eruption under consideration (Figs. 2.9, A.8, and A.9). Most models take up to 6 months before they can reproduce the vertical structure of effective radius, SAD and extinction in the tropics and up to a year at mid-latitudes. The vertical distribution of SAD and effective radius in three moments identifying the build-up, maximum and descent phase of the evolution of the sulfate burden (September and December 1991 and June 1992, respectively) shows an initial overestimation of the observations and an underestimation 1 year after the eruption. The lack of ash co-emission, a process not included in HErSEA simulations, could be crucial in the first days/month to better reproduce the initial cloud evolution (Stenchikov et al., 2021). On one hand, the ash may have removed parts of the initial sulfur cloud through the SO_2 or H_2SO_4 uptake on these coarse particles, which have a significant fall velocity (Zhu et al., 2020); on the other hand, the presence of smaller ash particles causes greater heating and vertical lofting of the volcanic cloud (Niemeier, Riede, and Timmreck, 2021; Kloss et al., 2021), which could result in slower meridional transport and longer lifetimes of stratospheric volcanic aerosols, depending on the latitude and injection altitude of SO_2 (Niemeier et al., 2009; Stenchikov et al., 2021). Aberystwyth lidar measurements from Vaughan et al. (1994) show a signature of depolarizing particles around

16 km between November and December 1991. That corresponds to the sudden enhancement of the SAD from the Laramie measurements and has been identified as ash-rich particles (Pueschel et al., 1994). The faster transport to the northern mid-latitudes in the models than observed may have removed most of the stratospheric particles, so that the aerosol lifetime in the models is about half that observed.

In addition to different transport and microphysical mechanisms, the neglection of the Cerro Hudson eruption in August 1991 that injected about 0.75-2.0 Tg-S of SO_2 between 12 and 18 km (e.g. Saxena, Anderson, and Lin, 1995; Bluth et al., 1997; Neely III and Schmidt, 2016; Carn, 2022) in the simulations, may partially explain the lack of the observed sulfate aerosol in the southern extratropics that we find in all model scenarios. The only exception is EMAC, which included the eruption of Cerro Hudson and nudged the meteorological variables. The importance of the Cerro Hudson eruption has therefore been evaluated with ULAQ-CCM performing two additional simulations that consider the lower and upper estimates of the SO_2 injection in addition to the Med-22km experiment. Significant deviations from the results of Med-22km emerge only when including the Cerro Hudson eruption with the injection of 4 Tg SO_2 at 12-18km altitudes (Fig. A.7c, g, k-n). We observe an increase in the stratospheric sulfate burden and optical depth in the SH that better reproduces the observations for the 2 months following the Cerro Hudson eruptions. However, the shorter e-folding time of stratospheric aerosol for the extra-tropical eruption does not affect the global stratospheric lifetime and is still not sufficient to explain the lack of aerosol in the SH in the following months, which we therefore attribute to transport.

The inter-model differences may depend on numerous factors that interact with one another; this makes it hard to group models by perceived similarities, for instance a similar modal scheme, similarities in the large-scale transport or an absence of interactive stratospheric chemistry. Laakso et al. (2022), for instance, used the same climate model (ECHAM-HAMMOZ) with two different aerosol microphysics schemes, one sectional and one modal. Even just this difference produced an effective radius up to 52% greater in the sectional scheme than in the modal scheme simulation for the same amount of injected SO_2. Further, Niemeier, Richter, and Tilmes (2020) showed that, in two models with a similar modal scheme but different vertical advection (CESM-WACCM-110L and MAECHAM-HAM), the resulting vertical distribution of the aerosol cloud can be substantially different. Even in the same model (CESM1-WACCM), Richter et al. (2017) showed that the presence or not of interactive chemistry could strongly affect the local stratospheric warming, and thus the residual vertical velocity changes, due to feedback from the changing ozone. In our case, all of these differences are compounded, therefore it is hard to identify which exactly is the cause of the disagreement. Furthermore, in all the works cited above, SO_2 was injected continuously for a number of years rather than in an impulsive way, whereas in the case of a volcanic eruption, the synoptical conditions at the time of the eruption play an important role (Thomas et al., 2009; Toohey et al., 2014;

Niemeier, Riede, and Timmreck, 2021; Jones et al., 2016). In our case, the experimental protocol requires the consistency of the QBO with observations through the post-eruption period; nonetheless, there are smaller-scale processes and variability that are not reproducible by models with a coarse resolution that would affect the initial state of the system, such as the formation of a mesocyclone during the first day after the eruption (Chakraborty, Gioia, and Kieffer, 2009) or the passage of Typhoon Yunya within 75 km northeast of the eruption (Oswalt, Nichols, and O'Hara, 1996).

2.4 Conclusion

The ISA-MIP HErSEA experiment protocol was designed to investigate the differences and the consensus among a group of climate models, all with interactive stratospheric aerosol microphysics, by comparing them with measurements after the Mt. Pinatubo eruption in 1991. This is done through a well-defined experimental protocol with different sets of initial parameters for the stratospheric SO_2, in terms of both magnitude (5, 7 or 10 Tg-S injected) and altitude of the SO_2 cloud (18-20, 21-23, 18-25 km, uniformly distributed). One important finding from this intercomparison is that there is now a general consensus among the models that an SO_2 emission amount at or below the lower end of the observed stratospheric SO_2 mass loading (14-23 Tg) is required to reproduce the observed sulfate aerosol loading from that time period. However, the set of injection parameters that best fits the observation changes in some models depending on the variables to be considered (aerosol optical depth, effective radius, sulfate burden, surface area density).

The main reason for the disagreement with observations is stratospheric transport, which is too fast towards the northern mid-latitudes for some models or results in stronger tropical confinement in others. The transport consequently influences the growth of sulfate aerosols and their global distribution, which in turn affects the persistence of aerosols in the stratosphere, with a feedback on the transport itself (Brühl et al., 2015; Niemeier and Schmidt, 2017; Visioni et al., 2018b). Other reasons could be related to the absence of processes such as the absence of the Cerro Hudson eruption in the southern extratropics 2 months after the Pinatubo eruption, which may partly explain the initial lack of sulfate aerosols in the Southern Hemisphere, and the omission of ash injection, which would be crucial in the early days/months to better reproduce the initial evolution of the cloud. Our results highlight the need for some specific experiments that might be needed to disentangle the different components that contribute to the overall uncertainty. For instance, simulations that nudge stratospheric transport to reanalyses (as done in Schmidt et al., 2018, in CESM(WACCM)) in multiple models could clarify the role of different microphysical schemes. Similarly, consistently turning interactive stratospheric chemistry on and off in multiple models could highlight the importance of ozone feedback (as done in Richter et al., 2017). Last but not least, dedicated tracer experiments of an

idealized volcanic cloud excluding chemical microphysical processes are necessary to assess the role of stratospheric transport in the models.

Overall, considering the best set of initial parameters, differences between models and observations remain, and the inter-model differences are still large, as found before in other multi-model experiments of explosive volcanic clouds (i.e., Tambora in Marshall et al., 2018; Clyne et al., 2021). We also note that the observations themselves show disagreement, sometimes as high as inter-model differences, because of various issues with the saturation or sensitivity of the particular instrument. Our observations around the reliability of the measurements during the Pinatubo event highlight the future need for more observations in order to be better prepared for future explosive volcanic eruptions (Newhall, Self, and Robock, 2018; Marshall et al., 2022), both for understanding short- and long-term impacts and as a benchmark test for current Earth System models. In the absence of large volcanic eruptions in the early 21 century, where a wealth of observational data exist it might therefore be also an alternative to focus on moderate eruptions in future aerosol model intercomparisons studies, e.g., the Raikoke eruption in 2019.

As a first study of the inter-model differences within ISA-MIP HErSEA, we focused on the aerosol optical depth and the variables on which it depends, such as the loading and size of the sulfate aerosols. Therefore, we suggest for follow-up studies the comparison of radiative forcing and ozone changes, which immediately follow the analyses done here.

Chapter 3

An approach to sulfate geoengineering with surface emissions of carbonyl sulfide

Reducing part of the incoming solar radiation has been proposed as a strategy to reduce surface temperatures and thus mitigate some of the worst side-effects of greenhouse-gases-induced global warming (Budyko, 1977; Institute of Medicine and National Academy of Sciences and National Academy of Engineering, 1992; Crutzen, 2006). Various methods have been proposed to achieve this, but the injection of sulfate precursors into the lower stratosphere to obtain a cloud of aerosols capable of reflective a portion of the incoming sunlight has been, by far, the most studied due to the observation of a similar cooling effect produced by explosive volcanic eruptions in the past (Robock, 2000). While preliminary estimates for the cost of an eventual deployment already exist (Smith and Wagner, 2018), from an engineering perspective there are no known technologies readily available to carry SO_2 or any other precursors considered up to now from the ground up to the lower stratosphere in the quantities needed to obtain a noticeable effect on the surface climate (Lockley, MacMartin, and Hunt, 2020). Since any proposed compound would quickly react to form sulfate aerosols, they would need to be carried, sealed, to the desired altitude, and then released, to ensure a high enough lifetime compared to that of the same aerosols in the troposphere (Lamarque et al., 2013).

We explore here a different approach to increasing the aerosol optical depth in the stratosphere, that makes use of emissions of a gaseous precursor of sulfate aerosols, i.e., COS. COS has a long atmospheric lifetime (4 to 6 years; Khalil and Rasmussen, 1984; Ulshofer et al., 1996) due to its very low reactivity in the troposphere. Because of this, it is also uniformly mixed in the atmosphere, with an average concentration of 0.5 ppbv (par per billion by volume), and therefore it easily reaches the stratosphere. In quiescent volcanic conditions, COS is the main contributor of sulfate aerosols in the Junge layer (Brühl et al., 2012), where after photodissociation by ultraviolet light and oxidation processes, it is turned into SO_2 and subsequently oxidized into sulfuric acid, forming sulfate aerosols (Crutzen, 1976). It is naturally produced by various biological processes and environments, such as saline ecosystems,

rainwater (Mu et al., 2004), and biomass burning. Furthermore, it is also produced in various industrial processes (Lee and Brimblecombe, 2016) after CS_2 is oxidized. Its chemical life is very long (35 years; Brühl et al., 2012), and thus, its main sink is the uptake from oxic soils (Kuhn and Kesselmeier, 2000; Steinbacher, Bingemer, and Schmidt, 2004) and vegetation (Sandoval-Soto and Stanimirov, 2005).

In the concentrations found in the atmosphere, it is not a toxic gas for humans: negative effects have not been found even at around 50 ppm (par per million), which is 100,000 times more than the background mixing ratio, and for long exposure times in mice and rabbits (Svoronos and Bruno, 2002). Higher concentrations than that can, however, be harmful (Bartholomaeus and Haritos, 2006). Not much is known, however, about the response of ecosystems in the presence of high concentrations of COS. Stimler et al. (2010) showed that high levels of COS enhance the stomatal conductance of some plants, which might in turn further increase COS uptake and *"alter the functioning of the terrestrial biosphere"* (Hobe et al., 2023); furthermore, Conrad and Meuser (2000) proposed that high COS concentrations may interact with soils and possibly change soil pH. For the reasons listed above, Crutzen (2006) discarded the idea of using surface emissions of COS to increase the stratospheric aerosol burden.

In this work, we use the University of L'Aquila Climate Chemistry Model (ULAQ-CCM) to perform simulations to verify if the increase in surface emissions of COS would be a viable form of sulfate geoengineering, by obtaining a stratospheric AOD similar to that obtained with the injection of 8 Tg-SO_2 in the stratosphere. We also perform simulations where the release of COS is localized in the tropical upper troposphere. This allows us to investigate whether the increase in surface concentrations of COS can be avoided, while, at the same time, circumventing the need to reach altitudes that are currently unattainable with modern aircraft (Smith et al., 2020). Together with assessing the resulting aerosol cloud, we also explore the eventual side effects on key chemical components in the atmosphere in order to determine how the side effects from COS-induced sulfate geoengineering compare with those from SO_2-induced sulfate geoengineering. For the latter, there is ample literature assessing its effect on stratospheric ozone (Tilmes, Müller, and Salawitch, 2008; Pitari et al., 2014; Xia et al., 2017; Vattioni et al., 2019). The increase in surface area density, stratospheric heating, and dynamical effect all play a part in determining the overall changes (Tilmes et al., 2018c; Richter et al., 2017) to the ozone column that, in turn, determine the changes in surface UV (Visioni, Pitari, and Aquila, 2017; Madronich et al., 2018) that would be important when considering adverse health effects (Eastham et al., 2018).

3.1 Model description and set-up of numerical experiments

The simulations presented in this paper have been carried out with the University of L'Aquila Climate Chemistry Model (ULAQ-CCM), a CCM robustly tested and used before in evaluating the radiative, chemical and dynamical effects of stratospheric

and tropospheric aerosols (Pitari et al., 2002; Eyring et al., 2006; Morgenstern et al., 2010). It has also been used for various sulfate geoengineering simulations (Pitari et al., 2014; Visioni et al., 2018a; Visioni et al., 2018b) and, as part of the Climate-Chemistry Model Intercomparison project (Morgenstern et al., 2018), where it has been extensively validated with other CCMs. The high vertical resolution (127 levels) allows for a proper representation of large-scale transport of gas and aerosol species in the troposphere (Orbe et al., 2018) and in the stratosphere (Visioni, Pitari, and Aquila, 2017; Eichinger et al., 2019), and the detailed chemistry, including heterogeneous chemical reactions on sulfuric acid aerosols, polar stratospheric cloud particles, upper tropospheric ice and liquid water cloud particles allows for a full assessment of the effects of the increased sulfate burden on the atmospheric composition. ULAQ-CCM-simulated COS also compares reasonably well with available measurements of seasonal COS concentrations (see Fig. B.1) from Kuai et al. (2015), with an average annual error of 6.5%, albeit with peaks in some areas and months of up to 30%.

In addition to a reference historical model experiment (1960-2015), we performed the following four sets of simulations: a baseline unperturbed (BG) case and three geoengineering experiments (SG-COS-SRF, SG-COS-TTL and SG-SO2), which were all run between the years 2021-2055, with analyses focusing on the 2046-2055 decade. All experiments take place under the Representative Concentration Pathway 6.0 (RCP; Meinshausen et al., 2011) emissions.

The first geoengineering experiment, SG-COS-SRF, tries to produce a significant stratospheric aerosol burden by enhancing current anthropogenic emission of COS (0.12 Tg-S/yr, see table B.1) by 40 Tg-S/yr. These emissions are located at the ground, in the main regions of anthropogenic COS surface emissions (see Fig. 3.1). The second experiment, SG-COS-TTL, tries to replicate the same stratospheric aerosol burden as SG-COS-SRF by injecting 6 Tg-S/yr of COS directly below the tropopause, at 16 km in altitude and at the Equator. In the following text, whenever we are referring to results pertaining to both COS experiments, we will use the term SG-COS. Finally, the experiment SG-SO2, similar to previous experiments discussed in the literature (Kravitz et al. (2011) in the G4 experiment), consists of the injection of 4 Tg-S/yr in the form of SO_2 at the Equator, between 18 and 25 km in altitude.

For the geoengineering experiments, ULAQ-CCM is driven by time-dependent sea surface temperatures (SSTs) from the Community Climate System Model-Community Atmosphere Model version 4 (CCSM-CAM4; Neale et al., 2013), an coupled atmosphere-ocean model that ran similar geoengineering experiments to those in SG-SO2 (as described by Tilmes et al., 2015). This allows for the inclusion of the cooling produced by geoengineering on the surface to the assessment of the dynamical and chemical effect as simulated by ULAQ-CCM. To include the important radiative effects produced by other atmospheric components (mainly, geoengineering-driven changes in greenhouse gases concentration and in ice clouds; Visioni, Pitari, and Aquila, 2017; Visioni et al., 2018a) the radiative module of ULAQ-CCM calculates, at

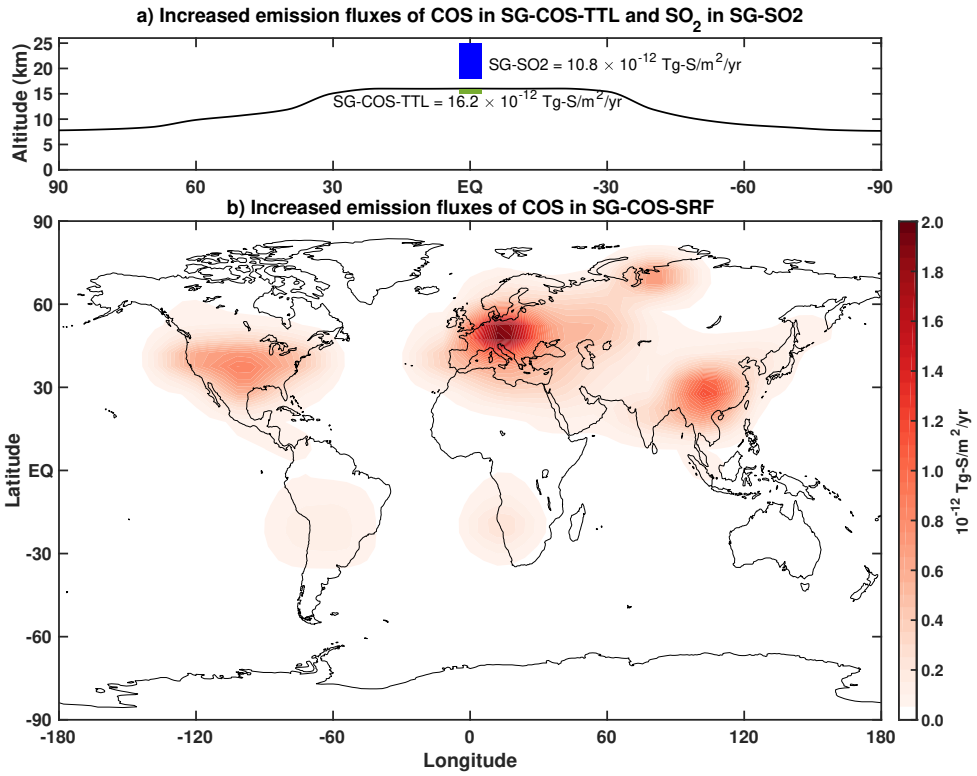

FIGURE 3.1: a) Vertical and latitudinal distribution of COS emissions per year and unit of surface area (10^{-12} Tg-S/m^2/yr) in the SG-COS-TTL experiment (green box) and SO_2 emission fluxes in the same unit in SG-SO2 (blue box). The quantities are distributed in a single vertical level for SG-COS-TTL, and in 12 vertical levels for SG-SO2. b) Geographical distribution of COS emission fluxes per year and unit of surface area (10^{-12} Tg-S/m^2/yr) in the SG-COS-SRF experiment. The annual upward flux is averaged over the period 2046-2055.

each time-step, the surface temperature perturbation produced by the radiative flux changes induced by these components and includes them in the CCSM-CAM4 SSTs. This approach has been further explained and validated by Visioni et al. (2018a). While the prescribed SST set-up has been shown to correctly capture the dynamical changes produced by SRM (Visioni, Pitari, and Aquila, 2017), it clearly does not capture the potential feedbacks that may be relevant for surface climate, such as those produced by the different latitudinal distribution of the aerosol optical depth that we will show later on. These differences may also, in turn, feed back onto changes in COS lifetime through precipitation changes (Whelan et al., 2016), which we cannot consider here. We will therefore limit ourselves to analyzing changes in atmospheric composition and dynamics and how those contribute to the overall radiative forcing from the aerosols. Future experiments with a more comprehensive Earth system model will be necessary to determine the full extent of the climatic response.

3.2 Results

3.2.1 Sulfate burden

COS is the most abundant sulfur-containing species in the atmosphere under quiescent conditions (i.e. not considering explosive volcanic eruptions). It is efficiently lost at the surface via dry deposition on soils and vegetation. Taking this sink into account, the net global lifetime (atmospheric chemistry plus surface deposition) is approximately 4 years, depending on the assumed magnitude of the soil and vegetation sink (Sandoval-Soto and Stanimirov, 2005; Van Diest and Kesselmeier, 2008). In the troposphere the COS chemical reactivity (mostly with the hydroxyl radical) is rather slow. COS is thus well-mixed and is easily transported in the stratosphere through the TTL. In the mid-stratosphere COS becomes efficiently photolyzed by solar UV radiation, becoming an important source for stratospheric SO_2 and, finally ,for sulfuric acid aerosols.

When increasing the surface emission fluxes in SG-COS-SRF, it takes $\sim$ 15 years before the concentration reaches a new equilibrium, from 0.5 to 35.5 ppbv (Fig. 3.2a), whereas in SG-COS-TTL the equilibrium value is 4.8 ppbv. In the same time span, the global AOD increases reaching a value of 0.08 by 2035 in SG-COS-SRF and by 2030 in SG-COS-TTL, similar to the global value that is reached by the direct injection of SO_2 in the Equatorial stratosphere in SG-SO2; in that case, however, the steady-state value is reached in only 1-2 years. In the GeoMIP G6sulfur experiment (Visioni et al. (2021)), the average global surface cooling reported by six Earth system models for a similar stratospheric OD was 0.46 K. At the end of 2055, the increased COS and SO_2 injections are stopped. Average tropospheric COS concentrations follow an exponential decay guided by the atmospheric lifetime (3.8 years due to chemistry but mainly due to soil deposition), reaching a value of 1.3 ppbv after 20 years in SG-COS-SRF (during 2075), whereas a similar value only takes 10 years to be reached

in SG-COS-TTL. This means an increase in 0.8 ppbv with respect to background condition, that would produce a direct RF that is negligible compared to other well-mixed greenhouse gases. The exponential decay of the stratospheric AOD in both SG-COS experiments is regulated by the stratospheric lifetime of COS (Fig. 3.2b), which is ∼10 years, and it is mainly due to the reaction with OH and photolysis, from which stratospheric SO_2 and finally sulfuric acid aerosols are formed. This is also combined with the depletion of the source of COS from the troposphere (Fig. 3.2a). Therefore, the e-folding time for stratospheric AOD is longer with respect to the one resulting from SG-SO2 (Fig. 3.2c). In 2075, the global stratospheric AOD reaches a value of 0.01 in the SG-COS experiments with respect to 0.003 in the background case.

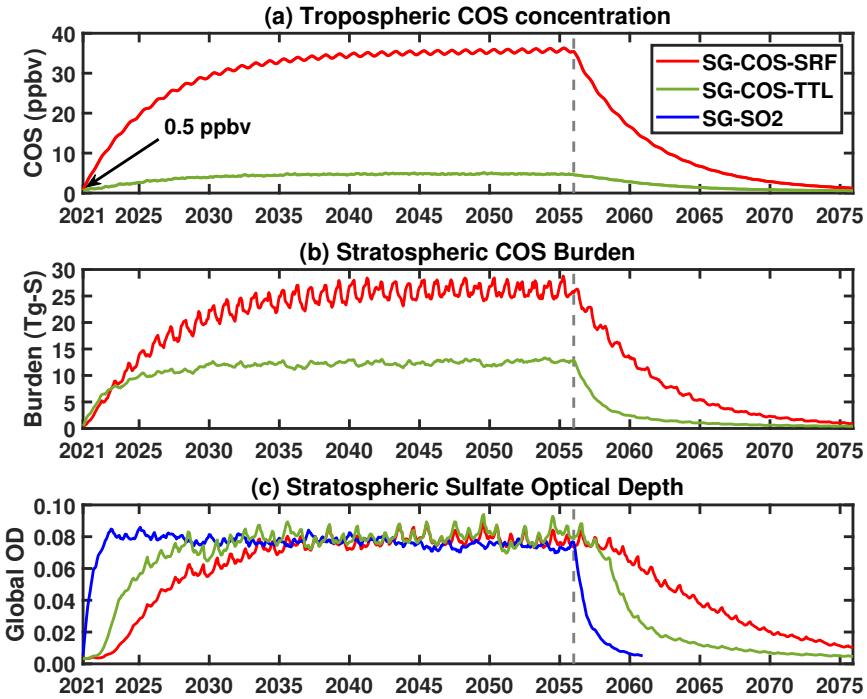

FIGURE 3.2: a) Monthly values of globally averaged tropospheric COS volume mixing ratio (ppbv) in both SG-COS experiments. The background value of 0.5 ppbv at the beginning of the simulation is highlighted. b) Monthly values of global stratospheric COS burden (in Tg-S) in both SG-COS experiments. c) Globally averaged stratospheric sulfate optical depth monthly values in SG-COS-SRF (red), SG-COS-TTL (green) and SG-SO2 (blue). The grey line in all panels indicates the time when emissions of COS and SO_2 are stopped, at the end of 2055.

3.2.2 Sulfate aerosol properties

In both COS experiments, COS emissions are adjusted so as to have the same global AOD ≈ 0.08 (see table 3.1). This is done in order to more easily compare the latitudinal distribution of the aerosols, and to better quantify the differences in the radiative

forcing from both direct and indirect (ozone, methane, and water vapor) changes in atmospheric composition.

	BG	SG-COS-SRF	SG-COS-TTL	SG-SO2	SG-COS-SRF - BG	SG-SO2 - BG
Total Sulfate OD	0.054±0.003	0.134±0.005	0.134±0.004	0.128±0.004	0.080±0.005	0.074±0.005
Tropospheric Sulfate OD	0.051±0.003	0.056±0.003	0.054±0.003	0.054±0.003	0.005±0.0054	0.003±0.004
Stratospheric Sulfate OD	0.003±0.001	0.078±0.002	0.080±0.004	0.074±0.001	0.075±0.002	0.071±0.001
Sulfate effective radius (μm)	0.18±0.01	0.46±0.01	0.47±0.01	0.59±0.01		
Ice OD	0.589±0.006	0.573±0.007	0.569±0.008	0.566±0.005	-0.016±0.008	-0.023±0.009
Ice effective radius (μm)	35±1	33±1	33±1	32±1		

TABLE 3.1: Summary of calculated sulfate aerosol and cirrus ice globally-annually averaged quantities relevant for RF calculations (i.e., optical depth at λ=0.55 μm and effective radius). Last two columns show the calculated SG changes with respect to the BG case (years 2046-2055).

There is a large difference in the latitudinal distribution of stratospheric sulfate optical depth, as shown in Figure 3.3a. Both SG-COS experiments produce an AOD that is more uniformly distributed over all latitudes with respect to the SG-SO2 case, where the increase in optical depth is most prominent in the tropics; this is due to the efficient tropospheric mixing of COS before it reaches the stratosphere even when, as in SG-COS-TTL, the injection happens close to the tropopause.

The differences in the latitudinal distribution of AOD are also observable in the differences in the particle sizes and in the SAD. Figure 3.3b shows that the stratospheric effective radius is smaller in the SG-COS experiments and uniform for all latitudes, with a global value of 0.46 μm. In SG-SO2, the effective radius is higher in the tropics (0.59 μm). AOD is also larger in the tropics in that case, due to a larger concentration of particles there, even if larger particles are less effective at scattering incoming solar radiation (English, Toon, and Mills, 2012).

Figure 3.4 shows a comparison of the effective radius (Fig. 3.4a) and SAD (Fig. 3.4b) between the BG, SG-COS-SRF, SG-COS-TTL and SG-SO2 cases, separating the tropics, mid-latitudes and polar regions. As SO_2 is injected at the Equator, all oxidation and nucleation happens in the tropics in SG-SO2. This is reflected in the vertical distribution which has a maximum in the lowermost stratosphere. On the other hand in SG-COS, the effective radius increase is reached at higher altitudes, between 18-30 km, which is consistent with COS reaching higher altitudes through deep tropical convection before it is photochemically destroyed (Barkley et al., 2008). The same explanation is valid for the tropical SAD in Fig. 3.4b.

As the size of the particles is determined by nucleation in the tropical region, where SO_2 oxidation occurs, mid-latitude and polar behaviour of the aerosols depends on the poleward transport by the BDC.

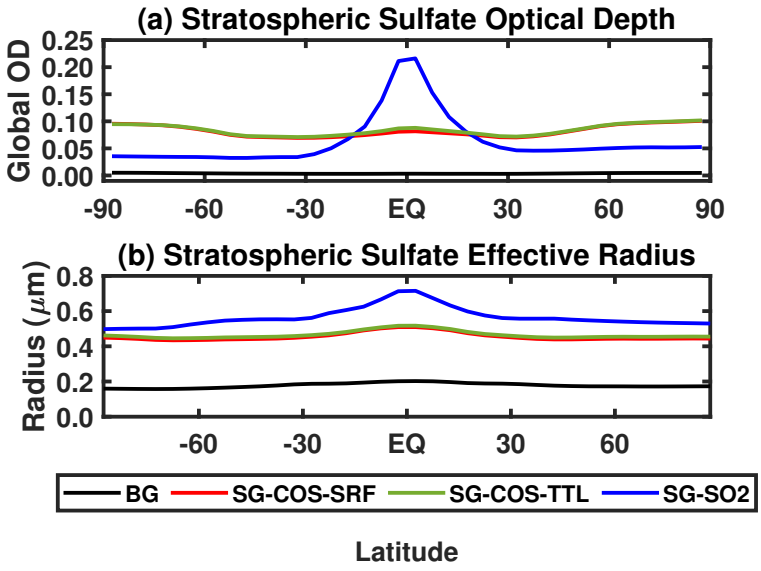

FIGURE 3.3: a) Latitudinal distribution of zonal mean values of stratospheric sulfate optical depth for the BG (black), SG-COS-SRF (red), SG-COS-TTL (green) and SG-SO2 (blue) cases. b) Stratospheric effective radius (in μm, from tropopause to 6hPa). All quantities are annually averaged over the years 2046-2055.

In SG-SO2, aerosols grow rapidly in the tropical region due to the high concentration of SO_2, and their larger size affects sedimentation rates, thus decreasing their lifetime. Consequently, the number of aerosols transported to higher latitudes is lower; in SG-COS, smaller particles with a higher lifetime are either easily transported towards the poles or directly formed there. Smaller particles at a higher concentration, and larger particles at a lower concentration may then result in a SAD, which looks similar at mid-latitudes and polar region, but for different reasons.

The vertical distribution of particles and their optical properties are shown in Figure 3.5 (see Fig. B.2 for COS, SO_2 and SO_4 concentration changes; only values for one of the SG-COS experiments is shown here, as they are indistinguishable). The vertical distribution of the SAD is fundamental for understanding the role of the heterogeneous reaction and their effect on stratospheric ozone. The baseline cases in Fig. 3.5a and b are a reference for understanding their changes in the SG-COS experiments (Fig. 3.5c and d). The particles transported via the BDC to the poles are large enough to efficiently scatter the solar radiation so that the SAD and extinction changes show a similar behaviour, with a global increase in stratospheric values with maxima at higher latitudes between 15-25 km.

Figure 3.5f and d show the extinction and SAD changes between the three SG experiments, to underline that in SG-SO2, the extinction of the radiation is confined in the tropical stratosphere between 15-25 km, meaning that there is a negative change in SG-COS. As discussed before, the formation of larger particles in SG-SO2 in the tropical region reduces the amount of aerosol transported to the poles compared to the SG-COS cases, where a larger number of smaller particles produce a positive change in SAD and, consequently, in extinction.

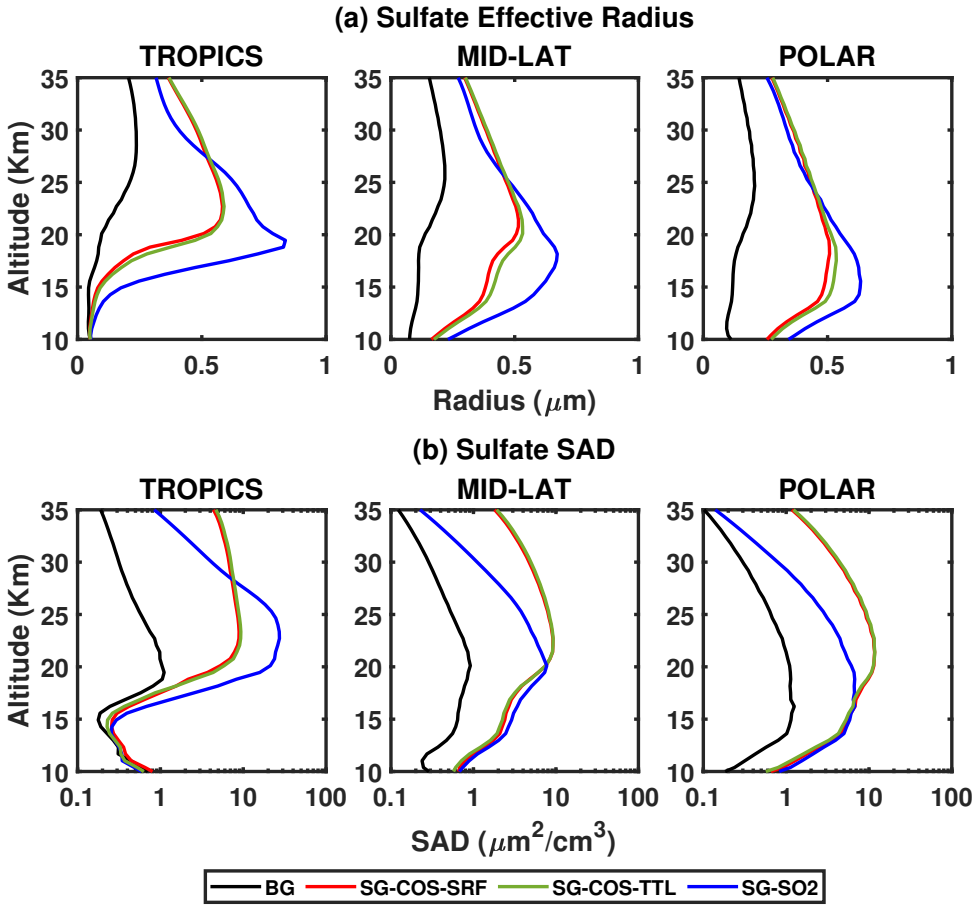

FIGURE 3.4: Vertical profiles of sulfate effective radius (in μm, a) and surface area density (in $\mu m^2/cm^3$, b) at different latitudinal bands (20°N-20°S for the Tropics, 30-50° at both N and S for the Mid-lat and 60°-90 at both N and S for the Polar plots). All quantities are annually averaged over the years 2046-2055.

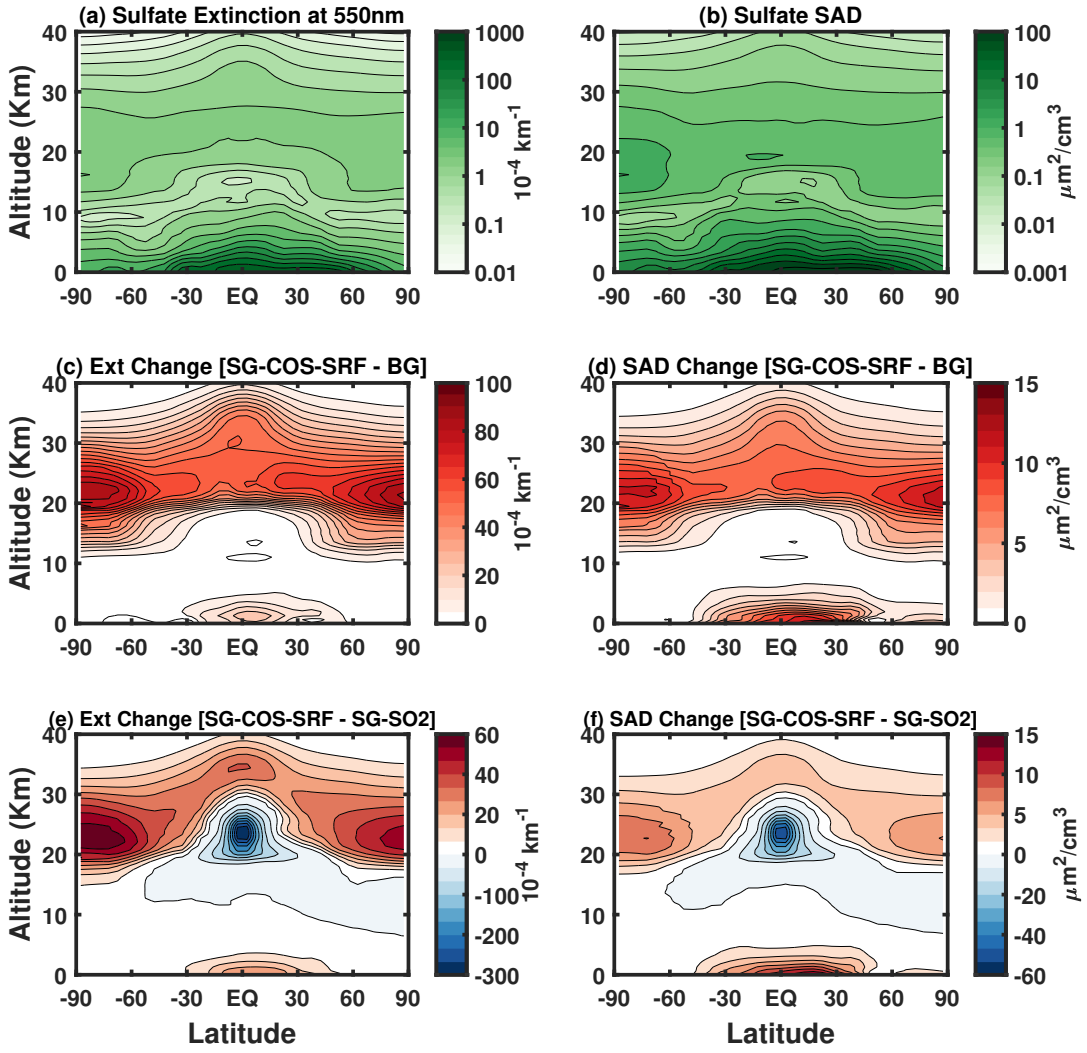

FIGURE 3.5: Zonal mean values of sulfate extinction (in 10^{-4} km^{-1}) and SAD (in μm^2/cm^3) in BG (panels a and b, respectively) and their change in the case of the SG-COS-SRF experiment (panels c and d). Panels e) and f) show extinction and SAD changes between SG-COS-SRF and SG-SO2. All quantities are annually averaged over the years 2046-2055.

3.2.3 Deposition

The enhancement of the stratospheric sulfate burden would produce an increase in sulfur deposition, both in dry form through acid gas deposition, and in wet form, through rain, fog, and aerosol particles.

Acid deposition may damage human health when high concentrations of particles with a diameter below certain thresholds (PM2.5 and PM10) are inhaled. The acidification of soils and water may damage plants, microorganisms and aquatic animals, but the impact on the ecosystem depends on the rate at which acidifying compounds are deposited from the atmosphere, compared with the rate at which acid neutralizing capacity is generated within the ecosystem (Driscoll et al., 2001).

Here we analyse how the dry and wet deposition of sulfur species are distributed globally as a result of the two SG interventions. Table 3.2 and 3.3 summarize the wet and dry deposition rates for the SG-COS, SG-SO2 and BG experiments, and they include the contribution of each species to the total deposition. In particular, in both SG-COS experiments the increase in COS fluxes produces both an increase in sulfuric deposition, after its photolysis and oxidation to sulfuric acid, and in the dry deposition of COS itself, as it is removed to the ground through uptake by vegetation and soils (Kettle, 2002).

Experiment	MSA	SO_2	SO_4	COS	CS_2	H2S	Total
BG	1.0±0.1	35.2±1.4	9.4±0.4	0.39±0.01	0.47±0.03	1.5±0.1	48.0±1.8
SG-COS-SRF	1.0±0.1	36.4±1.5	9.9±0.4	31.6±0.1	0.47±0.03	1.5±0.1	80.9±1.7
SG-COS-TTL	1.0±0.1	35.8±1.5	9.7±0.4	3.5±0.1	0.47±0.03	1.5±0.1	52.0±1.7
SG-SO2	1.0±0.1	35.6±1.5	9.5±0.4	0.39±0.01	0.47±0.03	1.5±0.1	48.5±1.8

TABLE 3.2: Globally-annually averaged dry deposition rates of sulfur species (Tg-S/yr) (years 2046-2055). Note: MSA is methanesulfonic acid.

Experiment	MSA	SO_2	SO_4	Total	Net [sources-sinks]
BG	1.5±0.1	3.0±0.1	43.2±1.5	47.7±1.6	+0.3±0.1
SG-COS-SRF	1.5±0.1	3.4±0.1	49.4±1.5	54.3±1.6	+0.8±0.1
SG-COS-TTL	1.5±0.1	3.2±0.1	45.2±1.5	49.9±1.6	+0.1±0.1
SG-SO2	1.5±0.1	3.2±0.1	46.5±1.5	51.2±1.6	+0.3±0.1

TABLE 3.3: Globally-annually averaged wet deposition rates of sulfur species (Tg-S/yr) (years 2046-2055). The last column shows the net balance of total sulfur sources and sinks (Tg-S/yr).

The global distribution of COS deposition for the baseline case is shown in Figure 3.6(a) while the increase in deposition from the SG-COS-SRF experiment is shown in Figure 3.6(b). For the SG-COS-TTL case, the spatial distribution is identical to SG-COS-SRF, but its magnitude is 10 times lower than in SG-COS-SRF. COS uptake by plants is concentrated mainly in the tropical rainforests of South America, Africa,

and southeast Asia and boreal coniferous forests across North America, northern Europe, and northern Asia. Uptake by soils occurs mainly in arid and semiarid regions, such as savanna regions in northern and southern Africa and in the south-western regions of North America, in the pampas of Argentina, in Australia, and in the steppes of central Asia (Kettle, 2002). Dry deposition of COS does not contribute to acid deposition, and currently, there is no information available on how different soils or ecosystems would be affected by higher local COS concentrations; therefore, we assumed that their uptake efficiency does not change. The robustness of this assumption will need to be studied.

The global distribution of SO_x deposition is also shown in Fig. 3.6c and d, which show dry and wet deposition, respectively, for the background case. Dry deposition maxima are localized in urban areas close to the source where the emitted sulfur dioxide is immediately oxidized, while wet deposition distribution depends both on sulfate concentration and precipitation.

Figure 3.6e and f show the total SO_x deposition change in SG-COS-SRF with respect to the baseline case, in absolute terms and as a percentage of the baseline case, and most of its increase is due to wet deposition (see tables 3.2 and 3.3; see Tables B.1-B.4 for a breakdown of global sources and sinks of sulfur species). In both figures, the distribution of deposition is more uniform over the globe with respect to the tropical injection of SO_2, except for the polar regions, because of the reduced precipitation rates. Consequently, Figure 3.6 (f) shows a large increase in percent deposition in the polar region (17% in the Arctic and 8% in Antarctic; these values are reduced to 1.7% and 0.8 % in SG-COS-TTL; see Fig. B.4) because of very low values in the baseline case. On the other hand, the deposition change is close to zero in polluted regions.

Globally, the annual differences in deposition fluxes for all species compared to the background case amount to 8.3 ± 0.2 Tg-S/yr for SG-COS-SRF and 3.1 ± 0.2 Tg-S/yr and 3.9 ± 0.2 Tg-S/yr for SG-SO2, which equates to an increase in 8.9 ± 0.3 %, 3.3 ± 0.3 %, and 4.2 ± 0.3 %, respectively.

3.3 Indirect effects

The simulated enhancement in the stratospheric aerosol layer would produce two main effects, namely, an increased scattering of solar radiation, that, in turn, would reduce surface temperatures, and the local absorption of more near-infrared solar and terrestrial radiation that would warm the stratospheric layer where the aerosols reside (as observed for volcanic eruptions, see Lacis, Hansen, and Sato, 1992; Labitzke and McCormick, 1992). Furthermore, the increase in the surface area density of the aerosols would affect the heterogeneous chemistry of ClO_x and NO_x, with implications for ozone concentration and UV radiation at the surface (Tilmes et al., 2009; Tilmes et al., 2018c; Tilmes et al., 2021).

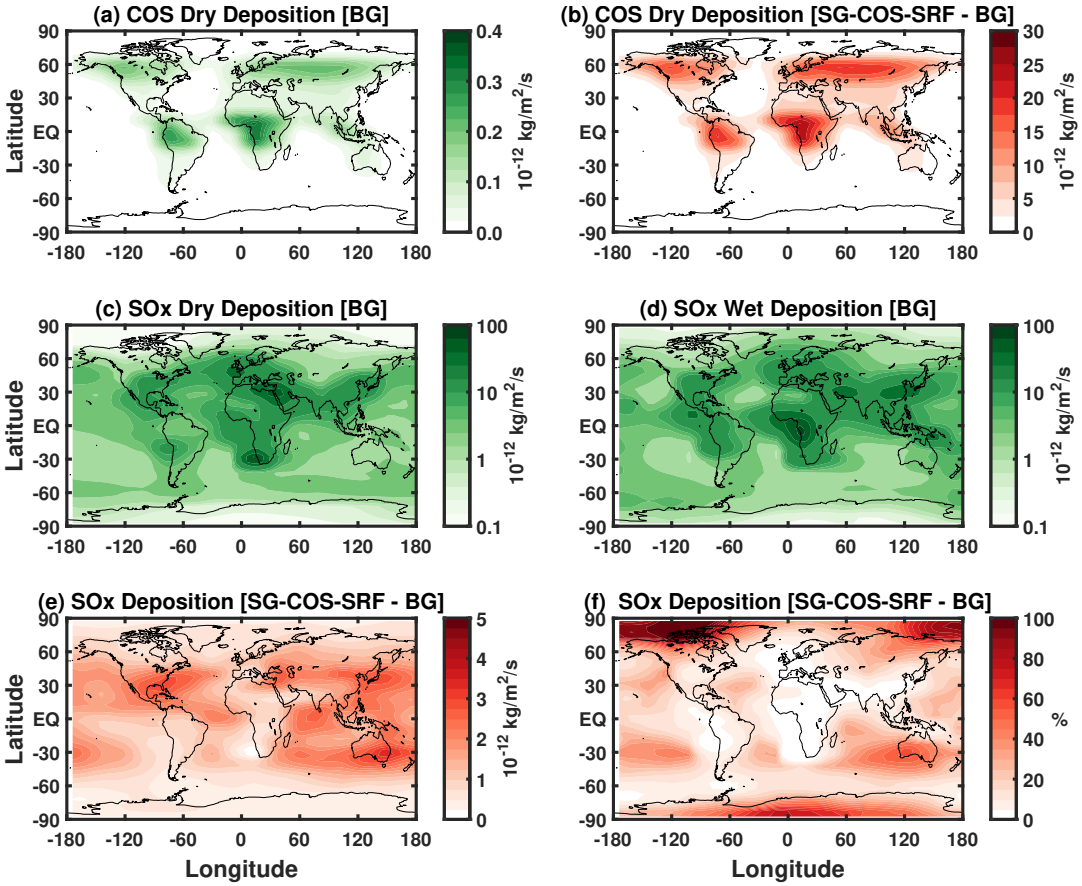

FIGURE 3.6: a) Surface dry deposition fluxes (10^{-12}kg/m^2/s) of COS in the background case. b) Change in COS dry deposition fluxes in SG-COS-SRF compared to a). c) SO_x dry deposition fluxes (10^{-12}kg/m^2/s) in the background case. d) SO_x dry deposition fluxes (10^{-12}kg/m^2/s) in the background case. e) Change in SO_x total deposition fluxes in SG-COS-SRF compared to the background. f) as e) but in % of the background values.

For SO_2, it has been shown that the combination of surface cooling, perturbation of stratospheric temperatures and changes in tropospheric ozone and in UV at the surface also affect methane lifetime (Visioni, Pitari, and Aquila, 2017). In this section we analyse the differences in these changes also for the SG-COS experiments.

Figure 3.7 shows the ozone changes in SG-COS-SRF and SG-SO2 with respect to the BG case. As expected from the similar value and distribution of the SAD, in SG-COS-TTL the ozone changes are equivalent to SG-COS-SRF (and are therefore not shown). Figure 3.7a and b show the monthly total ozone column changes as a function of latitude. Close to the Equator there is a small reduction in the overall column, mostly due to a reduction in tropospheric ozone, as visible in Fig. 3.7c and d, as a direct consequence of the surface cooling (Nowack et al., 2016). On the other hand, at higher latitudes, an overall increase in the total column is observable due to an increase in stratospheric ozone. This is particularly evident closer to the poles.

During springtime months, there is some Antarctic ozone depletion, while in the Arctic a recovery of ozone is observable. In the Antarctic spring, the polar vortex is strengthened by the stratospheric heating in the tropics that affects the Equator-to-pole thermal wind balance (Visioni et al., 2020a), resulting in greater confinement of cold air that, in turn, enhances the ozone depletion by the polar stratospheric clouds (PSCs). The tropical stratospheric heating is higher in SG-SO2 with respect to SG-COS as the aerosols are less confined (Fig. B.6). Consequently, the strengthening of polar vortex in SG-SO2 produces a higher ozone depletion. In the Arctic, on the other hand, PSC-related ozone loss is lower (Tilmes et al., 2018a), and the predominant effect is that from an acceleration of the BDC transporting ozone-rich air from lower latitudes.

Figure 3.7c and d show the annual mean of ozone mixing ratio percentage change as a function of altitude and latitude. In both SG experiments, negative changes below the tropopause are governed by the decrease in solar radiation which comes into play in the photo-dissociation reaction of NO_x as an ozone precursor (NO_2 + $h\nu$ ($\lambda < 420$ nm) $\rightarrow$ NO + $O(^3P)$). Sunlight reduction also affects the O_3 photolysis, decreasing the ozone loss. Positive changes are due to the balance of the previous reactions and the increase in methane (see table 3.4) as a source of ozone in its oxidation chain, and mainly due to the decrease in the tropospheric water vapour in a clean air environment (low NO_x), such as the tropics (Nowack et al., 2016; Xia et al., 2017).

Above the tropopause, there is a negative ozone change in the lower stratosphere in all SG experiments, except for the Arctic region where we observe a small increase in the Arctic lowermost stratosphere in all cases. The key drivers of stratospheric ozone change are the increase in heterogeneous reactions, as a result of the enhancement of stratospheric aerosols, and the perturbation of the dynamics governing ozone transport.

Negative ozone changes correspond to the region where the SAD reaches its

maximum values (fig. 3.5d and f): between 10-20 km in the polar regions for SG-COS and mainly between 15-25 km at tropics for SG-SO2. The increase in the SAD enhances heterogeneous chemistry and results in denitrification via hydrolysis of dinitrogen pentoxide (N_2O_5 + $H_2O \xrightarrow{M} 2HNO_3$). The loss of NO_x decreases the rate of ozone depletion through its catalytic cycle. Whereas in the mid-stratosphere, where the cycles of chlorine (ClO_x) and bromine (BrO_x) are dominant, there is an increase in ozone loss since there is a reduction in NO_x that normally bounds chlorine ($ClONO_2$), thus allowing more ClO-driven ozone destruction (Tilmes et al., 2018c; Grant et al., 1992).

At low latitudes, stratospheric ozone concentration is also driven by changes in tropical upwelling (Visioni, MacMartin, and Kravitz, 2021). The reduction in the tropical upwelling of ozone-poor air coming from the lowermost stratosphere leads to higher ozone concentration at altitudes of about 20-22 km (Tilmes et al., 2018c).

Figure B.7e shows the change in tropical upwelling in relation to changes in the residual vertical velocity (w^*) with respect to the baseline case. Negative w^* anomalies in SG-COS mean weaker tropical upwelling as consequence of tropospheric cooling. In SG-SO2, the highest concentration of absorbing aerosols leads to positive w^* above 20 km due to the local warming. but this does not affect the transport of ozone-poor air from the lower layers.

Above the discussed altitudes, there is a net ozone production in all SG experiments, with a higher increase in the ozone mixing ratio in the SG-COS experiment with respect to SG-SO2, especially in the extra-tropical region. Ozone depletion at these altitudes is mainly controlled by the catalytic cycle of NO_x, that is inhibited by the denitrification process due to heterogeneous reactions on aerosols.

Globally, the annually averaged ozone column increases by $\sim$5 and 1.5 DU for SG-COS and SG-SO2, respectively (table 3.4). Increasing stratospheric ozone affects ultraviolet B (UVB) at the surface because it is absorbed by ozone during its photodissociation, while aerosol could affect ultraviolet A (UVA) radiation by scattering processes. The projected changes are shown in Figure 3.8 for both UVA and UVB for each season and for the annual mean. We estimated these changes using the tropospheric ultraviolet and visible (TUV) radiation model (`https://www2.acom.ucar.edu/modeling/tropospheric-ultraviolet-and-visible-tuv-radiation-model`, last access: 29 April 2022), using in input our model latitudinal and monthly values for the period of 2046-2055, for aerosol optical depth, total ozone column, climatological cloud cover and surface albedo.

	BG	SG-COS-SRF	SG-COS-TTL	SG-SO2	SG-COS-SRF - BG	SG-COS-TTL - BG	SG-SO2 - BG
COS [troposphere] (ppbv)	0.47±0.1	35.5±0.2	4.8±0.1	0.47±0.1	35.0±0.2	4.3±0.2	0.00±0.1
CH_4 lifetime (yr)	8.72±0.13	9.83±0.18	9.85±0.17	9.78±0.20	1.11±0.13 [(+12.7±1.4) %]	1.13±0.13 [(+13.0±1.4) %]	1.06±0.17 [(+12.2±2.0) %]
H_2O [stratosphere] (ppmv)	6.08±0.08	5.99±0.16	5.95±0.15	6.13±0.13	-0.09±0.14	-0.13±0.15	0.05±0.12
O_3 column (DU)	289.3±1.8	294.2±1.5	294.8±1.6	290.7±1.6	4.9±2.3	5.5±2.4	1.4±1.7

TABLE 3.4: Summary of calculated globally-annually averaged quantities of greenhouse gases directly and indirectly perturbed by SG and relevant for RF calculations (i.e., COS mean tropospheric mixing ratio, CH_4 atmospheric lifetime, H_2O mean stratospheric mixing ratio, O_3 column). Last two columns show the calculated SG changes with respect to the BG case (years 2046-2055).

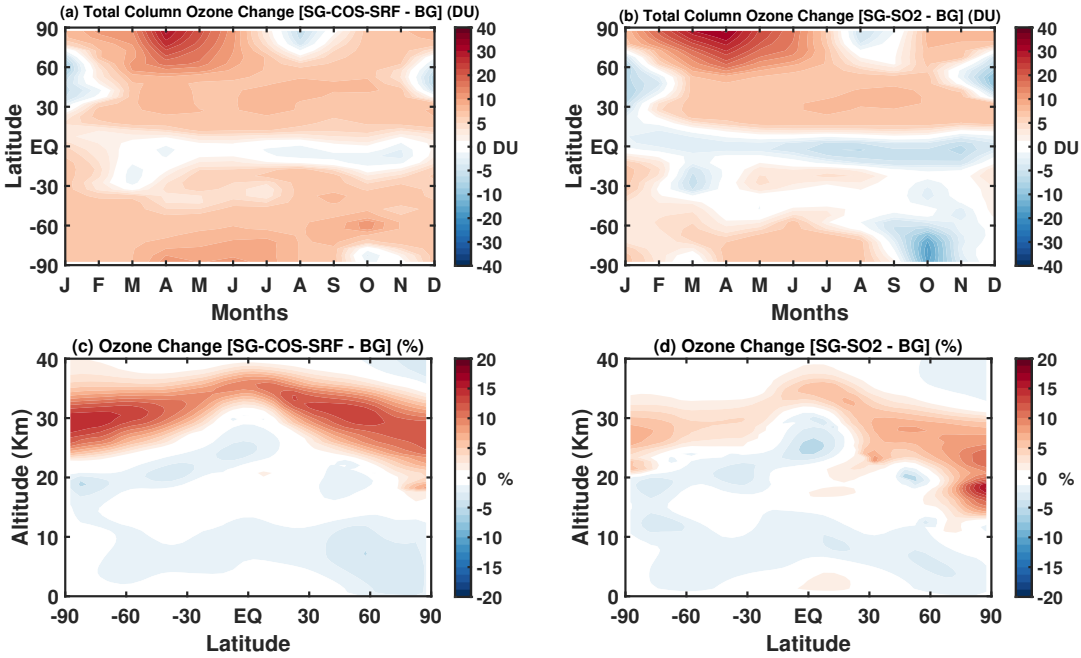

FIGURE 3.7: a,b) Monthly mean zonal values of SG ozone total column changes (DU) with respect to the BG case for SG-COS-SRF and SG-SO2 respectively. c, d) ozone mixing ratio percent changes with respect to the BG case. All quantities are annually averaged over the years 2046-2055.

In all SG experiments, the negative changes of UVB radiation at the surface, except in the Antarctic region, are related to changes in stratospheric ozone and the interannual variations that are larger at the poles, due to the seasonal variability, as discussed before. In the Antarctic spring (September-November; SON) the ozone depletion is enhanced in SG-SO2, while in SG-COS-SRF it is limited to the month of October, with differences compared to BG of less than -5 DU. Therefore, the UVB change compared to BG for SON over Antarctica remains negative in SG-COS-SRF with a value of -2.7% versus a +5.8% increase in the SG-SO2 experiment. In DJF (December-February), on the other hand, a small increase in UVB is observable at mid-to high latitudes in the Northern Hemisphere. This is connected to an observable decrease in stratospheric ozone in the same locations, possibly due to a reduced

advection of air from the tropics. UVA decreases everywhere in all SG experiments. In particular, the correlation between UVA change and particles scattering is evident if we compare this latitudinal distribution with the stratospheric AOD of Figure 3.3a. The globally averaged UVB and UVA changes at surface are summarized in table 3.5.

Methane is an indirect source of tropospheric ozone (West and Fiore, 2005), and it is also a greenhouse gas. Knowing its variation is fundamental for understanding the final contribution to the radiative forcing that one would wish to achieve with this geoengineering method. From table 3.4, we find a global increase in methane lifetime of $\sim$ 13% in SG-COS and 12.2% in SG-SO2, which we can identify in the increase in methane itself. The reason for the increase in methane is to be found in the behaviour of OH, as the main sink of methane is the oxidation reaction with OH; a decrease in OH means an increase in the methane lifetime. As discussed by Visioni, Pitari, and Aquila (2017), mechanisms that cause an increase in OH are as follows: (a) surface cooling lessens the amount of tropospheric water vapor and inhibits the temperature-dependent reaction of NO + O_3; (b) a decrease in tropospheric UV, due to enhancement of ozone and scattering radiation, reduces $O(^1D)$ that takes part of the reaction $O(^1D)$ + $H_2O \rightarrow$ 2 OH; (c) an increase in SAD enhances the heterogeneous chemistry, reducing the amount of NO_x (NO + HO_2, NO + RO_2); (d) a increase in the tropical lower stratosphere temperature that regulates the stratosphere-troposphere exchange, which can be positive or negative, depending on the net result of the superimposed species (CH_4, NO_y, O_3, SO_4) in the extratropical upper troposphere-lower stratosphere (UTLS).

The warming of the TTL is shown in Figure B.7d. In SG-SO2, larger particles confined in the tropical region produce a greater warming of the TTL with respect to smaller ones distributed all over the globe in SG-COS. The role of the dimensions and distributions of aerosols in stratospheric warming is confirmed by the heating rates, as shown in Fig.B.6.

	BG (W/m^2)	SG-COS-SRF (W/m^2)	SG-COS-TTL (W/m^2)	SG-SO2 (W/m^2)	SG-COS-SRF - BG (%)	SG-COS-TTL - BG (%)	SG-SO2 - BG (%)
UVB	0.206±0.002	0.197±0.001	0.196±0.001	0.201±0.001	-4.4±0.6	-5.8±0.6	-2.4±0.9
UVA	11.35±0.01	11.13±0.01	11.12±0.01	11.17±0.01	-1.9±0.1	-2.0±0.1	-1.6±0.1

TABLE 3.5: Summary of calculated globally-annually averaged quantities of UVB and UVA at surface. Last two columns show the calculated SG percentage changes with respect to the BG case (years 2046-2055).

3.4 Radiative forcing

The ULAQ-CCM radiative transfer module calculates online the radiative forcing due to aerosols, GHGs, and low and high clouds. The effects of single components have been estimated offline for both shortwaves (SWs) and longwaves (LWs) with the same radiative transfer core, for sulfate aerosols, clouds, COS, CH_4, stratospheric

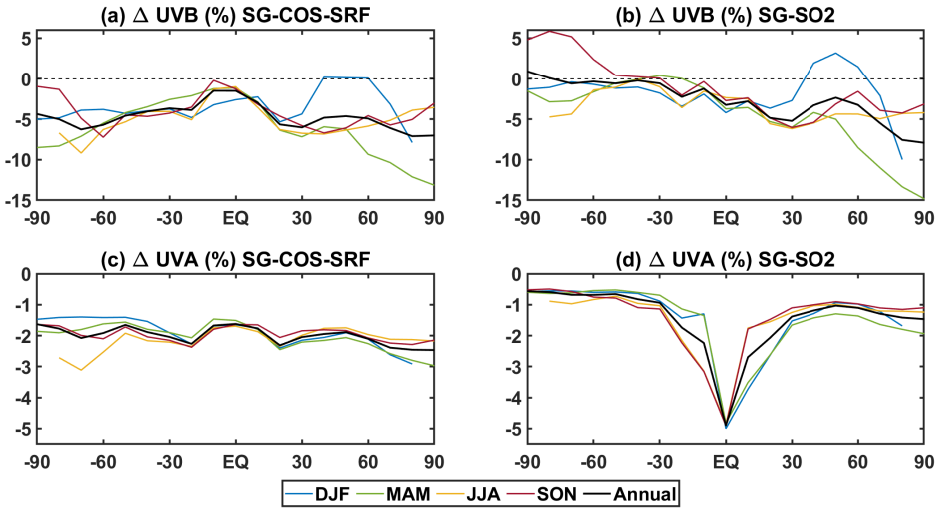

FIGURE 3.8: Zonal UVB and UVA surface changes per each season in percentage with respect to BG case in SG-COS-SRF (panels a and b, respectively) and SG-SO2 (panels c and d). All quantities are averaged over the years 2046-2055.

H_2O, stratospheric and tropospheric O_3 in order to properly separate the contributions.

Tables B.8, B.9 and B.10 summarize the individual contributions of GHGs changes for SG-COS-SRF, SG-COS-TTL and SG-SO2, respectively. Similar increases of methane in all SG experiments produce the same positive LW RF; the TTL warming (which results in an increase in stratospheric water vapor), results in a small but positive contribution from H_2O in SG-SO2. Contributions from both stratospheric and tropospheric O_3 changes have also been estimated, but are negligible.

In both SG-COS experiments, obviously, the increase in COS concentration, which is a GHG, must be taken into account. We estimated its contribution to the radiative forcing based on the definition of global warming potential (GWP) on a mass/mass basis as in Brühl et al. (2012) for a time horizons of 30 years (2021-2050). GWP can be approximated, as follows, by the expression of Roehl et al. (1995), assuming that the perturbation of the radiation balance of the Earth by greenhouse gases COS and CO_2 decays exponentially after a pulse emission for a time horizon ΔT.

$$GWP_{\Delta_t} \simeq \frac{RF_{COS}}{RF_{CO_2}} \times \frac{\tau_{COS}}{\tau_{CO_2}} \times \frac{1 - e^{\frac{-\Delta_t}{\tau_{COS}}}}{1 - e^{\frac{-\Delta_t}{\tau_{CO_2}}}} \tag{3.1}$$

We assumed an overall lifetime of τ_{COS}=3.8 yr and τ_{CO_2}=75 yr, and the radiative forcing of 1 kg of COS relative to 1 kg of CO_2 added to the present atmosphere (RF_{COS}/RF_{CO_2}) is 724 (Brühl and Crutzen, 1988). This results in a GWP of 111. For our time period, the mass of COS and CO_2 added to the atmosphere (Δm) is 1.97 $\times$ 10^{12} kg of COS (for SG-COS-SRF), 0.35 $\times$ 10^{12} kg of COS (for SG-COS-TTL) and 1.23 $\times$ 10^{15} kg of CO_2. Therefore, the COS radiative forcing can be calculated as follows:

$$RF_{COS} = GWP_{\Delta t} \times RF_{CO_2} \times \frac{\Delta m_{COS}}{\Delta m_{CO_2}} \tag{3.2}$$

where RF_{CO_2} in RCP6.0 is estimated to be 0.83 W/m^2 considering an increase in 68.5 ppm from a baseline of 409.2 ppm. Overall, this results in a radiative forcing from the COS increase in 0.17 W/m^2 in SG-COS-SRF and of 0.03 W/m^2 in SG-COS-TTL.

The main contributions of sulfate aerosols and clouds are summarized in tables B.5, B.6 and B.7 for SG-COS-SRF, SG-COS-TTL and SG-SO2, respectively. The contribution of sulfate aerosols is the sum of the cooling effects given by the efficient scattering of solar radiation by particles of radius of around 0.5 μm and the absorption of LW by larger ones. Globally, the estimated values are similar for the clear-sky SW and LW forcing from the sulfate aerosols: in terms of the latitudinal distribution, however, SG-SO2 presents a peak in the tropics whereas the forcing from SG-COS is much more latitudinally even.

The reduction in optical depth from cirrus clouds (see table 3.1) produced by the aerosols (Kuebbeler, Lohmann, and Feichter, 2012; Visioni et al., 2018a) results in a net negative radiative forcing. This is given by the balance between the positive RF in the SWs due to the reduction of reflected solar radiation and the negative RF in the LWs due to the decrease in the trapped planetary radiation, which reduces the contribution to the greenhouse effect. In the SG-COS cases, at the Equator the positive RF from the cirrus ice thinning locally balances the direct forcing from the aerosol (Figs.3.9 and B.8).

Table 3.6 summarizes the total contribution of sulfate aerosols and greenhouse gases under all-sky conditions.

Total RF (W/m^2)	**SW**	**LW**	**NET**
SG-COS-SRF	-1.47±0.12	+0.21±0.25	-1.26±0.13
SG-COS-TTL	-1.41±0.12	-0.06±0.25	-1.47±0.13
SG-SO2	-1.58±0.10	-0.11±0.23	-1.69±0.13

TABLE 3.6: Globally-annually averaged total RF of sulfate aerosols and greenhouse gases for the SG experiments with respect to BG (shortwave, longwave and net) (W/m^2) (years 2046-2055).

3.5 Technical feasibility of SG through COS emissions

We briefly discuss here the technical feasibility of the approach described in this paper, as it is mainly related to the increase in surface COS emissions (for SO_2 injections, see for instance Smith and Wagner, 2018; Smith et al., 2020).

Patent number 3,409,399 (1968) has developed a method for the high yield synthesis of COS (93.2-96.6%) as follows:

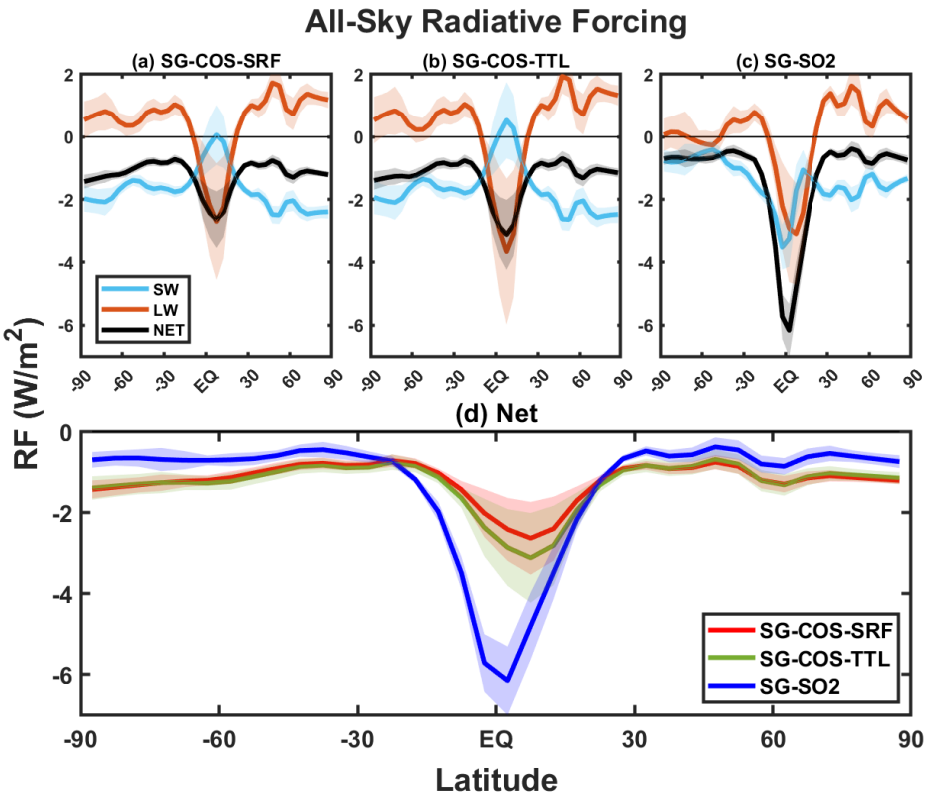

FIGURE 3.9: a-c) Mean zonal shortwave (cyan), longwave (orange), and net (black) All-Sky radiative forcing (in W/m^2) in SG-COS-SRF, SG-COS-TTL and SG-SO2 respectively. d) Comparison of the net radiative forcings from SG-COS-SRF (red), SG-COS-TTL (green) and SG-SO2 (blue). All quantities are annually averaged over the years 2046-2055. Shadings in all panels represent 1 standard deviation in the interannual variability.

$$CO_2 + CS_2 \xrightarrow{100-600^\circ C} 2COS$$

CO_2 is abundant, even in concentrated (90%+) streams, from various natural and industrial sources, particularly with cooperation from states or industries. For example, capturing flue gas from coal-fired power plants is an established technology and may yield over 90% CO_2 (Wang et al., 2013). CS_2 is produced via numerous means, perhaps the easiest being from coke (carbon) and molten sulfur, as follows:

$$C + 2S \xrightarrow{\text{high temperature}} CS_2$$

Approximately 1 × 10^6t of CS_2 is produced per year (Madon and Strickland-Constable, 1958), with China consuming approximately half of the global production of CS_2 for rayon manufacture. CS_2 is highly unstable and is flammable in air. It is also toxic at low concentrations (10 ppm).

Given the reactions above, about 0.5 Tg of S will produce 0.94 Tg of COS. This amounts to 0.16 Tg of C (coke) and 0.55 Tg of molten sulfur. In the last decade, approximately 70 Tg of sulfur were produced worldwide, so this would constitute an increase in S production of 0.8%. The price varied between USD 50 and USD 200 per ton, leading to an annual cost of approximately USD 25 million-USD 100 million. The worldwide production of coke was around 640 Tg, so this increase in production is negligible. The price of coke varies between USD 50 and USD 100 per ton, leading to an annual cost of approximately USD 8 million-USD 16 million. To this we would have to add the cost of CO_2, in addition to the production and energy costs. Considering an estimate of USD 400 million per year for each Tg of S between CO_2 and production and energy cost, and assuming an effort shared between 1000 locations, this would add up to USD 400.000 per location per year per each Tg of S. The overall cost is roughly of the same order of magnitude as that in Smith and Wagner (2018) for a stratospheric aerosol deployment at $\sim$ 20 km of injection (so different from the injection set-up in our study for SG-SO2), but without the need to develop a new aircraft-based delivery system. For the SG-COS-TTL case, the overall cost would be a combination of the production costs of COS as described above (but almost 10 times less per year to obtain the same AOD as SG-COS-SRF) and those of a deployment in the upper troposphere, which may result in being less expensive than a deployment in the lower stratosphere as needed for SO_2.

3.6 Conclusion

We have presented here the results of a modeling experiment with the aim of producing an optically thick cloud of sulfate aerosols in the stratosphere without the injection of sulfate precursors directly into the stratosphere but rather by using increased surface or upper tropospheric emissions of COS. The low reactivity of COS

in the troposphere, where it is not reactive and where it is predominantly absorbed by some soils and by plants, allows for a large portion of its emissions to reach the stratosphere, where it is turned into sulfate aerosols by photo-dissociation and oxidation.

We compare the results obtained in the following injection scenarios: (i) 40 Tg-S/yr of COS injected from the surface (roughly 400 times more than the background emissions), (ii) 6 Tg-S/yr of COS injected in the Equatorial upper troposphere (15 km), and (iii) 4 Tg-S/yr of SO_2 injected in the Equatorial stratosphere, as prescribed in previous experiments (Kravitz et al., 2011; Visioni, Pitari, and Aquila, 2017). All experiments result in a similar global optical depth from the produced stratospheric aerosols ($\sim$ 0.08), but with different latitudinal distributions. For SO_2, as previously observed in various modeling experiments, Equatorial injections result in an increased concentration of aerosols in the tropical stratosphere that tends to overcool the tropics and undercool the high latitudes (Kravitz et al., 2018; Jiang et al., 2019), while also reducing the efficacy of the backscattering from the aerosols due to the increased size of the particles (Visioni et al., 2018b). On the other hand, with COS emissions, independently from the injection height, the uniform mixing of the gas allows for a more uniform distribution of the produced aerosols in the stratosphere, resulting in increased optical depth that is also at very high latitude.

The differences in the distribution and size of the particles result in different changes to the composition of the atmosphere. Smaller particles absorb and heat the stratosphere less, thus resulting in fewer dynamical changes. From a chemical perspective, stratospheric ozone would be impacted differently from the two geoengineering schemes. For SO_2 injections, previous studies have shown that the overall effect is the result of a combination of various dynamical and chemical factors that behave differently depending on the latitude and altitude of the aerosols. At low latitudes the increase in lower stratospheric water vapor produced by the warming of the tropopause layer enhances the halogen-driven destruction of ozone in the lower stratosphere (Tilmes et al., 2018c) due to NO_x depletion. This effect is balanced by reduced ozone destruction in the middle stratosphere due to the slowing down of the NO_x cycle produced by enhanced heterogeneous chemistry (Pitari et al., 2014; Richter et al., 2017; Franke, Niemeier, and Visioni, 2021).

Overall, in the case of COS emissions the further increase in surface area density produced by smaller particles increases the inhibition of the ozone cycles in the middle stratosphere, resulting in a net increase in stratospheric ozone and, thus, in a larger decrease in UV radiation at the surface. Similarly, the larger sulfate burden at high latitudes produces further ozone recovery and thus also less UV radiation at the poles for the COS case.

Our results point to the feasibility of increased emissions of COS as a possible substitute to stratospheric SO_2 (or other sulfate precursors) injections to produce

stratospheric sulfate aerosols. Surface emissions would sidestep the problem of deploying methods not already available to bring the sulfate at those altitudes, including the development of novel aircraft (Bingaman et al., 2020). Since COS is already a byproduct of human activities, it might be possible to devise methods of mass production of the required quantities that may be cheaper than the known proposed methods (Smith et al., 2020). However, this strategy necessitates a larger amount of emissions to achieve the same global stratospheric AOD, resulting in larger amounts of deposition. Furthermore, while the toxic levels of COS concentrations are orders of magnitude larger than the one achieved in our simulation (Kilburn and Warshaw, 1995; Bartholomaeus and Haritos, 2006), the effects of prolonged exposure to lower concentrations would have to be assessed; the effect of increased COS concentrations on ecosystems would also require careful investigation. Estimations of the tropospheric radiative effect would also need to be refined to make sure that it is not larger than previously estimated, thus, reducing the efficacy of the aerosol-induced cooling. We have shown that tropospheric injections of lower quantities of COS would produce the same optical depth and indirect effects while resulting in an increase in tropospheric COS concentrations 10 times lower than those with surface emissions. This would, however, still require the deployment of an aircraft fleet as in SO_2 emissions, but the technical challenges of reaching 15 km might be less than those faced when reaching 20 km Smith et al. (2020).

Overall, there may be other weak points in the geoengineering strategies using COS emissions compared to SO_2 that need to be addressed. They would be less easily scalable, and both the deployment and phaseout, as we have shown, would require a longer time frame compared to the almost instantaneous effect produced by SO_2 injections. Considering the dangers to ecosystems presented by a too fast deployment or termination of sulfate geoengineering (Trisos et al., 2018), this might not actually be a large drawback, but it does remove the possibility of rapidly regulating the necessary amount of stratospheric sulfate in case of changes in strategy or external conditions (such as a Pinatubo-like volcanic eruption; Laakso et al., 2016). The comparison between our two COS experiments suggests that the mixing happening in the troposphere would not allow any control in the latitudinal or seasonal distribution of the resulting aerosols, as proposed elsewhere for SO_2 injections (MacMartin et al., 2017; Dai, Weisenstein, and Keith, 2018; Visioni et al., 2019); however, future investigations may expand on this work by exploring whether a different combination of injection altitudes and locations may offer at least some control over the aerosol cloud.

Clearly, this study is intended to be just a pilot study of this method, and further simulations with other climate models, possibly with a coupled ocean and interactive land model to determine the full surface response, are needed. The agreement between the baseline results presented here and the information present in the literature point to a robustness of our results, but further studies are required to understand different aspects of the climate response. For instance, studies would need

to investigate the possible response of vegetation and soils to the increased concentration of COS in the troposphere, and if the efficacy of the sinks would change due to shifts in temperature and precipitation produced by both climate change and the intervention.

Overall, however, the results obtained in this work show that, as a geoengineering technique, emissions of carbonyl sulfide should be further studied and considered by the scientific community as a possible alternative to the others already studied in the literature.

Chapter 4

Reassessing the risks of an explosive volcanic eruption during a Stratospheric Aerosol Injection deployment

The enhancement of the stratospheric aerosol layer after explosive volcanic eruptions perturbs the energy budget of the atmosphere and oceans by reducing incoming solar radiation and warming the lower stratosphere and, consequently, altering atmospheric dynamics and ocean circulation, in turn modifying stratospheric ozone concentrations and affecting the hydrologic cycle, reducing global precipitation, weakening monsoons, and shifting the position of the Inter-Tropical Convergence Zone (ITCZ) (Robock, 2000; Timmreck et al., 2012; Aquila et al., 2013; Marshall et al., 2022).

The eruption of Mt. Pinatubo in June 1991, which injected between 14 and 22 Tg of SO_2 (Bluth et al., 1992b; Guo et al., 2004a), was estimated to produce a global cooling between 0.14-0.5 K compared to pre-Pinatubo levels in 1992-1993 (Dutton and Christy, 1992; Soden et al., 2002; Canty et al., 2013) and substantially decrease precipitation over land (Trenberth and Dai, 2007). Idealized simulations of the Pinatubo eruption within the Max Planck Institute Grand Ensemble framework show that a sulfur injection of ≥ 20 Tg may lead to a significantly decreased monsoon precipitation beyond the effect of internal variability, driven by changes in atmospheric circulation (D'Agostino and Timmreck, 2022). Even smaller eruptions, such as Agung in 1963 and Santa Maria in 1902 (5-13 and 13 Tg of SO_2 injected in the stratosphere, respectively; Textor et al., 2004) that still produce asymmetric inter-hemispheric forcing, may have produced a significant impact on regional hemispheric precipitation (Yang et al., 2019).

The altered hemispherical thermal contrast due to the asymmetry of the zonal stratospheric aerosol distribution can shift the position of the Hadley cell and, therefore, of the ITCZ, which is pushed away from the cooler hemisphere towards the warmer one, altering regional precipitation patterns (Broccoli, Dahl, and Stouffer, 2006; Iles and Hegerl, 2014; Zuo, Zhou, and Man, 2019; Jacobson et al., 2020). Through

this mechanism, volcanic eruptions in the Northern Hemisphere (NH) may move the ITCZ southward and cause droughts in the Sahel region (Haywood et al., 2013; Jacobson et al., 2020), whereas Southern Hemisphere (SH) eruptions may shift the ITCZ northwards, as evidenced by the increased rainfall in Belize in the year following the Mt. Tambora eruption in 1815 (Ridley et al., 2015).

Through a similar mechanism, the increase in anthropogenic aerosol emissions in the NH since the early 1900s produced an asymmetric cooling between the hemispheres that has led to a southward migration of the ITCZ, a drying of the northern tropics, most significant in the Sahel region, and a moistening of the southern tropics (Hwang, Frierson, and Kang, 2013).

Stratospheric Aerosol Injection (SAI) would mimic the mechanism behind volcanic eruptions-induced cooling by continuously injecting SO_2 in the lower stratosphere to temporarily offset the greenhouse gas induced global warming (Crutzen, 2006; Institute of Medicine and National Academy of Sciences and National Academy of Engineering, 1992). If the locations of the artificial injections are limited to one hemisphere, SAI might produce a forcing asymmetry and lead to similar changes in regional precipitation as observed for volcanic eruptions (Jones et al., 2010; Haywood et al., 2013). On the other hand, a combination of multiple injection locations might result in a more even aerosol distribution and potentially allow the management of not just global mean temperature, but also inter-hemispheric and equator-to-pole temperature gradients. (MacMartin et al., 2014; Kravitz et al., 2016; Lee et al., 2020).

Such an injection strategy was used in the Stratospheric Aerosol Geoengineering Large Ensemble (GLENS; Tilmes et al., 2018b), which considered four injection locations (30°N, 15°N, 15°S, and 30°S) with an injection rate based on a feedback algorithm (Kravitz et al., 2016; Kravitz et al., 2017; MacMartin et al., 2014) to keep the global mean near-surface air temperature and its inter-hemispheric and equator-to-pole gradients at their 2020 values under the Representative Concentration Pathway 8.5 (RCP8.5). These simulations showed that strategic SAI may ameliorate some of the effects of global warming by offsetting changes in precipitation in the tropics and mid-latitudes (Simpson et al., 2019; Da-Allada et al., 2020).

Subsequently, a more realistic emission scenario (SSP2–4.5) was considered in MacMartin et al., 2022; in that case, lower injection latitudes (21.5 km, compared to 25 km in GLENS) where chosen, while using the same injection latitudes and a similar feedback-control algorithm to maintain global mean near-surface air temperatures at 1.5 K above preindustrial levels. Richter et al., 2022 showed that under this strategy the precipitation increases over the equatorial Pacific Ocean in the warming climate can be decreased with SAI; however, both SSP2-4.5 and SAI showed a drying of the regions north of the equator, and SAI also showed more intense drying of the southern tropics compared to SSP2-4.5.

Since large explosive eruptions have a recurrence frequency of about one eruption every 50-60 years on average (Schmidt et al., 2018), it is likely that under potential future deployments of SAI, a large volcanic eruption could occur, and thus it is necessary to assess volcanic contributions under SAI conditions: such an occurrence would further increase the stratospheric aerosol layer and potentially overcool the hemisphere where it occurs, compromising the targeted cooling.

Laakso et al. (2016) simulated a volcanic eruption of 17 Tg of SO_2 injected at the location of Mt. Pinatubo occurring during a SAI deployment, which in their case consisted of a constant injection of 16 Tg-SO_2/yr between 30°N and 30°S; after the simulated eruption, they considered the possibility of either continuing or completely suspending the SAI deployment. They found that in all simulations (with or without SAI) surface cooling and precipitation change occur mainly in the tropics with different patterns based on the background in which occur. They also found that the volcanic contribution to the increase in negative radiative forcing, as well as the decrease in global temperature and precipitation, is less when the eruption occurs under SAI conditions than when it occurs under non-SAI conditions, due to microphysical factors that determine the non-additivity of volcanic eruption and SAI.

Here we expand upon that study by considering two potential eruptions: a "medium" one (10 Tg-SO_2), and a "large" (50 Tg-SO_2) occurring at the latitude of Pinatubo during SAI deployment, and by considering the same simulated SAI deployment framework as MacMartin et al., 2022, where injection amounts are laittude-dependant to manage multiple temperature-dependant degrees of freedom. Withing this framework, we will demonstrate that in such a scenario it would be possible to modify the injection strategy in different ways in order to account for the exogenous increase in aerosol load, and that each way may come with different trade-offs in terms of impacts on the surface climate. Nonetheless, we show that, were an eruption to happen under an SAI deployment, less detectable surface impacts may be expected as opposed to an eruption happening without an SAI deployment.

4.1 Model and simulations

4.1.1 The CESM2(WACCM6) earth system model

We use the Community Earth System Model, version 2, with the Whole Atmosphere Community Climate Model version 6 as the atmospheric component, CESM2(WACCM6) (Gettelman et al., 2019; Danabasoglu et al., 2020). CESM2(WACCM6) is a global climate model that includes interactive atmosphere, ocean, land, and sea ice components, with an horizontal resolution of 0.95° latitude × 1.25° longitude, and 70 vertical layers up to 140 km; the resolution allows a reasonable simulation of internal variability in the stratosphere (e.g., internally-generated Quasi-Biennial Oscillation).

The WACCM6-MA configuration used includes the Middle-Atmosphere (stratospheric) chemistry without representation of species and reactions that are significant only in the troposphere (Mills et al., 2017; Davis et al., 2022). Aerosols are simulated using the Modal Aerosol Model version 4 (MAM4) that includes black carbon, primary organic matter, secondary organic aerosols, sea salt, dust, and sulfate internally mixed in four lognormal modes (Primary carbon, Aitken, Accumulation, and Coarse modes) (Liu et al., 2016).

4.1.2 Simulations

The volcanic eruptions and SAI simulations happen under the Shared Socioeconomic Pathway 2-4.5 (SSP2-4.5; Meinshausen et al., 2020) as a background greenhouse gas emission scenario (MacMartin et al., 2022).

The SAI simulations are 35 years long, starting in 2035, and consist of yearly injections of SO_2 at four latitudes (30°N, 15°N, 15°S, and 30°S), at longitude 180°E in the gridbox centered at 21.5 km (with a vertical resolution of 1.2 km). The injection rates of SO_2 are controlled by a feedback algorithm (Fig. 4.1) aimed at maintaining global mean temperature at 1.5 °C above the preindustrial level (defined as the average over the 2020-2039 period in CESM2), and also at maintaining interhemispheric and equator-to-pole temperature gradient constant at the same reference period (2020-2040) (Kravitz et al., 2016; MacMartin et al., 2022).

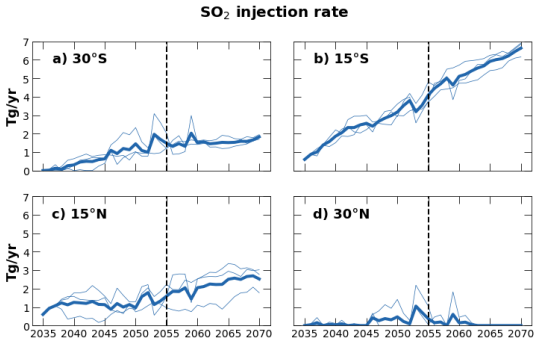

FIGURE 4.1: Time series of SO_2 injection rate (Tg/year) in SAI at the four injection locations with longitude 180°E and latitude a) 30°S, b) 15°S, c) 15°N, and d) 30°S. The dashed black line indicates the time when the eruption occurs.

The volcanic eruptions of 10 and 50 Tg-SO_2 are simulated both in the background scenario without SAI (Volc10Tg and Volc50Tg, respectively) and in the SAI scenario; they consist of an injection between 18-25 km at the location of Mt. Pinatubo (15.1°N, 120.4°E); for simplicity, we chose the date of January 1 2055 for the eruption.

4.2 Process for strategy determination

For the eruptions happening under an SAI deployment, we consider different changes to the injection strategy based on the global evolution and latitudinal distribution of

TABLE 4.1: Summary of simulations

Simulation name	Description
SSP2-4.5	Background emission scenario SSP2-4.5
SAI	SSP2-4.5 + continuous injection of SO_2 controlled by feedback algorithm
Volc10Tg	10 Tg of SO_2 eruption on January 1st, 2055
Volc50Tg	50 Tg of SO_2 eruption on January 1st, 2055
Volc10Tg+SAI_off	SAI suspended everywhere on January 1st, 2055 + Volc10
Volc10Tg+SAI_nhoff	SAI suspended in NH on January 1st, 2055 + Volc10
Volc50Tg+SAI_off	SAI suspended everywhere on January 1st, 2055 + Volc50

stratospheric sulfate burden and stratospheric aerosol optical depth (sAOD) in the two cases simulated under background conditions (Fig. 4.2).

We start from the assumption that the risks associated to a volcanic eruption with a change in the inter-hemispheric and equator-to-pole temperature gradients can be limited during an SAI deployment by controlling the distribution of the sulfate aerosols in the stratosphere.

Figure 4.2 shows the evolution of global sulfate burden changes with respect to SSP2-4.5 and stratospheric aerosol optical depth, and the zonal change of sAOD averaged during the first year after the eruption (2055), for both eruption magnitudes.

Both Volc10Tg and Volc50Tg sulfate burden and sAOD reach their maximum value 5 months after the eruption (May 2055) at 6.3 and 28.1 Tg for the sulfate burden and at 0.13 and 0.55 for the sAOD, respectively. Sulfate burden and sAOD in Volc10Tg reach a peak that is close in value to the SAI ones, and a value 4.4 times larger in Volc50Tg, with an e-folding time for sulfate burden and sAOD of between 16 and 18 months for all cases. The eruptions mainly increase sAOD in the northern hemisphere, where they occur. During the first year after the eruption (2055) when both sulfate burden and sAOD show the highest values (Fig. 4.2c and f), Volc10Tg produces a sAOD of 0.18 in NH (and 0.03 in SH) which is higher than that produced in SAI in the same hemisphere of 0.10 but comparable to that in SH of 0.16. For the same year, Volc50Tg results in a sAOD of of 0.77 in the NH and 0.15 in the SH.

This latitudinal distribution of the lower eruption case suggests two possible strategies: i) stopping sulfate injections only in the hemisphere where the eruption occurs (Volc10g+SAI_nhoff), in order to equalize the differences in the horizontal distribution of stratospheric aerosols between the two hemispheres and, thus, keep the inter-hemispheric temperature gradient constant and ii) stopping sulfate injections in both hemispheres (Volc10Tg+SAI_off) in order to prevent global overcooling by reducing sAOD quickly. For the higher eruption case, achieving the same goal of offsetting the disparity between the two hemisphere would require an injection of SO_2 of roughly the same magnitude as the eruption, which would have extreme impacts on global mean temperature and precipitation. In this case, therefore, the only plausible choice is to stop SAI everywhere (Volc50g+SAI_off).

The additional stratospheric aerosol burden and sAOD from the volcanic eruptions on top of the already increased ones from SAI (Volc10Tg+SAI_off and

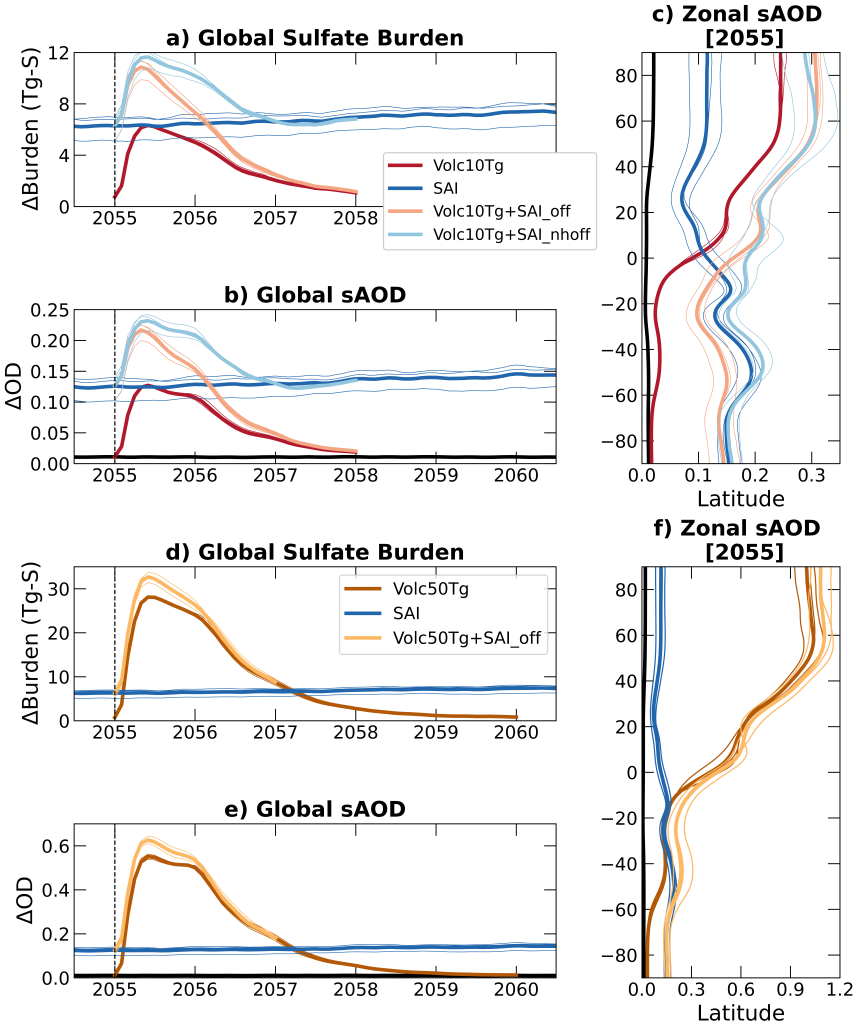

FIGURE 4.2: Monthly values of globally averaged sulfate burden change with respect to SSP2-4.5 for 10 Tg and 50 Tg of SO_2 eruption in a) and d), respectively. b) and e) as before for the globally averaged stratospheric aerosol optical depth, c) and f) for the zonal aerosol optical depth averaged over 2055.

Volc50Tg+SAI_off) are smaller and decrease more rapidly than those on top of SSP2-4.5 (Volc10Tg and Volc50Tg) (Fig. 4.2b and e). This happens both because SAI injections are reduced post-eruption, but also because when SO_2 is injected into a perturbed stratospheric aerosol layer, aerosols growth by condensation prevails on nucleation producing larger aerosols and, in turns, resulting in faster sedimentation (Laakso et al., 2016; Visioni et al., 2019). Thus, independently from the background on which the eruption occurs, the stratospheric sulfate burden and aerosol optical depth returns to the unperturbed levels in almost 3 years.

In the cases with a 10 Tg-SO_2 eruption under SAI, the global sulfate burden and the sAOD take 1 year to return to pre-eruption SAI values if SAI is stopped everywhere, whereas it takes 2 year if SAI is stopped only in one hemisphere; for the 50TgSO_2, two years are necessary. In Volc10Tg+SAI_nhoff, NH SAI injections are restarted 2 years after the eruption in order for the global sulfate burden and sAOD to return to pre-eruption values. In Volc10Tg+SAI_off and Volc50Tg+SAI_off, SAI is not restarted at all.

Even if SAI is stopped, the latitudinal distribution of sAOD during the first year after the eruption results in the NH in a 0.05 higher value with respect to the Volc10Tg case, whereas in the SH it results in a value 0.03 lower with respect to the SAI case. Stopping the injection only in the NH results therefore in a more symmetrical inter-hemispheric distribution, but a higher global sAOD. The climatic-trade-offs between these two cases will be analyzed in the next sections.

4.3 Results

4.3.1 Temperature

Figure 4.3 shows the time series of the running mean (5 months) of the three degrees of freedom for surface temperatures that are being managed by the multi-location SAI injections: global mean temperature (GMT, T_0), the inter-hemispheric temperature gradient (T_1), and the equator-to-pole temperature gradient (T_2).

Figure 4.3a shows that under SAI GMT is held at 1.5$\pm$0.1 K above preindustrial (PI), while SSP2-4.5 temperature continues to increase at a rate of 0.3 K decade^{-1}. Following the eruption, a cooling of 0.3 K and 1.1 K in Volc10Tg and Volc50Tg is detected under SSP2-4.5; this cooling is 0.2 K lower when the eruption happens under SAI. GMT returns to the respective background values after 3 years for Volc10Tg under SSP2-4.5, while it takes more than 5 years Volc50Tg. Under SAI, the return time for GMT depends on the strategy: if injections are stopped everywhere, it takes only 2 years, whereas if injections are maintained in one hemisphere, the time is similar to that under SSP2-4.5.

While both SSP2-4.5 and SAI maintain a roughly-constant inter-hemispheric temperature gradient (0.93$\pm$0.07 K in SSP2-4.5 and at 0.84$\pm$0.06 K in SAI, Fig. 4.3b), all simulations with volcanic eruptions which mainly cool the NH and result in lower

values of T_1. For the 10 Tg SO_2 eruptions, there is a similar decrease in T_1 in the two following years: 0.76±0.8 K in Volc10Tg, 0.73±0.07 K Volc10Tg+SAI_off and 0.74±0.08 K Volc10Tg+SAI_nhoff, whereas the 50 Tg SO_2 eruptions lead to the much lower values of T_1 (lowest value of 0.13 in Volc50Tg and 0.14 K in Volc50Tg+SAI_off) and a subsequent return towards higher values.

In Figure 4.3c, T_2 increases (becomes less negative) in SSP2-4.5 from 2035 at a rate of 0.03 K/decade due to increased Arctic warming, while under SAI it roughly constant at -5.89±0.06 K. After the volcanic eruption, as a result of a larger cooling in the northern extratropics compared to the tropics, T_2 decreases by 0.1 and 0.3 K for the 10 and 50 Tg-SO_2 eruptions compared to the respective background, with a slightly smaller decrease when SAI is continued in SH for the medium eruption and for the larger eruption occurring during SAI.

In Figure 4.4 we show maps of temperature changes, only highlighting regions where the differences are statistically significant at the 95% significance level. Panels 4.4a and b show the temperature change in SSP2-4.5 and SAI for 2050-2069 compared to the 20-years average over 2020-2040 in SSP2-4.5 (Baseline): in this case, statistical significance is meant to imply a deviation of the two compared steady states, either introduced by the longwave-induced warming or because of an imperfect balance from SAI.

In SSP2-4.5 the increase in greenhouse gases results in a warming that affects almost the entire globe except for a region in the North Atlantic Ocean (due to a projected continued slowdown of the Atlantic Meridional Overturning Circulation; see Figure 3 in MacMartin et al., 2022; Gervais, Shaman, and Kushnir, 2018). A higher warming compared to the global mean is evident in the Artic region (1.8 K) due to Arctic amplification which produces a fast melting of sea ice (Fig. C.1, black line) and weaker ice-albedo feedback (Rantanen et al., 2022). Under SAI, the balance between the cooling exerted by increased aerosol reflection and the GHGs-induced warming results in some residual warming relative to Baseline with a temperature change of 0.1 K (globally averaged) and a faction of land with statistically significant change of 25.2% versus the of 0.9 K and 99.9% in SSP2-4.5.

In Figure 4.4c and d we show the temperature change over the 2 years following the eruptions compared to 20-years average in SSP2-4.5 (2050-2069); likewise panels 4.4e-f show the changes for the eruptions occurring under SAI (Volc10Tg+SAI_off, Volc10Tg+SAI_nhoff, Volc50Tg+SAI_off) compared to the 20-years average in SAI. Unlike for panels a and b), here we aim to highlight the direct perturbation produced by the eruption compared to the simulated climatology: shaded areas here are meant to indicate regions where the change produced by the eruption are comparable to the variability calculated over the 20 years periods.

As discussed before, the eruptions mainly decrease the surface air temperature in the hemisphere where they occur, however, the temperature change compared to the respective background is significantly smaller when the eruptions occur during SAI: the average cooling contribution from the eruption in the NH is 0.6 K in

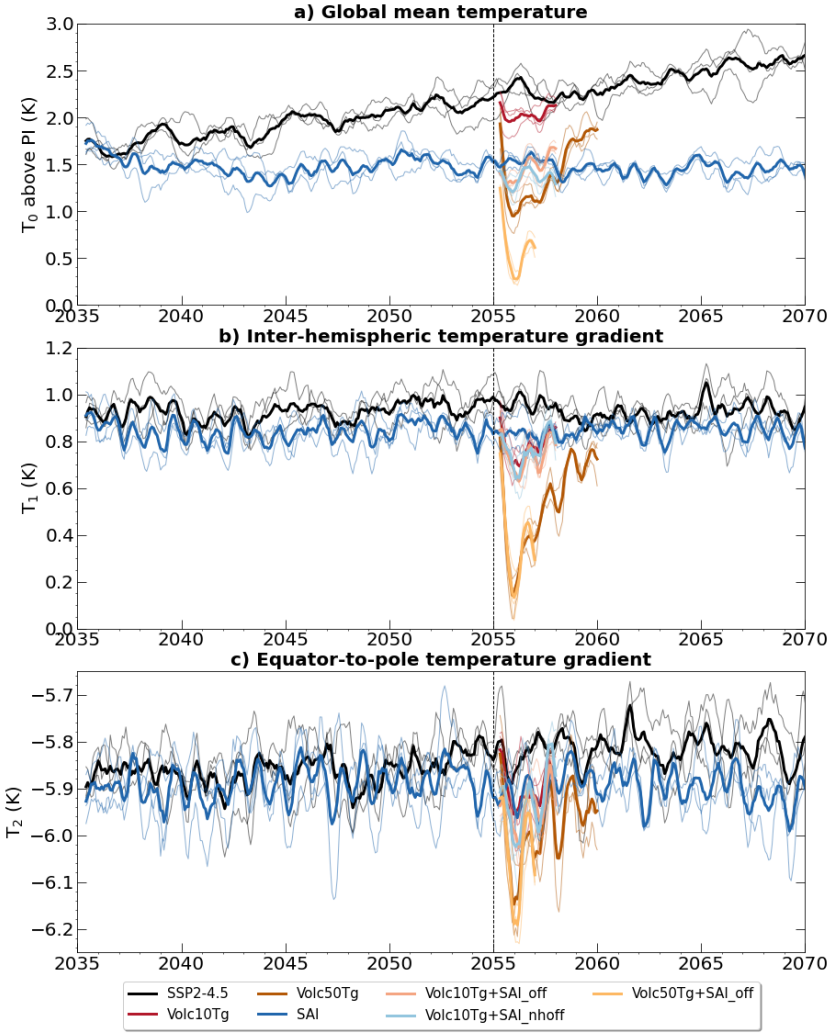

FIGURE 4.3: Time series of monthly mean of (a) global temperature (T_0) in K above preindustrial levels (PI), (b) inter-hemispheric temperature gradient (T_1) and (c) equator-pole temperature gradient (T_2). T_1 and T_2 are calculated from the monthly values of T_0 from which seasonality, given by detrended background values with a linear fit over the years 2035-2069, was subtracted. All variables are rolling mean over 5 months.

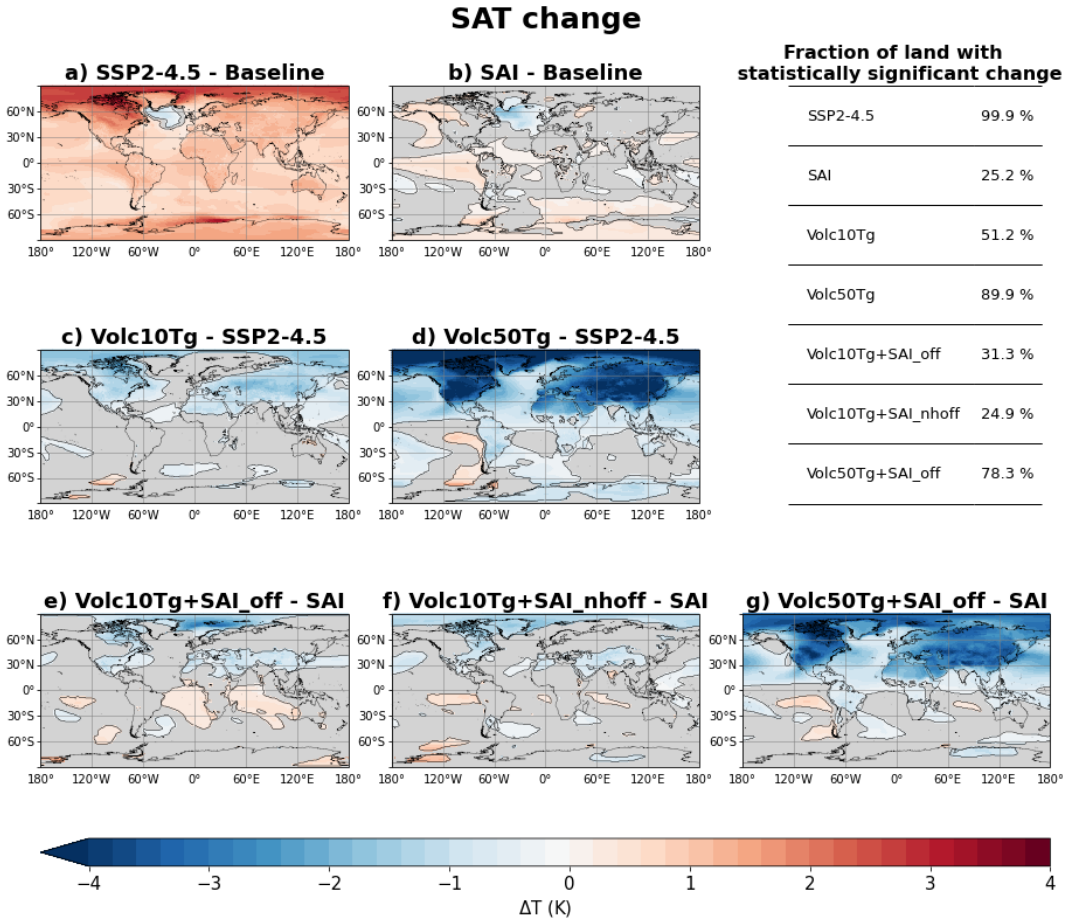

FIGURE 4.4: Maps of statistically significant change of temperature from different background simulation based on the considered simulation. Gray areas are the region where the differences are non statistically significant at the 5% significance level. (a, b) show the temperature change in SSP2-4.5 and SAI averaged over 2050-2069 from Baseline (SSP2-4.5 averaged over 2020-2039) and the statistics are calculated over all the simulation years for the three ensemble members. (c, d) as (a, b) for Volc10Tg and Volc50Tg averaged over 2055-2056 from the 20-years average in SSP2-4.5. (e-g) as (a, b) for Volc10Tg+SAI_off, Volc10Tg+SAI_nhoff and Volc50Tg+SAI_off averaged over 2055-2056 from the 20-years average in SAI.

Volc10Tg and 2.0 K in Volc50Tg, and it is 0.4 K smaller, regardless of eruption magnitude, when it occurs during SAI. As for the sAOD, the smaller cooling under SAI is due to the suspension of the injection to contain the over-cooling and because of the presence of a larger aerosol load when the SO_2 injection happens. Furthermore, the fraction of land with statistically significant temperature changes from the background is lower for eruptions occurring under SAI background, as shown in the table in Figure 4.4.

Stopping SAI injections to compensate for the volcanic eruption, thereby trying to avoid a GMT overcooling, implies that while NH changes are reduced for the eruption happening under SAI compared to those under SSP2-4.5, there are regions in the SH that result less cooled than under the SAI case alone: for the 10 Tg volcanic eruption, an overall warming of 0.13 K (if injections are stopped everywhere) and 0.05 K (if injections are stopped only in the NH) is detected. For the 50 Tg case, where the overall cooling is stronger (-0.30K in the SH under SSP2-4.5) stopping injections results less than half (-0.12K) overall cooling compared to the SAI case in the SH.

4.3.2 Precipitation and ITCZ shift

Variations in surface temperature affect global precipitation, and variations in the inter-hemispheric thermal contrast affect the location of the tropical Hadley circulation, identified by the location of the ITCZ, in turn resulting in changes in the regional distribution of precipitation. We note that the metric we choose to predict ITCZ-shifts (T_1 in Figure 4.3b) constitutes only a rough estimate of its behavior (see Figure 8 of Lee et al., 2020).

Figure 4.5 shows the change in global precipitation with respect to the mean precipitation in Baseline. In SSP2-4.5 the global precipitation increases compared to the reference period, with a rate of 0.02 mm/day per decade from 2040, whereas Under SAI it remains similar to Baseline.

Due to the global temperature changes, volcanic eruptions decrease global mean precipitation with a reduction that depends on their magnitude; the volcanic-driven precipitation reduction is also smaller when occurring under SAI. Under SSP2-4.5 the precipitation change due to a medium to large eruption ranges between -0.03 and -0.07 mm/day over 2055-2056, respectively, and the precipitation decrease is 0.02 mm/day smaller under SAI, independently from the magnitude of the eruption and SAI strategy adopted for the medium case.

The main change in precipitation occurs over the Tropics, as shown in Figure 4.6 (calculated as in Figure 4.4). Global warming in the panel 4.6a produces an increase in precipitation around the equator in the Pacific Ocean, in the Atlantic Ocean extending over Brazil and regions of west-central Africa, and over a small eastern region on the Indian Ocean facing east-central Africa. Above these regions, a drying belt extends into the northern tropic and the overall change in precipitation (wetting

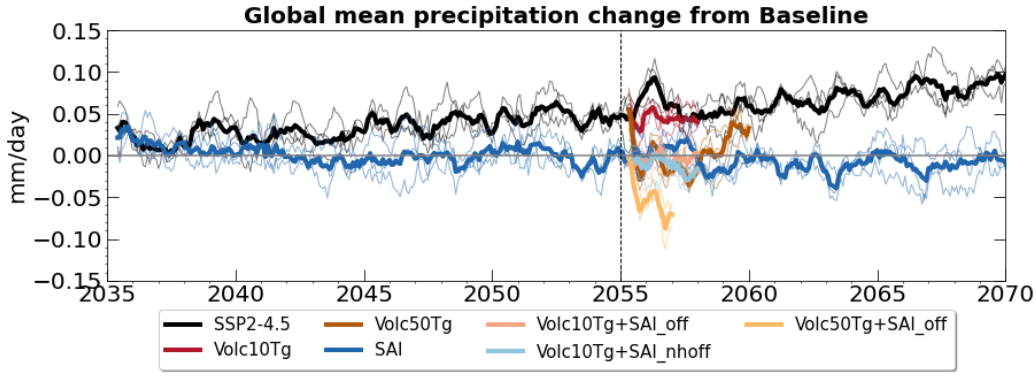

FIGURE 4.5: Time series of the monthly values of the five-month rolling-mean of the globally averaged precipitation change from SSP2-4.5 averaged over the reference period (2020-2039).

plus drying) that is statistically significant involves 29.9% of lands. This percentage decreases to 14.0% when SAI is deployed, and the main difference compared to SSP2.4 is a drying belt over the Indian Ocean below the equator that extends to the tropical South Pacific through Indonesia and northern Australia and no significant changes in the Atlantic Ocean.

The clear response of volcanic eruptions is a decrease in precipitation in the northern tropics and an increase in the southern tropics, with changes that are larger in magnitude and cover wider regions latitudinally and longitudinally depending on the magnitude of the eruption. The fraction of land affected by the change in precipitation (see table in Figure 4.4) and the magnitude of wetting and drying are comparable (medium eruption) or even attenuated (large eruption) when the eruption occurs during SAI compared with that occurring in SSP2-4.5.

The reduction in precipitation in the northern tropic and an increase in precipitation in the southern tropic determine a southward shift of ITCZ. In Figure 4.7, the annual mean position of the ITCZ is calculated as the latitude around the equator where the meridional mass stream function at 500 hPa changes sign, and the shift is calculated compared to the ITCZ position in Baseline, which is the mean value of the ITCZ position in SSP2-4.5 over the reference period (2020-2039).

The ITCZ position undergoes a southward shift in both SSP2-4.5 and SAI, and keeps moving southward in SSP2-4.5 with a rate of 0.2°/decade from 2040 while is almost constant in SAI (0.02°/decade). The displacement is larger in SSP2-4.5 with a 30-year mean (2040-2069) of -0.7±1.5 degrees and smaller in in SAI, with -0.1±1.3 degrees, but the differences between the two simulations are not statistically significant. For volcanic eruptions, with or without SAI, the decrease in T_1 about a year after the eruption results in a southward ITCZ shift, the magnitude of which increases with respect to the change in T_1 but with a no strong linear correlation.

One year after the eruption, the ITCZ displacement from Baseline is at its maximum for all simulations with volcanic eruptions. The ITCZ shift is -4.4° in Volc10Tg and decreases to -3.0° in Volc10Tg+SAI_off and further to -2.6° in Volc10Tg+SAI_nhoff.

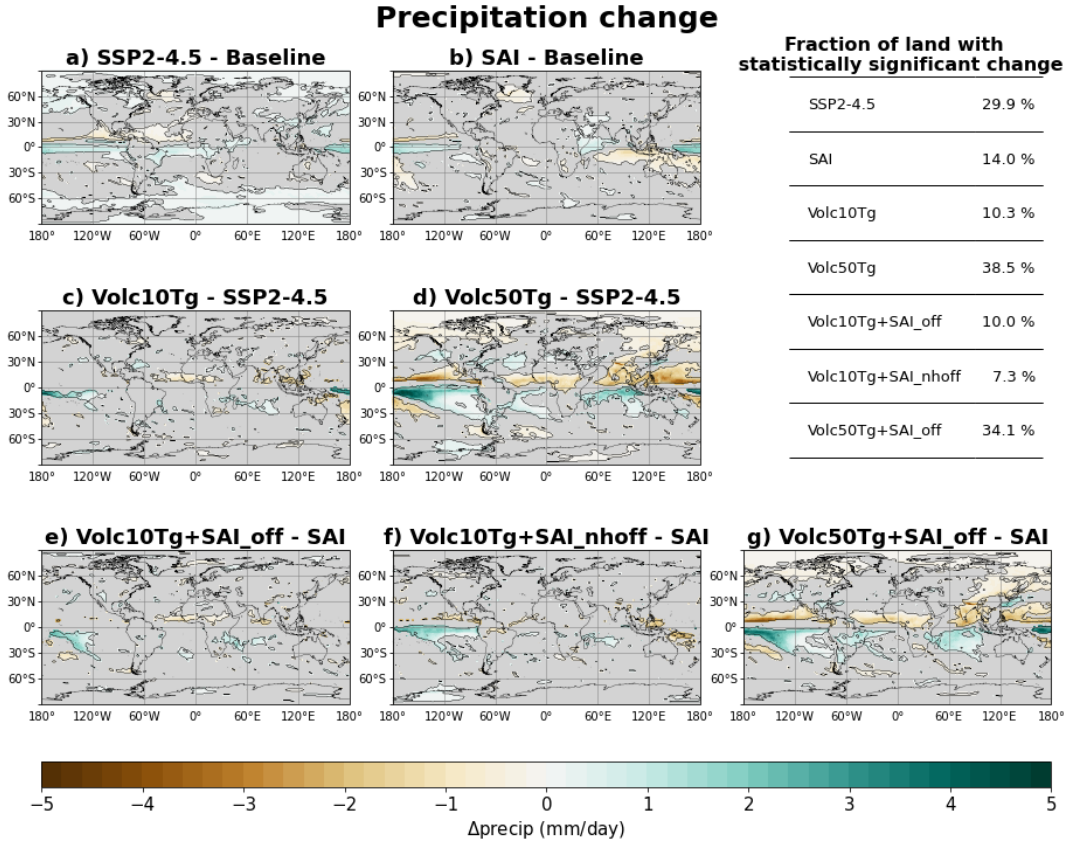

FIGURE 4.6: Maps statistically significant change of precipitation from different background simulation based on the considered simulation. Gray areas are the region where the differences are non statistically significant at the 5% significance level. (a, b) show the precipitation change in SSP2-4.5 and SAI averaged over 2050-2069 from Baseline (SSP2-4.5 averaged over 2020-2039) and the statistics are calculated over all the simulation years for the three ensemble members. (c, d) as (a, b) for Volc10Tg and Volc50Tg averaged over 2055-2056 from the 20-years average in SSP2-4.5. (e-g) as (a, b) for Volc10Tg+SAI_off, Volc10Tg+SAI_nhoff and Volc50Tg+SAI_off averaged over 2055-2056 from the 20-years average in SAI.

Similarly, the ITCZ shift is larger in Volc50Tg with -8.2° and decrease to -7.3° Volc50Tg+SAI_off. When compared with the corresponding background simulation, the ITCZ response, is smaller in case the eruption occurs under non-SAI background than under SAI, however, the ITCZ shift from the Baseline is smaller when the eruption occurs under a SAI.

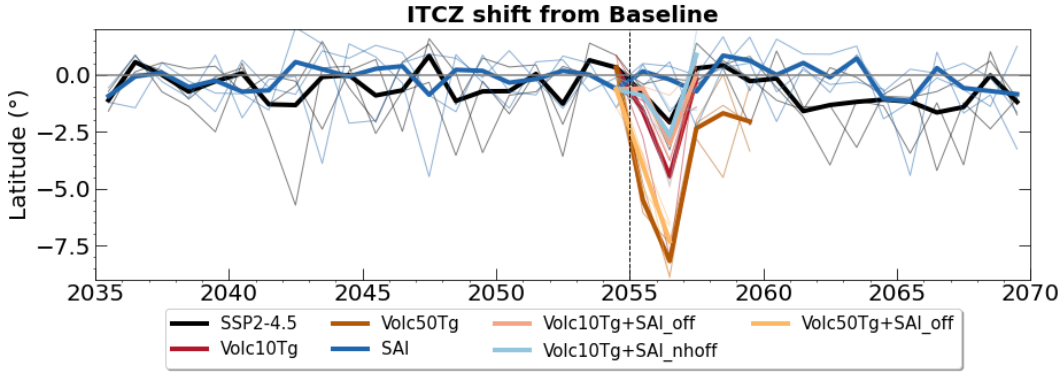

FIGURE 4.7: Time series of annual mean of the ITCZ shift with respect to ITCZ position in Baseline, calculated as the average position of the ITCZ in SSP2-4.5 over the reference period (2020-2039).

4.4 Discussion and conclusion

If SAI is ever deployed, it is extremely likely that it would have to be maintained over many decades (Baur et al., 2023): it is therefore also extremely likely that, given the frequency of large-magnitude volcanic eruptions (about 1 every 50-60 years (Schmidt et al., 2018)), at least one would happen during a deployment, underscoring the importance of assessing the combined effects of the two.

In particular, the increased sulfate loading in the stratosphere after a volcanic eruption rich in sulfur may result in a strong and asymmetric surface cooling, which would in turn affect the hydrological cycle. A further increase of sulfate loading in the stratosphere after a volcanic eruption under SAI could result in an asymmetric surface cooling with effects on the hydrologic cycle and in a decrease in the scattering efficiency of sulfate aerosols, due to the competitive processes of formation of smaller fresh particles or growth of particles formed through condensation.

Here we consider the injection of 10 and 50 Tg of SO_2 at the location of Mount Pinatubo (15.1°N, 120.4°E) on January 1, 2055 during an SAI deployment where multiple injection locations and amounts are varied yearly in order to maintain the global mean near-surface air temperature and its inter-hemispheric and equator-to-pole gradients at levels corresponding to 1.5 K above preindustrial: furthermore, together with analyzing cases where all SAI is stopped, we also consider a case where the injection strategy is modified, but not completely stopped, in order to avoid interhemispheric imbalances.

Other differences from previous work concern the SAI strategy in terms of injection location, here by injecting at 15°S/N in addition to 30°S/N, and the SO_2 injection rate that is adjusted in order to maintain the global mean near-surface air temperature and its inter-hemispheric and equator-to-pole gradients at levels corresponding to 1.5 K above the preindustrial. In the period close to the eruption (2054-2056), the SO_2 injection rate is about 7.5 Tg, including 5.5 Tg in SH and 2 Tg in NH, compared with the constant rate of 16 Tg of SO_2 in Laakso et al. (2016).

The decrease of the hemispherical and land-ocean thermal contrast due to the overcooling of one hemisphere weakens the cross-equatorial flow, consequently shifting the ITCZ position, causing drying and wetting of the climatological wet and dry regions, respectively (Haywood et al., 2013; Iles and Hegerl, 2014; Zuo, Zhou, and Man, 2019). In background conditions, the two tropical eruptions in the Northern Hemisphere mainly increase the sAOD in the respective hemisphere, amplified by the fact that in this case the eruption occurs in the boreal winter, when the upper branch of the BDC is directed toward the winter hemisphere. The use of four injection latitudes allows us to interrupt SAI only at select latitudes in order to compensate for the asymmetric enhancement of the stratospheric aerosol layer, depending on the magnitude of the perturbation.

To limit the risks associated with overcooling of a single hemisphere, we decided to interrupt SAI in the hemisphere where the eruption occurs to reduce the changes in T_1 and T_2. For the upper limit case, maintaining injection in the southern hemisphere would not compensate for the hemispheric asymmetry in stratospheric aerosol loading, and increasing injection in the southern hemisphere to compensate for it would have a drastic impact on global temperature and precipitation. Therefore, we interrupt the injections everywhere, although the magnitude of SAI is small compared to the 50 Tg eruption, therefore it would probably not matter in either case.

In agreement with the findings Laakso et al. (2016), we found the eruption radiative impact of SAI and volcanic eruption is not additive, producing global surface cooling and precipitation reduction that is smaller when the eruption occurs in a geoengineering background than in a non-geoengineering background, and microphysical-related issues cause pre-eruption conditions to be recovered faster for a volcanic eruption under SAI conditions Laakso et al. (2016). However, in our simulations, both temperature and precipitation patterns are similar among volcanic simulations, and differences are in the magnitude and size of regions with statistically significant changes.

All volcanic eruption cases mainly cool the hemisphere in which occur and result in a global mean cooling that is about 0.2 K lower when the eruption occurs in a geoengineered background for both lower and upper-limit eruptions. The cooling contribution by a lower and upper-limit eruption occurring during SAI would further decrease the global mean temperature change in SAI compared to pre-industrial

levels by a maximum between 22.1% and 82.4%, respectively, with the largest perturbation involving the Arctic region. In a non-geoengineerd background a warming of the southern oceans is observed after the eruptions, a warming of the southern oceans is observed after all eruptions and in a geoengineerd background also a warming over the southern continents when SAI is interrupted everywhere for the lower-limit eruption. While for the eruption of 10 Tg of SO_2 the stratospheric sulfate load in the SH decreases below the respective background values, the eruption of 50 Tg of SO_2 also increases the sulfate load in the SH with values similar to those of SAI at least for the 2 years following the eruption, which is the reason why the same warming is not observed on lands.

As with the temperature, the decrease in global precipitation due to a volcanic eruption is on average, in the 2 years following the eruption, about 0.02 mm/day lower when the eruption occurs in a geoengineering background. In all eruption simulations the regional response of precipitation results in a decrease in the northern tropics and an increase in the southern tropics, which in turn determines a southward shift of the ITCZ. The magnitude of drying and wetting of the climatological wet and dry regions and the size of regions where the changes are statistically significant increases for larger eruptions, and changes under SAI are comparable or even attenuated than under a non-SAI background. Despite the similarity among the precipitation patterns, the exact lcoation of drying and wetting regions results in a larger displacement of the ITCZ when eruption occurs under geoengineering conditions. However, the deployment of SAI allows to keep the ITCZ constant in time, within its variability, from the current position (average position over the period 2020-2039), reducing the overall displacement when concurrent eruption occurs.

We found that, overall, the climate risks posed by a large volcanic eruption during SAI are no worse than under background conditions. For eruptions occurring in the SH, we can similarly optimize the SAI strategy and find a latitudinal precipitation change opposite to that observed for NH eruptions and a different latitudinal of temperature change, especially in the Arctic, but with similar consideration when comparing results between SAI and non-SAI conditions.

Chapter 5

Conclusions

This thesis has explored the consequences of the perturbation of the stratospheric aerosol layer as a result of natural events or deliberate interventions. The stratospheric aerosol layer consists mainly of sulfate particles formed from the photolysis of the long-lived COS species after entering the stratosphere, under background conditions, and by direct injections of SO_2 after explosive volcanic eruptions. The global cooling observed after the explosive volcanic eruptions (Robock and Mao, 1995; Canty et al., 2013), suggested the hypothesis of mimicking volcanic eruptions with sustained injections of SO_2 as a climate intervention to counteract global warming
(Crutzen, 2006). The study of climate interventions, and stratospheric aerosol injection in particular, consist of a vast amount of modeling studies that have shown some broad areas of agreement, but also large discrepancies in the evolution in time and space of the aerosol cloud after geoengineering interventions even within the same model, if the spatial resolution and microphysical schemes are changed (Visioni et al., 2021; Tilmes et al., 2022; Weisenstein et al., 2022; Laakso et al., 2022). The analogy between climate engineering experiments and large volcanic eruptions has highlighted the possibility of testing the reliability of climate models by comparing them with measurements from volcanic eruptions, of which Mount Pinatubo in June 1991 is the best observed one.

In Chapter 2, we present the results of a model inter-comparison study on Mt. Pinatubo eruption in June 1991, based on the original paper Quaglia et al. (2023). The study follows the prescriptions of the Historical Eruptions SO_2 Emission Assessment experiments which is part of the Interactive Stratospheric Aerosol Model Intercomparison Project (Timmreck et al., 2018). Six global models with interactive aerosol microphysics (ECHAM6-SALSA, EMAC, ECHAM5-HAM, SOCOL-AERv2, ULAQ-CCM and UM-UKCA) performed different simulations of the eruption to explores the uncertainties related to the initial SO_2 emission by varying the amount of injected SO_2 (ranging between 5 and 10 Tg-S), and injection altitude (between 18-25 km). Comparison with several satellite and balloon-borne observations shows that simulations in which more than 5 Tg-S of SO_2 are injected overestimate the initial

sulfate burden in the tropics and, in some models, in the northern hemisphere, followed by a more rapid reduction from the sulfate-burden peak in the tropical stratosphere. The shorter e-folding time in the models than in the observations is related to stronger transport towards the extratropics in the Northern Hemisphere at the expense of the observed tropical confinement, suggesting a much weaker subtropical barrier in all models. Furthermore, the higher surface density a few months after the eruption compared with values measured in the tropics and in-situ measurements over Laramie draws attention to the importance of including processes such as ash injection for removal of initial SO_2 and aerosol lofting through local heating.

Because of the discrepancies discussed above, in Chapter 3 we propose a pilot study based on the original paper Quaglia et al. (2022) on the increased surface emission of carbonyl sulfide among the SAI strategies proposed so far, which we recommend to be tested further with other climate models. We ran two experiments with the ULAQ-CCM model from 2021 to 2055 on increasing of COS emissions, assuming an artificial global COS flux of 40 Tg-S/yr (SG-COS-SRF), geographically distributed according to current anthropogenic COS emissions at the surface and the injection of 6 Tg-S/yr of COS into the tropical upper troposphere (SG-COS-TTL). Results are discussed in comparison with the more common SAI strategy consisting in the injection of 4 Tg-S/yr in the form of SO_2 at the equator (SG-SO_2), between 18 and 25 km of altitude. The amount of COS and SO_2 emitted per year are chosen in order to obtain the same global sulfate aerosol optical depth ($\sim \Delta\tau$=0.080 in years 2046-2055) for the three experiments as a common reference to discuss the differences on aerosol microphysical properties, surface SO_x deposition, radiative forcing and effects on ozone. The convenience of intervening directly at the surface with SG-COS-SRF compared with using aircraft to bring sulfate to the lower stratosphere (SG-COS-TTL and SG-SO_2) involves the use of more COS, which would result in more SO_x deposition at the surface (+8.9 % for SG-COS-SRF vs. +3.3 % for SG-COS-TTL +4.2 % for SG-SO_2). The resulting net radiative forcing (RF), which includes indirect effects on ozone, methane, and stratospheric water vapor, is -1.3 W/m^2 for SG-COS-SRF and -1.5 W/m^2 for SG-COS-TTL, and is comparable to the corresponding RF of -1.7 W/m^2 obtained in SG-SO_2, but with a more latitudinally uniform forcing for SG-COS experiments than for SG-SO_2, which is mainly concentrated in the tropics. Significant changes for stratospheric ozone are found in both SG-COS experiments with respect to SG-SO_2 ($\sim$5 DU versus +1.4 DU, globally). According to the model results, the resulting UVB perturbation at the surface accounts for -4.3% as a global-annual average (versus -2.4% in the SG-SO_2 case), with a springtime Antarctic decrease of -2.7% (versus a +5.8% increase in the SG-SO_2 experiment). Overall, we find that an increase in COS emissions may be feasible as an alternative to stratospheric SO_2 injections in the context of SRM, however, our assumption that the rate of COS uptake by soils and plants does not vary with increasing COS concentrations will need to be investigated in future works, and more studies are needed on the prolonged exposure effects to higher COS values in humans and ecosystems.

The spatial and size distribution of aerosol for SO_2 injections can be partially managed by the combination of different latitudes and altitudes for injection to optimise the climate impact Tilmes et al. (2017) and MacMartin et al. (2017). In Chapter 4 we consider an SAI experiment performed with CESM2(WACCM6) consisting of the continuous injection of SO_2 at four latitudes (30°N, 15°N, 15°S) with the aim to to maintain the global mean temperature 1.5 K above the pre-industrial and mantain the interhemispheric temperature gradient and equator-to-pole temperature gradient which control the precipitation patterns. The focus of this work is the hydrological impact of further increasing the stratospheric aerosol layer due to volcanic eruptions occurring during SAI deployment. We simulate two large volcanic eruptions consisting of the injection of 10 Tg and 50 Tg of SO_2 at the location of Mt. Pinatubo (15.1°N, 120.4°E) on January 1, 2055, both under background conditions and during SAI. We find a global decrease in surface temperature followed by a global decrease in precipitation that is not linearly dependent on the amount of SO_2 injected, and the non-additivity of volcanic eruptions and SAI results in changes in the wet and dry climatological region and the shift in the ITCZ that are comparable or even smaller when the eruption occurs during SAI than when it occurs under background conditions. Therefore, overall, the risks of a large volcanic eruption occurring during SAI are no worse than under background conditions.

Appendix A

Supplementary material: Interactive stratospheric aerosol models' response to different amounts and altitudes of SO2 injection during the 1991 Pinatubo eruption

A.1 Analysis of model output

A.1.1 Taylor Diagrams

In section 3.1 we use Taylor diagrams (Taylor, 2001) in order to summarize all the information regarding the reproducibility of the stratospheric optical depth simulated compared to satellite observations. Taylor diagrams provide a concise statistical summary of how well patterns from simulations and observations match each other in terms of their correlation (COR, azimuthal angle), their root-mean-square difference (RMSD, proportional to the distance between the observations - grey and black circles on the x axis- and experiments - colored circle), and the ratio of their variances (SDs on x and y axis). SDs, RMSs and CORs are calculated for zonal values of the stratospheric AOD for two different time periods (first year and second year after the eruption). Therefore, similar STD, higher COR and lower RMSD mean similar amplitudes of variation in terms of latitudinal distribution and time evolution.

A.1.2 Effective radius

The effective radius is calculated as the ratio of the third and second moments of the number size distribution of the aerosol particles. This results in Eq. A.1 for models with a sectional scheme; in this case, the sum is over the bins and n_i is the number

of particles and r_i is the radius of particles in each bin. In models with a modal scheme, the effective radius is calculated as the sum over the modes as in Eq. A.2, where SAD_i is the surface area density and vol_i is the volume density. In EMAC (modal scheme) the quantity is estimated from the median radii for accumulation and coarse mode particles since it was not stored in the output.

$$reff = \frac{\sum_i n_i \cdot r_i^3}{\sum_i n_i \cdot r_i^2} \tag{A.1}$$

$$reff = \frac{3 \cdot \sum_i voli}{\sum_i SADi} \tag{A.2}$$

The stratospheric effective radius ($reff_{strat}$) for the models and SAGE II is calculated in Eq. A.3 by integrating the provided effective radius (reff) from the tropopause to the top of the atmosphere weighted with the SAD. The thickness of the vertical layer (h) is calculated from the hypsometric equation (Eq A.4)

$$reff_{strat} = \frac{\sum_z (SAD \cdot h \cdot reff)_z}{\sum_z (SAD \cdot h)_z} \tag{A.3}$$

$$h = \frac{R \cdot T}{g} \cdot \ln \frac{P_{z+1}}{P_z} \tag{A.4}$$

For the OPC measurements, we calculate the stratospheric effective radius (Eq. A.5) as in Kleinschmitt et al., 2017 for the updated UWv2.0 data set. The measurement error bars consider a 40% uncertainty in SAD and vol and assume a correlation coefficient of 0.5 between SAD at different altitudes, vol at different altitudes and SAD and vol at the same altitude.

$$reff_{strat} = \frac{3 \cdot \sum_z vol_z}{\sum_z SAD_z} \tag{A.5}$$

A.2 Tables

TABLE A.1: Models overview

Model	Horizontal resolution (lat x lon)	Vertical resolution (model top, # levels)	Reference
ECHAM6-SALSA	1.9 1.9T63)	0.01 hPa, 95 levels	Kokkola et al. (2018) and Laakso et al. (2017)
ECHAM5-HAM	2.8 2.8T42)	0.01 hPa, 90 levels	Niemeier et al. (2009) and Toohey et al. (2013b)
EMAC*	1.91.9T63)	0.01 hPa, 90 levels	Jöckel et al, (2010), Brühl et al. (2018)
SOCOL-AERv2	2.8 2.8T42)	0.01 hPa, 39 levels	Sheng et al. (2015) and Sukhodolov et al. (2018)
ULAQ-CCM	5 6T21)	0.04 hPa, 126 levels	Pitari et al. (2016) and Visioni et al. (2018)
UM-UKCA	1.25 1.875N96)	80 km, 85 levels	Marshall et al. (2019) and Dhomse et al. (2020)

* highlights models with spatially distributed SO_2 injections.

A.3 Figures

TABLE A.2: Peak value of the global stratospheric sulfate burden (in Tg-S), month in which it is reached since January 1991 and e-folding time for each model and experiment.

	Low-22km			Med-22km			High-22km			Med-19km			Med-18-25km		
Model	Peak	Month	e-fold	Peak	Month	e-fold	Peak	Month	e-fold	Peak	Month	e-fold	Peak	Month	e-fold
ECHAM6-SALSA	4.8	10	10	6.7	10	11	9.5	11	12	6.1	10	9	6.7	10	13
ECHAM5-HAM	5.0	12	11	7.0	12	10	9.9	12	9	6.0	10	11	6.5	11	11
EMAC*				7.0	9	8									
SOCOL-AERv2	4.8	10	14	6.6	10	13	9.4	10	13	5.4	9	13	6.6	10	14
ULAQ-CCM	5.0	11	13	7.0	11	13	9.8	11	12	6.6	11	10	6.9	11	13
UM-UKCA	4.2	11	21	5.9	11	19	8.4	11	18	5.4	10	14	5.7	11	17
UM-UKCA*	4.2	11	23	6.0	11	21	8.6	11	20	5.3	10	15	5.6	11	19

* highlights models with spatially distributed SO_2 injections.

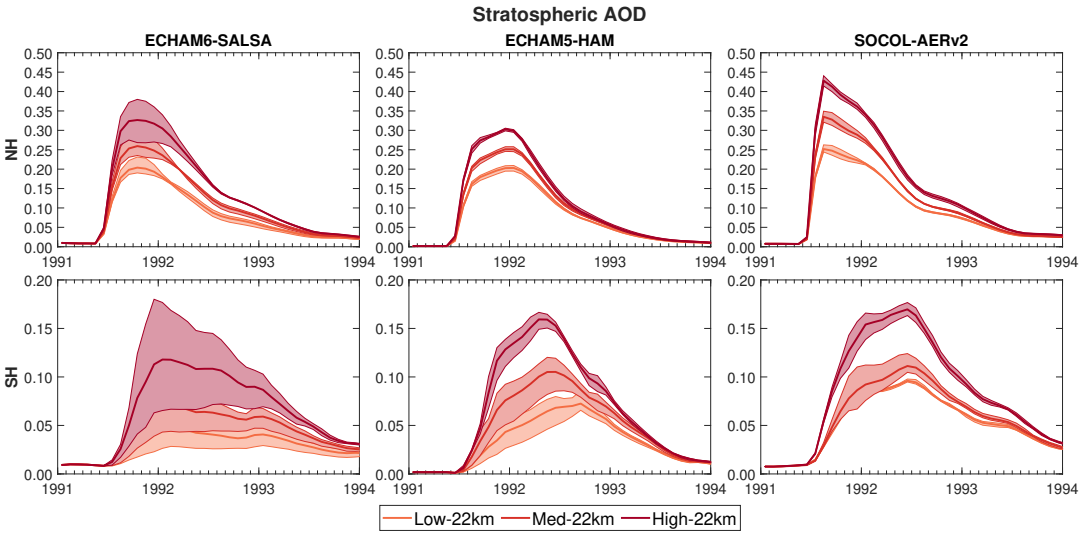

FIGURE A.1: Time evolution of the stratospheric AOD in the northern (NH) and southern hemisphere (SH) simulated by ECHAM6-SALSA, ECHAM5-HAM and SOCOL-AERv2 for the experiments with different amounts of SO_2 injected at about 22 km altitude. The thick line represents the ensemble mean, the shaded area the region between the minimum and maximum values between the ensemble members (thin lines).

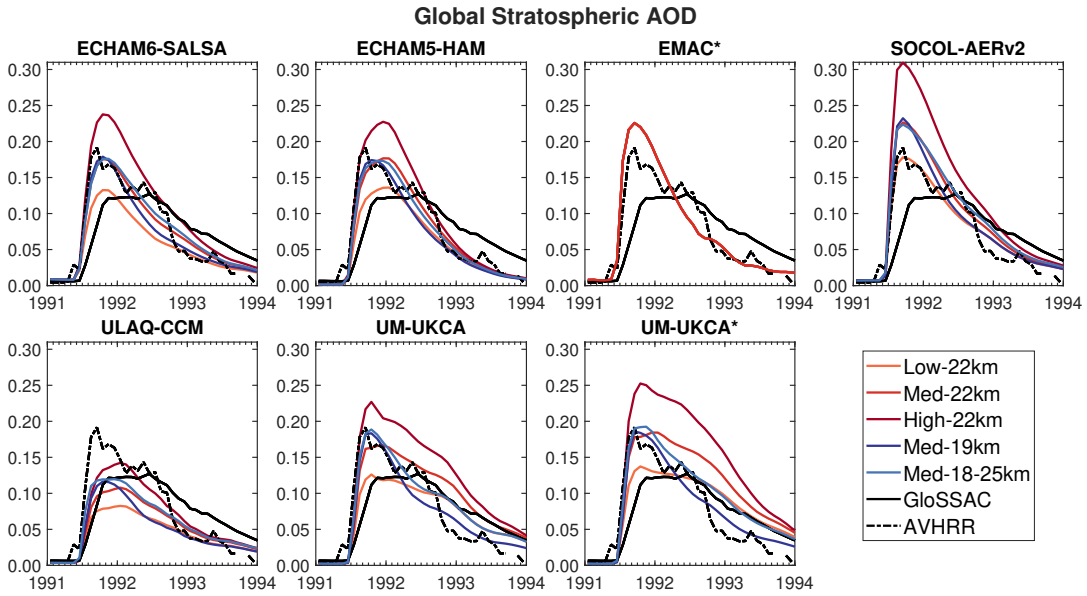

FIGURE A.2: Temporal evolution of monthly global stratospheric AOD values. Each panel refers to the respective model in which the results of the different experiments (coloured lines) are compared with GloSSAC and AVHRR measurements (black lines). * Models with spatially spread SO_2 injections.

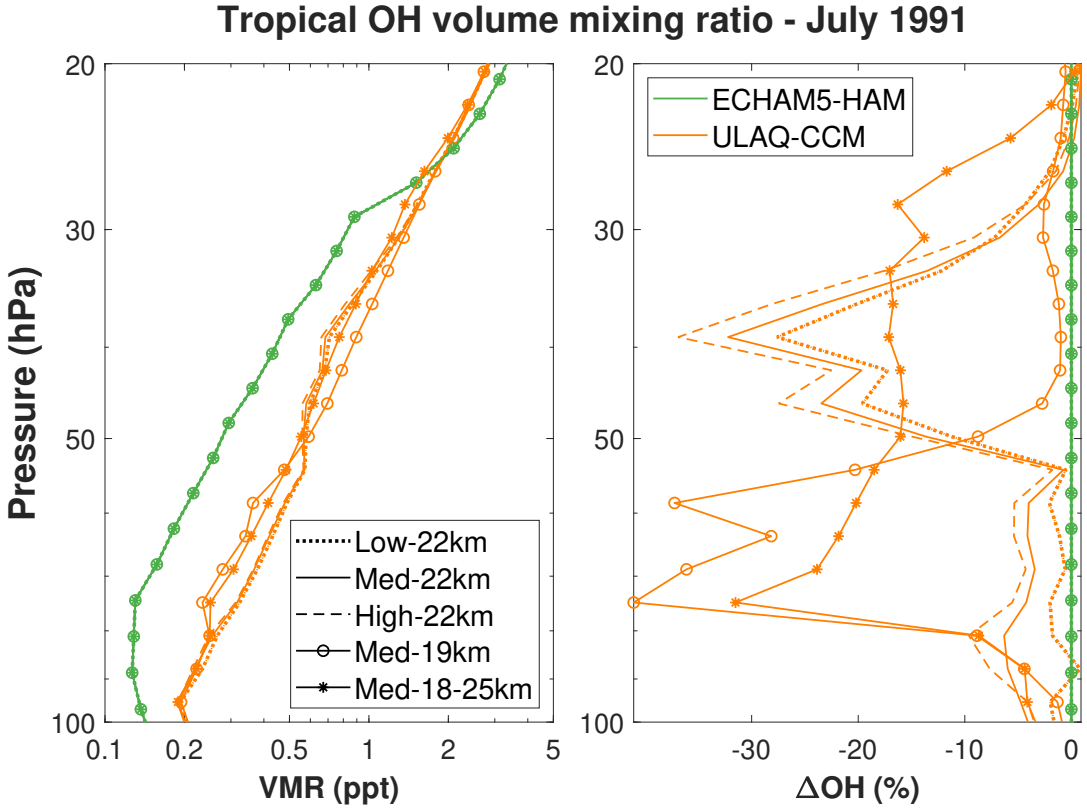

FIGURE A.3: Vertical distribution of OH mixing ratio in July 1991 and its change from the background conditions (July 1991 without eruption) in ECHAM5-HAM (prescribed OH) and ULAQ-CCM (interactive OH). Experiments are identified here with different line styles, the different colors refer to the models.

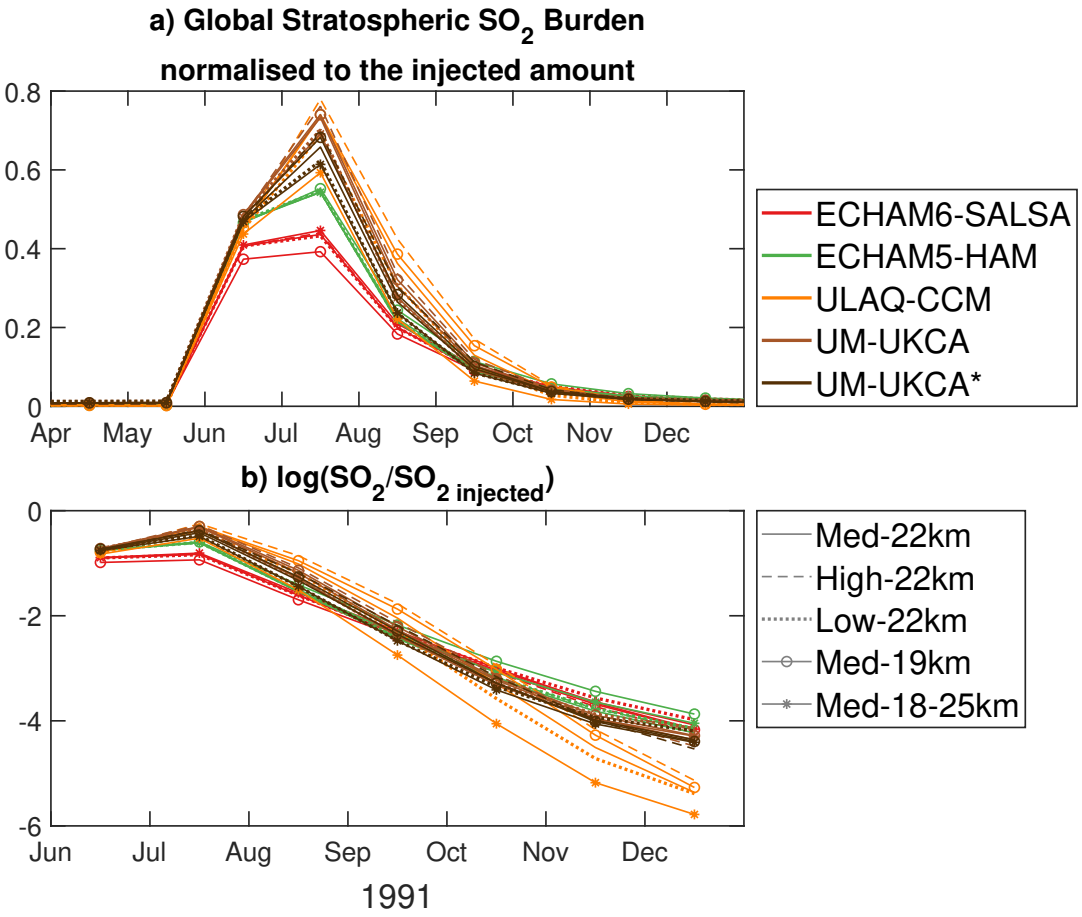

FIGURE A.4: Time evolution of global stratospheric SO_2 burden in Tg-S (a) and logarithm of SO_2 burden divided by the amount of SO_2 injected (b) in all model experiments. The models are identified by the different colours (top legend), the different scenarios by the different line styles (bottom legend). * Models with spatially spread SO_2 injections.

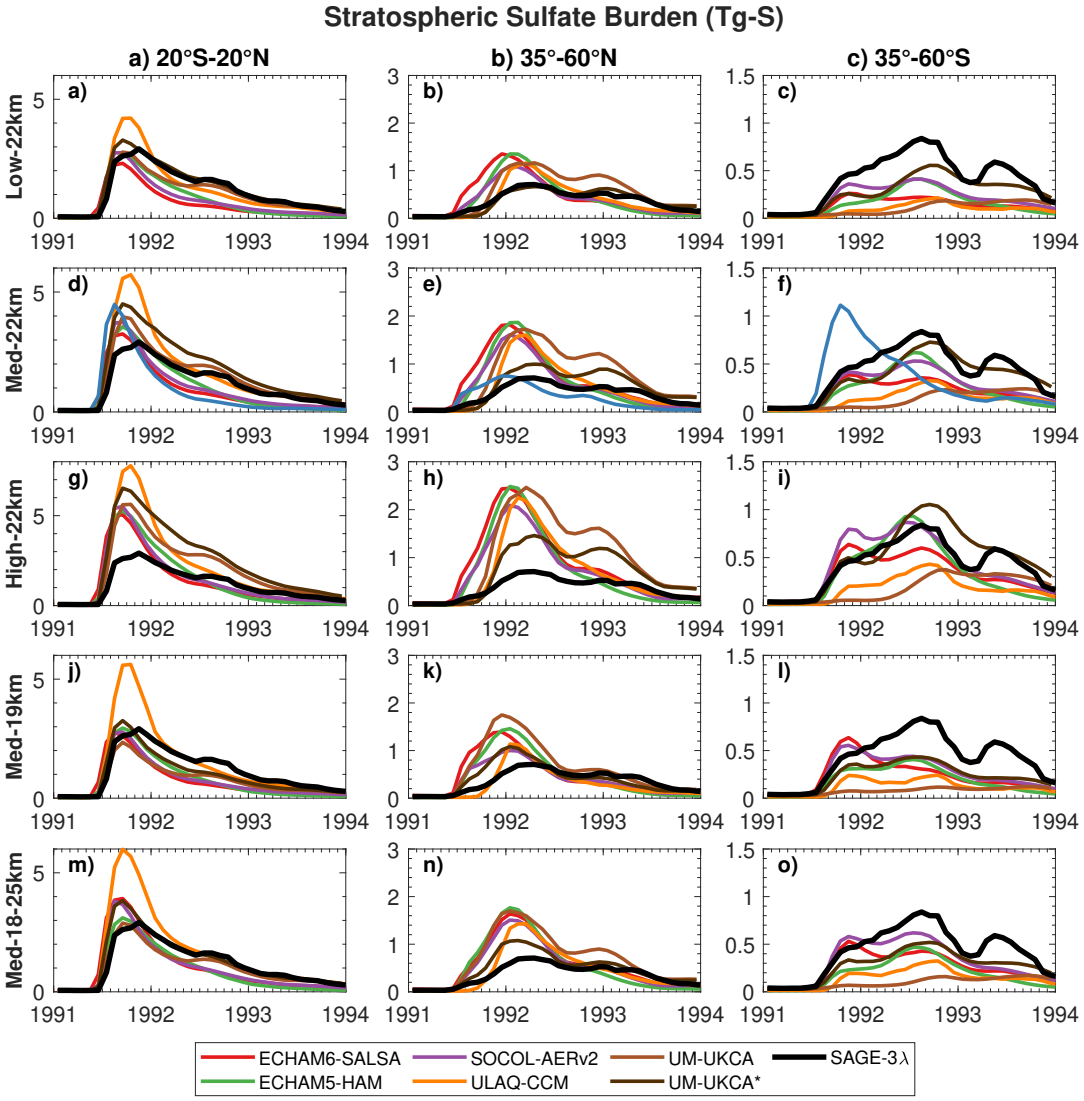

FIGURE A.5: Time evolution of stratospheric sulfate burden in Tg-S in the tropics (first column), in the NH (second column) and SH mid-latitudes (third column) simulated by models and compared with observations. Each row identifies a different experiment.

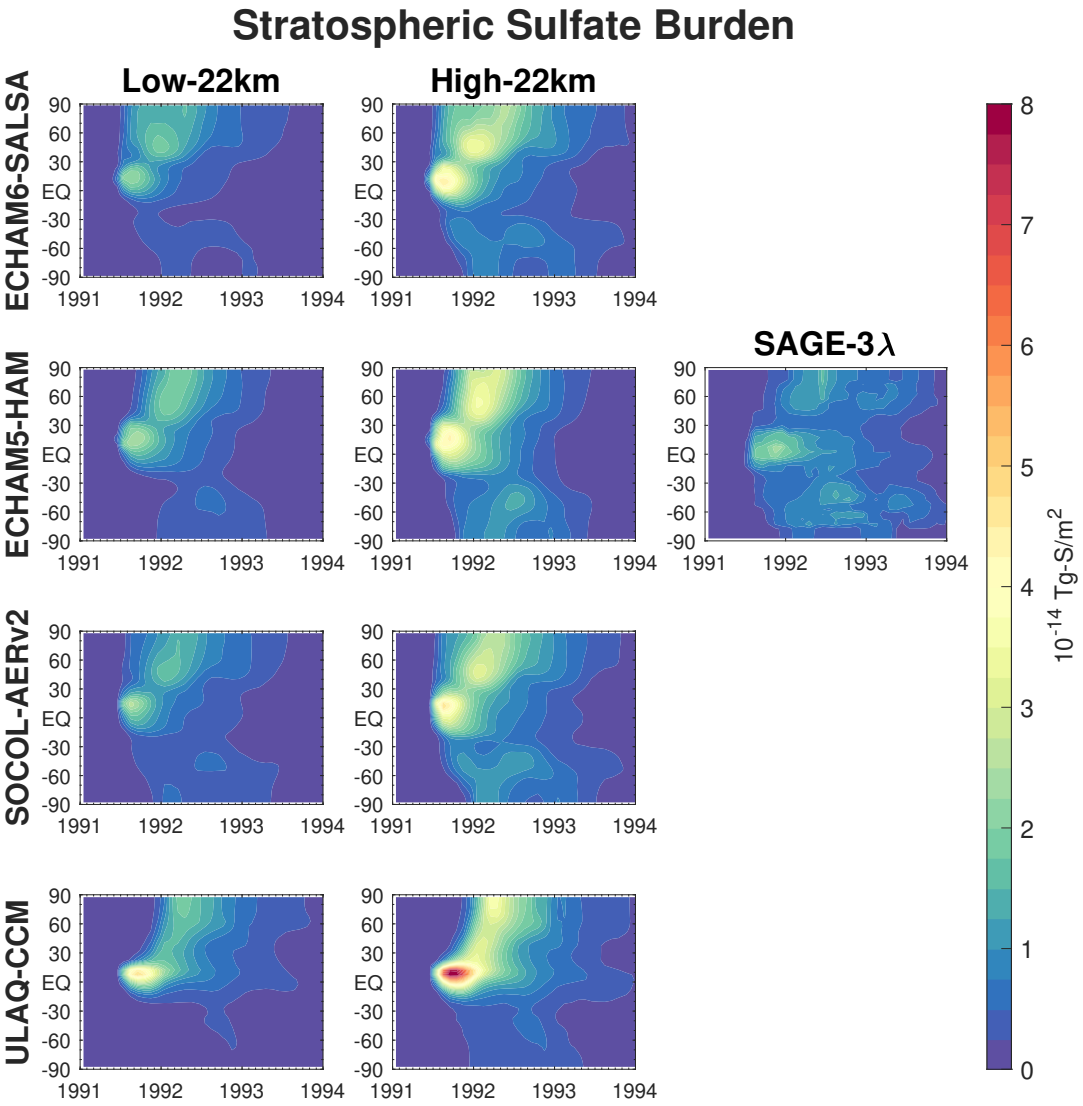

FIGURE A.6: Time evolution of zonal stratospheric sulfate burden (in 10^{-14} Tg-S/m^2) in Low-22km (first column) and High-22km (second column) for all models, and zonal stratospheric sulfate burden of SAGE-3λ (third column).

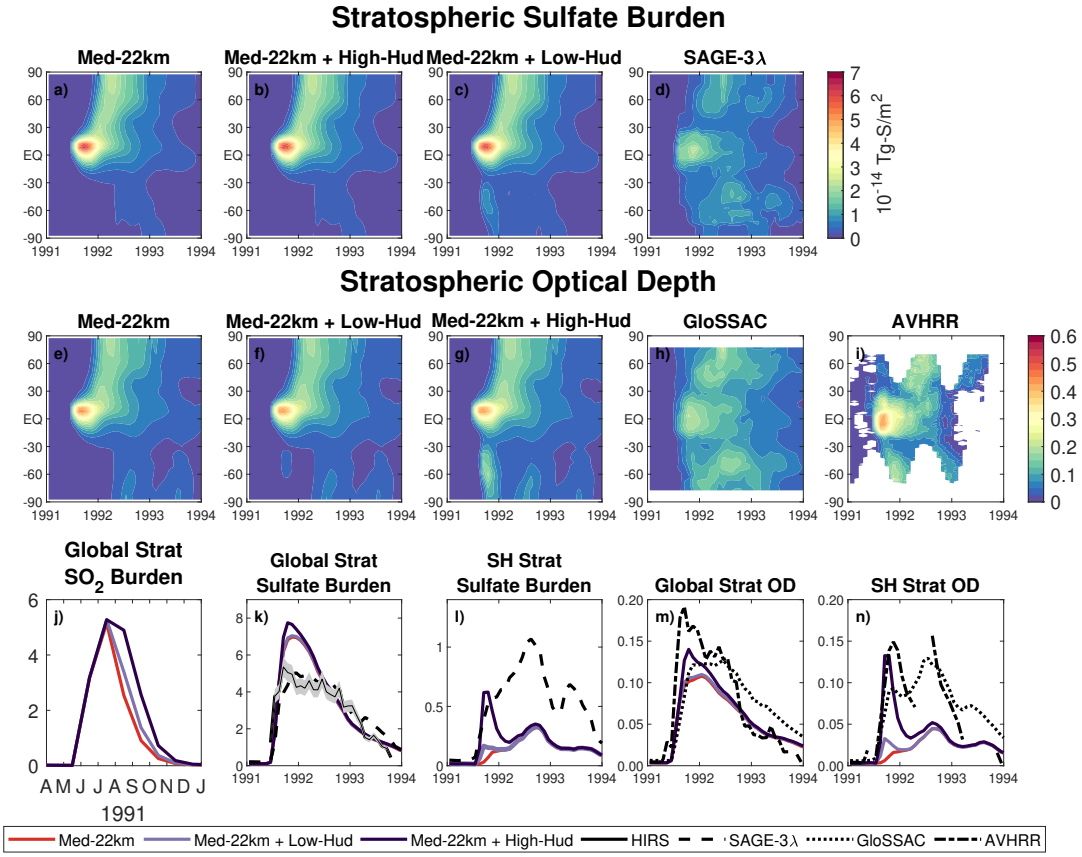

FIGURE A.7: Time evolution of zonal stratospheric sulfate burden (in 10^{-14} Tg-S/m^2) and optical depth (first and second row, respectively) for Med-22km (a, e), Med-22km with Cerro Hudson lower-end emission (b, f) and with the upper-end emission (c, g). Observations for stratospheric sulfate burden are form SAGE-3λ (d), and for optical depth from GloSSAC and AVHRR (h and i). The third row includes the global mean of stratospheric SO_2 (j), global and SH mean of stratospheric sulfate burden (k and l), global and SH mean of optical depth (m and n) for the same simulations and observations as panels a-i.

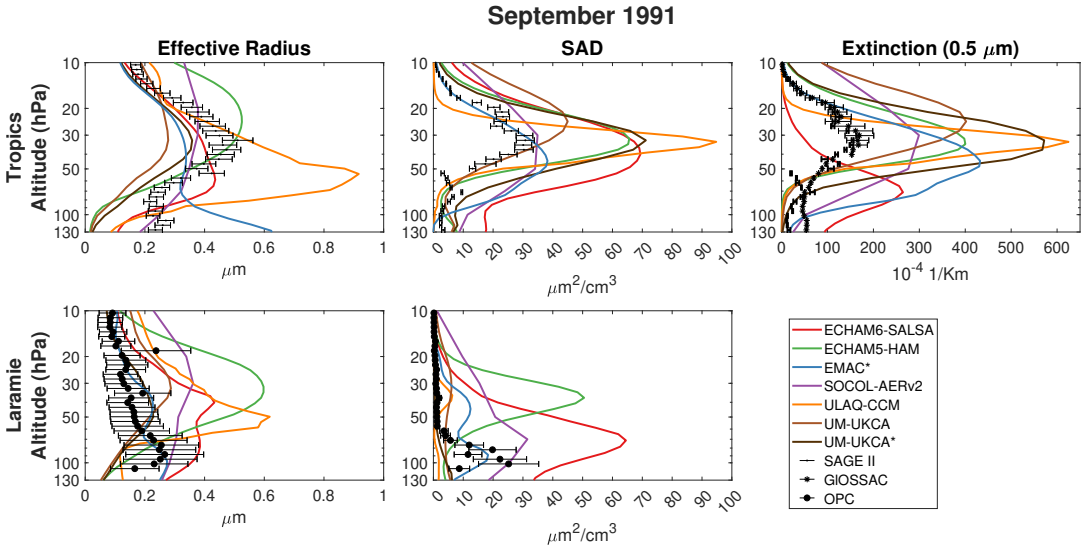

FIGURE A.8: Vertical profile of the effective radius in μm (left panels), surface area density (SAD) in $\mu m^2/cm^3$ (middle panels), and extinction at 0.5 μm in 1/km (right panel) in the tropics (first row) and over Laramie (second row) for Med-22km in September 1991. Model results are compared with SAGE II and GloSSAC in the tropics and with OPC over Laramie. * Models with spatially spread SO_2 injections.

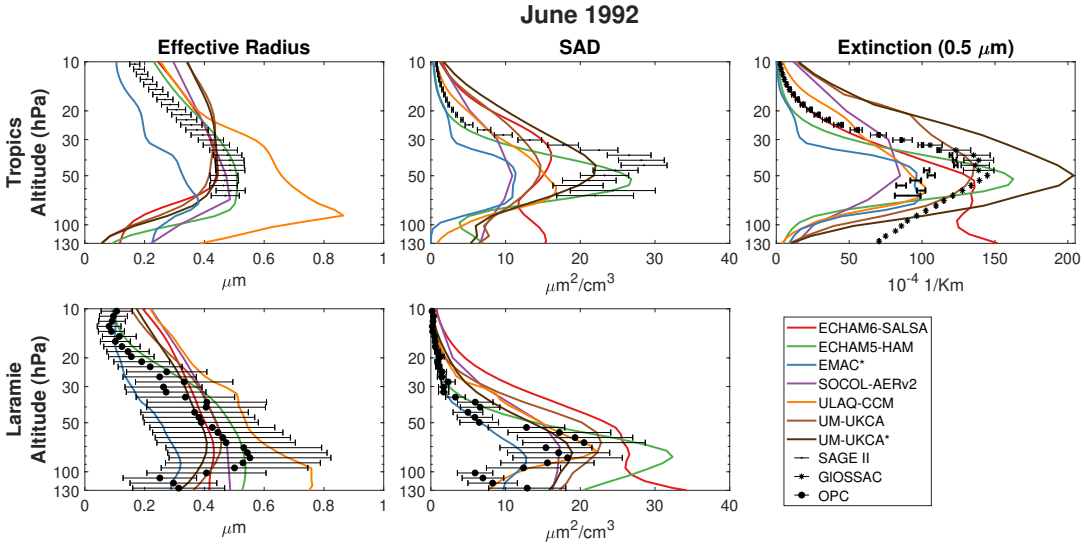

FIGURE A.9: Vertical profile of the effective radius in μm (left panels), surface area density (SAD) in $\mu m^2/cm^3$ (middle panels), and extinction at 0.5 μm in 1/km (right panel) in the tropics (first row) and over Laramie (second row) for Med-22km in June 1992. Model results are compared with SAGE II and GloSSAC in the tropics and with OPC over Laramie. * Models with spatially spread SO_2 injections.

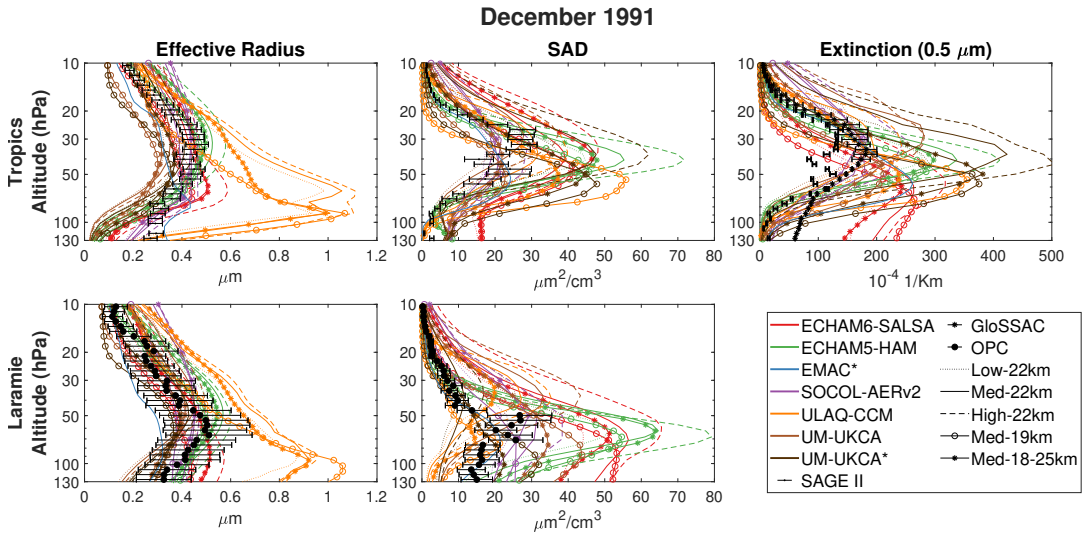

FIGURE A.10: Vertical profile of the effective radius in μm (left panels), surface area density (SAD) in $\mu m^2/cm^3$ (middle panels), and extinction at 0.5 μm in 1/km (right panel) in the tropics (first row) and over Laramie (second row) for all experiments in December 1991. Model results are compared with SAGE II and GloSSAC in the tropics and with OPC over Laramie. Experiments are identified here with different line styles, the different colors refer to the models. * Models with spatially spread SO_2 injections.

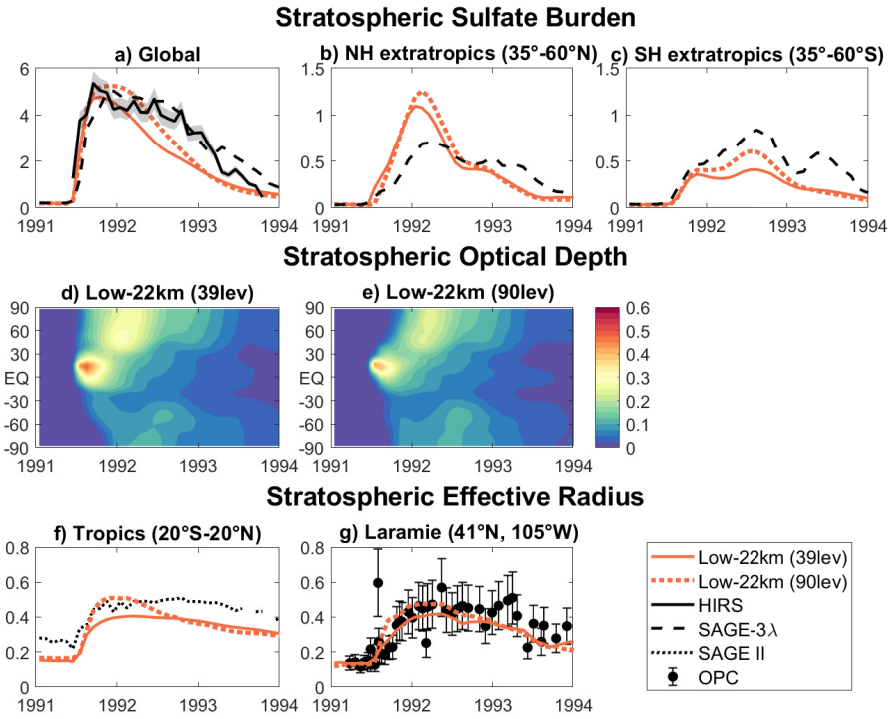

FIGURE A.11: Time evolution of the monthly averages of global stratospheric sulfate burden (a), in extratropical NH, and extratropical SH (c) for Low-22km performed in SOCOL-AERv2 with 39 and 90 vertical levels (light orange lines, different line style) compared with the observations (black lines, different line style). Panels d and e show the time evolution of zonal stratospheric AOD for Low-22km performed in SOCOL-AERv2 with the two vertical resolutions. Panels f and g are the same as panels a-c but for the stratospheric effective radius in the tropics and over Laramie. The legend is common to panels a-c and f-g.

Appendix B

Supplementary material: An approach to sulfate geoengineering with surface emissions of carbonyl sulfide

B.1 Tables

Experiment	Surface upward flux	Chemical production	Surface dry deposition	Chemical loss	Net [sources-sinks]
BG	0.12 ±0.01	0.40±0.01	0.39±0.01	0.13±0.01	0.00±0.01
SG-COS-SRF	40.1 ±0.1	0.39±0.01	31.6 ±0.1	8.8 ±0.1	+0.1 ±0.1
SG-COS-TTL	(0.12+6.0*)±0.1	0.39±0.01	3.5 ±0.1	3.1 ±0.1	-0.1 ±0.1

TABLE B.1: Globally-annually averaged COS sources and sinks (Tg-S/yr) [years 2046-2055]. *Additional flux of COS injected in the tropical upper troposphere.

COS sources	Gg-S/yr	%
Surface flux from oceans	39.8	8.3
Surface anthropogenic flux	76.3	15.8
Chem prod from CS2 ocean sources	76.8	15.9
Chem prod from CS2 anthropogenic sources	117.6	24.4
Chem prod from DMS ocean sources	171.5	35.6

TABLE B.2: Globally-annually averaged COS sources for BG (Gg-S/yr and percent of the total direct surface upward flux and total atmospheric chemical production) [years 2046-2055].

COS sink	Gg-S/yr	%
Dry deposition on soils	125.6	24.1
Surface dry dep on vegetation	252.6	48.5
Chemical loss by OH	102.7	19.7
Chemical loss by photolysis	30.1	5.8
Chemical loss by O	9.7	1.9

TABLE B.3: Globally-annually averaged COS sinks for BG (Gg-S/yr and percent of the total surface dry deposition or total atmospheric chemical loss) [years 2046-2055].

Experiment	DMS	SO_2	SO_4	COS	CS_2	H_2S	Total
BG	25.9	63.7	1.41	0.12	0.88	4.0	96.0
SG-COS-SRF	25.9	63.7	1.41	40.1	0.88	4.0	136.0
SG-COS-TTL	25.9	63.7	1.41	6.1	0.88	4.0	102.0
SG-SO2	25.9	67.7	1.41	0.12	0.88	4.0	100.0

TABLE B.4: Globally-annually averaged sources of sulfur species (Tg-S/yr) [years 2046-2055].

SG-COS-SRF - BG: Sulfate aerosols RF (W/m^2)	SW	LW	NET
Clear sky	-2.49	+0.48	-2.01
Cloud adjustment [background clouds]	+0.81	-0.06	+0.75
Cloud adjustment [cirrus ice thinning]	+0.26	-0.51	-0.25
Cloud adjusted	-1.42±0.12	-0.09±0.25	-1.51±0.13

TABLE B.5: Temperature-adjusted tropopause RF of sulfate aerosols in the SG-COS-SRF case with respect to BG (shortwave, longwave and net) (W/m^2) [years 2046-2055]. First row shows RFs under clear sky conditions. Second and third rows present the cloud adjustment of RFs, separately for the mere presence of background clouds and for the cirrus ice thinning produced in SG conditions (see Kuebbeler et al., 2012; Visioni et al., 2018).

SG-COS-TTL - BG: Sulfate aerosols RF (W/m^2)	SW	LW	NET
Clear sky	-2.49	+0.48	-2.01
Cloud adjustment [background clouds]	+0.80	-0.06	+0.74
Cloud adjustment [cirrus ice thinning]	+0.33	-0.64	-0.31
Cloud adjusted	-1.36±0.16	-0.22±0.26	-1.58±0.13

TABLE B.6: As in Table B.5, but for the SG-COS-TTL case.

SG-SO2 - BG: Sulfate aerosols RF (W/m^2)	SW	LW	NET
Clear sky	-2.72	+0.52	-2.20
Cloud adjustment [background clouds]	+0.80	-0.06	+0.74
Cloud adjustment [cirrus ice thinning]	+0.36	-0.71	-0.35
Cloud adjusted	-1.56±0.10	-0.25±0.23	-1.81±0.13

TABLE B.7: As in Table B.5, but for the SG-SO2 case.

SG-COS-SRF - BG: Greenhouse gases RF (W/m^2)	SW	LW	NET
COS	0.00	+0.17±0.02	+0.17±0.02
CH_4	0.00	+0.12±0.01	+0.12±0.01
H_2O [stratosphere]	0.00	-0.024±0.004	-0.024±0.004
O_3 [stratosphere]	-0.048±0.005	+0.010±0.001	-0.038±0.005
O_3 [troposphere]	0.00±0.01	+0.02±0.01	+0.02±0.01
Total	-0.05±0.01	+0.30±0.03	+0.25±0.03

TABLE B.8: Temperature-adjusted tropopause RF of greenhouse gases in the SG-COS-SRF case with respect to BG (shortwave, longwave and net) (W/m^2) [years 2046-2055]. First five rows present the RF contributions of specific greenhouse gases affected directly and indirectly by SG (*i.e.*, COS, CH_4, stratospheric H_2O, stratospheric and tropospheric O_3. Last row shows the gas net total RF.

SG-COS-TTL - BG: Greenhouse gases RF (W/m^2)	**SW**	**LW**	**NET**
COS	0.00	0.03±0.01	0.03±0.01
CH_4	0.00	+0.12±0.02	+0.12±0.02
H_2O [stratosphere]	0.00	-0.024±0.004	-0.024±0.004
O_3 [stratosphere]	-0.048±0.005	+0.010±0.001	-0.038±0.005
O_3 [troposphere]	0.00±0.01	+0.02±0.01	+0.02±0.01
Total	-0.05±0.01	+0.16±0.03	+0.11±0.03

TABLE B.9: As in Table B.8, but for the SG-SO2 case.

SG-SO2 - BG: Greenhouse gases RF (W/m^2)	**SW**	**LW**	**NET**
COS	0.00	0.00	0.00
CH_4	0.00	+0.11±0.02	+0.11±0.02
H_2O [stratosphere]	0.00	+0.009±0.001	+0.009±0.001
O_3 [stratosphere]	-0.015±0.01	0.00±0.01	-0.015±0.01
O_3 [troposphere]	0.00±0.01	+0.02±0.01	+0.02±0.01
Total	-0.02±0.01	+0.14±0.02	+0.12±0.02

TABLE B.10: As in Table B.8, but for the SG-SO2 case.

B.2 Figures

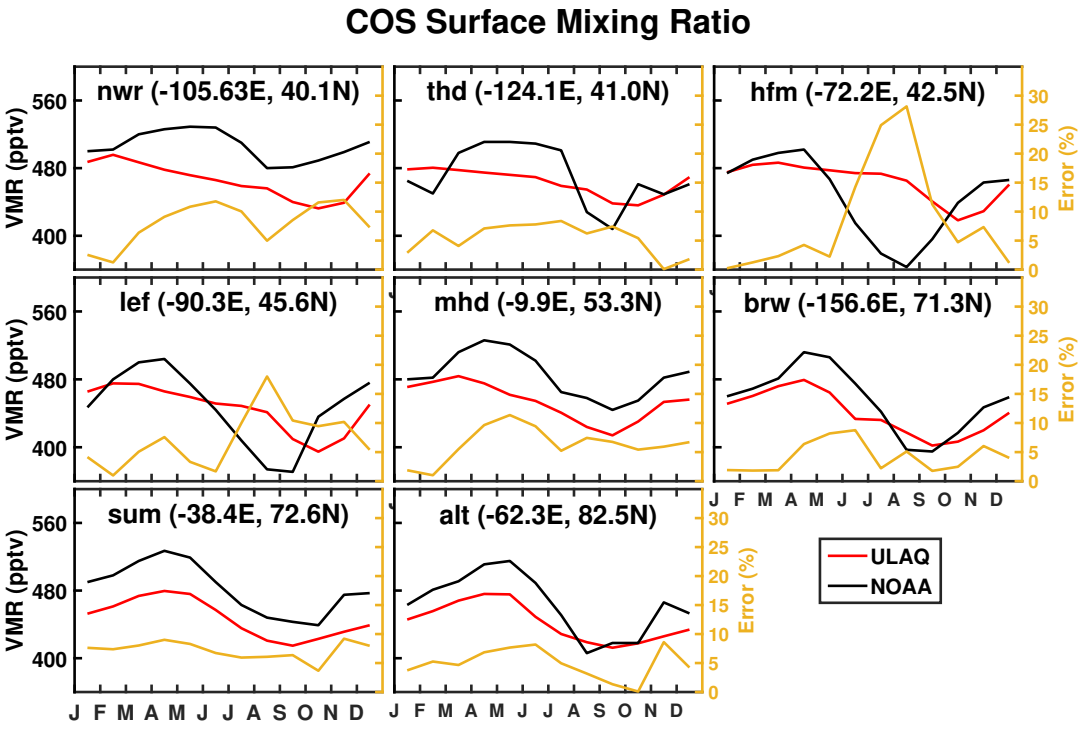

FIGURE B.1: COS surface mixing ratio (in pptv, left axis) evaluation at NOAA stations: NWR: Niwot Ridge, United States; THD: Trinidad Head, United States; HFM: Harvard Forest, United States; LEF: Wisconsin, United States; MHD: Mace Head, Ireland; BRW: Barrow, United States; SUM: Summit, Greenland; ALT: Alert, Canada. Red line is the COS surface mixing ratio averaged over 2046-2055 as calculated by ULAQ-CCM, black line is the NOAA observations in 2006. On the right axis, we report the absolute difference (in %) between the two lines.

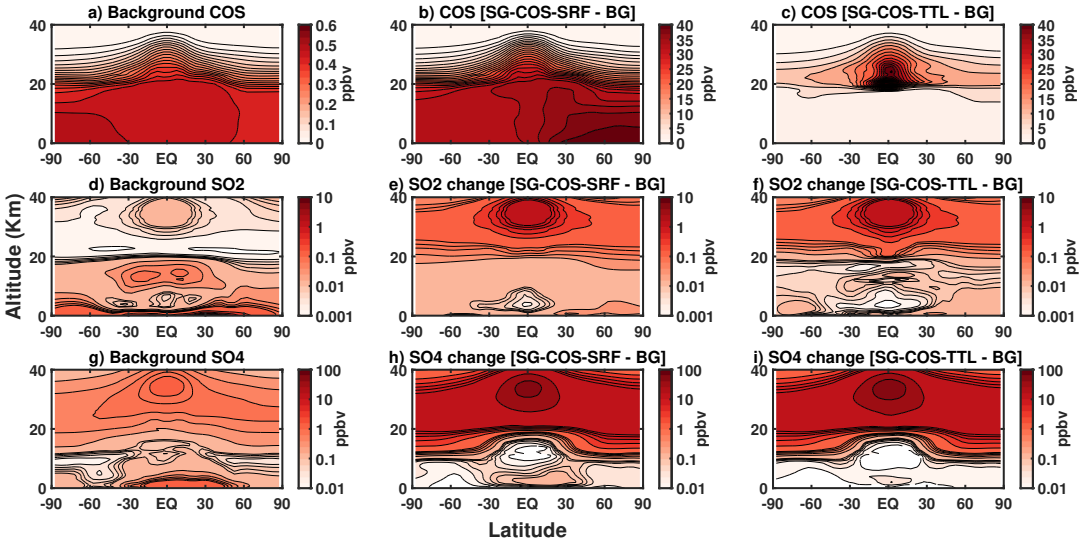

FIGURE B.2: Mean zonal values of volume mixing ration (in ppbv) in BG and changes in both SG-COS experiments of COS (a, b and c, respectively), SO_2 (d, e and f) and SO_4 (g, h and i) . All quantities are annually averaged over the years 2046-2055.

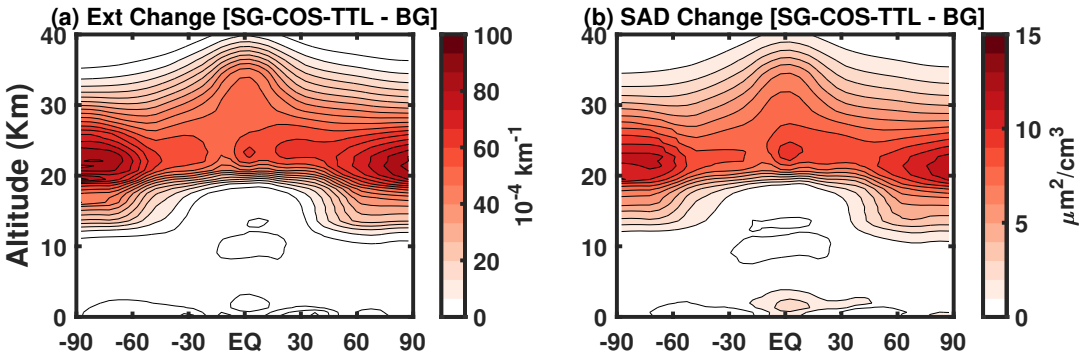

FIGURE B.3: Zonal mean values of sulfate extinction (in 10^{-4} km^{-1}) and SAD change (in μm^2/cm^3) in SG-COS-TTL with respect to the background. All quantities are annually averaged over the years 2046-2055.

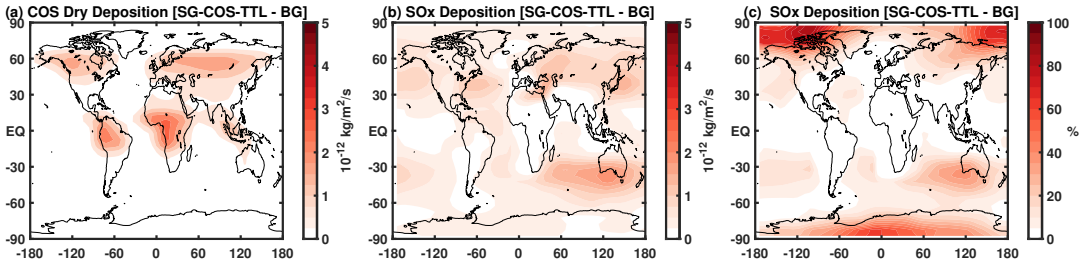

FIGURE B.4: a) Change in COS dry deposition fluxes in SG-COS-TTL compared to the background. b) Change in SO_x total deposition fluxes in SG-COS-TTL compared to the background. c) as b) but in % of the background values.

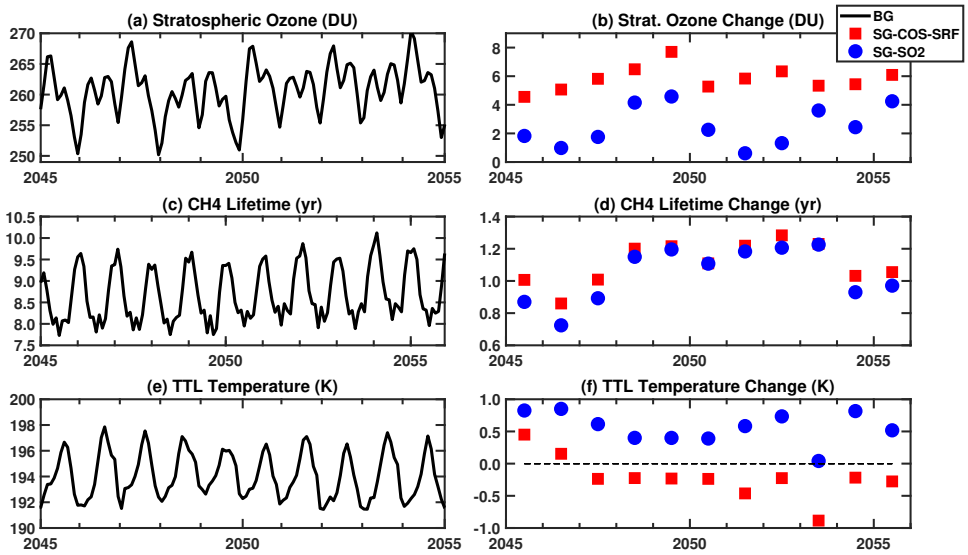

FIGURE B.5: Monthly values and annually averaged changes in SG-COS-SRF (red) and SG-SO2 (blue) [years 2046-2055] with respect to BG of atmospheric stratospheric ozone column (in DU) (panels a and b, respectively), methane lifetime (in yr) (panels c and d), and TTL temperature (in K) (panels e and f).

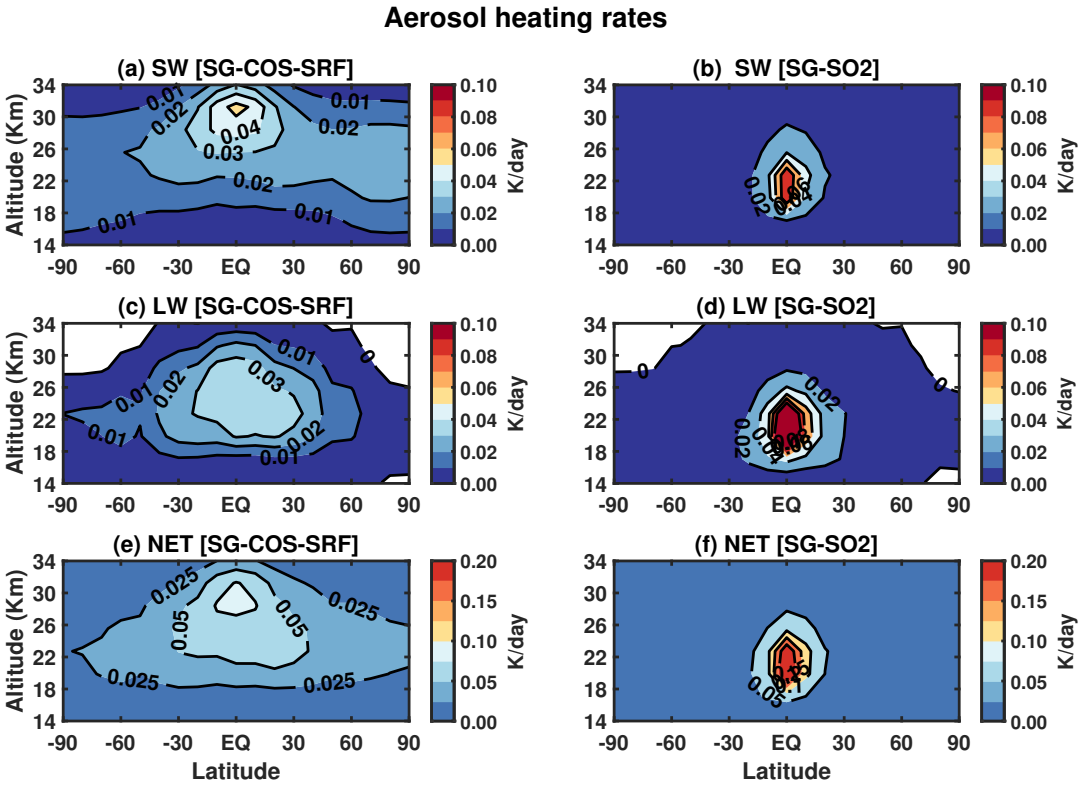

FIGURE B.6: Mean zonal values of aerosol heating rates for shortwave (SW) and longwave (LW) wavelengths, and net (NET) in SG-COS-SRF (a, c and e, respectively), and SG-SO2 (b, d and f). All quantities are annually averaged over the years 2046-2055.

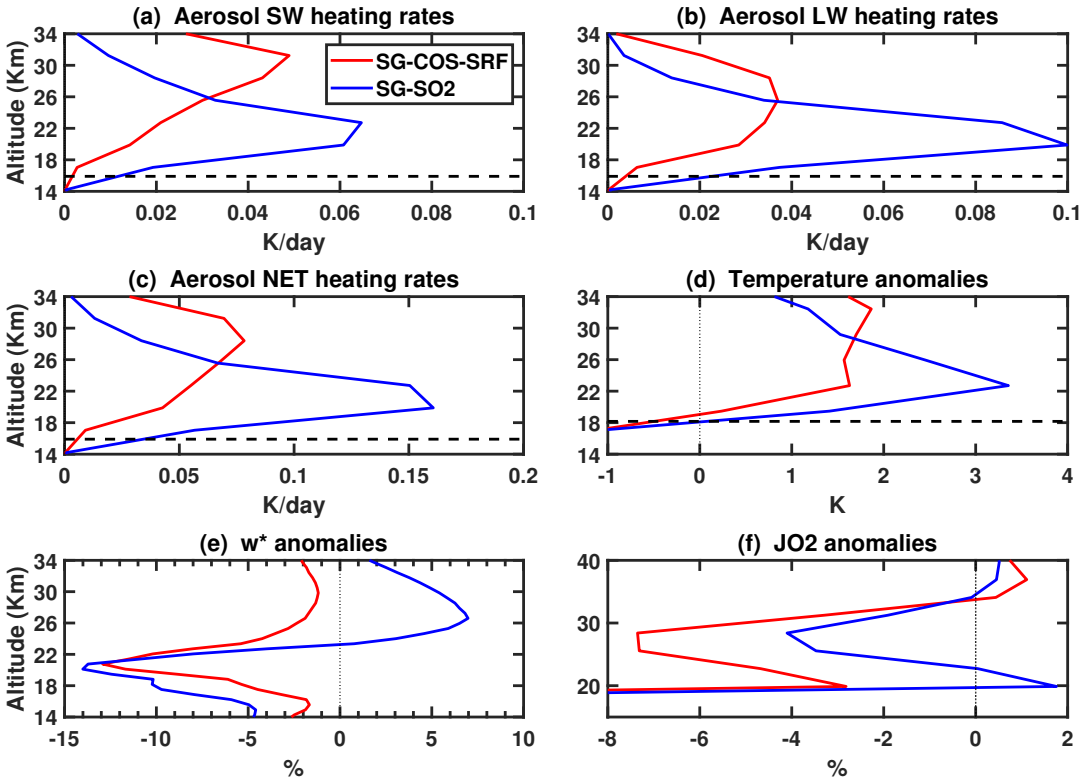

FIGURE B.7: Tropical vertical profiles of the aerosol shortwave (SW), longwave (LW) and net (NET) heating rates (a, b, c) anomalies (in K/day), temperature anomaly (in K, d), and residual vertical velocity (in %, e) and O_2 photodissociation coefficient percentage anomalies (f). All quantities are annually averaged over the years 2046-2055.

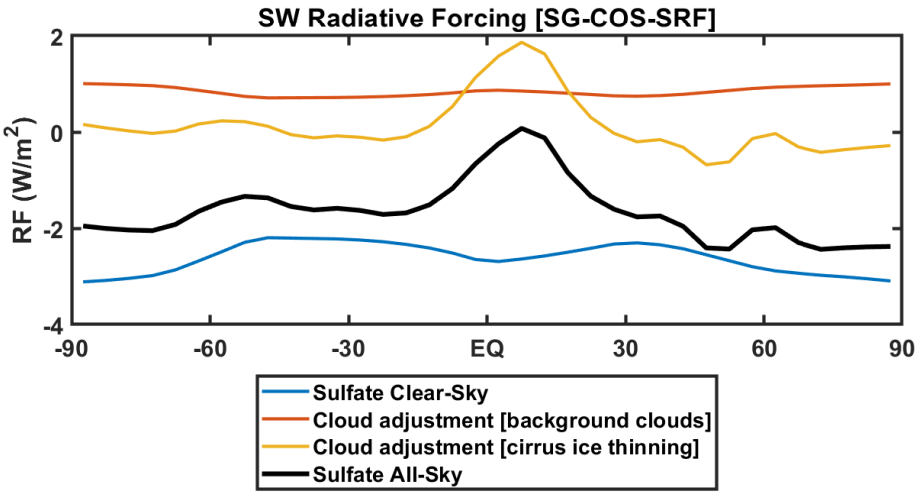

FIGURE B.8: Latitudinal distribution of zonal mean values of single contribution to shortwave RF (in W/m^2) in SG-COS-SRF: sulfate aerosols in Clear-1sky condition (blue), cloud adjustment for the presence of background clouds (orange) and for the cirrus ice thinning produced (yellow). Sulfate All-Sky RF in black is the sum of all previous contributions.

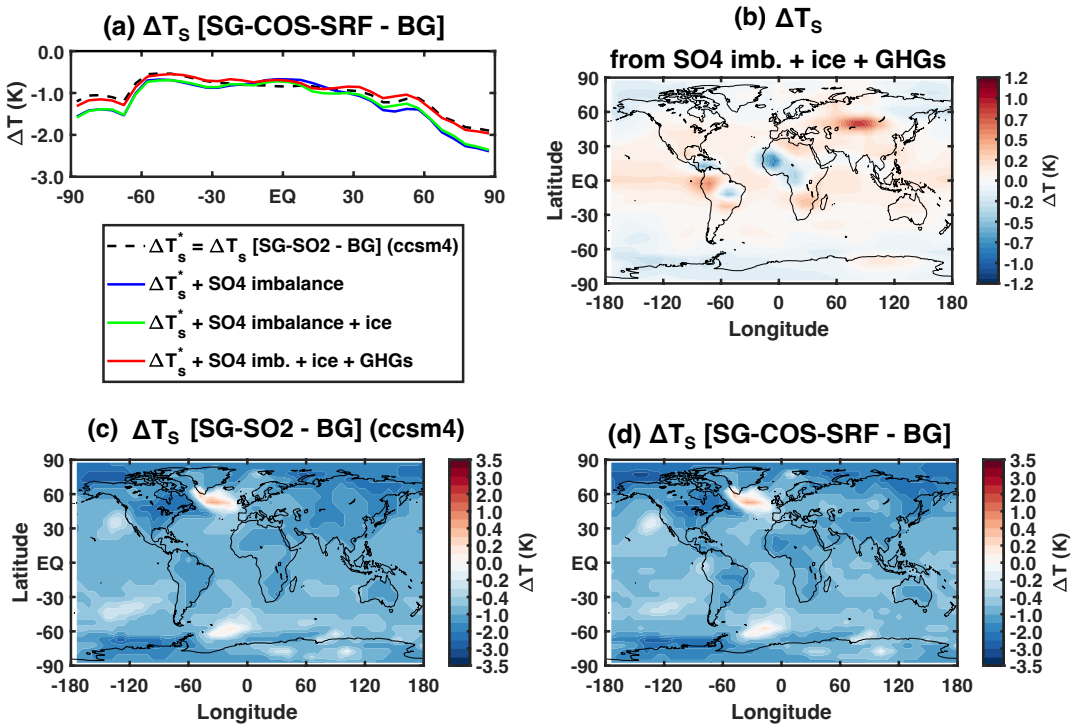

FIGURE B.9: (a) Zonally averaged surface temperature (T_s, in K) anomalies between SG-COS-SRF and BG under different conditions: T_s anomalies between SG-SO2 and BG (black dashed line); as above, but adding the T_s anomalies due to the SO_4 imbalance between SG-COS-SRF and SG-SO2 (blue line); as above, but adding the T_s anomalies due to cirrus ice changes (green line); as above, but also adding the T_s anomalies due to GHG changes (red line). (b) Lat–lon distribution of the T_s anomalies calculated online in the ULAQ-CCM model considering cirrus ice changes, the SO_4 imbalance between SG-COS-SRF and SG-SO2 and GHG changes. (c) Lat–lon distribution of the T_s anomalies between SG-SO2 and BG. (d) Lat–lon distribution of the T_s anomalies between SG-COS-SRF and BG.

Appendix C

Supplementary material: Reassessing the risks of an explosive volcanic eruption during a Stratospheric Aerosol Injection deployment

C.1 Figures

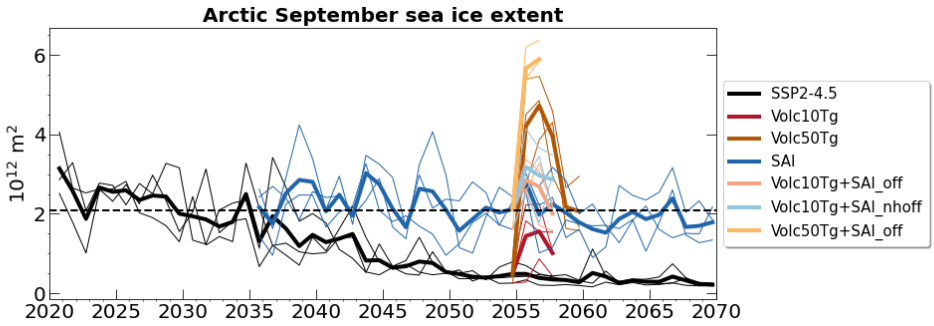

FIGURE C.1: Time series of monthly mean values of Arctic September sea ice extent in m^2 in all simulations (solid lines). The black dashed line represents the average of Arctic September sea ice extent over 2020-2039 in SSP2-4.5.

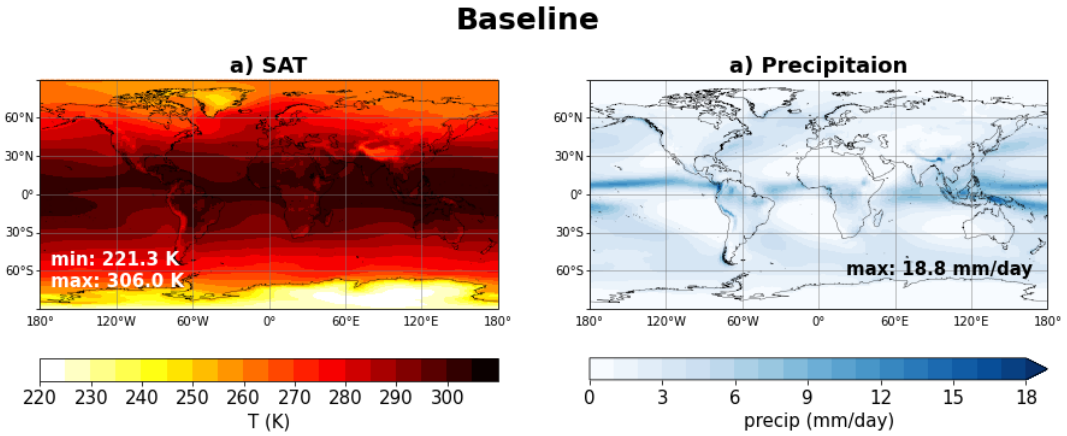

FIGURE C.2: Time series of zonal mean precipitation change in mm/day in (a) SSP2-4.5 and (b) SAI from Baseline, defined as the mean over 2020-2039 in SSP2-4.5. The minimum and maximum values of SAT and precipitation are shown in each panel.

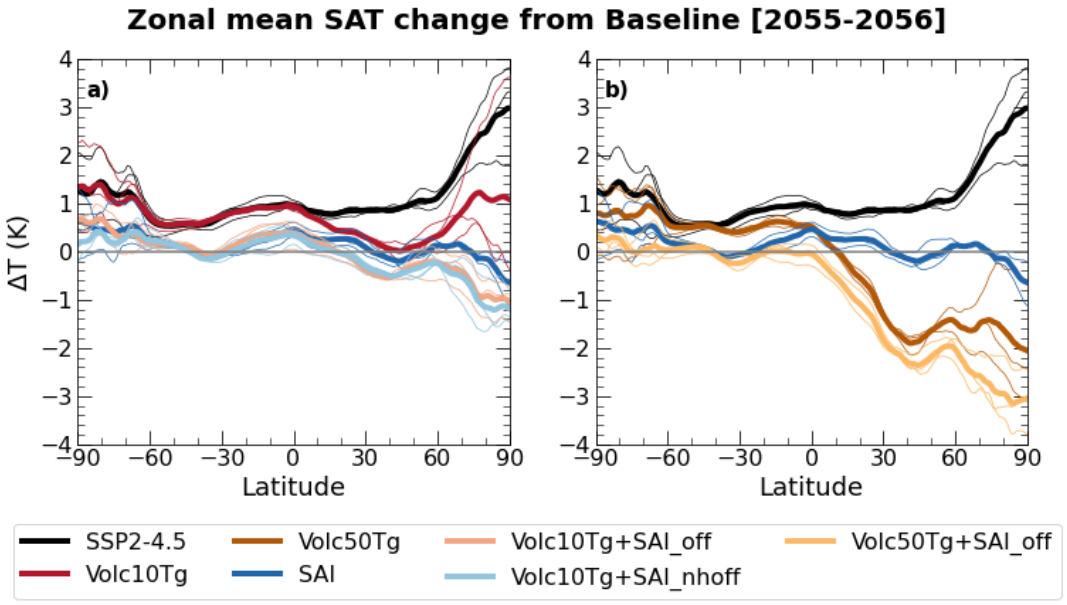

FIGURE C.3: Latitudinal distribution of zonal mean SAT (surface air temperature) averaged over 2 year following the eruption (2055-2056) minus the zonal SAT in SSP2-4.5 averaged over the reference period (2020-2039).

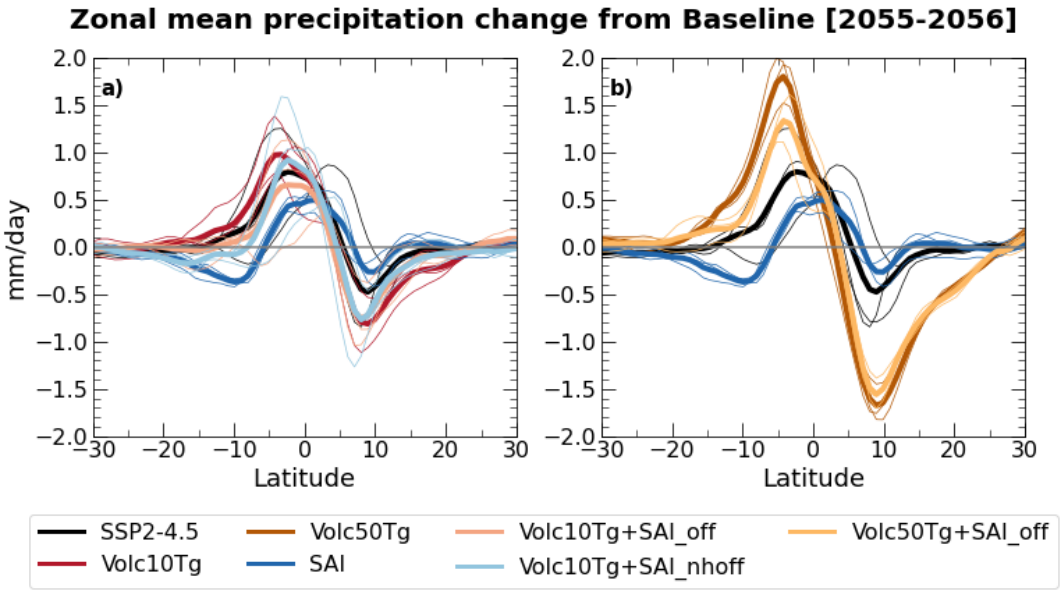

FIGURE C.4: Latitudinal distribution of zonal mean precipitation averaged over 2 year following the eruption (2055-2056) minus the zonal precipitation in SSP2-4.5 averaged over the reference period (2020-2039).

Bibliography

Antuña, Juan Carlos (2002). "Lidar validation of SAGE II aerosol measurements after the 1991 Mount Pinatubo eruption". en. In: *Journal of Geophysical Research* 107.D14, p. 4194. ISSN: 0148-0227. DOI: 10.1029/2001JD001441. URL: http://doi.wiley.com/10.1029/2001JD001441 (visited on 10/18/2022).

Aquila, V., C. I. Garfinkel, P.A. Newman, L.D. Oman, and D.W. Waugh (Mar. 2014). "Modifications of the quasi-biennial oscillation by a geoengineering perturbation of the stratospheric aerosol layer: Aquila et al.: QBO modifications by geoengineering". en. In: *Geophysical Research Letters* 41.5, pp. 1738–1744. ISSN: 00948276. DOI: 10.1002/2013GL058818. URL: http://doi.wiley.com/10.1002/2013GL058818 (visited on 12/13/2021).

Aquila, V., L. D. Oman, R. Stolarski, A. R. Douglass, and P. A. Newman (Mar. 2013). "The Response of Ozone and Nitrogen Dioxide to the Eruption of Mt. Pinatubo at Southern and Northern Midlatitudes". en. In: *Journal of the Atmospheric Sciences* 70.3, pp. 894–900. ISSN: 0022-4928, 1520-0469. DOI: 10.1175/JAS-D-12-0143.1. URL: https://journals.ametsoc.org/doi/10.1175/JAS-D-12-0143.1 (visited on 05/03/2023).

Aquila, Valentina, Luke D. Oman, Richard S. Stolarski, Peter R. Colarco, and Paul A. Newman (Mar. 2012). "Dispersion of the volcanic sulfate cloud from a Mount Pinatubo-like eruption: DISPERSION OF A MOUNT PINATUBO CLOUD". en. In: *Journal of Geophysical Research: Atmospheres* 117.D6, p. D06216. ISSN: 01480227. DOI: 10.1029/2011JD016968. URL: http://doi.wiley.com/10.1029/2011JD016968 (visited on 06/30/2021).

Archibald, A. T., F. M. O'Connor, N. L. Abraham, S. Archer-Nicholls, M. P. Chipperfield, M. Dalvi, G. A. Folberth, F. Dennison, S. S. Dhomse, P. T. Griffiths, C. Hardacre, A. J. Hewitt, R. S. Hill, C. E. Johnson, J. Keeble, M. O. Köhler, O. Morgenstern, J. P. Mulcahy, C. Ordóñez, R. J. Pope, S. T. Rumbold, M. R. Russo, N. H. Savage, A. Sellar, M. Stringer, S. T. Turnock, O. Wild, and G. Zeng (2020). "Description and evaluation of the UKCA stratosphere–troposphere chemistry scheme (StratTrop vn 1.0) implemented in UKESM1". In: *Geoscientific Model Development* 13.3, pp. 1223–1266. DOI: 10.5194/gmd-13-1223-2020. URL: https://gmd.copernicus.org/articles/13/1223/2020/.

Aubry, Thomas J., Samantha Engwell, Costanza Bonadonna, Guillaume Carazzo, Simona Scollo, Alexa R. Van Eaton, Isabelle A. Taylor, David Jessop, Julia Eychenne, Mathieu Gouhier, Larry G. Mastin, Kristi L. Wallace, Sébastien Biass, Marcus Bursik, Roy G. Grainger, A. Mark Jellinek, and Anja Schmidt (Sept. 2021).

"The Independent Volcanic Eruption Source Parameter Archive (IVESPA, version 1.0): A new observational database to support explosive eruptive column model validation and development". en. In: *Journal of Volcanology and Geothermal Research* 417, p. 107295. ISSN: 03770273. DOI: 10.1016/j.jvolgeores.2021.107295. URL: https://linkinghub.elsevier.com/retrieve/pii/S0377027321001244 (visited on 10/18/2022).

Ayris, P.M., A.F. Lee, K. Wilson, U. Kueppers, D.B. Dingwell, and P. Delmelle (June 2013). "SO2 sequestration in large volcanic eruptions: High-temperature scavenging by tephra". en. In: *Geochimica et Cosmochimica Acta* 110, pp. 58–69. ISSN: 00167037. DOI: 10.1016/j.gca.2013.02.018. URL: https://linkinghub.elsevier.com/retrieve/pii/S0016703713001130 (visited on 07/12/2022).

Bala, G., P. B. Duffy, and K. E. Taylor (June 2008). "Impact of geoengineering schemes on the global hydrological cycle". en. In: *Proceedings of the National Academy of Sciences* 105.22, pp. 7664–7669. ISSN: 0027-8424, 1091-6490. DOI: 10.1073/pnas.0711648105. URL: https://pnas.org/doi/full/10.1073/pnas.0711648105 (visited on 06/08/2022).

Baldwin, M. P., L. J. Gray, T. J. Dunkerton, K. Hamilton, P. H. Haynes, W. J. Randel, J. R. Holton, M. J. Alexander, I. Hirota, T. Horinouchi, D. B. A. Jones, J. S. Kinnersley, C. Marquardt, K. Sato, and M. Takahashi (2001). "The quasi-biennial oscillation". In: *Reviews of Geophysics* 39.2, pp. 179–229. DOI: https://doi.org/10.1029/1999RG000073. eprint: https://agupubs.onlinelibrary.wiley.com/doi/pdf/10.1029/1999RG000073. URL: https://agupubs.onlinelibrary.wiley.com/doi/abs/10.1029/1999RG000073.

Baran, A. J. and J. S. Foot (1994). "New application of the operational sounder HIRS in determining a climatology of sulphuric acid aerosol from the Pinatubo eruption". en. In: *Journal of Geophysical Research* 99.D12, p. 25673. ISSN: 0148-0227. DOI: 10.1029/94JD02044. URL: http://doi.wiley.com/10.1029/94JD02044 (visited on 06/30/2021).

Baran, A. J., J. S. Foot, and P. C. Dibben (Sept. 1993). "Satellite detection of volcanic sulphuric acid aerosol". en. In: *Geophysical Research Letters* 20.17, pp. 1799–1801. ISSN: 00948276. DOI: 10.1029/93GL01965. URL: http://doi.wiley.com/10.1029/93GL01965 (visited on 06/30/2021).

Barkley, Michael P., Paul I. Palmer, Chris D. Boone, Peter F. Bernath, and Parvadha Suntharalingam (July 2008). "Global distributions of carbonyl sulfide in the upper troposphere and stratosphere". en. In: *Geophysical Research Letters* 35.14, p. L14810. ISSN: 0094-8276. DOI: 10.1029/2008GL034270. URL: http://doi.wiley.com/10.1029/2008GL034270 (visited on 10/04/2021).

Bartholomaeus, Andrew and Victoria Haritos (Jan. 2006). "Review of the toxicology of carbonyl sulfide, a new grain fumigant". In: *Food and chemical toxicology : an international journal published for the British Industrial Biological Research Association* 43, pp. 1687–701. DOI: 10.1016/j.fct.2005.06.016.

Baur, S., A. Nauels, Z. Nicholls, B. M. Sanderson, and C.-F. Schleussner (2023). "The deployment length of solar radiation modification: an interplay of mitigation, net-negative emissions and climate uncertainty". In: *Earth System Dynamics* 14.2, pp. 367–381. DOI: 10.5194/esd-14-367-2023. URL: https://esd.copernicus.org/articles/14/367/2023/.

Bellouin, Nicolas and Hongbin Yu (2022). "Chapter 11 - Aerosol–radiation interactions". In: *Aerosols and Climate*. Ed. by Ken S. Carslaw. Elsevier, pp. 445–487. ISBN: 978-0-12-819766-0. DOI: https://doi.org/10.1016/B978-0-12-819766-0.00004-3. URL: https://www.sciencedirect.com/science/article/pii/B9780128197660000043.

Bingaman, Donald C., Christian V. Rice, Wake Smith, and Patrick Vogel (2020). "A Stratospheric Aerosol Injection Lofter Aircraft Concept: Brimstone Angel". In: *AIAA Scitech 2020 Forum*. AIAA SciTech Forum. Orlando, FL: American Institute of Aeronautics and Astronautics. DOI: 10.2514/6.2020-0618. URL: https://doi.org/10.2514/6.2020-0618 (visited on 11/20/2020).

Bluth, Gregg, Scott Doiron, Charles Schnetzler, A. Krueger, and Louis Walter (Feb. 1992a). "Global tracking of the SO2 clouds from the June, 1991 Mount Pinatubo eruptions". In: *Geophysical Research Letters* 19, pp. 151–154. DOI: 10.1029/91GL02792.

Bluth, Gregg J. S., Scott D. Doiron, Charles C. Schnetzler, Arlin J. Krueger, and Louis S. Walter (Jan. 1992b). "Global tracking of the SO_2 clouds from the June, 1991 Mount Pinatubo eruptions". en. In: *Geophysical Research Letters* 19.2, pp. 151–154. ISSN: 00948276. DOI: 10.1029/91GL02792. URL: http://doi.wiley.com/10.1029/91GL02792 (visited on 10/18/2022).

Bluth, Gregg J. S., William I. Rose, Ian E. Sprod, and Arlin J. Krueger (Nov. 1997). "Stratospheric Loading of Sulfur From Explosive Volcanic Eruptions". en. In: *The Journal of Geology* 105.6, pp. 671–684. ISSN: 0022-1376, 1537-5269. DOI: 10.1086/515972. URL: https://www.journals.uchicago.edu/doi/10.1086/515972 (visited on 03/14/2022).

Borbas, Eva E. and Paul W. Menzel (Jan. 2021). "Observed HIRS and Aqua MODIS Thermal Infrared Moisture Determinations in the 2000s". en. In: *Remote Sensing* 13.3, p. 502. ISSN: 2072-4292. DOI: 10.3390/rs13030502. URL: https://www.mdpi.com/2072-4292/13/3/502 (visited on 03/15/2022).

Broccoli, Anthony J., Kristina A. Dahl, and Ronald J. Stouffer (Jan. 2006). "Response of the ITCZ to Northern Hemisphere cooling: ITCZ RESPONSE TO N. HEMISPHERE COOLING". en. In: *Geophysical Research Letters* 33.1, n/a–n/a. ISSN: 00948276. DOI: 10.1029/2005GL024546. URL: http://doi.wiley.com/10.1029/2005GL024546 (visited on 04/28/2022).

Brodowsky, Christina, Timofei Sukhodolov, Aryeh Feinberg, Michael Höpfner, Thomas Peter, Andrea Stenke, and Eugene Rozanov (2021). "Modeling the Sulfate Aerosol Evolution After Recent Moderate Volcanic Activity, 2008–2012". In: *Journal of Geophysical Research: Atmospheres* 126.23. e2021JD035472 2021JD035472, e2021JD035472. DOI: https://doi.org/10.1029/2021JD035472. eprint: https://agupubs.

onlinelibrary.wiley.com/doi/pdf/10.1029/2021JD035472. URL: https://agupubs.onlinelibrary.wiley.com/doi/abs/10.1029/2021JD035472.

Brühl, C., J. Lelieveld, P. J. Crutzen, and H. Tost (Feb. 2012). "The role of carbonyl sulphide as a source of stratospheric sulphate aerosol and its impact on climate". en. In: *Atmospheric Chemistry and Physics* 12.3, pp. 1239–1253. ISSN: 1680-7324. DOI: 10.5194/acp-12-1239-2012. URL: https://acp.copernicus.org/articles/12/1239/2012/ (visited on 12/02/2021).

Brühl, C., J. Lelieveld, H. Tost, M. Höpfner, and N. Glatthor (Mar. 2015). "Stratospheric sulfur and its implications for radiative forcing simulated by the chemistry climate model EMAC". en. In: *Journal of Geophysical Research: Atmospheres* 120.5, pp. 2103–2118. ISSN: 2169-897X, 2169-8996. DOI: 10.1002/2014JD022430. URL: https://onlinelibrary.wiley.com/doi/10.1002/2014JD022430 (visited on 05/09/2022).

Brühl, Christoph and Paul J Crutzen (Feb. 1988). "Scenarios of possible changes in atmospheric temperatures and ozone concentrations due to man's activities, estimated with a one-dimensional coupled photochemical climate model". en. In: *Climate Dynamics* 2.3, pp. 173–203. ISSN: 0930-7575, 1432-0894. DOI: 10.1007/BF01053474. URL: http://link.springer.com/10.1007/BF01053474 (visited on 08/30/2021).

Brühl, Christoph, Jennifer Schallock, Klaus Klingmüller, Charles Robert, Christine Bingen, Lieven Clarisse, Andreas Heckel, Peter North, and Landon Rieger (Sept. 2018). "Stratospheric aerosol radiative forcing simulated by the chemistry climate model EMAC using Aerosol CCI satellite data". en. In: *Atmospheric Chemistry and Physics* 18.17, pp. 12845–12857. ISSN: 1680-7324. DOI: 10.5194/acp-18-12845-2018. URL: https://acp.copernicus.org/articles/18/12845/2018/ (visited on 05/27/2021).

Budyko, M. I. (1977). *Climatic Changes, Volume 10*. American Geophysical Union, pp. 197–245. ISBN: 9780875902067. DOI: DOI:10.1029/SP010. URL: http://dx.doi.org/10.1002/9781118665251.ch7.

Butchart, Neal (June 2014). "The Brewer-Dobson circulation". en. In: *Reviews of Geophysics* 52.2, pp. 157–184. ISSN: 8755-1209, 1944-9208. DOI: 10.1002/2013RG000448. URL: https://onlinelibrary.wiley.com/doi/10.1002/2013RG000448 (visited on 11/04/2021).

Canty, T., N. R. Mascioli, M. D. Smarte, and R. J. Salawitch (2013). "An empirical model of global climate – Part 1: A critical evaluation of volcanic cooling". In: *Atmospheric Chemistry and Physics* 13.8, pp. 3997–4031.

Cao, Long, Govindasamy Bala, and Ken Caldeira (Sept. 2012). "Climate response to changes in atmospheric carbon dioxide and solar irradiance on the time scale of days to weeks". en. In: *Environmental Research Letters* 7.3, p. 034015. ISSN: 1748-9326. DOI: 10.1088/1748-9326/7/3/034015. URL: https://iopscience.iop.org/article/10.1088/1748-9326/7/3/034015 (visited on 01/17/2023).

Carn, Simon (2022). *Multi-Satellite Volcanic Sulfur Dioxide L4 Long-Term Global Database V4*. DOI: https://doi.org/10.5067/MEASURES/SO2/DATA405.

Chakraborty, Pinaki, Gustavo Gioia, and Susan W. Kieffer (Mar. 2009). "Volcanic mesocyclones". In: *Nature* 458.7237, pp. 497–500. ISSN: 1476-4687. DOI: 10.1038/nature07866. URL: https://doi.org/10.1038/nature07866.

Clyne, Margot, Jean-Francois Lamarque, Michael J Mills, Myriam Khodri, William Ball, Slimane Bekki, Sandip S Dhomse, Nicolas Lebas, Graham Mann, Lauren Marshall, Ulrike Niemeier, Virginie Poulain, Alan Robock, Eugene Rozanov, Anja Schmidt, Andrea Stenke, Timofei Sukhodolov, Claudia Timmreck, Matthew Toohey, Fiona Tummon, Davide Zanchettin, Yunqian Zhu, and Owen B Toon (2021). "Model physics and chemistry causing intermodel disagreement within the VolMIP-Tambora Interactive Stratospheric Aerosol ensemble". en. In: *Atmos. Chem. Phys.*, p. 27.

Conrad, Ralf and Katja Meuser (2000). "Soils contain more than one activity consuming carbonyl sulfide". In: *Atmospheric Environment* 34.21, pp. 3635–3639.

Crutzen, Paul J. (1976). "The possible importance of CSO for the sulfate layer of the stratosphere". In: *Geophysical Research Letters* 3.2, pp. 73–76. DOI: https://doi.org/10.1029/GL003i002p00073. URL: https://agupubs.onlinelibrary.wiley.com/doi/abs/10.1029/GL003i002p00073.

Crutzen, Paul J. (2006). "Albedo Enhancement by Stratospheric Sulfur Injections: A Contribution to Resolve a Policy Dilemma?" In: *Climatic Change* 77.3, pp. 211–220. ISSN: 1573-1480. DOI: 10.1007/s10584-006-9101-y. URL: http://dx.doi.org/10.1007/s10584-006-9101-y.

Curtius, Joachim (2006). "Nucleation of atmospheric aerosol particles". In: *Comptes Rendus Physique* 7.9, pp. 1027–1045. ISSN: 1631-0705. DOI: https://doi.org/10.1016/j.crhy.2006.10.018. URL: https://www.sciencedirect.com/science/article/pii/S1631070506002301.

Da-Allada, C. Y., E. Baloïtcha, E. A. Alamou, F. M. Awo, F. Bonou, Y. Pomalegni, E. I. Biao, E. Obada, J. E. Zandagba, S. Tilmes, and P. J. Irvine (2020). "Changes in West African Summer Monsoon Precipitation Under Stratospheric Aerosol Geoengineering". In: *Earth's Future* 8.7, e2020EF001595. DOI: https://doi.org/10.1029/2020EF001595. URL: https://agupubs.onlinelibrary.wiley.com/doi/abs/10.1029/2020EF001595.

Dai, Z., D. K. Weisenstein, and D. W. Keith (2018). "Tailoring Meridional and Seasonal Radiative Forcing by Sulfate Aerosol Solar Geoengineering". In: *Geophysical Research Letters* 45.2, pp. 1030–1039. ISSN: 19448007. DOI: 10.1002/2017GL076472.

Dai, Zhen, Debra K. Weisenstein, Frank N. Keutsch, and David W. Keith (Dec. 2020). "Experimental reaction rates constrain estimates of ozone response to calcium carbonate geoengineering". en. In: *Communications Earth & Environment* 1.1, p. 63. ISSN: 2662-4435. DOI: 10.1038/s43247-020-00058-7. URL: https://www.nature.com/articles/s43247-020-00058-7 (visited on 04/03/2023).

Damadeo, R. P., J. M. Zawodny, L. W. Thomason, and N. Iyer (Dec. 2013). "SAGE version 7.0 algorithm: application to SAGE II". en. In: *Atmospheric Measurement*

Techniques 6.12, pp. 3539–3561. ISSN: 1867-8548. DOI: 10.5194/amt-6-3539-2013. URL: https://amt.copernicus.org/articles/6/3539/2013/ (visited on 03/16/2022).

Danabasoglu, G., J.-F. Lamarque, J. Bacmeister, D. A. Bailey, A. K. DuVivier, J. Edwards, L. K. Emmons, J. Fasullo, R. Garcia, A. Gettelman, C. Hannay, M. M. Holland, W. G. Large, P. H. Lauritzen, D. M. Lawrence, J. T. M. Lenaerts, K. Lindsay, W. H. Lipscomb, M. J. Mills, R. Neale, K. W. Oleson, B. Otto-Bliesner, A. S. Phillips, W. Sacks, S. Tilmes, L. van Kampenhout, M. Vertenstein, A. Bertini, J. Dennis, C. Deser, C. Fischer, B. Fox-Kemper, J. E. Kay, D. Kinnison, P. J. Kushner, V. E. Larson, M. C. Long, S. Mickelson, J. K. Moore, E. Nienhouse, L. Polvani, P. J. Rasch, and W. G. Strand (2020). "The Community Earth System Model Version 2 (CESM2)". In: *Journal of Advances in Modeling Earth Systems* 12.2. e2019MS001916 2019MS001916, e2019MS001916. DOI: https://doi.org/10.1029/2019MS001916. eprint: https://agupubs.onlinelibrary.wiley.com/doi/pdf/10.1029/2019MS001916. URL: https://agupubs.onlinelibrary.wiley.com/doi/abs/10.1029/2019MS001916.

Davis, N. A., P. Callaghan, I. R. Simpson, and S. Tilmes (2022). "Specified dynamics scheme impacts on wave-mean flow dynamics, convection, and tracer transport in CESM2 (WACCM6)". In: *Atmospheric Chemistry and Physics* 22.1, pp. 197–214. DOI: 10.5194/acp-22-197-2022. URL: https://acp.copernicus.org/articles/22/197/2022/.

Dee, D. P., S. M. Uppala, A. J. Simmons, P. Berrisford, P. Poli, S. Kobayashi, U. Andrae, M. A. Balmaseda, G. Balsamo, P. Bauer, P. Bechtold, A. C. M. Beljaars, L. van de Berg, J. Bidlot, N. Bormann, C. Delsol, R. Dragani, M. Fuentes, A. J. Geer, L. Haimberger, S. B. Healy, H. Hersbach, E. V. Hólm, L. Isaksen, P. Kållberg, M. Köhler, M. Matricardi, A. P. McNally, B. M. Monge-Sanz, J.-J. Morcrette, B.-K. Park, C. Peubey, P. de Rosnay, C. Tavolato, J.-N. Thépaut, and F. Vitart (2011). "The ERA-Interim reanalysis: configuration and performance of the data assimilation system". In: *Quarterly Journal of the Royal Meteorological Society* 137.656, pp. 553–597. DOI: https://doi.org/10.1002/qj.828. eprint: https://rmets.onlinelibrary.wiley.com/doi/pdf/10.1002/qj.828. URL: https://rmets.onlinelibrary.wiley.com/doi/abs/10.1002/qj.828.

DeFoor, Thomas E., Elmer Robinson, and Steven Ryan (1992). "Early lidar observations of the June 1991 Pinatubo eruption plume at Mauna Loa Observatory, Hawaii". In: *Geophysical Research Letters* 19.2, pp. 187–190. DOI: https://doi.org/10.1029/91GL02791. eprint: https://agupubs.onlinelibrary.wiley.com/doi/pdf/10.1029/91GL02791. URL: https://agupubs.onlinelibrary.wiley.com/doi/abs/10.1029/91GL02791.

Deshler, T. (2003). "Thirty years of in situ stratospheric aerosol size distribution measurements from Laramie, Wyoming (41°N), using balloon-borne instruments". en. In: *Journal of Geophysical Research* 108.D5, p. 4167. ISSN: 0148-0227. DOI: 10.

1029/2002JD002514. URL: http://doi.wiley.com/10.1029/2002JD002514 (visited on 06/30/2021).

Deshler, T., D. J. Hofmann, B. J. Johnson, and W. R. Rozier (Jan. 1992). "Balloonborne measurements of the Pinatubo aerosol size distribution and volatility at Laramie, Wyoming during the summer of 1991". en. In: *Geophysical Research Letters* 19.2, pp. 199–202. ISSN: 00948276. DOI: 10.1029/91GL02787. URL: http://doi.wiley.com/10.1029/91GL02787 (visited on 10/11/2022).

Deshler, Terry, Beiping Luo, Mahesh Kovilakam, Thomas Peter, and Lars E. Kalnajs (May 2019). "Retrieval of Aerosol Size Distributions From In Situ Particle Counter Measurements: Instrument Counting Efficiency and Comparisons With Satellite Measurements". en. In: *Journal of Geophysical Research: Atmospheres* 124.9, pp. 5058–5087. ISSN: 2169-897X, 2169-8996. DOI: 10.1029/2018JD029558. URL: https://onlinelibrary.wiley.com/doi/10.1029/2018JD029558 (visited on 06/30/2021).

Dhomse, S. S., K. M. Emmerson, G. W. Mann, N. Bellouin, K. S. Carslaw, M. P. Chipperfield, R. Hommel, N. L. Abraham, P. Telford, P. Braesicke, M. Dalvi, C. E. Johnson, F. O'Connor, O. Morgenstern, J. A. Pyle, T. Deshler, J. M. Zawodny, and L. W. Thomason (Oct. 2014). "Aerosol microphysics simulations of the Mt.~Pinatubo eruption with the UM-UKCA composition-climate model". en. In: *Atmospheric Chemistry and Physics* 14.20, pp. 11221–11246. ISSN: 1680-7324. DOI: 10.5194/acp-14-11221-2014. URL: https://acp.copernicus.org/articles/14/11221/2014/ (visited on 06/30/2021).

Dhomse, Sandip S., Graham W. Mann, Juan Carlos Antuña Marrero, Sarah E. Shallcross, Martyn P. Chipperfield, Kenneth S. Carslaw, Lauren Marshall, N. Luke Abraham, and Colin E. Johnson (Nov. 2020). "Evaluating the simulated radiative forcings, aerosol properties, and stratospheric warmings from the 1963 Mt Agung, 1982 El Chichón, and 1991 Mt Pinatubo volcanic aerosol clouds". en. In: *Atmospheric Chemistry and Physics* 20.21, pp. 13627–13654. ISSN: 1680-7324. DOI: 10.5194/acp-20-13627-2020. URL: https://acp.copernicus.org/articles/20/13627/2020/ (visited on 06/30/2021).

Driscoll, Charles T., Gregory B. Lawrence, Arthur J. Bulger, Thomas J. Butler, Christopher S. Cronan, Christopher Eagar, Kathleen F. Lambert, Gene E. Likens, John L. Stoddard, and Kathleen C. Weathers (2001). "Acidic Deposition in the Northeastern United States: Sources and Inputs, Ecosystem Effects, and Management Strategies". en. In: *BioScience* 51.3, p. 180. ISSN: 0006-3568. DOI: 10.1641/0006-3568(2001)051[0180:ADITNU]2.0.CO;2. URL: https://academic.oup.com/bioscience/article/51/3/180-198/256122 (visited on 05/27/2021).

Dutton, Ellsworth G. and John R. Christy (Dec. 1992). "Solar radiative forcing at selected locations and evidence for global lower tropospheric cooling following the eruptions of El Chichón and Pinatubo". en. In: *Geophysical Research Letters* 19.23, pp. 2313–2316. ISSN: 00948276. DOI: 10.1029/92GL02495. URL: http://doi.wiley.com/10.1029/92GL02495 (visited on 01/17/2023).

D'Agostino, Roberta and Claudia Timmreck (May 2022). "Sensitivity of regional monsoons to idealised equatorial volcanic eruption of different sulfur emission strengths". en. In: *Environmental Research Letters* 17.5, p. 054001. ISSN: 1748-9326. DOI: 10.1088/1748-9326/ac62af. URL: https://iopscience.iop.org/article/10.1088/1748-9326/ac62af (visited on 04/26/2022).

Eastham, Sebastian D., Debra K. Weisenstein, David W. Keith, and Steven R. H. Barrett (2018). "Quantifying the impact of sulfate geoengineering on mortality from air quality and UV-B exposure". In: *Atmospheric Environment* 187, pp. 424 –434. ISSN: 1352-2310. DOI: https://doi.org/10.1016/j.atmosenv.2018.05.047. URL: http://www.sciencedirect.com/science/article/pii/S1352231018303510.

Egorova, T., E. Rozanov, V.A. Zubov, and I. Karol (May 2003). "Model for investigating ozone trends (MEZON)". In: *Izvestiya - Atmospheric and Ocean Physics* 39, pp. 277–292.

Eichinger, R., S. Dietmüller, H. Garny, P. Šácha, T. Birner, H. Bönisch, G. Pitari, D. Visioni, A. Stenke, E. Rozanov, L. Revell, D. A. Plummer, P. Jöckel, L. Oman, M. Deushi, D. E. Kinnison, R. Garcia, O. Morgenstern, G. Zeng, K. A. Stone, and R. Schofield (2019). "The influence of mixing on the stratospheric age of air changes in the 21st century". In: *Atmospheric Chemistry and Physics* 19.2, pp. 921–940. DOI: 10.5194/acp-19-921-2019. URL: https://acp.copernicus.org/articles/19/921/2019/.

English, J. M., O. B. Toon, and M. J. Mills (May 2012). "Microphysical simulations of sulfur burdens from stratospheric sulfur geoengineering". en. In: *Atmospheric Chemistry and Physics* 12.10, pp. 4775–4793. ISSN: 1680-7324. DOI: 10.5194/acp-12-4775-2012. URL: https://acp.copernicus.org/articles/12/4775/2012/ (visited on 07/15/2021).

Eyring, V., N. Butchart, D. W. Waugh, H. Akiyoshi, J. Austin, S. Bekki, G. E. Bodeker, B. A. Boville, C. Brühl, M. P. Chipperfield, E. Cordero, M. Dameris, M. Deushi, V. E. Fioletov, S. M. Frith, R. R. Garcia, A. Gettelman, M. A. Giorgetta, V. Grewe, L. Jourdain, D. E. Kinnison, E. Mancini, E. Manzini, M. Marchand, D. R. Marsh, T. Nagashima, P. A. Newman, J. E. Nielsen, S. Pawson, G. Pitari, D. A. Plummer, E. Rozanov, M. Schraner, T. G. Shepherd, K. Shibata, R. S. Stolarski, H. Struthers, W. Tian, and M. Yoshiki (Nov. 2006). "Assessment of temperature, trace species, and ozone in chemistry-climate model simulations of the recent past". en. In: *Journal of Geophysical Research* 111.D22, p. D22308. ISSN: 0148-0227. DOI: 10.1029/2006JD007327. URL: http://doi.wiley.com/10.1029/2006JD007327 (visited on 09/05/2021).

Eyring, Veronika, Jean-François Lamarque, Peter Hess, Florian Arfeuille, Kevin Bowman, Bryan Duncan, Arlene Fiore, Andrew Gettelman, Marco A Giorgetta, Claire Granier, Michaela Hegglin, Doug Kinnison, Markus Kunze, Ulrike Langematz, Beiping Luo, Randall Martin, Katja Matthes, Paul A Newman, Thomas Peter, Alan Robock, Tom Ryerson, Alfonso Saiz-Lopez, Ross Salawitch, Martin Schultz,

Theodore G Shepherd, Drew Shindell, Johannes Staehelin, Larry Thomason, Simone Tilmes, Jean-Paul Vernier, Darryn W Waugh, and Paul J Young (2013). "Overview of IGAC/SPARC Chemistry-Climate Model Initiative (CCMI) Community Simulations in Support of Upcoming Ozone and Climate Assessments". en. In: pp. 48–66. URL: https://www.sparc-climate.org/publications/newsletter/.

F. Forster, Piers M. de and Keith P. Shine (Nov. 1999). "Stratospheric water vapour changes as a possible contributor to observed stratospheric cooling". en. In: *Geophysical Research Letters* 26.21, pp. 3309–3312. ISSN: 00948276. DOI: 10.1029/1999GL010487. URL: http://doi.wiley.com/10.1029/1999GL010487 (visited on 01/16/2023).

Feinberg, A., T. Sukhodolov, B.-P. Luo, E. Rozanov, L. H. E. Winkel, T. Peter, and A. Stenke (2019). "Improved tropospheric and stratospheric sulfur cycle in the aerosol–chemistry–climate model SOCOL-AERv2". In: *Geoscientific Model Development* 12.9, pp. 3863–3887. DOI: 10.5194/gmd-12-3863-2019. URL: https://gmd.copernicus.org/articles/12/3863/2019/.

Franke, H., U. Niemeier, and D. Visioni (2021). "Differences in the quasi-biennial oscillation response to stratospheric aerosol modification depending on injection strategy and species". In: *Atmospheric Chemistry and Physics* 21.11, pp. 8615–8635.

Gates, W. Lawrence, James S. Boyle, Curt Covey, Clyde G. Dease, Charles M. Doutriaux, Robert S. Drach, Michael Fiorino, Peter J. Gleckler, Justin J. Hnilo, Susan M. Marlais, Thomas J. Phillips, Gerald L. Potter, Benjamin D. Santer, Kenneth R. Sperber, Karl E. Taylor, and Dean N. Williams (1999). "An Overview of the Results of the Atmospheric Model Intercomparison Project (AMIP I)". In: *Bulletin of the American Meteorological Society* 80.1, pp. 29–55. ISSN: 00030007, 15200477. URL: http://www.jstor.org/stable/26214897 (visited on 01/12/2023).

Gerstell, M. F., Joy Crisp, and David Crisp (1995). "Radiative Forcing of the Stratosphere by SO2 Gas, Silicate Ash, and H2SO4 Aerosols Shortly after the 1982 Eruptions of El Chichón". In: *Journal of Climate* 8.5, pp. 1060 –1070. DOI: 10.1175/1520-0442(1995)008<1060:RFOTSB>2.0.CO;2. URL: https://journals.ametsoc.org/view/journals/clim/8/5/1520-0442_1995_008_1060_rfotsb_2_0_co_2.xml.

Gervais, Melissa, Jeffrey Shaman, and Yochanan Kushnir (2018). "Mechanisms Governing the Development of the North Atlantic Warming Hole in the CESM-LE Future Climate Simulations". In: *Journal of Climate* 31.15, pp. 5927 –5946. DOI: https://doi.org/10.1175/JCLI-D-17-0635.1. URL: https://journals.ametsoc.org/view/journals/clim/31/15/jcli-d-17-0635.1.xml.

Gettelman, A., M. J. Mills, D. E. Kinnison, R. R. Garcia, A. K. Smith, D. R. Marsh, S. Tilmes, F. Vitt, C. G. Bardeen, J. McInerny, H.-L. Liu, S. C. Solomon, L. M. Polvani, L. K. Emmons, J.-F. Lamarque, J. H. Richter, A. S. Glanville, J. T. Bacmeister, A. S. Phillips, R. B. Neale, I. R. Simpson, A. K. DuVivier, A. Hodzic, and W. J. Randel (2019). "The Whole Atmosphere Community Climate Model Version 6

(WACCM6)". In: *Journal of Geophysical Research: Atmospheres* 124.23, pp. 12380–12403. DOI: https://doi.org/10.1029/2019JD030943. eprint: https://agupubs.onlinelibrary.wiley.com/doi/pdf/10.1029/2019JD030943. URL: https://agupubs.onlinelibrary.wiley.com/doi/abs/10.1029/2019JD030943.

Giorgetta, M. A., E. Manzini, E. Roeckner, M. Esch, and L. Bengtsson (Aug. 2006). "Climatology and Forcing of the Quasi-Biennial Oscillation in the MAECHAM5 Model". en. In: *Journal of Climate* 19.16, pp. 3882–3901. ISSN: 1520-0442, 0894-8755. DOI: 10.1175/JCLI3830.1. URL: http://journals.ametsoc.org/doi/10.1175/JCLI3830.1 (visited on 05/09/2022).

Grainger, Roy G. (2018). "Some Useful Formulae for Aerosol Size Distributions and Optical Properties". In.

Grant, W., J. Fishman, E. Browell, V. Brackett, D. Nganga, A. Minga, B. Cros, Robert E. Veiga, C. Butler, M. Fenn, and G. Nowicki (1992). "Observations of reduced ozone concentrations in the tropical stratosphere after the eruption of Mt. Pinatubo". In: *Geophysical Research Letters* 19, pp. 1109–1112.

Guo, Song, Gregg J. S. Bluth, William I. Rose, I. Matthew Watson, and A. J. Prata (2004a). "Re-evaluation of SO2 release of the 15 June 1991 Pinatubo eruption using ultraviolet and infrared satellite sensors". In: *Geochemistry, Geophysics, Geosystems* 5.4, Q04001. DOI: https://doi.org/10.1029/2003GC000654. eprint: https://agupubs.onlinelibrary.wiley.com/doi/pdf/10.1029/2003GC000654. URL: https://agupubs.onlinelibrary.wiley.com/doi/abs/10.1029/2003GC000654.

Guo, Song, William I. Rose, Gregg J. S. Bluth, and I. Matthew Watson (May 2004b). "Particles in the great Pinatubo volcanic cloud of June 1991: The role of ice: JUNE 1991 PINATUBO VOLCANIC CLOUDS". en. In: *Geochemistry, Geophysics, Geosystems* 5.5, Q05003. ISSN: 15252027. DOI: 10.1029/2003GC000655. URL: http://doi.wiley.com/10.1029/2003GC000655 (visited on 02/07/2022).

Hansen, James, Andrew Lacis, Reto Ruedy, and Makiko Sato (Jan. 1992). "Potential climate impact of Mount Pinatubo eruption". en. In: *Geophysical Research Letters* 19.2, pp. 215–218. ISSN: 00948276. DOI: 10.1029/91GL02788. URL: http://doi.wiley.com/10.1029/91GL02788 (visited on 02/07/2023).

Haywood, Jim M., Andy Jones, Nicolas Bellouin, and David Stephenson (July 2013). "Asymmetric forcing from stratospheric aerosols impacts Sahelian rainfall". en. In: *Nature Climate Change* 3.7, pp. 660–665. ISSN: 1758-678X, 1758-6798. DOI: 10.1038/nclimate1857. URL: http://www.nature.com/articles/nclimate1857 (visited on 04/28/2022).

Held, Isaac M. and Brian J. Soden (Nov. 2006). "Robust Responses of the Hydrological Cycle to Global Warming". en. In: *Journal of Climate* 19.21, pp. 5686–5699. ISSN: 1520-0442, 0894-8755. DOI: 10.1175/JCLI3990.1. URL: http://journals.ametsoc.org/doi/10.1175/JCLI3990.1 (visited on 02/03/2023).

Hendricks, J., E. Lippert, H. Petry, and A. Ebel (Mar. 1999). "Heterogeneous reactions on and in sulfate aerosols: Implications for the chemistry of the midlatitude

tropopause region". en. In: *Journal of Geophysical Research: Atmospheres* 104.D5, pp. 5531–5550. ISSN: 01480227. DOI: 10.1029/1998JD100098. URL: http://doi.wiley.com/10.1029/1998JD100098 (visited on 07/21/2021).

Hobe, M. von, C. Brühl, S. T. Lennartz, M. E. Whelan, and A. Kaushik (2023). "Comment on "An approach to sulfate geoengineering with surface emissions of carbonyl sulfide" by Quaglia et al. (2022)". In: *EGUsphere* 2023, pp. 1–13. DOI: 10.5194/egusphere-2023-268. URL: https://egusphere.copernicus.org/preprints/2023/egusphere-2023-268/.

Holasek, R. E., S. Self, and A. W. Woods (Dec. 1996). "Satellite observations and interpretation of the 1991 Mount Pinatubo eruption plumes". en. In: *Journal of Geophysical Research: Solid Earth* 101.B12, pp. 27635–27655. ISSN: 01480227. DOI: 10.1029/96JB01179. URL: http://doi.wiley.com/10.1029/96JB01179 (visited on 10/18/2022).

Holton, James R., Peter H. Haynes, Michael E. McIntyre, Anne R. Douglass, Richard B. Rood, and Leonhard Pfister (1995). "Stratosphere-troposphere exchange". In: *Reviews of Geophysics* 33.4, pp. 403–439. DOI: https://doi.org/10.1029/95RG02097. eprint: https://agupubs.onlinelibrary.wiley.com/doi/pdf/10.1029/95RG02097. URL: https://agupubs.onlinelibrary.wiley.com/doi/abs/10.1029/95RG02097.

Hommel, R., C. Timmreck, M. A. Giorgetta, and H. F. Graf (May 2015). "Quasi-biennial oscillation of the tropical stratospheric aerosol layer". en. In: *Atmospheric Chemistry and Physics* 15.10, pp. 5557–5584. ISSN: 1680-7324. DOI: 10.5194/acp-15-5557-2015. URL: https://acp.copernicus.org/articles/15/5557/2015/ (visited on 06/30/2021).

Hommel, R., C. Timmreck, and H. F. Graf (2011). "The global middle-atmosphere aerosol model MAECHAM5-SAM2: comparison with satellite and in-situ observations". In: *Geoscientific Model Development* 4.3, pp. 809–834. DOI: 10.5194/gmd-4-809-2011. URL: https://gmd.copernicus.org/articles/4/809/2011/.

Hwang, Yen-Ting, Dargan M. W. Frierson, and Sarah M. Kang (June 2013). "Anthropogenic sulfate aerosol and the southward shift of tropical precipitation in the late 20th century". en. In: *Geophysical Research Letters* 40.11, pp. 2845–2850. ISSN: 0094-8276, 1944-8007. DOI: 10.1002/grl.50502. URL: https://onlinelibrary.wiley.com/doi/10.1002/grl.50502 (visited on 04/28/2022).

Iles, Carley E and Gabriele C Hegerl (Oct. 2014). "The global precipitation response to volcanic eruptions in the CMIP5 models". en. In: *Environmental Research Letters* 9.10, p. 104012. ISSN: 1748-9326. DOI: 10.1088/1748-9326/9/10/104012. URL: https://iopscience.iop.org/article/10.1088/1748-9326/9/10/104012 (visited on 02/03/2023).

Iles, Carley E., Gabriele C. Hegerl, Andrew P. Schurer, and Xuebin Zhang (Aug. 2013). "The effect of volcanic eruptions on global precipitation: VOLCANOES AND PRECIPITATION". en. In: *Journal of Geophysical Research: Atmospheres* 118.16,

pp. 8770–8786. ISSN: 2169897X. DOI: 10.1002/jgrd.50678. URL: http://doi.wiley.com/10.1002/jgrd.50678 (visited on 02/03/2023).

Institute of Medicine and National Academy of Sciences and National Academy of Engineering (1992). *Policy Implications of Greenhouse Warming: Mitigation, Adaptation, and the Science Base*. Washington, DC: The National Academies Press. ISBN: 978-0-309-04386-1. DOI: 10.17226/1605. URL: https://www.nap.edu/catalog/1605/policy-implications-of-greenhouse-warming-mitigation-adaptation-and-the-science.

Jacobson, Tess W. P., Wenchang Yang, Gabriel A. Vecchi, and Larry W. Horowitz (Oct. 2020). "Impact of volcanic aerosol hemispheric symmetry on Sahel rainfall". en. In: *Climate Dynamics* 55.7-8, pp. 1733–1758. ISSN: 0930-7575, 1432-0894. DOI: 10.1007/s00382-020-05347-7. URL: https://link.springer.com/10.1007/s00382-020-05347-7 (visited on 04/28/2022).

Jiang, Jiu, Long Cao, Douglas G. MacMartin, Isla R. Simpson, Ben Kravitz, Wei Cheng, Daniele Visioni, Simone Tilmes, Jadwiga H. Richter, and Michael J. Mills (2019). "Stratospheric Sulfate Aerosol Geoengineering Could Alter the High-Latitude Seasonal Cycle". In: *Geophysical Research Letters* 46.23, pp. 14153–14163. ISSN: 19448007. DOI: 10.1029/2019GL085758.

Jones, A., J. Haywood, O. Boucher, B. Kravitz, and A. Robock (2010). "Geoengineering by stratospheric SO_2 injection: results from the Met Office HadGEM2 climate model and comparison with the Goddard Institute for Space Studies ModelE". In: *Atmospheric Chemistry and Physics* 10.13, pp. 5999–6006. DOI: 10.5194/acp-10-5999-2010. URL: https://acp.copernicus.org/articles/10/5999/2010/.

Jones, Anthony C., James M. Haywood, Nick Dunstone, Kerry Emanuel, Matthew K. Hawcroft, Kevin I. Hodges, and Andy Jones (Dec. 2017). "Impacts of hemispheric solar geoengineering on tropical cyclone frequency". en. In: *Nature Communications* 8.1, p. 1382. ISSN: 2041-1723. DOI: 10.1038/s41467-017-01606-0. URL: http://www.nature.com/articles/s41467-017-01606-0 (visited on 10/10/2022).

Jones, Anthony C., James M. Haywood, Andy Jones, and Valentina Aquila (June 2016). "Sensitivity of volcanic aerosol dispersion to meteorological conditions: A Pinatubo case study: Volcanic Aerosol and Meteorology". en. In: *Journal of Geophysical Research: Atmospheres* 121.12, pp. 6892–6908. ISSN: 2169897X. DOI: 10.1002/2016JD025001. URL: http://doi.wiley.com/10.1002/2016JD025001 (visited on 09/09/2022).

Junge, Christian E., Charles W. Chagnon, and James E. Manson (Feb. 1961). "STRATOSPHERIC AEROSOLS". en. In: *Journal of Meteorology* 18.1, pp. 81–108. ISSN: 0095-9634, 0095-9634. DOI: 10.1175/1520-0469(1961)018<0081:SA>2.0.CO;2. URL: http://journals.ametsoc.org/doi/10.1175/1520-0469(1961)018<0081:SA>2.0.CO;2 (visited on 01/03/2023).

Junge, Christian E. and James E. Manson (July 1961). "Stratospheric aerosol studies". en. In: *Journal of Geophysical Research* 66.7, pp. 2163–2182. ISSN: 01480227.

DOI: 10.1029/JZ066i007p02163. URL: http://doi.wiley.com/10.1029/JZ066i007p02163 (visited on 05/27/2021).

Keith, David W., Debra K. Weisenstein, John A. Dykema, and Frank N. Keutsch (Dec. 2016). "Stratospheric solar geoengineering without ozone loss". en. In: *Proceedings of the National Academy of Sciences* 113.52, pp. 14910–14914. ISSN: 0027-8424, 1091-6490. DOI: 10.1073/pnas.1615572113. URL: https://pnas.org/doi/full/10.1073/pnas.1615572113 (visited on 12/14/2022).

Kettle, A. J. (2002). "Global budget of atmospheric carbonyl sulfide: Temporal and spatial variations of the dominant sources and sinks". en. In: *Journal of Geophysical Research* 107.D22, p. 4658. ISSN: 0148-0227. DOI: 10.1029/2002JD002187. URL: http://doi.wiley.com/10.1029/2002JD002187 (visited on 10/04/2021).

Khalil, M. A. K. and R. A. Rasmussen (1984). "Global sources, lifetimes and mass balances of carbonyl sulfide (OCS) and carbon disulfide (CS2) in the earth's atmosphere". In: *Atmospheric Environment (1967)* 18.9, pp. 1805–1813.

Kilburn, Kaye H. and Raphael H. Warshaw (1995). "Hydrogen Sulfide and Reduced-Sulfur Gases Adversely Affect Neurophysiological Functions". In: *Toxicology and Industrial Health* 11.2, pp. 185–197.

Kleinschmitt, Christoph, Olivier Boucher, Slimane Bekki, François Lott, and Ulrich Platt (Sept. 2017). "The Sectional Stratospheric Sulfate Aerosol module (S3A-v1) within the LMDZ general circulation model: description and evaluation against stratospheric aerosol observations". en. In: *Geoscientific Model Development* 10.9, pp. 3359–3378. ISSN: 1991-9603. DOI: 10.5194/gmd-10-3359-2017. URL: https://gmd.copernicus.org/articles/10/3359/2017/ (visited on 05/27/2021).

Kloss, Corinna, Gwenaël Berthet, Pasquale Sellitto, Felix Ploeger, Ghassan Taha, Mariam Tidiga, Maxim Eremenko, Adriana Bossolasco, Fabrice Jégou, Jean-Baptiste Renard, and Bernard Legras (Jan. 2021). "Stratospheric aerosol layer perturbation caused by the 2019 Raikoke and Ulawun eruptions and their radiative forcing". en. In: *Atmospheric Chemistry and Physics* 21.1, pp. 535–560. ISSN: 1680-7324. DOI: 10.5194/acp-21-535-2021. URL: https://acp.copernicus.org/articles/21/535/2021/ (visited on 07/09/2022).

Kokkola, H., T. Kühn, A. Laakso, T. Bergman, K. E. J. Lehtinen, T. Mielonen, A. Arola, S. Stadtler, H. Korhonen, S. Ferrachat, U. Lohmann, D. Neubauer, I. Tegen, C. Siegenthaler-Le Drian, M. G. Schultz, I. Bey, P. Stier, N. Daskalakis, C. L. Heald, and S. Romakkaniemi (2018). "SALSA2.0: The sectional aerosol module of the aerosol–chemistry–climate model ECHAM6.3.0-HAM2.3-MOZ1.0". In: *Geoscientific Model Development* 11.9, pp. 3833–3863. DOI: 10.5194/gmd-11-3833-2018. URL: https://gmd.copernicus.org/articles/11/3833/2018/.

Kovilakam, Mahesh and Terry Deshler (Aug. 2015). "On the accuracy of stratospheric aerosol extinction derived from in situ size distribution measurements and surface area density derived from remote SAGE II and HALOE extinction measurements". en. In: *Journal of Geophysical Research: Atmospheres* 120.16, pp. 8426–8447. ISSN: 2169-897X, 2169-8996. DOI: 10.1002/2015JD023303. URL: https:

//onlinelibrary.wiley.com/doi/abs/10.1002/2015JD023303 (visited on 06/30/2021).

Kovilakam, Mahesh, Larry W. Thomason, Nicholas Ernest, Landon Rieger, Adam Bourassa, and Luis Millán (Oct. 2020). "The Global Space-based Stratospheric Aerosol Climatology (version 2.0): 1979–2018". en. In: *Earth System Science Data* 12.4, pp. 2607–2634. ISSN: 1866-3516. DOI: 10.5194/essd-12-2607-2020. URL: https://essd.copernicus.org/articles/12/2607/2020/ (visited on 06/30/2021).

Kravitz, B., P. J. Rasch, H. Wang, A. Robock, C. Gabriel, O. Boucher, J. N. S. Cole, J. Haywood, D. Ji, A. Jones, A. Lenton, J. C. Moore, H. Muri, U. Niemeier, S. Phipps, H. Schmidt, S. Watanabe, S. Yang, and J.-H. Yoon (2018). "The climate effects of increasing ocean albedo: an idealized representation of solar geoengineering". In: *Atmospheric Chemistry and Physics* 18.17, pp. 13097–13113. DOI: 10.5194/acp-18-13097-2018. URL: https://acp.copernicus.org/articles/18/13097/2018/.

Kravitz, B., A. Robock, S. Tilmes, O. Boucher, J. M. English, P. J. Irvine, A. Jones, M. G. Lawrence, M. MacCracken, H. Muri, J. C. Moore, U. Niemeier, S. J. Phipps, J. Sillmann, T. Storelvmo, H. Wang, and S. Watanabe (Oct. 2015). "The Geoengineering Model Intercomparison Project Phase 6 (GeoMIP6): simulation design and preliminary results". en. In: *Geoscientific Model Development* 8.10, pp. 3379–3392. ISSN: 1991-9603. DOI: 10.5194/gmd-8-3379-2015. URL: https://gmd.copernicus.org/articles/8/3379/2015/ (visited on 03/23/2022).

Kravitz, Ben, Jean-Francois Lamarque, Joseph J. Tribbia, Simone Tilmes, Francis Vitt, Jadwiga H. Richter, Douglas G. MacMartin, and Michael J. Mills (2017). "First Simulations of Designing Stratospheric Sulfate Aerosol Geoengineering to Meet Multiple Simultaneous Climate Objectives". In: *Journal of Geophysical Research: Atmospheres* 122.23, pp. 12,616–12,634. DOI: 10.1002/2017jd026874.

Kravitz, Ben, Douglas G. MacMartin, Hailong Wang, and Philip J. Rasch (May 2016). "Geoengineering as a design problem". en. In: *Earth System Dynamics* 7.2, pp. 469–497. ISSN: 2190-4987. DOI: 10.5194/esd-7-469-2016. URL: https://esd.copernicus.org/articles/7/469/2016/ (visited on 10/26/2022).

Kravitz, Ben, Alan Robock, Olivier Boucher, Hauke Schmidt, Karl E. Taylor, Georgiy Stenchikov, and Michael Schulz (2011). "The Geoengineering Model Intercomparison Project (GeoMIP)". In: *Atmospheric Science Letters* 12.2, pp. 162–167. DOI: 10.1002/asl.316. URL: https://rmets.onlinelibrary.wiley.com/doi/abs/10.1002/asl.316.

Kremser, Stefanie, Larry W. Thomason, Marc von Hobe, Markus Hermann, Terry Deshler, Claudia Timmreck, Matthew Toohey, Andrea Stenke, Joshua P. Schwarz, Ralf Weigel, Stephan Fueglistaler, Fred J. Prata, Jean-Paul Vernier, Hans Schlager, John E. Barnes, Juan-Carlos Antuña-Marrero, Duncan Fairlie, Mathias Palm, Emmanuel Mahieu, Justus Notholt, Markus Rex, Christine Bingen, Filip Vanhellemont, Adam Bourassa, John M. C. Plane, Daniel Klocke, Simon A. Carn, Lieven Clarisse, Thomas Trickl, Ryan Neely, Alexander D. James, Landon Rieger, James C. Wilson, and Brian Meland (June 2016). "Stratospheric aerosol-Observations,

processes, and impact on climate: Stratospheric Aerosol". en. In: *Reviews of Geophysics* 54.2, pp. 278–335. ISSN: 87551209. DOI: 10.1002/2015RG000511. URL: http://doi.wiley.com/10.1002/2015RG000511 (visited on 05/27/2021).

Kuai, Le, John R. Worden, J. Elliott Campbell, Susan S. Kulawik, King-Fai Li, Meemong Lee, Richard J. Weidner, Stephen A. Montzka, Fred L. Moore, Joe A. Berry, Ian Baker, A. Scott Denning, Huisheng Bian, Kevin W. Bowman, Junjie Liu, and Yuk L. Yung (Oct. 2015). "Estimate of carbonyl sulfide tropical oceanic surface fluxes using Aura Tropospheric Emission Spectrometer observations: FLUX INVERSION FOR OCS OCEAN SOURCE". en. In: *Journal of Geophysical Research: Atmospheres* 120.20, pp. 11,012–11,023. ISSN: 2169897X. DOI: 10.1002/2015JD023493. URL: http://doi.wiley.com/10.1002/2015JD023493 (visited on 05/27/2021).

Kuebbeler, Miriam, Ulrike Lohmann, and Johann Feichter (2012). "Effects of stratospheric sulfate aerosol geo-engineering on cirrus clouds". In: *Geophysical Research Letters* 39.23. DOI: https://doi.org/10.1029/2012GL053797. eprint: https://agupubs.onlinelibrary.wiley.com/doi/pdf/10.1029/2012GL053797. URL: https://agupubs.onlinelibrary.wiley.com/doi/abs/10.1029/2012GL053797.

Kuhn, U. and J. Kesselmeier (2000). "Environmental variables controlling the uptake of carbonyl sulfide by lichens". In: *Journal of Geophysical Research: Atmospheres* 105.D22, pp. 26783–26792. DOI: https://doi.org/10.1029/2000JD900436. URL: https://agupubs.onlinelibrary.wiley.com/doi/abs/10.1029/2000JD900436.

Laakso, A., H. Kokkola, A.-I. Partanen, U. Niemeier, C. Timmreck, K. E. J. Lehtinen, H. Hakkarainen, and H. Korhonen (Jan. 2016). "Radiative and climate impacts of a large volcanic eruption during stratospheric sulfur geoengineering". en. In: *Atmospheric Chemistry and Physics* 16.1, pp. 305–323. ISSN: 1680-7324. DOI: 10.5194/acp-16-305-2016. URL: https://acp.copernicus.org/articles/16/305/2016/ (visited on 03/03/2022).

Laakso, Anton, Hannele Korhonen, Sami Romakkaniemi, and Harri Kokkola (June 2017). "Radiative and climate effects of stratospheric sulfur geoengineering using seasonally varying injection areas". en. In: *Atmospheric Chemistry and Physics* 17.11, pp. 6957–6974. ISSN: 1680-7324. DOI: 10.5194/acp-17-6957-2017. URL: https://acp.copernicus.org/articles/17/6957/2017/ (visited on 12/16/2022).

Laakso, Anton, Ulrike Niemeier, Daniele Visioni, Simone Tilmes, and Harri Kokkola (Jan. 2022). "Dependency of the impacts of geoengineering on the stratospheric sulfur injection strategy – Part 1: Intercomparison of modal and sectional aerosol modules". en. In: *Atmospheric Chemistry and Physics* 22.1, pp. 93–118. ISSN: 1680-7324. DOI: 10.5194/acp-22-93-2022. URL: https://acp.copernicus.org/articles/22/93/2022/ (visited on 03/14/2022).

Labitzke, K. and M. P. McCormick (Jan. 1992). "Stratospheric temperature increases due to Pinatubo aerosols". en. In: *Geophysical Research Letters* 19.2, pp. 207–210.

ISSN: 00948276. DOI: 10.1029/91GL02940. URL: http://doi.wiley.com/10.1029/91GL02940 (visited on 07/21/2021).

Lacis, Andrew, James Hansen, and Makiko Sato (Aug. 1992). "Climate forcing by stratospheric aerosols". en. In: *Geophysical Research Letters* 19.15, pp. 1607–1610. ISSN: 00948276. DOI: 10.1029/92GL01620. URL: http://doi.wiley.com/10.1029/92GL01620 (visited on 07/22/2021).

Lamarque, J.-F., F. Dentener, J. McConnell, C.-U. Ro, M. Shaw, R. Vet, D. Bergmann, P. Cameron-Smith, S. Dalsoren, R. Doherty, G. Faluvegi, S. J. Ghan, B. Josse, Y. H. Lee, I. A. MacKenzie, D. Plummer, D. T. Shindell, R. B. Skeie, D. S. Stevenson, S. Strode, G. Zeng, M. Curran, D. Dahl-Jensen, S. Das, D. Fritzsche, and M. Nolan (Aug. 2013). "Multi-model mean nitrogen and sulfur deposition from the Atmospheric Chemistry and Climate Model Intercomparison Project (ACCMIP): evaluation of historical and projected future changes". en. In: *Atmospheric Chemistry and Physics* 13.16, pp. 7997–8018. ISSN: 1680-7324. DOI: 10.5194/acp-13-7997-2013. URL: https://acp.copernicus.org/articles/13/7997/2013/ (visited on 05/27/2021).

Lambert, A., R. G. Grainger, J. J. Remedios, C. D. Rodgers, M. Corney, and F. W. Taylor (June 1993). "Measurements of the evolution of the Mt. Pinatubo aerosol cloud by ISAMS". en. In: *Geophysical Research Letters* 20.12, pp. 1287–1290. ISSN: 00948276. DOI: 10.1029/93GL00827. URL: http://doi.wiley.com/10.1029/93GL00827 (visited on 02/11/2022).

Lary, D. J., M. Balluch, and S. Bekki (1994). "Solar heating rates after a volcanic eruption: The importance of SO2 absorption". In: *Quarterly Journal of the Royal Meteorological Society* 120.520, pp. 1683–1688. DOI: https://doi.org/10.1002/qj.49712052011. eprint: https://rmets.onlinelibrary.wiley.com/doi/pdf/10.1002/qj.49712052011. URL: https://rmets.onlinelibrary.wiley.com/doi/abs/10.1002/qj.49712052011.

Lee, Chon-Lin and Peter Brimblecombe (2016). "Anthropogenic contributions to global carbonyl sulfide, carbon disulfide and organosulfides fluxes". In: *Earth-Science Reviews* 160, pp. 1–18. ISSN: 0012-8252. DOI: https://doi.org/10.1016/j.earscirev.2016.06.005. URL: https://www.sciencedirect.com/science/article/pii/S0012825216301210.

Lee, Walker, Douglas MacMartin, Daniele Visioni, and Ben Kravitz (Nov. 2020). "Expanding the design space of stratospheric aerosol geoengineering to include precipitation-based objectives and explore trade-offs". en. In: *Earth System Dynamics* 11.4, pp. 1051–1072. ISSN: 2190-4987. DOI: 10.5194/esd-11-1051-2020. URL: https://esd.copernicus.org/articles/11/1051/2020/ (visited on 05/27/2021).

LeGrande, Allegra N., Kostas Tsigaridis, and Susanne E. Bauer (Sept. 2016). "Role of atmospheric chemistry in the climate impacts of stratospheric volcanic injections". en. In: *Nature Geoscience* 9.9, pp. 652–655. ISSN: 1752-0894, 1752-0908. DOI: 10.1038/ngeo2771. URL: http://www.nature.com/articles/ngeo2771 (visited on 01/16/2023).

Liu, X., P.-L. Ma, H. Wang, S. Tilmes, B. Singh, R. C. Easter, S. J. Ghan, and P. J. Rasch (2016). "Description and evaluation of a new four-mode version of the Modal Aerosol Module (MAM4) within version 5.3 of the Community Atmosphere Model". In: *Geoscientific Model Development* 9.2, pp. 505–522. DOI: 10.5194/gmd-9-505-2016. URL: https://gmd.copernicus.org/articles/9/505/2016/.

Lockley, Andrew, Doug MacMartin, and Hugh Hunt (Aug. 2020). "An update on engineering issues concerning stratospheric aerosol injection for geoengineering". In: *Environmental Research Communications* 2.8, p. 082001.

Long, Craig S. and Larry L. Stowe (Oct. 1994). "using the NOAA/AVHRR to study stratospheric aerosol optical thicknesses following the Mt. Pinatubo Eruption". en. In: *Geophysical Research Letters* 21.20, pp. 2215–2218. ISSN: 00948276. DOI: 10.1029/94GL01322. URL: http://doi.wiley.com/10.1029/94GL01322 (visited on 06/30/2021).

MacMartin, D. G., D. Visioni, B. Kravitz, J.H. Richter, T. Felgenhauer, W. R. Lee, D. R. Morrow, E. A. Parson, and M. Sugiyama (Aug. 2022). "Scenarios for modeling solar radiation modification". en. In: *Proceedings of the National Academy of Sciences* 119.33, e2202230119. ISSN: 0027-8424, 1091-6490. DOI: 10.1073/pnas.2202230119. URL: https://pnas.org/doi/full/10.1073/pnas.2202230119 (visited on 12/12/2022).

MacMartin, Douglas G., Ben Kravitz, David W. Keith, and Andrew Jarvis (July 2014). "Dynamics of the coupled human–climate system resulting from closed-loop control of solar geoengineering". en. In: *Climate Dynamics* 43.1-2, pp. 243–258. ISSN: 0930-7575, 1432-0894. DOI: 10.1007/s00382-013-1822-9. URL: http://link.springer.com/10.1007/s00382-013-1822-9 (visited on 02/08/2023).

MacMartin, Douglas G., Ben Kravitz, Michael J. Mills, Joseph J. Tribbia, Simone Tilmes, Jadwiga H. Richter, Francis Vitt, and Jean-Francois Lamarque (2017). "The Climate Response to Stratospheric Aerosol Geoengineering Can Be Tailored Using Multiple Injection Locations". In: *Journal of Geophysical Research: Atmospheres* 122.23, pp. 12,574–12,590. DOI: 10.1002/2017jd026868.

Madon, H. N. and R. F. Strickland-Constable (Aug. 1958). "Production of CS2". In: *Industrial & Engineering Chemistry* 50.8, pp. 1189–1192.

Madronich, Sasha, Simone Tilmes, Ben Kravitz, Douglas G. MacMartin, and Jadwiga H. Richter (2018). "Response of surface ultraviolet and visible radiation to stratospheric SO2 injections". In: *Atmosphere* 9.11, p. 432. ISSN: 20734433. DOI: 10.3390/atmos9110432.

Mann, G. W., K. S. Carslaw, D. V. Spracklen, D. A. Ridley, P. T. Manktelow, M. P. Chipperfield, S. J. Pickering, and C. E. Johnson (2010). "Description and evaluation of GLOMAP-mode: a modal global aerosol microphysics model for the UKCA composition-climate model". In: *Geoscientific Model Development* 3.2, pp. 519–551. DOI: 10.5194/gmd-3-519-2010. URL: https://gmd.copernicus.org/articles/3/519/2010/.

Marshall, Lauren, Jill S. Johnson, Graham W. Mann, Lindsay Lee, Sandip S. Dhomse, Leighton Regayre, Masaru Yoshioka, Ken S. Carslaw, and Anja Schmidt (Jan. 2019). "Exploring How Eruption Source Parameters Affect Volcanic Radiative Forcing Using Statistical Emulation". en. In: *Journal of Geophysical Research: Atmospheres* 124.2, pp. 964–985. ISSN: 2169-897X, 2169-8996. DOI: 10.1029/2018JD028675. URL: https://onlinelibrary.wiley.com/doi/10.1029/2018JD028675 (visited on 03/20/2022).

Marshall, Lauren, Anja Schmidt, Matthew Toohey, Ken S. Carslaw, Graham W. Mann, Michael Sigl, Myriam Khodri, Claudia Timmreck, Davide Zanchettin, William T. Ball, Slimane Bekki, James S. A. Brooke, Sandip Dhomse, Colin Johnson, Jean-Francois Lamarque, Allegra N. LeGrande, Michael J. Mills, Ulrike Niemeier, James O. Pope, Virginie Poulain, Alan Robock, Eugene Rozanov, Andrea Stenke, Timofei Sukhodolov, Simone Tilmes, Kostas Tsigaridis, and Fiona Tummon (Feb. 2018). "Multi-model comparison of the volcanic sulfate deposition from the 1815 eruption of Mt. Tambora". en. In: *Atmospheric Chemistry and Physics* 18.3, pp. 2307–2328. ISSN: 1680-7324. DOI: 10.5194/acp-18-2307-2018. URL: https://acp.copernicus.org/articles/18/2307/2018/ (visited on 05/27/2021).

Marshall, Lauren R., Elena C. Maters, Anja Schmidt, Claudia Timmreck, Alan Robock, and Matthew Toohey (May 2022). "Volcanic effects on climate: recent advances and future avenues". en. In: *Bulletin of Volcanology* 84.5, p. 54. ISSN: 1432-0819. DOI: 10.1007/s00445-022-01559-3. URL: https://link.springer.com/10.1007/s00445-022-01559-3 (visited on 05/04/2022).

Mauldin L. E., III, N. H. Zaun, Jr. McCormick M. P., J. H. Guy, and W. R. Vaughn (Apr. 1985). "Stratospheric Aerosol And Gas Experiment II Instrument: A Functional Description". In: *Optical Engineering* 24.2, p. 307. DOI: 10.1117/12.7973473.

McCormick, M. Patrick, Larry W. Thomason, and Charles R. Trepte (Feb. 1995). "Atmospheric effects of the Mt Pinatubo eruption". en. In: *Nature* 373.6513, pp. 399–404. ISSN: 0028-0836, 1476-4687. DOI: 10.1038/373399a0. URL: http://www.nature.com/articles/373399a0 (visited on 05/09/2022).

Meinshausen, M., Z. R. J. Nicholls, J. Lewis, M. J. Gidden, E. Vogel, M. Freund, U. Beyerle, C. Gessner, A. Nauels, N. Bauer, J. G. Canadell, J. S. Daniel, A. John, P. B. Krummel, G. Luderer, N. Meinshausen, S. A. Montzka, P. J. Rayner, S. Reimann, S. J. Smith, M. van den Berg, G. J. M. Velders, M. K. Vollmer, and R. H. J. Wang (2020). "The shared socio-economic pathway (SSP) greenhouse gas concentrations and their extensions to 2500". In: *Geoscientific Model Development* 13.8, pp. 3571–3605. DOI: 10.5194/gmd-13-3571-2020. URL: https://gmd.copernicus.org/articles/13/3571/2020/.

Meinshausen, Malte, S. J. Smith, K. Calvin, J. S. Daniel, M. L. T. Kainuma, J-F. Lamarque, K. Matsumoto, S. A. Montzka, S. C. B. Raper, K. Riahi, A. Thomson, G. J. M. Velders, and D. P. P. van Vuuren (2011). "The RCP greenhouse gas concentrations and their extensions from 1765 to 2300". In: *Climatic Change* 109.1, p. 213.

Mills, Michael J., Jadwiga H. Richter, Simone Tilmes, Ben Kravitz, Douglas G. MacMartin, Anne A. Glanville, Joseph J. Tribbia, Jean-François Lamarque, Francis Vitt, Anja Schmidt, Andrew Gettelman, Cecile Hannay, Julio T. Bacmeister, and Douglas E. Kinnison (Dec. 2017). "Radiative and Chemical Response to Interactive Stratospheric Sulfate Aerosols in Fully Coupled CESM1(WACCM)". en. In: *Journal of Geophysical Research: Atmospheres* 122.23, pp. 13,061 –13,078. ISSN: 2169-897X, 2169-8996. DOI: 10.1002/2017JD027006. URL: https://onlinelibrary.wiley.com/doi/10.1002/2017JD027006 (visited on 10/12/2021).

Mills, Michael J., Anja Schmidt, Richard Easter, Susan Solomon, Douglas E. Kinnison, Steven J. Ghan, Ryan R. Neely, Daniel R. Marsh, Andrew Conley, Charles G. Bardeen, and Andrew Gettelman (Mar. 2016). "Global volcanic aerosol properties derived from emissions, 1990–2014, using CESM1(WACCM)". en. In: *Journal of Geophysical Research: Atmospheres* 121.5, pp. 2332–2348. ISSN: 2169-897X, 2169-8996. DOI: 10.1002/2015JD024290. URL: https://onlinelibrary.wiley.com/doi/10.1002/2015JD024290 (visited on 12/11/2021).

Morgenstern, O., M. A. Giorgetta, K. Shibata, V. Eyring, D. W. Waugh, T. G. Shepherd, H. Akiyoshi, J. Austin, A. J. G. Baumgaertner, S. Bekki, P. Braesicke, C. Brühl, M. P. Chipperfield, D. Cugnet, M. Dameris, S. Dhomse, S. M. Frith, H. Garny, A. Gettelman, S. C. Hardiman, M. I. Hegglin, P. Jöckel, D. E. Kinnison, J.-F. Lamarque, E. Mancini, E. Manzini, M. Marchand, M. Michou, T. Nakamura, J. E. Nielsen, D. Olivié, G. Pitari, D. A. Plummer, E. Rozanov, J. F. Scinocca, D. Smale, H. Teyssèdre, M. Toohey, W. Tian, and Y. Yamashita (Aug. 2010). "Review of the formulation of present-generation stratospheric chemistry-climate models and associated external forcings". en. In: *Journal of Geophysical Research* 115. ISSN: 0148-0227. DOI: 10.1029/2009JD013728. URL: http://doi.wiley.com/10.1029/2009JD013728 (visited on 05/27/2021).

Morgenstern, O., M. I. Hegglin, E. Rozanov, F. M. O'Connor, N. L. Abraham, H. Akiyoshi, A. T. Archibald, S. Bekki, N. Butchart, M. P. Chipperfield, M. Deushi, S. S. Dhomse, R. R. Garcia, S. C. Hardiman, L. W. Horowitz, P. Jöckel, B. Josse, D. Kinnison, M. Lin, E. Mancini, M. E. Manyin, M. Marchand, V. Marécal, M. Michou, L. D. Oman, G. Pitari, D. A. Plummer, L. E. Revell, D. Saint-Martin, R. Schofield, A. Stenke, K. Stone, K. Sudo, T. Y. Tanaka, S. Tilmes, Y. Yamashita, K. Yoshida, and G. Zeng (2017). "Review of the global models used within phase 1 of the Chemistry–Climate Model Initiative (CCMI)". In: *Geoscientific Model Development* 10.2, pp. 639–671. DOI: 10.5194/gmd-10-639-2017. URL: https://gmd.copernicus.org/articles/10/639/2017/.

Morgenstern, O., K. A. Stone, R. Schofield, H. Akiyoshi, Y. Yamashita, D. E. Kinnison, R. R. Garcia, K. Sudo, D. A. Plummer, J. Scinocca, L. D. Oman, M. E. Manyin, G. Zeng, E. Rozanov, A. Stenke, L. E. Revell, G. Pitari, E. Mancini, G. Di Genova, D. Visioni, S. S. Dhomse, and M. P. Chipperfield (2018). "Ozone sensitivity to varying greenhouse gases and ozone-depleting substances in CCMI-1 simulations".

In: *Atmospheric Chemistry and Physics* 18.2, pp. 1091–1114. DOI: 10.5194/acp-18-1091-2018. URL: https://acp.copernicus.org/articles/18/1091/2018/.

Mu, Yujing, Chunmei Geng, Meizhen Wang, Hai Wu, Xiaoshan Zhang, and Guibin Jiang (2004). "Photochemical production of carbonyl sulfide in precipitation". In: *Journal of Geophysical Research: Atmospheres* 109.D13, p. D13301. DOI: https://doi.org/10.1029/2003JD004206. URL: https://agupubs.onlinelibrary.wiley.com/doi/abs/10.1029/2003JD004206.

NASA/LARC/SD/ASDC (Dec. 2012). *Stratospheric Aerosol and Gas Experiment (SAGE) II Version 7.0 Aerosol, O3, NO2 and H2O Profiles in binary format*. URL: https://doi.org/10.5067/ERBS/SAGEII/SOLAR_BINARY_L2-V7.0.

NASA/LARC/SD/ASDC (May 2012). *Surface Radiation Budget (SRB) Release 3.0 QC Shortwave monthly data in netcdf format*. URL: https://doi.org/10.5067/SRB/REL3.0_LPSA_MONTHLY_NC_L3.

Neale, Richard B., Jadwiga Richter, Sungsu Park, Peter H. Lauritzen, Stephen J. Vavrus, Philip J. Rasch, and Minghua Zhang (2013). "The Mean Climate of the Community Atmosphere Model (CAM4) in Forced SST and Fully Coupled Experiments". In: *Journal of Climate* 26.14, pp. 5150 –5168.

Neely III, Ryan R. and Anja Schmidt (Feb. 2016). *VolcanEESM: Global volcanic sulphur dioxide (SO2) emissions database from 1850 to present - Version 1.0*. DOI: https://doi:10.5285/76ebdc0b-0eed-4f70-b89e-55e606bcd568. URL: http://dx.doi.org/10.5285/76ebdc0b-0eed-4f70-b89e-55e606bcd568.

Newhall, Chris, Stephen Self, and Alan Robock (Apr. 2018). "Anticipating future Volcanic Explosivity Index (VEI) 7 eruptions and their chilling impacts". en. In: *Geosphere* 14.2, pp. 572–603. ISSN: 1553-040X. DOI: 10.1130/GES01513.1. URL: https://pubs.geoscienceworld.org/gsa/geosphere/article/14/2/572/529016/Anticipating-future-Volcanic-Explosivity-Index-VEI (visited on 03/23/2022).

Niemeier, U., C. Timmreck, H.-F. Graf, S. Kinne, S. Rast, and S. Self (2009). "Initial fate of fine ash and sulfur from large volcanic eruptions". In: *Atmospheric Chemistry and Physics* 9.22, pp. 9043–9057. DOI: 10.5194/acp-9-9043-2009. URL: https://acp.copernicus.org/articles/9/9043/2009/.

Niemeier, Ulrike, Jadwiga H. Richter, and Simone Tilmes (July 2020). "Differing responses of the quasi-biennial oscillation to artificial SO₂ injections in two global models". en. In: *Atmospheric Chemistry and Physics* 20.14, pp. 8975–8987. ISSN: 1680-7324. DOI: 10.5194/acp-20-8975-2020. URL: https://acp.copernicus.org/articles/20/8975/2020/ (visited on 11/25/2021).

Niemeier, Ulrike, Felix Riede, and Claudia Timmreck (Mar. 2021). "Simulation of ash clouds after a Laacher See-type eruption". en. In: *Climate of the Past* 17.2, pp. 633–652. ISSN: 1814-9332. DOI: 10.5194/cp-17-633-2021. URL: https://cp.copernicus.org/articles/17/633/2021/ (visited on 07/08/2022).

Niemeier, Ulrike and Hauke Schmidt (Dec. 2017). "Changing transport processes in the stratosphere by radiative heating of sulfate aerosols". en. In: *Atmospheric*

Chemistry and Physics 17.24, pp. 14871–14886. ISSN: 1680-7324. DOI: 10.5194/acp-17-14871-2017. URL: https://acp.copernicus.org/articles/17/14871/2017/ (visited on 12/01/2022).

Nowack, Peer Johannes, Nathan Luke Abraham, Peter Braesicke, and John Adrian Pyle (Mar. 2016). "Stratospheric ozone changes under solar geoengineering: implications for UV exposure and air quality". en. In: *Atmospheric Chemistry and Physics* 16.6, pp. 4191–4203. ISSN: 1680-7324. DOI: 10.5194/acp-16-4191-2016. URL: https://acp.copernicus.org/articles/16/4191/2016/ (visited on 08/08/2021).

Orbe, C., H. Yang, D. W. Waugh, G. Zeng, O. Morgenstern, D. E. Kinnison, J.-F. Lamarque, S. Tilmes, D. A. Plummer, J. F. Scinocca, B. Josse, V. Marecal, P. Jöckel, L. D. Oman, S. E. Strahan, M. Deushi, T. Y. Tanaka, K. Yoshida, H. Akiyoshi, Y. Yamashita, A. Stenke, L. Revell, T. Sukhodolov, E. Rozanov, G. Pitari, D. Visioni, K. A. Stone, R. Schofield, and A. Banerjee (2018). "Large-scale tropospheric transport in the Chemistry–Climate Model Initiative (CCMI) simulations". In: *Atmospheric Chemistry and Physics* 18.10, pp. 7217–7235.

Oswalt, J Scott, William Nichols, and John F O'Hara (1996). "Meteorological Observations of the 1991 Mount Pinatubo Eruption". en. In: *Fire and Mud Eruptions and Lahars of Mount Pinatubo, Philippines*, pp. 625–636.

Pierce, Jeffrey R., Debra K. Weisenstein, Patricia Heckendorn, Thomas Peter, and David W. Keith (2010). "Efficient formation of stratospheric aerosol for climate engineering by emission of condensible vapor from aircraft". In: *Geophysical Research Letters* 37.18. DOI: https://doi.org/10.1029/2010GL043975. eprint: https://agupubs.onlinelibrary.wiley.com/doi/pdf/10.1029/2010GL043975. URL: https://agupubs.onlinelibrary.wiley.com/doi/abs/10.1029/2010GL043975.

Pitari, G., E. Mancini, V. Rizi, and D. T. Shindell (2002). "Impact of Future Climate and Emission Changes on Stratospheric Aerosols and Ozone". In: *Journal of the Atmospheric Sciences* 59.3, pp. 414 –440. DOI: 10.1175/1520-0469(2002)059<0414:IOFCAE>2.0.CO;2. URL: https://journals.ametsoc.org/view/journals/atsc/59/3/1520-0469_2002_059_0414_iofcae_2.0.co_2.xml.

Pitari, G., V. Rizi, L. Ricciardulli, and G. Visconti (1993). "High-speed civil transport impact: Role of sulfate, nitric acid trihydrate, and ice aerosols studied with a two-dimensional model including aerosol physics". In: *Journal of Geophysical Research: Atmospheres* 98.D12, pp. 23141–23164. DOI: https://doi.org/10.1029/93JD02600. eprint: https://agupubs.onlinelibrary.wiley.com/doi/pdf/10.1029/93JD02600. URL: https://agupubs.onlinelibrary.wiley.com/doi/abs/10.1029/93JD02600.

Pitari, Giovanni, Valentina Aquila, Ben Kravitz, Alan Robock, Shingo Watanabe, Irene Cionni, Natalia De Luca, Glauco Di Genova, Eva Mancini, and Simone Tilmes (2014). "Stratospheric ozone response to sulfate geoengineering: Results from the Geoengineering Model Intercomparison Project (GeoMIP)". In: *Journal*

of Geophysical Research: Atmospheres 119.5, pp. 2629–2653. DOI: https://doi.org/10.1002/2013JD020566. eprint: https://agupubs.onlinelibrary.wiley.com/doi/pdf/10.1002/2013JD020566. URL: https://agupubs.onlinelibrary.wiley.com/doi/abs/10.1002/2013JD020566.

Pitari, Giovanni, Irene Cionni, Glauco Di Genova, Daniele Visioni, Ilaria Gandolfi, and Eva Mancini (2016a). "Impact of Stratospheric Volcanic Aerosols on Age-of-Air and Transport of Long-Lived Species". In: *Atmosphere* 7.11. ISSN: 2073-4433. DOI: 10.3390/atmos7110149. URL: https://www.mdpi.com/2073-4433/7/11/149.

Pitari, Giovanni, Daniele Visioni, Eva Mancini, Irene Cionni, Glauco Di Genova, and Ilaria Gandolfi (2016b). "Sulfate Aerosols from Non-Explosive Volcanoes: Chemical-Radiative Effects in the Troposphere and Lower Stratosphere". In: *Atmosphere* 7.7. ISSN: 2073-4433. DOI: 10.3390/atmos7070085. URL: https://www.mdpi.com/2073-4433/7/7/85.

Plumb, R. Alan (Feb. 1996). "A "tropical pipe" model of stratospheric transport". en. In: *Journal of Geophysical Research: Atmospheres* 101.D2, pp. 3957–3972. ISSN: 01480227. DOI: 10.1029/95JD03002. URL: http://doi.wiley.com/10.1029/95JD03002.

— (2002). "Stratospheric Transport". In: *Journal of the Meteorological Society of Japan. Ser. II* 80.4B, pp. 793–809. DOI: 10.2151/jmsj.80.793.

Pope, F. D., P. Braesicke, R. G. Grainger, M. Kalberer, I. M. Watson, P. J. Davidson, and R. A. Cox (Oct. 2012). "Stratospheric aerosol particles and solar-radiation management". en. In: *Nature Climate Change* 2.10, pp. 713–719. ISSN: 1758-678X, 1758-6798. DOI: 10.1038/nclimate1528. URL: http://www.nature.com/articles/nclimate1528 (visited on 12/09/2022).

Pringle, K. J., H. Tost, S. Message, B. Steil, D. Giannadaki, A. Nenes, C. Fountoukis, P. Stier, E. Vignati, and J. Lelieveld (2010). "Description and evaluation of GMXe: a new aerosol submodel for global simulations (v1)". In: *Geoscientific Model Development* 3.2, pp. 391–412. DOI: 10.5194/gmd-3-391-2010. URL: https://gmd.copernicus.org/articles/3/391/2010/.

Pueschel, R. F., P. B. Russell, D. A. Allen, G. V. Ferry, K. G. Snetsinger, J. M. Livingston, and S. Verma (1994). "Physical and optical properties of the Pinatubo volcanic aerosol: Aircraft observations with impactors and a Sun-tracking photometer". In: *Journal of Geophysical Research: Atmospheres* 99.D6, pp. 12915–12922. DOI: https://doi.org/10.1029/94JD00621. eprint: https://agupubs.onlinelibrary.wiley.com/doi/pdf/10.1029/94JD00621. URL: https://agupubs.onlinelibrary.wiley.com/doi/abs/10.1029/94JD00621.

Punge, H. J., P. Konopka, M. A. Giorgetta, and R. Müller (2009). "Effects of the quasi-biennial oscillation on low-latitude transport in the stratosphere derived from trajectory calculations". In: *Journal of Geophysical Research: Atmospheres* 114.D3, p. D03102. DOI: https://doi.org/10.1029/2008JD010518. eprint: https://agupubs.onlinelibrary.wiley.com/doi/pdf/10.1029/2008JD010518.

URL: https://agupubs.onlinelibrary.wiley.com/doi/abs/10.1029/2008JD010518.

Quaglia, I., C. Timmreck, U. Niemeier, D. Visioni, G. Pitari, C. Brodowsky, C. Brühl, S. S. Dhomse, H. Franke, A. Laakso, G. W. Mann, E. Rozanov, and T. Sukhodolov (2023). "Interactive stratospheric aerosol models' response to different amounts and altitudes of SO injection during the 1991 Pinatubo eruption". In: *Atmospheric Chemistry and Physics* 23.2, pp. 921–948. DOI: 10.5194/acp-23-921-2023. URL: https://acp.copernicus.org/articles/23/921/2023/.

Quaglia, Ilaria, Daniele Visioni, Giovanni Pitari, and Ben Kravitz (May 2022). "An approach to sulfate geoengineering with surface emissions of carbonyl sulfide". en. In: *Atmospheric Chemistry and Physics* 22.9, pp. 5757–5773. ISSN: 1680-7324. DOI: 10.5194/acp-22-5757-2022. URL: https://acp.copernicus.org/articles/22/5757/2022/ (visited on 12/20/2022).

Rantanen, Mika, Alexey Yu. Karpechko, Antti Lipponen, Kalle Nordling, Otto Hyvärinen, Kimmo Ruosteenoja, Timo Vihma, and Ari Laaksonen (Aug. 2022). "The Arctic has warmed nearly four times faster than the globe since 1979". en. In: *Communications Earth & Environment* 3.1, p. 168. ISSN: 2662-4435. DOI: 10.1038/s43247-022-00498-3. URL: https://www.nature.com/articles/s43247-022-00498-3 (visited on 02/23/2023).

RAO, C. R. NAGARAJA, L. L. STOWE, and E. P. McCLAIN (1989). "Remote sensing of aerosols over the oceans using AVHRR data Theory, practice and applications". In: *International Journal of Remote Sensing* 10.4-5, pp. 743–749. DOI: 10.1080/01431168908903915. URL: https://doi.org/10.1080/01431168908903915.

Rapp, M., J. M. C. Plane, B. Strelnikov, G. Stober, S. Ernst, J. Hedin, M. Friedrich, and U.-P. Hoppe (Dec. 2012). "In situ observations of meteor smoke particles (MSP) during the Geminids 2010: constraints on MSP size, work function and composition". en. In: *Annales Geophysicae* 30.12, pp. 1661–1673. ISSN: 1432-0576. DOI: 10.5194/angeo-30-1661-2012. URL: https://angeo.copernicus.org/articles/30/1661/2012/ (visited on 05/27/2021).

Rayner, N. A., D. E. Parker, E. B. Horton, C. K. Folland, L. V. Alexander, D. P. Rowell, E. C. Kent, and A. Kaplan (2003). "Global analyses of sea surface temperature, sea ice, and night marine air temperature since the late nineteenth century". In: *Journal of Geophysical Research: Atmospheres* 108.D14, p. 4407. DOI: https://doi.org/10.1029/2002JD002670. eprint: https://agupubs.onlinelibrary.wiley.com/doi/pdf/10.1029/2002JD002670. URL: https://agupubs.onlinelibrary.wiley.com/doi/abs/10.1029/2002JD002670.

Revell, Laura, Andrea Stenke, Beiping Luo, Stefanie Kremser, Eugene Rozanov, Timofei Sukhodolov, and Thomas Peter (July 2017). *Chemistry-climate model simulations of the Mt. Pinatubo eruption using CCMI and CMIP6 stratospheric aerosol data*. en. preprint. Aerosols/Atmospheric Modelling/Stratosphere/Chemistry (chemical composition and reactions). DOI: 10.5194/acp-2017-633. URL: https:

//acp.copernicus.org/preprints/acp-2017-633/acp-2017-633.pdf (visited on 11/15/2021).

Richter, Jadwiga H., Simone Tilmes, Michael J. Mills, Joseph J. Tribbia, Ben Kravitz, Douglas G. MacMartin, Francis Vitt, and Jean-Francois Lamarque (Dec. 2017). "Stratospheric Dynamical Response and Ozone Feedbacks in the Presence of SO_2 Injections". en. In: *Journal of Geophysical Research: Atmospheres* 122.23, pp. 12,557–12,573. ISSN: 2169-897X, 2169-8996. DOI: 10.1002/2017JD026912. URL: https://onlinelibrary.wiley.com/doi/10.1002/2017JD026912 (visited on 10/01/2021).

Richter, Jadwiga H., Daniele Visioni, Douglas G. MacMartin, David A. Bailey, Nan Rosenbloom, Brian Dobbins, Walker R. Lee, Mari Tye, and Jean-Francois Lamarque (Nov. 2022). "Assessing Responses and Impacts of Solar climate intervention on the Earth system with stratospheric aerosol injection (ARISE-SAI): protocol and initial results from the first simulations". en. In: *Geoscientific Model Development* 15.22, pp. 8221–8243. ISSN: 1991-9603. DOI: 10.5194/gmd-15-8221-2022. URL: https://gmd.copernicus.org/articles/15/8221/2022/ (visited on 02/27/2023).

Ridley, Harriet E., Yemane Asmerom, James U. L. Baldini, Sebastian F. M. Breitenbach, Valorie V. Aquino, Keith M. Prufer, Brendan J. Culleton, Victor Polyak, Franziska A. Lechleitner, Douglas J. Kennett, Minghua Zhang, Norbert Marwan, Colin G. Macpherson, Lisa M. Baldini, Tingyin Xiao, Joanne L. Peterkin, Jaime Awe, and Gerald H. Haug (Mar. 2015). "Aerosol forcing of the position of the intertropical convergence zone since ad 1550". en. In: *Nature Geoscience* 8.3, pp. 195–200. ISSN: 1752-0894, 1752-0908. DOI: 10.1038/ngeo2353. URL: http://www.nature.com/articles/ngeo2353 (visited on 04/28/2022).

Rind, David and Patrick Lonergan (1995). "Modeled impacts of stratospheric ozone and water vapor perturbations with implications for high-speed civil transport aircraft". In: *Journal of Geophysical Research: Atmospheres* 100.D4, pp. 7381–7396. DOI: https://doi.org/10.1029/95JD00196. eprint: https://agupubs.onlinelibrary.wiley.com/doi/pdf/10.1029/95JD00196. URL: https://agupubs.onlinelibrary.wiley.com/doi/abs/10.1029/95JD00196.

Robock, Alan (2000). "Volcanic eruptions and climate". In: *Reviews of Geophysics* 38.2, pp. 191–219. DOI: 10.1029/1998RG000054. URL: https://agupubs.onlinelibrary.wiley.com/doi/abs/10.1029/1998RG000054.

Robock, Alan, Caspar M. Ammann, Luke Oman, Drew Shindell, Samuel Levis, and Georgiy Stenchikov (May 2009). "Did the Toba volcanic eruption of 74 ka B.P. produce widespread glaciation?" en. In: *Journal of Geophysical Research* 114.D10, p. D10107. ISSN: 0148-0227. DOI: 10.1029/2008JD011652. URL: http://doi.wiley.com/10.1029/2008JD011652 (visited on 05/09/2022).

Robock, Alan and Jianping Mao (1995). "The Volcanic Signal in Surface Temperature Observations". In: *Journal of Climate* 8.5, pp. 1086 –1103. DOI: 10.1175/1520-0442(1995)008<1086:TVSIST>2.0.CO;2. URL: https://journals.ametsoc.org/view/journals/clim/8/5/1520-0442_1995_008_1086_tvsist_2_0_co_2.xml.

Roehl, C. M., D. Boglu, C. Brühl, and G. K. Moortgat (1995). "Infrared band intensities and global warming potentials of CF4, C2F6, C3F8, C4F10, C5F12, and C6F14". In: *Geophysical Research Letters* 22.7, pp. 815–818. DOI: https://doi.org/10.1029/95GL00488. URL: https://agupubs.onlinelibrary.wiley.com/doi/abs/10.1029/95GL00488.

Rose, W.I. and A.J. Durant (Sept. 2009). "Fine ash content of explosive eruptions". en. In: *Journal of Volcanology and Geothermal Research* 186.1-2, pp. 32–39. ISSN: 03770273. DOI: 10.1016/j.jvolgeores.2009.01.010. URL: https://linkinghub.elsevier.com/retrieve/pii/S037702730900016X (visited on 01/16/2023).

Rosen, James M. (Nov. 1964). "The vertical distribution of dust to 30 kilometers". en. In: *Journal of Geophysical Research* 69.21, pp. 4673–4676. ISSN: 01480227. DOI: 10.1029/JZ069i021p04673. URL: http://doi.wiley.com/10.1029/JZ069i021p04673 (visited on 05/09/2022).

Rosenlof, Karen H. (Nov. 2018). "Changes in water vapor and aerosols and their relation to stratospheric ozone". en. In: *Comptes Rendus Geoscience* 350.7, pp. 376–383. ISSN: 16310713. DOI: 10.1016/j.crte.2018.06.014. URL: https://linkinghub.elsevier.com/retrieve/pii/S1631071318301184 (visited on 01/16/2023).

Russell, P. B., J. M. Livingston, R. F. Pueschel, J. J. Bauman, J. B. Pollack, S. L. Brooks, P. Hamill, L. W. Thomason, L. L. Stowe, T. Deshler, E. G. Dutton, and R. W. Bergstrom (Aug. 1996). "Global to microscale evolution of the Pinatubo volcanic aerosol derived from diverse measurements and analyses". en. In: *Journal of Geophysical Research: Atmospheres* 101.D13, pp. 18745–18763. ISSN: 01480227. DOI: 10.1029/96JD01162. URL: http://doi.wiley.com/10.1029/96JD01162 (visited on 10/04/2021).

Sandoval-Soto, L and M Stanimirov (2005). "Global uptake of carbonyl sulfide (COS) by terrestrial vegetation: Estimates corrected by deposition velocities normalized to the uptake of carbon dioxide (CO2)". en. In: p. 8.

Saxena, V. K., John Anderson, and N.-H. Lin (1995). "Changes in Antarctic stratospheric aerosol characteristics due to volcanic eruptions as monitored by the Stratospheric Aerosol and Gas Experiment II satellite". en. In: *Journal of Geophysical Research* 100.D8, p. 16735. ISSN: 0148-0227. DOI: 10.1029/95JD01537. URL: http://doi.wiley.com/10.1029/95JD01537 (visited on 05/09/2022).

Schallock, Jennifer, Christoph Brühl, Christine Bingen, Michael Höpfner, Landon Rieger, and Jos Lelieveld (2021). "Radiative forcing by volcanic eruptions since 1990, calculated with a chemistry-climate model and a new emission inventory based on vertically resolved satellite measurements". In: *Atmospheric Chemistry and Physics Discussions*. DOI: 10.5194/acp-2021-654.

Schmidt, Anja, Michael J. Mills, Steven Ghan, Jonathan M. Gregory, Richard P. Allan, Timothy Andrews, Charles G. Bardeen, Andrew Conley, Piers M. Forster, Andrew Gettelman, Robert W. Portmann, Susan Solomon, and Owen B. Toon (Nov. 2018). "Volcanic Radiative Forcing From 1979 to 2015". en. In: *Journal of*

Geophysical Research: Atmospheres 123.22, pp. 12491–12508. ISSN: 2169-897X, 2169-8996. DOI: 10.1029/2018JD028776. URL: https://onlinelibrary.wiley.com/doi/abs/10.1029/2018JD028776 (visited on 05/27/2021).

Schultz, M. G., S. Stadtler, S. Schröder, D. Taraborrelli, B. Franco, J. Krefting, A. Henrot, S. Ferrachat, U. Lohmann, D. Neubauer, C. Siegenthaler-Le Drian, S. Wahl, H. Kokkola, T. Kühn, S. Rast, H. Schmidt, P. Stier, D. Kinnison, G. S. Tyndall, J. J. Orlando, and C. Wespes (2018). "The chemistry–climate model ECHAM6.3-HAM2.3-MOZ1.0". In: *Geoscientific Model Development* 11.5, pp. 1695–1723. DOI: 10.5194/gmd-11-1695-2018. URL: https://gmd.copernicus.org/articles/11/1695/2018/.

Shallcross, Sarah Elizabeth (Aug. 2020). "The role of volcanic ash in the global dispersion of the aerosol cloud from major tropical eruptions". URL: https://etheses.whiterose.ac.uk/28125/.

Sheng, J.-X., D. K. Weisenstein, B.-P. Luo, E. Rozanov, F. Arfeuille, and T. Peter (2015a). "A perturbed parameter model ensemble to investigate Mt. Pinatubo's 1991 initial sulfur mass emission". In: *Atmospheric Chemistry and Physics* 15.20, pp. 11501–11512. DOI: 10.5194/acp-15-11501-2015. URL: https://acp.copernicus.org/articles/15/11501/2015/.

Sheng, Jian-Xiong, Debra K. Weisenstein, Bei-Ping Luo, Eugene Rozanov, Andrea Stenke, Julien Anet, Heinz Bingemer, and Thomas Peter (Jan. 2015b). "Global atmospheric sulfur budget under volcanically quiescent conditions: Aerosol-chemistry-climate model predictions and validation". en. In: *Journal of Geophysical Research: Atmospheres* 120.1, pp. 256–276. ISSN: 2169897X. DOI: 10.1002/2014JD021985. URL: http://doi.wiley.com/10.1002/2014JD021985 (visited on 05/09/2022).

Shepherd, J.G. (Sept. 2009). *Geoengineering the climate: science, governance and uncertainty*. Project Report. URL: https://eprints.soton.ac.uk/156647/.

Simpson, I.R., S. Tilmes, J.H. Richter, B. Kravitz, D.G. MacMartin, M.J. Mills, J.T. Fasullo, and A.G. Pendergrass (2019). "The regional hydroclimate response to stratospheric sulfate geoengineering and the role of stratospheric heating". In: *Journal of Geophysical Research: Atmospheres*, 2019JD031093. ISSN: 2169-897X. DOI: 10.1029/2019JD031093. URL: https://onlinelibrary.wiley.com/doi/abs/10.1029/2019JD031093.

Smith, C. J., R. J. Kramer, G. Myhre, K. Alterskjær, W. Collins, A. Sima, O. Boucher, J.-L. Dufresne, P. Nabat, M. Michou, S. Yukimoto, J. Cole, D. Paynter, H. Shiogama, F. M. O'Connor, E. Robertson, A. Wiltshire, T. Andrews, C. Hannay, R. Miller, L. Nazarenko, A. Kirkev\aag, D. Olivié, S. Fiedler, A. Lewinschal, C. Mackallah, M. Dix, R. Pincus, and P. M. Forster (2020). "Effective radiative forcing and adjustments in CMIP6 models". In: *Atmospheric Chemistry and Physics* 20.16, pp. 9591–9618. DOI: 10.5194/acp-20-9591-2020. URL: https://acp.copernicus.org/articles/20/9591/2020/.

Smith, Wake and Gernot Wagner (2018). "Stratospheric aerosol injection tactics and costs in the first 15 years of deployment". In: *Environmental Research Letters* 13.12,

p. 124001. DOI: 10.1088/1748-9326/aae98d. URL: https://dx.doi.org/10.1088/1748-9326/aae98d.

Soden, Brian J., Richard T. Wetherald, Georgiy L. Stenchikov, and Alan Robock (Apr. 2002). "Global Cooling After the Eruption of Mount Pinatubo: A Test of Climate Feedback by Water Vapor". en. In: *Science* 296.5568, pp. 727–730. ISSN: 0036-8075, 1095-9203. DOI: 10.1126/science.296.5568.727. URL: https://www.science.org/doi/10.1126/science.296.5568.727 (visited on 02/11/2022).

Solomon, Susan, Karen H. Rosenlof, Robert W. Portmann, John S. Daniel, Sean M. Davis, Todd J. Sanford, and Gian-Kasper Plattner (2010). "Contributions of Stratospheric Water Vapor to Decadal Changes in the Rate of Global Warming". In: *Science* 327.5970, pp. 1219–1223. DOI: 10.1126/science.1182488. eprint: https://www.science.org/doi/pdf/10.1126/science.1182488. URL: https://www.science.org/doi/abs/10.1126/science.1182488.

Steinbacher, Martin, Heinz G. Bingemer, and Ulrich Schmidt (2004). "Measurements of the exchange of carbonyl sulfide (OCS) and carbon disulfide (CS2) between soil and atmosphere in a spruce forest in central Germany". In: *Atmospheric Environment* 38.35, pp. 6043–6052. ISSN: 1352-2310. DOI: https://doi.org/10.1016/j.atmosenv.2004.06.022. URL: https://www.sciencedirect.com/science/article/pii/S135223100400617X.

Stenchikov, Georgiy, Alexander Ukhov, Sergey Osipov, Ravan Ahmadov, Georg Grell, Karen Cady-Pereira, Eli Mlawer, and Michael Iacono (May 2021). "How Does a Pinatubo-Size Volcanic Cloud Reach the Middle Stratosphere?" en. In: *Journal of Geophysical Research: Atmospheres* 126.10, e2020JD033829. ISSN: 2169-897X, 2169-8996. DOI: 10.1029/2020JD033829. URL: https://onlinelibrary.wiley.com/doi/10.1029/2020JD033829 (visited on 09/14/2022).

Stevens, Bjorn, Marco Giorgetta, Monika Esch, Thorsten Mauritsen, Traute Crueger, Sebastian Rast, Marc Salzmann, Hauke Schmidt, Jürgen Bader, Karoline Block, Renate Brokopf, Irina Fast, Stefan Kinne, Luis Kornblueh, Ulrike Lohmann, Robert Pincus, Thomas Reichler, and Erich Roeckner (2013). "Atmospheric component of the MPI-M Earth System Model: ECHAM6". In: *Journal of Advances in Modeling Earth Systems* 5.2, pp. 146–172. DOI: https://doi.org/10.1002/jame.20015. eprint: https://agupubs.onlinelibrary.wiley.com/doi/pdf/10.1002/jame.20015. URL: https://agupubs.onlinelibrary.wiley.com/doi/abs/10.1002/jame.20015.

Stier, P., J. Feichter, S. Kinne, S. Kloster, E. Vignati, J. Wilson, L. Ganzeveld, I. Tegen, M. Werner, Y. Balkanski, M. Schulz, O. Boucher, A. Minikin, and A. Petzold (2005). "The aerosol-climate model ECHAM5-HAM". In: *Atmospheric Chemistry and Physics* 5.4, pp. 1125–1156. DOI: 10.5194/acp-5-1125-2005. URL: https://acp.copernicus.org/articles/5/1125/2005/.

Stimler, Keren, Stephen A. Montzka, Joseph A. Berry, Yinon Rudich, and Dan Yakir (2010). "Relationships between carbonyl sulfide (COS) and CO2 during leaf gas exchange". In: *New Phytologist* 186.4, pp. 869–878. DOI: https://doi.org/10.

1111/j.1469-8137.2010.03218.x. URL: https://nph.onlinelibrary.wiley.com/doi/abs/10.1111/j.1469-8137.2010.03218.x.

Sukhodolov, Timofei, Jian-Xiong Sheng, Aryeh Feinberg, Bei-Ping Luo, Thomas Peter, Laura Revell, Andrea Stenke, Debra K. Weisenstein, and Eugene Rozanov (July 2018). "Stratospheric aerosol evolution after Pinatubo simulated with a coupled size-resolved aerosol–chemistry–climate model, SOCOL-AERv1.0". en. In: *Geoscientific Model Development* 11.7, pp. 2633–2647. ISSN: 1991-9603. DOI: 10.5194/gmd-11-2633-2018. URL: https://gmd.copernicus.org/articles/11/2633/2018/ (visited on 06/30/2021).

Svoronos, Paris D. N. and Thomas J. Bruno (Oct. 2002). "Carbonyl Sulfide: A Review of Its Chemistry and Properties". In: *Industrial & Engineering Chemistry Research* 41.22, pp. 5321–5336. DOI: https://doi.org/10.1021/ie020365n.

Taylor, Karl E. (Apr. 2001). "Summarizing multiple aspects of model performance in a single diagram". en. In: *Journal of Geophysical Research: Atmospheres* 106.D7, pp. 7183–7192. ISSN: 01480227. DOI: 10.1029/2000JD900719. URL: http://doi.wiley.com/10.1029/2000JD900719 (visited on 05/27/2021).

Telford, P J, P Braesicke, O Morgenstern, and J A Pyle (2008). "Technical Note: Description and assessment of a nudged version of the new dynamics Unified Model". en. In: *Atmos. Chem. Phys.*, p. 12.

Textor, Christiane, Hans-F. Graf, Michael Herzog, and J. M. Oberhuber (2003). "Injection of gases into the stratosphere by explosive volcanic eruptions". In: *Journal of Geophysical Research: Atmospheres* 108.D19. DOI: https://doi.org/10.1029/2002JD002987. eprint: https://agupubs.onlinelibrary.wiley.com/doi/pdf/10.1029/2002JD002987. URL: https://agupubs.onlinelibrary.wiley.com/doi/abs/10.1029/2002JD002987.

Textor, Christiane, Hans-F Graf, Claudia Timmreck, and Alan Robock (Jan. 2004). "Emissions from volcanoes". In: *Advances in Global Change Research* 18. DOI: 10.1007/978-1-4020-2167-1_7.

Thomas, M. A., M. A. Giorgetta, C. Timmreck, H.-F. Graf, and G. Stenchikov (May 2009). "Simulation of the climate impact of Mt. Pinatubo eruption using ECHAM5 – Part 2: Sensitivity to the phase of the QBO and ENSO". en. In: *Atmospheric Chemistry and Physics* 9.9, pp. 3001–3009. ISSN: 1680-7324. DOI: 10.5194/acp-9-3001-2009. URL: https://acp.copernicus.org/articles/9/3001/2009/ (visited on 02/08/2022).

Thomason, L W and S P Burton (2008). "SAGE II measurements of stratospheric aerosol properties at non-volcanic levels". en. In: *Atmos. Chem. Phys.*, p. 13.

Thomason, L. W., L. R. Poole, and T. Deshler (Apr. 1997). "A global climatology of stratospheric aerosol surface area density deduced from Stratospheric Aerosol and Gas Experiment II measurements: 1984-1994". en. In: *Journal of Geophysical Research: Atmospheres* 102.D7, pp. 8967–8976. ISSN: 01480227. DOI: 10.1029/96JD02962. URL: http://doi.wiley.com/10.1029/96JD02962 (visited on 03/07/2022).

Thomason, Larry W., Nicholas Ernest, Luis Millán, Landon Rieger, Adam Bourassa, Jean-Paul Vernier, Gloria Manney, Beiping Luo, Florian Arfeuille, and Thomas Peter (Mar. 2018). "A global space-based stratospheric aerosol climatology: 1979–2016". en. In: *Earth System Science Data* 10.1, pp. 469–492. ISSN: 1866-3516. DOI: 10.5194/essd-10-469-2018. URL: https://essd.copernicus.org/articles/10/469/2018/ (visited on 06/30/2021).

Tilmes, S., M. J. Mills, U. Niemeier, H. Schmidt, A. Robock, B. Kravitz, J.-F. Lamarque, G. Pitari, and J. M. English (2015). "A new Geoengineering Model Intercomparison Project (GeoMIP) experiment designed for climate and chemistry models". In: *Geoscientific Model Development* 8.1, pp. 43–49. DOI: 10.5194/gmd-8-43-2015. URL: https://gmd.copernicus.org/articles/8/43/2015/.

Tilmes, S., J. H. Richter, B. Kravitz, D. G. MacMartin, A. S. Glanville, D. Visioni, D. E. Kinnison, and R. Müller (2021). "Sensitivity of Total Column Ozone to Stratospheric Sulfur Injection Strategies". In: *Geophysical Research Letters* 48.19. e2021GL094058 2021GL094058, e2021GL094058. DOI: https://doi.org/10.1029/2021GL094058. eprint: https://agupubs.onlinelibrary.wiley.com/doi/pdf/10.1029/2021GL094058. URL: https://agupubs.onlinelibrary.wiley.com/doi/abs/10.1029/2021GL094058.

Tilmes, Simone, Rolando R. Garcia, Douglas E. Kinnison, Andrew Gettelman, and Philip J. Rasch (June 2009). "Impact of geoengineered aerosols on the troposphere and stratosphere". en. In: *Journal of Geophysical Research* 114.D12, p. D12305. ISSN: 0148-0227. DOI: 10.1029/2008JD011420. URL: https://onlinelibrary.wiley.com/doi/10.1029/2008JD011420 (visited on 07/20/2021).

Tilmes, Simone, Rolf Müller, and Ross Salawitch (2008). "The Sensitivity of Polar Ozone Depletion to Proposed Geoengineering Schemes". In: *Science* 320.5880, pp. 1201–1204. ISSN: 0036-8075. DOI: 10.1126/science.1153966. URL: https://science.sciencemag.org/content/320/5880/1201.

Tilmes, Simone, Jadwiga H. Richter, Ben Kravitz, Douglas G. Macmartin, Michael J. Mills, Isla R. Simpson, Anne S. Glanville, John T. Fasullo, Adam S. Phillips, Jean Francois Lamarque, Joseph Tribbia, Jim Edwards, Sheri Mickelson, and Siddhartha Ghosh (2018a). "CESM1(WACCM) stratospheric aerosol geoengineering large ensemble project". In: *Bulletin of the American Meteorological Society* 11, pp. 2361–2371. ISSN: 00030007. DOI: 10.1175/BAMS-D-17-0267.1.

Tilmes, Simone, Jadwiga H. Richter, Ben Kravitz, Douglas G. MacMartin, Michael J. Mills, Isla R. Simpson, Anne S. Glanville, John T. Fasullo, Adam S. Phillips, Jean-Francois Lamarque, Joseph Tribbia, Jim Edwards, Sheri Mickelson, and Siddhartha Ghosh (2018b). "CESM1(WACCM) Stratospheric Aerosol Geoengineering Large Ensemble Project". In: *Bulletin of the American Meteorological Society* 99.11, pp. 2361 –2371. DOI: 10.1175/BAMS-D-17-0267.1. URL: https://journals.ametsoc.org/view/journals/bams/99/11/bams-d-17-0267.1.xml.

Tilmes, Simone, Jadwiga H. Richter, Michael J. Mills, Ben Kravitz, Douglas G. MacMartin, Rolando R. Garcia, Douglas E. Kinnison, Jean-Francois Lamarque, Joseph

Tribbia, and Francis Vitt (May 2018c). "Effects of Different Stratospheric SO_2 Injection Altitudes on Stratospheric Chemistry and Dynamics". en. In: *Journal of Geophysical Research: Atmospheres* 123.9, pp. 4654–4673. ISSN: 2169-897X, 2169-8996. DOI: 10.1002/2017JD028146. URL: https://onlinelibrary.wiley.com/doi/10.1002/2017JD028146 (visited on 05/27/2021).

Tilmes, Simone, Jadwiga H. Richter, Michael J. Mills, Ben Kravitz, Douglas G. MacMartin, Francis Vitt, Joseph J. Tribbia, and Jean-Francois Lamarque (Dec. 2017). "Sensitivity of Aerosol Distribution and Climate Response to Stratospheric SO_2 Injection Locations". en. In: *Journal of Geophysical Research: Atmospheres* 122.23. ISSN: 2169-897X, 2169-8996. DOI: 10.1002/2017JD026888. URL: https://onlinelibrary.wiley.com/doi/10.1002/2017JD026888 (visited on 02/09/2022).

Tilmes, Simone, Daniele Visioni, Andy Jones, James Haywood, Roland Séférian, Pierre Nabat, Olivier Boucher, Ewa Monica Bednarz, and Ulrike Niemeier (Apr. 2022). "Stratospheric ozone response to sulfate aerosol and solar dimming climate interventions based on the G6 Geoengineering Model Intercomparison Project (GeoMIP) simulations". en. In: *Atmospheric Chemistry and Physics* 22.7, pp. 4557–4579. ISSN: 1680-7324. DOI: 10.5194/acp-22-4557-2022. URL: https://acp.copernicus.org/articles/22/4557/2022/ (visited on 04/18/2022).

Timmreck, Claudia (Nov. 2001). "Three-dimensional simulation of stratospheric background aerosol: First results of a multiannual general circulation model simulation". In: 106.D22, pp. 28,313–28,332. DOI: 10.1029/2001JD000765.

Timmreck, Claudia, Hans-F. Graf, and Ingo Kirchner (1999). "A one and half year interactive MA/ECHAM4 simulation of Mount Pinatubo Aerosol". In: *Journal of Geophysical Research: Atmospheres* 104.D8, pp. 9337–9359. DOI: https://doi.org/10.1029/1999JD900088. eprint: https://agupubs.onlinelibrary.wiley.com/doi/pdf/10.1029/1999JD900088. URL: https://agupubs.onlinelibrary.wiley.com/doi/abs/10.1029/1999JD900088.

Timmreck, Claudia, Hans-F. Graf, Davide Zanchettin, Stefan Hagemann, Thomas Kleinen, and Kirstin Krüger (May 2012). "Climate response to the Toba supereruption: Regional changes". en. In: *Quaternary International* 258, pp. 30–44. ISSN: 10406182. DOI: 10.1016/j.quaint.2011.10.008. URL: https://linkinghub.elsevier.com/retrieve/pii/S1040618211005817 (visited on 04/28/2022).

Timmreck, Claudia, Graham W. Mann, Valentina Aquila, Rene Hommel, Lindsay A. Lee, Anja Schmidt, Christoph Brühl, Simon Carn, Mian Chin, Sandip S. Dhomse, Thomas Diehl, Jason M. English, Michael J. Mills, Ryan Neely, Jianxiong Sheng, Matthew Toohey, and Debra Weisenstein (July 2018). "The Interactive Stratospheric Aerosol Model Intercomparison Project (ISA-MIP): motivation and experimental design". en. In: *Geoscientific Model Development* 11.7, pp. 2581–2608. ISSN: 1991-9603. DOI: 10.5194/gmd-11-2581-2018. URL: https://gmd.copernicus.org/articles/11/2581/2018/ (visited on 06/09/2021).

Toohey, M., K. Krüger, M. Bittner, C. Timmreck, and H. Schmidt (Dec. 2014). "The impact of volcanic aerosol on the Northern Hemisphere stratospheric polar vortex: mechanisms and sensitivity to forcing structure". en. In: *Atmospheric Chemistry and Physics* 14.23, pp. 13063–13079. ISSN: 1680-7324. DOI: 10.5194/acp-14-13063-2014. URL: https://acp.copernicus.org/articles/14/13063/2014/ (visited on 07/13/2022).

Toohey, M., K. Krüger, U. Niemeier, and C. Timmreck (2011). "The influence of eruption season on the global aerosol evolution and radiative impact of tropical volcanic eruptions". In: *Atmospheric Chemistry and Physics* 11.23, pp. 12351–12367. DOI: 10.5194/acp-11-12351-2011. URL: https://acp.copernicus.org/articles/11/12351/2011/.

Toon, Owen B., C. P. McKay, T. P. Ackerman, and K. Santhanam (1989). "Rapid calculation of radiative heating rates and photodissociation rates in inhomogeneous multiple scattering atmospheres". In: *Journal of Geophysical Research: Atmospheres* 94.D13, pp. 16287–16301. DOI: https://doi.org/10.1029/JD094iD13p16287. eprint: https://agupubs.onlinelibrary.wiley.com/doi/pdf/10.1029/JD094iD13p16287. URL: https://agupubs.onlinelibrary.wiley.com/doi/abs/10.1029/JD094iD13p16287.

Trenberth, Kevin E. and Aiguo Dai (Aug. 2007). "Effects of Mount Pinatubo volcanic eruption on the hydrological cycle as an analog of geoengineering: PINATUBO AND THE HYDROLOGICAL CYCLE". en. In: *Geophysical Research Letters* 34.15. ISSN: 00948276. DOI: 10.1029/2007GL030524. URL: http://doi.wiley.com/10.1029/2007GL030524 (visited on 04/21/2022).

Trepte, Charles R. and Matthew H. Hitchman (Feb. 1992). "Tropical stratospheric circulation deduced from satellite aerosol data". en. In: *Nature* 355.6361, pp. 626–628. ISSN: 0028-0836, 1476-4687. DOI: 10.1038/355626a0. URL: http://www.nature.com/articles/355626a0 (visited on 10/13/2021).

Trisos, Christopher H., Giuseppe Amatulli, Jessica Gurevitch, Alan Robock, Lili Xia, and Brian Zambri (Mar. 2018). "Potentially dangerous consequences for biodiversity of solar geoengineering implementation and termination". en. In: *Nature Ecology & Evolution* 2.3, pp. 475–482. ISSN: 2397-334X. DOI: 10.1038/s41559-017-0431-0. URL: http://www.nature.com/articles/s41559-017-0431-0 (visited on 08/25/2021).

Ulshofer, V. S., O. R. Flock, G. Uher, and M. O. Andreae (1996). "Photochemical production and air-sea exchange of carbonyl sulfide in the eastern Mediterranean Sea". In: *Marine Chemistry* 53.1, pp. 25–39.

Van Diest, H. and J. Kesselmeier (2008). "Soil atmosphere exchange of carbonyl sulfide (COS) regulated by diffusivity depending on water-filled pore space". In: *Biogeosciences* 5.2, pp. 475–483. DOI: 10.5194/bg-5-475-2008. URL: https://bg.copernicus.org/articles/5/475/2008/.

Vattioni, S., D. Weisenstein, D. Keith, A. Feinberg, T. Peter, and A. Stenke (2019). "Exploring accumulation-mode H_2SO_4 versus SO_2 stratospheric sulfate geoengineering in a sectional aerosol–chemistry–climate model". In: *Atmospheric Chemistry and Physics* 19.7, pp. 4877–4897. DOI: 10.5194/acp-19-4877-2019. URL: https://acp.copernicus.org/articles/19/4877/2019/.

Vaughan, G., D. P. Wareing, S. B. Jones, L. Thomas, and N. Larsen (June 1994). "Lidar measurements of Mt. Pinatubo aerosols at Aberystwyth from August 1991 through March 1992". en. In: *Geophysical Research Letters* 21.13, pp. 1315–1318. ISSN: 00948276. DOI: 10.1029/93GL02893. URL: http://doi.wiley.com/10.1029/93GL02893 (visited on 11/21/2022).

Vehkamäki, H., M. Kulmala, I. Napari, K. E. J. Lehtinen, C. Timmreck, M. Noppel, and A. Laaksonen (2002). "An improved parameterization for sulfuric acid–water nucleation rates for tropospheric and stratospheric conditions". In: *Journal of Geophysical Research: Atmospheres* 107.D22, AAC 3–1–AAC 3–10. DOI: https://doi.org/10.1029/2002JD002184. eprint: https://agupubs.onlinelibrary.wiley.com/doi/pdf/10.1029/2002JD002184. URL: https://agupubs.onlinelibrary.wiley.com/doi/abs/10.1029/2002JD002184.

Visioni, D., G. Pitari, and V. Aquila (2017). "Sulfate geoengineering: a review of the factors controlling the needed injection of sulfur dioxide". In: *Atmospheric Chemistry and Physics* 17.6, pp. 3879–3889. DOI: 10.5194/acp-17-3879-2017. URL: https://acp.copernicus.org/articles/17/3879/2017/.

Visioni, Daniele, Douglas G. MacMartin, and Ben Kravitz (2021). "Is Turning Down the Sun a Good Proxy for Stratospheric Sulfate Geoengineering?" In: *Journal of Geophysical Research: Atmospheres* 126.5, e2020JD033952. DOI: https://doi.org/10.1029/2020JD033952. URL: https://agupubs.onlinelibrary.wiley.com/doi/abs/10.1029/2020JD033952.

Visioni, Daniele, Douglas G. MacMartin, Ben Kravitz, Olivier Boucher, Andy Jones, Thibaut Lurton, Michou Martine, Michael J. Mills, Pierre Nabat, Ulrike Niemeier, Roland Séférian, and Simone Tilmes (July 2021). "Identifying the sources of uncertainty in climate model simulations of solar radiation modification with the G6sulfur and G6solar Geoengineering Model Intercomparison Project (GeoMIP) simulations". en. In: *Atmospheric Chemistry and Physics* 21.13, pp. 10039–10063. ISSN: 1680-7324. DOI: 10.5194/acp-21-10039-2021. URL: https://acp.copernicus.org/articles/21/10039/2021/ (visited on 03/23/2022).

Visioni, Daniele, Douglas G. MacMartin, Ben Kravitz, Walker Lee, Isla R. Simpson, and Jadwiga H. Richter (Sept. 2020a). "Reduced Poleward Transport Due to Stratospheric Heating Under Stratospheric Aerosols Geoengineering". en. In: *Geophysical Research Letters* 47.17. ISSN: 0094-8276, 1944-8007. DOI: 10.1029/2020GL089470. URL: https://onlinelibrary.wiley.com/doi/10.1029/2020GL089470 (visited on 10/04/2021).

Visioni, Daniele, Douglas G. MacMartin, Ben Kravitz, Jadwiga H. Richter, Simone Tilmes, and Michael J. Mills (June 2020b). "Seasonally Modulated Stratospheric

Aerosol Geoengineering Alters the Climate Outcomes". en. In: *Geophysical Research Letters* 47.12. ISSN: 0094-8276, 1944-8007. DOI: 10.1029/2020GL088337. URL: https://onlinelibrary.wiley.com/doi/10.1029/2020GL088337 (visited on 12/05/2022).

Visioni, Daniele, Douglas G. MacMartin, Ben Kravitz, Simone Tilmes, Michael J. Mills, Jadwiga H. Richter, and Matthew P. Boudreau (July 2019). "Seasonal Injection Strategies for Stratospheric Aerosol Geoengineering". en. In: *Geophysical Research Letters* 46.13, pp. 7790–7799. ISSN: 0094-8276, 1944-8007. DOI: 10.1029/2019GL083680. URL: https://onlinelibrary.wiley.com/doi/10.1029/2019GL083680 (visited on 02/09/2022).

Visioni, Daniele, Giovanni Pitari, Glauco di Genova, Simone Tilmes, and Irene Cionni (Oct. 2018a). "Upper tropospheric ice sensitivity to sulfate geoengineering". en. In: *Atmospheric Chemistry and Physics* 18.20, pp. 14867–14887. ISSN: 1680-7324. DOI: 10.5194/acp-18-14867-2018. URL: https://acp.copernicus.org/articles/18/14867/2018/ (visited on 05/27/2021).

Visioni, Daniele, Giovanni Pitari, Paolo Tuccella, and Gabriele Curci (Feb. 2018b). "Sulfur deposition changes under sulfate geoengineering conditions: quasi-biennial oscillation effects on the transport and lifetime of stratospheric aerosols". en. In: *Atmospheric Chemistry and Physics* 18.4, pp. 2787–2808. ISSN: 1680-7324. DOI: 10.5194/acp-18-2787-2018. URL: https://acp.copernicus.org/articles/18/2787/2018/ (visited on 05/27/2021).

Walters, D. N., K. D. Williams, I. A. Boutle, A. C. Bushell, J. M. Edwards, P. R. Field, A. P. Lock, C. J. Morcrette, R. A. Stratton, J. M. Wilkinson, M. R. Willett, N. Bellouin, A. Bodas-Salcedo, M. E. Brooks, D. Copsey, P. D. Earnshaw, S. C. Hardiman, C. M. Harris, R. C. Levine, C. MacLachlan, J. C. Manners, G. M. Martin, S. F. Milton, M. D. Palmer, M. J. Roberts, J. M. Rodríguez, W. J. Tennant, and P. L. Vidale (2014). "The Met Office Unified Model Global Atmosphere 4.0 and JULES Global Land 4.0 configurations". In: *Geoscientific Model Development* 7.1, pp. 361–386. DOI: 10.5194/gmd-7-361-2014. URL: https://gmd.copernicus.org/articles/7/361/2014/.

Wang, Lu, Ying Yang, Wenlong Shen, Xiangming Kong, Ping Li, Jianguo Yu, and Alirio E. Rodrigues (June 2013). "CO2 Capture from Flue Gas in an Existing Coal-Fired Power Plant by Two Successive Pilot-Scale VPSA Units". In: *Industrial & Engineering Chemistry Research* 52.23, pp. 7947–7955.

Waugh, D. W., K. M. Grise, W. J. M. Seviour, S. M. Davis, N. Davis, O. Adam, S.-W. Son, I. R. Simpson, P. W. Staten, A. C. Maycock, C. C. Ummenhofer, T. Birner, and A. Ming (Sept. 2018). "Revisiting the Relationship among Metrics of Tropical Expansion". en. In: *Journal of Climate* 31.18, pp. 7565–7581. ISSN: 0894-8755, 1520-0442. DOI: 10.1175/JCLI-D-18-0108.1. URL: https://journals.ametsoc.org/view/journals/clim/31/18/jcli-d-18-0108.1.xml (visited on 06/17/2022).

Weisenstein, D. K., D. W. Keith, and J. A. Dykema (Oct. 2015). "Solar geoengineering using solid aerosol in the stratosphere". en. In: *Atmospheric Chemistry and Physics*

15.20, pp. 11835–11859. ISSN: 1680-7324. DOI: 10.5194/acp-15-11835-2015. URL: https://acp.copernicus.org/articles/15/11835/2015/ (visited on 12/14/2022).

Weisenstein, D. K., D. Visioni, H. Franke, U. Niemeier, S. Vattioni, G. Chiodo, T. Peter, and D. W. Keith (2022). "An interactive stratospheric aerosol model intercomparison of solar geoengineering by stratospheric injection of SO_2 or accumulation-mode sulfuric acid aerosols". In: *Atmospheric Chemistry and Physics* 22.5, pp. 2955–2973. DOI: 10.5194/acp-22-2955-2022. URL: https://acp.copernicus.org/articles/22/2955/2022/.

Weisenstein, Debra K., Glenn K. Yue, Malcolm K. W. Ko, Nien-Dak Sze, Jose M. Rodriguez, and Courtney J. Scott (1997). "A two-dimensional model of sulfur species and aerosols". In: *Journal of Geophysical Research: Atmospheres* 102.D11, pp. 13019–13035. DOI: https://doi.org/10.1029/97JD00901. eprint: https://agupubs.onlinelibrary.wiley.com/doi/pdf/10.1029/97JD00901. URL: https://agupubs.onlinelibrary.wiley.com/doi/abs/10.1029/97JD00901.

West, J. Jason and Arlene M. Fiore (July 2005). "Management of Tropospheric Ozone by Reducing Methane Emissions". en. In: *Environmental Science & Technology* 39.13, pp. 4685–4691. ISSN: 0013-936X, 1520-5851. DOI: 10.1021/es048629f. URL: https://pubs.acs.org/doi/10.1021/es048629f (visited on 08/11/2021).

Whelan, M. E., T. W. Hilton, J. A. Berry, M. Berkelhammer, A. R. Desai, and J. E. Campbell (2016). "Carbonyl sulfide exchange in soils for better estimates of ecosystem carbon uptake". In: *Atmospheric Chemistry and Physics* 16.6, pp. 3711–3726.

Winker, D. M. and M. T. Osborn (1992a). "Airborne lidar observations of the Pinatubo volcanic plume". In: *Geophysical Research Letters* 19.2, pp. 167–170. DOI: https://doi.org/10.1029/91GL02867. eprint: https://agupubs.onlinelibrary.wiley.com/doi/pdf/10.1029/91GL02867. URL: https://agupubs.onlinelibrary.wiley.com/doi/abs/10.1029/91GL02867.

— (1992b). "Preliminary analysis of observations of the Pinatubo volcanic plume with a polarization-sensitive lidar". In: *Geophysical Research Letters* 19.2, pp. 171–174. DOI: https://doi.org/10.1029/91GL02866. eprint: https://agupubs.onlinelibrary.wiley.com/doi/pdf/10.1029/91GL02866. URL: https://agupubs.onlinelibrary.wiley.com/doi/abs/10.1029/91GL02866.

Xia, Lili, Peer J. Nowack, Simone Tilmes, and Alan Robock (Oct. 2017). "Impacts of stratospheric sulfate geoengineering on tropospheric ozone". en. In: *Atmospheric Chemistry and Physics* 17.19, pp. 11913–11928. ISSN: 1680-7324. DOI: 10.5194/acp-17-11913-2017. URL: https://acp.copernicus.org/articles/17/11913/2017/ (visited on 08/11/2021).

Yang, Wenchang, Gabriel A. Vecchi, Stephan Fueglistaler, Larry W. Horowitz, David J. Luet, Ángel G. Muñoz, David Paynter, and Seth Underwood (2019). "Climate Impacts From Large Volcanic Eruptions in a High-Resolution Climate Model: The Importance of Forcing Structure". In: *Geophysical Research Letters* 46.13, pp. 7690–

7699. DOI: https://doi.org/10.1029/2019GL082367. URL: https://agupubs.onlinelibrary.wiley.com/doi/abs/10.1029/2019GL082367.

Young, Richard E., Howard Houben, and Owen B. Toon (Mar. 1994). "Radiatively forced dispersion of the Mt. Pinatubo volcanic cloud and induced temperature perturbations in the stratosphere during the first few months following the eruption". en. In: *Geophysical Research Letters* 21.5, pp. 369–372. ISSN: 00948276. DOI: 10.1029/93GL03302. URL: http://doi.wiley.com/10.1029/93GL03302 (visited on 10/06/2021).

Yue, Glenn K. (1981). "The formation and growth of sulfate aerosols in the stratosphere". In: *Atmospheric Environment (1967)* 15.4, pp. 549–556. ISSN: 0004-6981. DOI: https://doi.org/10.1016/0004-6981(81)90185-2. URL: https://www.sciencedirect.com/science/article/pii/0004698181901852.

Zanchettin, Davide, Myriam Khodri, Claudia Timmreck, Matthew Toohey, Anja Schmidt, Edwin P. Gerber, Gabriele Hegerl, Alan Robock, Francesco S. R. Pausata, William T. Ball, Susanne E. Bauer, Slimane Bekki, Sandip S. Dhomse, Allegra N. LeGrande, Graham W. Mann, Lauren Marshall, Michael Mills, Marion Marchand, Ulrike Niemeier, Virginie Poulain, Eugene Rozanov, Angelo Rubino, Andrea Stenke, Kostas Tsigaridis, and Fiona Tummon (Aug. 2016). "The Model Intercomparison Project on the climatic response toVolcanic forcing (VolMIP): experimental design and forcing input data for CMIP6". en. In: *Geoscientific Model Development* 9.8, pp. 2701–2719. ISSN: 1991-9603. DOI: 10.5194/gmd-9-2701-2016. URL: https://gmd.copernicus.org/articles/9/2701/2016/ (visited on 11/18/2021).

Zhu, Yunqian, Owen B. Toon, Eric J. Jensen, Charles G. Bardeen, Michael J. Mills, Margaret A. Tolbert, Pengfei Yu, and Sarah Woods (Dec. 2020). "Persisting volcanic ash particles impact stratospheric SO2 lifetime and aerosol optical properties". en. In: *Nature Communications* 11.1, p. 4526. ISSN: 2041-1723. DOI: 10.1038/s41467-020-18352-5. URL: http://www.nature.com/articles/s41467-020-18352-5 (visited on 06/08/2021).

Zuo, Meng, Tianjun Zhou, and Wenmin Man (July 2019). "Hydroclimate Responses over Global Monsoon Regions Following Volcanic Eruptions at Different Latitudes". en. In: *Journal of Climate* 32.14, pp. 4367–4385. ISSN: 0894-8755, 1520-0442. DOI: 10.1175/JCLI-D-18-0707.1. URL: https://journals.ametsoc.org/view/journals/clim/32/14/jcli-d-18-0707.1.xml (visited on 04/28/2022).